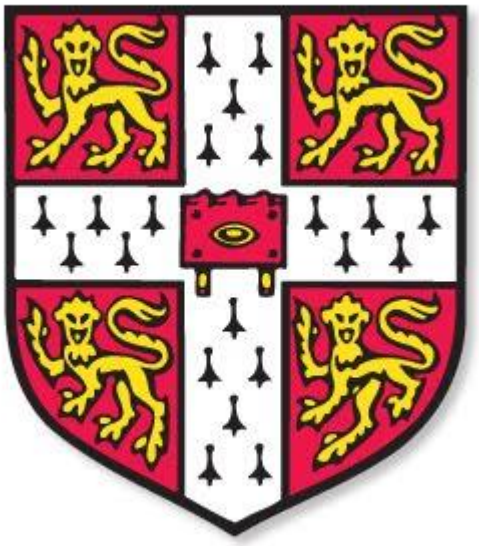

Design Space Exploration for Salt Cooled Reactor Systems

Zhiyao Xing

Department of Engineering

University of Cambridge

This dissertation is submitted for the degree of

Doctor of Philosophy

Hughes Hall

December 2021

I would like to dedicate this thesis to my loving parents,

without whom, I would not have achieved so far.

Declaration

I hereby declare that except where specific reference is made to the work of others, the contents of this dissertation are original and have not been submitted in whole or in part for consideration for any other degree or qualification in this, or any other university. This dissertation is my own work and contains nothing which is outcome of work done in collaboration with others, except as specified in the text and Acknowledgements. This dissertation contains fewer than 65,000 words including appendices, bibliography, footnotes, tables and equations and has fewer than 150 figures.

Zhiyao Xing

April 2021

Design Space Exploration for Salt Cooled Reactor Systems

Zhiyao Xing

Abstract

Fluoride salt-cooled Hight-temperature Reactor (FHR) is a new concept that has seen growing interest as a potential candidate to improve on the safety and economics of existing reactors. It has been suggested that FHR can benefit from advanced Gas-cooled Reactor (AGR) technologies and by that reducing the scale and time of the required R&D. This thesis contributes to the global FHR development effort by proposing and investigating an AGR-like FHR concept. It explored the thermal-hydraulic and neutronic design space of a number of AGR-like FHR assembly options covering combinations of three fuel geometries: 1) solid pin, 2) annular pin and 3) plate type fuel; three coolant options: 1) FLiBe 2) FLiNaK and 3) NaF-ZrF_4, and three fuel forms: 1) Uranium Dioxide (UO_2), Uranium Carbide (UC), and Fully Ceramic Microencapsulated (FCM) fuel. A package of thermal-hydraulic operating domain search and design optimisation codes was created that can identify the optimum primary and secondary loop operating condition and the corresponding maximum power and Levelised Cost of Electricity (LCOE) of the reactor. Based on preliminary thermal-hydraulic test results, which ruled out some of the design options, a series of neutronic analyses were carried out to further narrow down the design space. Neutronic simulations were first performed at Beginning of Life (BOL) conditions to identify design streams that demonstrated potential for the most favourable fuel cycle economic performance and/or other strategic advantages such as accident tolerance of FCM fuels or tritium-free NaF-ZrF_4 coolant. Depletion calculations were then performed for the best performing neutronic designs at BOL. Constrained by reactivity coefficients and burnup while targeting high burnup-to-enrichment ratios (BU/e), four optimised neutronic design streams were recommended: 1) solid UC fuelled FLiBe cooled FHR, 2) solid FCM fuelled FLiBe cooled FHR, 3) annular FCM fuelled FLiBe cooled FHR and 4) solid UC fuelled NaF-ZrF_4 cooled FHR. Thermal-hydraulic calculations were then carried out for these design streams to produce coupled design optimisation. Final optimisation results suggest that solid FCM pin fuelled FHR with FLiBe in AGR-like assemblies is the best design option among all, delivering thermal powers from 16349 MWt to 28861 MWt (~21 times

power uprate from AGR), LCOEs from 35.3 £/MWh to 41.7 £/MWh (less than half of the Hinkley Point C strike price of 92.5 £/MWh) and BU/e ratios from 7.2 MWd/kg to 9.5 MWd/kg, which is comparable to the current fleet of Light Water Reactors (LWRs). Other design streams offer advantages in other aspects such as being tritium-free or having more manageable on-power refuelling schemes or even lower LCOEs.

Acknowledgements

I am so grateful to the many wonderful people who have supported me throughout this work. Dr Eugene Shwageraus, who has been my supervisor since my Masters' studies, has always been a source of encouragement, instruction and patient mentorship throughout my research. His expertise was invaluable in the formulating, exercising and completing of this thesis. I could not have imagined having a better supervisor and mentor for my PhD study.

Besides my supervisor, I would like to thank Dr Dan Kotlyar, and Dr Marat Margulis for their mentorship, guidance, and especially the many work-break conversations we had that have helped me mentally during my four-year PhD journey. My sincere thanks also go to my advisor Dr Geoffrey Parks, who has demonstrated to me the importance of academic rigour and provided me with kind support in my research. I must also thank Mr Tony Roulstone, Dr Ben Lindley and Dr Hassan Mohamed for their guidance since my MPhil years.

I thank my fellow lab mates for the stimulating discussions, and for all the fun we have had in the last four years. I would like to gratefully acknowledge the help from Andy Whyte during my first quest in the field of machine learning in our collaborative FHR design work.

To my dearest friends in Cambridge, London and Beijing, Qi Qi, Yiyang Li, Yi Zhu, Cong Lu, Xinyu Zhao, Yaxin Zhang, Andhika Feri Wibisono, Hao Wang, Jintao Hong, Haode Sun, Zhen Zhen, Rui Li, Xinke Tang, Chang Chang, Zhiyi Pan, Cyndi Zhao, Xi Chao, Zidong Zhang and many more: I would not have survived my PhD without you! To my brothers, Dongdong He, Chunlin Zhao, Peng Peng, Shuchen Zhang: you have been more than brothers-by-blood to me all these years. Without the love and support from you guys, none of my achievements would have been possible.

I would like to thank China Scholarship Council for funding this PhD.

Last but not least, I would like to thank my loving parents for always being unconditionally supportive of me, both spiritually and financially, throughout my education and my life.

Table of Contents

Chapter 1 Introduction 1
1.1 Generation IV Reactor Concepts – The Answer to All? 1
1.2 FHR Answers to Next Generation Nuclear Technology Requirements 1
1.2.1 Manageable Development Timeframe 2
1.2.2 Improved Reliability and Safety 3
1.2.3 Improved Economics 4
1.3 Previous FHR Development 5
1.4 FHR with AGR Design Features 6
1.4.1 The Advanced Gas-Cooled Reactor (AGR) 8
1.4.2 Potential Improvements upon AGR with FHR Concepts 10
1.5 Research Framework and Design Scope 12
1.6 Project Objectives 14
1.6.1 Power Density Maximisation and Tool Development 14
1.6.2 System Thermal-hydraulic Design Optimisation and Tool Development 14
1.6.3 Neutronic Design Optimisation 16
1.6.4 Coupled Neutronic and Thermal-hydraulic Design Optimisation 16
1.7 Organisation of the Thesis 16
Chapter 2 Computational Tools 17
2.1 Thermal-hydraulic Modelling Tools 17
2.1.1 Sub-Channel Thermal-hydraulic and Heat Transfer Solvers in SODom 18
2.1.1 Heat Exchanger and Pump Solvers in optSys 24
2.1.2 LCOE Estimation – Capital Cost Scaling Rule in CapCost 27
2.2 Neutronic Modelling 34
Chapter 3 Preliminary Thermal-hydraulic Design Space Exploration 36
3.1 Preliminary AGR-like FHR Design Options 36
3.1.1 Reference FHR Design – Sold Pin Fuel 36

3.1.2 Alternative FHR Assembly Designs – Annular Pin Fuel 37
3.1.3 Alternative FHR Assembly Design – Plate Type Fuel 40
3.1.4 Coolant Salt Options 42
3.2 Nominal State Safety Limits 43
3.3 Search for Operating Domain 45
3.4 Operating Domain Search Results 47
3.4.1 Operating Domain for the Reference Design 47
3.4.2 Operating Domain for Annular Pin Designs 49
3.4.3 Operating Domain for Plate Type Designs 52
Chapter 4 System Thermal-hydraulic Optimisation 55
4.1 AGR-like FHR Power Plant Layout 55
4.2 Understanding the Optimisation Problem 57
4.3 System Thermal-hydraulic Design Optimisation with sysOpt 60
4.4 Identifying the Optimum Core and System Operating Parameters with SCOOP 62
4.4.1 Sensitivity Studies of the Capital Cost Scaling Model 63
Chapter 5 Preliminary Neutronic Design Space Search 67
5.1 Assembly-Level Neutronic Design Space 67
5.1.1 General Discussion on Neutron Spectrum and CTC 70
5.2 Initial Neutronic design Space Search Results 71
5.2.1 Effect of Material Choices on k_∞ and CTC 73
5.2.2 Effect of Assembly Configuration on k_∞ 74
5.2.3 Effect of Assembly Configuration on CTC 77
5.2.4 Effect of Fuel Enrichment on k_∞ and CTC 79
5.2.5 Summary of Assembly Model Neutronics 82
5.3 Single Pin Unit Cell Model 84
5.3.1 Comparison of Assembly and Unit Cell Models 87
Chapter 6 Unit Cell Model Neutronic Design 92

6.1 Unit Cell Level Neutronic Design Space 92
6.2 BOL Neutronic Sensitivities Studies - Solid Pin Model 94
6.2.1 Effect of P/D, Salt Fraction and Enrichment on BOL k_∞ 95
6.2.2 Effect of Pitch to Diameter ratio on CTC 98
6.2.3 Effect of Salt Fraction on CTC 100
6.2.4 Effect of Fuel Enrichment on CTC 103
6.2.5 BOL Neutronic Performance Optimum Frontier 104
6.2.6 BOL Neutronic Performance Domain Sensitivities 107
6.3 BOL Neutronic Performance Domains for Alternative Designs 109
6.3.1 Annular Pin Fuel Designs 109
6.3.2 Plate Type Fuel Designs 112
6.4 Unit Cell Models Neutronic Performance Domain Summary 114
Chapter 7 Unit Cell Model Depletion Analysis 116
7.1 Unit Cell Models Depletion Analysis 116
7.1.1 Solid UC pin FLiBe Cooled FHR 117
7.1.2 Alternative Design - Solid FCM pin FLiBe cooled FHR 124
7.1.3 Alternative Design - Annular FCM pin FLiBe Cooled FHR 125
7.1.4 Alternative Design - Solid UC pin NaF-ZrF4 Cooled FHR 126
7.2 Unit Cell Depletion Analysis Summary 126
Chapter 8 Bringing Together Thermal-hydraulics and Neutronics 129
8.1 Revisiting Thermal-hydraulics with Extended Design Space 129
8.2 Thermal-hydraulic Results in the Extended Design Space 132
8.2.1 Effect of P/D and SF on Maximum Achievable Power 132
8.2.2 Effect of P/D and SF on LCOE 134
8.2.3 Effect of Core Pressure Drop on Maximum Achievable Power and LCOE 137
8.2.4 Discussion of Thermal-hydraulic Results 139
8.3 FHR Design Accounting for both Neutronics and Thermal-hydraulics 141

8.3.1 AGR-like FHR Design 142
8.3.2 PWR-like FHR Design 146
8.4 Thermal-hydraulic and Neutronic Design summary 153
Chapter 9 Conclusions and Future Work 155
9.1 Thesis Summary 155
9.2 Summary of Research Findings 156
9.2.1 Summary of Neutronic Design Optimisation Findings 157
9.2.2 Summary of Thermal-hydraulic Design Optimisation Findings 159
9.2.3 Summary of Multi-objective Neutronic and Thermal-hydraulic Design Findings 161
9.3 Discussions on FHR Design Options 163
9.4 Recommendations for Future Work 166
9.4.1 Refinement of Assumptions 166
9.4.2 Refinement of Computational Tools 167
9.4.3 Further Work on Reactor Design, Materials and Engineering 169
References 172
Appendix A - FHR Technology Background 177
Appendix B – Benchmark of TH_Sol with THERMO 188
Appendix C – Verification of calcHX model 190
Appendix D – Verification of sizeHX model 193
Appendix E –Power Scaling vs Heat Transfer System Cost Scaling 196
Appendix F – Alternative Unit Cell Depletion Results 198
Appendix G – Effects of P/D and SF on LCOE and Power for Annular Pin FHRs 206

List of Figures

Figure 1-1. Illustration of a TRISO fuel particle 3
Figure 1-2. Evolution of FHR pebble bed reactors 6
Figure 1-3. FHR FIRM test reactor assembly and an AGR-like FHR 8
Figure 1-4. AGR core layout – nearly ¼ core symmetry 9
Figure 1-5. Interconnection of graphite bricks with keys 9
Figure 1-6. Illustration of an AGR fuel element 10
Figure 1-7. Examples of 2-D AGR-like FHR models 13
Figure 1-8. Proposed simplified FHR plant layout 15
Figure 2-1. Flow chart for SCOOP 18
Figure 2-2. Effect of heat exchanger frontal area on the cost of heat transfer unit. 26
Figure 3-1. 2-D Serpent models for 3-ring and 4-ring AGR-like FHR designs 37
Figure 3-2. 2D Serpent models for 3-ring and 4-ring annular fuel AGR-like FHR designs 39
Figure 3-3. Serpent models for 5-plate Sleeved assembly and 6-plate No-Sleeve assembly 40
Figure 3-4. Schematic plot of hot channel core component temperatures and LSSS limits 45
Figure 3-5. Schematic plot of operating domain of an example FHR. 46
Figure 3-6. Allowable Reactor Power for different reference plate type fuel designs 52
Figure 3-7. Trade-off between power output and reactor heavy metal loading 54
Figure 4-1. Proposed FHR plant layout 56
Figure 4-2. Cross-sectional view of an example PCHE 57
Figure 4-3. Schematic T-S diagram for the FHR. 58
Figure 4-4. Interdependencies of operating conditions with power density, heat exchanger cost and pump cost 60
Figure 5-1. Examples 2-D Serpent models of proposed FHR assembly designs 69
Figure 5-2. BOL CTC vs BOL k_∞ performance domain for all searched assembly designs 72
Figure 5-3. Non-positive BOL CTC part of the BOL CTC vs BOL k_∞ performance domain 72
Figure 5-4. Vm/Vf effects on BOL k_∞ for different coolants and channel radii 74
Figure 5-5. V_m/V_f effects on BOL CTC for different coolants and channel radii 77
Figure 5-6. V_{cool_c}/V_f effects on BOL CTC for different coolants and channel radii 79
Figure 5-7. Effects of U235 enrichment on BOL k_∞ for different number fuel rings and channel radii with FLiBe coolant 80
Figure 5-8. Effects of U235 enrichment on BOL CTC for different number fuel rings and channel radii with FLiBe coolant 81

Figure 5-9. BOL CTC vs k_∞ performance trade-off for FLiBe cooled FHRs with different radii and U235 enrichments....82
Figure 5-10. BOL CTC vs k_∞ performance for selected best assembly designs....84
Figure 5-11. Unit cell model of FHR (not to scale) 86
Figure 5-12. Comparison of BOL CTC variation with P/D in pin and assembly models 88
Figure 5-13. Comparison of BOL k_∞ variation with P/D in pin and assembly models....90
Figure 5-14. Comparison of BOL neutronic performance space of pin and assembly models91
Figure 6-1. a) annular fuel model with FCM fuel, 2) annular fuel with UC fuel, 3) solid pin model with FCM fuel and d) plate type fuel model (x-z cross-section) with FCM fuel.....93
Figure 6-2. Effects of P/D on BOL k_∞ for FLiBe cooled unit cell models (5 wt% and 12.5 wt% enrichments)....95
Figure 6-3 Effects of P/D on BOL k_∞ for NaF-ZrF_4 cooled unit cell models (5 wt% and 20 wt% enrichments)....97
Figure 6-4 Effects of P/D on BOL CTC for FLiBe cooled models (7.5 wt% enrichment) 99
Figure 6-5 Effects of P/D on BOL CTC for NaF-ZrF_4 cooled unit cell models (5 wt% and 20 wt% enrichments)....100
Figure 6-6. Effects of SF on BOL CTC for FLiBe cooled unit cell models (7.5 wt% enrichment) 101
Figure 6-7. Effects of SF on BOL CTC for NaF-ZrF_4 cooled unit cell models (7.5wt% enrichments)....102
Figure 6-8. One-group U238 absorption XS vs. P/D (7.5 wt% enrichment) 103
Figure 6-9. Effects of fuel enrichment on BOL CTC for FLiBe cooled FHR (P/D = 3.2) 103
Figure 6-10. BOL CTC vs k_∞ performance domain a) grouped by enrichment b) grouped by SF for FLiBe cooled FHR....105
Figure 6-11. BOL CTC vs k_∞ grouped by P/D for $4 \leqslant P/D \leqslant 6.4$ for FLiBe cooled FHR .106
Figure 6-12. BOL CTC vs k_∞ grouped by P/D for $4 \leqslant P/D \leqslant 6.4$ for NaF-ZrF_4 cooled FHR 106
Figure 6-13. BOL CTC vs k_∞ performance domains for solid pin type FLiBe and NaF-ZrF4 cooled FHR 108
Figure 6-14. BOL CTC vs k_∞ performance domains for annular pin type FLiBe and NaF-ZrF_4 cooled FHR 109
Figure 6-15. BOL CTC vs k_∞ domain for annular pin FCM fuel FLiBe cooled FHR....110

Figure 6-16. BOL CTC vs k_∞ performance domain a) (up) grouped by enrichment b) (down) grouped by SF for annular FCM pin FLiBe cooled FHR 111
Figure 6-17. BOL CTC vs k_∞ performance domain a) (up) grouped by enrichment b) (down) grouped by SF for Plate FCM fuel NaF-ZrF_4 cooled FHR 113
Figure 6-18. BOL CTC vs k_∞ performance optimum frontiers for all selected design streams 115
Figure 7-1. Depletion curves for all selected solid UC pin FLiBe cooled unit cell models .. 118
Figure 7-2. CTC behaviour with depletion for solid UC pin FLiBe cooled unit cell models 119
Figure 7-3. DC behaviour with depletion for solid UC pin FLiBe cooled unit cell models .. 120
Figure 7-4. BOL CTC vs BU/e performance domain for solid UC pin FLiBe cooled models 121
Figure 7-5. BOL DC vs BU/e performance domain for solid UC pin FLiBe cooled models 121
Figure 7-6. BU/e vs burnup for solid UC pin FLiBe cooled FHR with different enrichments 122
Figure 8-1. Schematic plot of operating domain using safety constraints. 131
Figure 8-2. Effect of P/D on maximum allowable power for FLiBe cooled solid UC pin FHR 133
Figure 8-3. Effect of SF on maximum allowable power for FLiBe cooled solid UC pin FHR 133
Figure 8-4. Effect of P/D on LCOE for FLiBe cooled solid UC pin FHR..... 135
Figure 8-5. Effect of SF on LCOE for FLiBe cooled solid UC pin FHR 136
Figure 8-6. Effect of coolant pressure drop on maximum allowable power for FLiBe cooled solid UC pin FHR..... 138
Figure 8-7. Effect of coolant pressure drop on LCOE for FLiBe cooled solid UC pin FHR 139
Figure 8-8. Illustrations of PWR-like FHR deigns. a) graphite content > 0 and are wrapped around the PWR-like assembly in form of a sleeve; b) graphite content = 0 147
Figure 8-9. Polynomial fit of LCOE against P/D for PWR-like designs mapped from AGR-like assembly models with 36 pins..... 149
Figure 9-1. LCOE vs reactor power for all optimised unit cell neutronic models..... 159
Figure A-1. Cut-away view of the Mk1 core and reactor vessel 178
Figure A-2. Schematic plot of the PB-FHR power plant 178
Figure A-3. Comparison of the original LS-VHTR core to an improved design 179
Figure A-4. Cross-sectional view of the LS-VHTR prismatic fuel assembly..... 180

Figure A-5. Basic (top-left) and clustered-rod fuel block configurations of the AHTR.....181
Figure A-6. Stringer-type fuel assmelby evaluted for use with SmAHTR 182
Figure A-7. Annular-pin stringer type fuel bundle evaluated for use in the SmAHTR.....183
Figure A-8. Cross-sectional view of the SmAHTR plate-type fuel assembly 184
Figure A-9. Isometric view of a plate-type fuel assembly for the SmAHTR 184
Figure A-10. Cross-sectional view of the SmAHTR core 185
Figure A-11. Cross-sectional view of the AHTR plate-type fuel assembly.....186
Figure A-12. Cross-sectional View of the updated AHTR fuel plate (dimensions in cm) 187
Figure B-1. Absolute Error in temperature profiles between TH_Sol and THERMO 189
Figure C-1. Channel arrangement of PCHE used in the benchmark study.....191
Figure E-1. Relationship between power scaling and heat transfer system cost scaling 196
Figure F-1. Depletion curves for all selected solid pin FCM pin FLiBe cooled models 198
Figure F-2. CTC depletion behaviour for solid UC pin FLiBe cooled models.....198
Figure F-3. DC depletion behaviour for solid UC pin FLiBe cooled models.....199
Figure F-4. BOL CTC vs BU/e performance domain for solid FCM pin FLiBe cooled models 199
Figure F-5. BOL DC vs BU/e performance domain for solid FCM pin FLiBe cooled models 200
Figure F-6. Depletion curves for all selected annular pin FCM pin FLiBe cooled models...200
Figure F-7. CTC depletion behaviour for annular pin FCM pin FLiBe cooled models 201
Figure F-8. DC depletion behaviour for annular pin FCM pin FLiBe cooled models.....201
Figure F-9. BOL CTC vs BU/e domain for annular FCM pin FLiBe cooled models 202
Figure F-10. BOL CTC vs BU/e domain for annular FCM pin FLiBe cooled models 202
Figure F-11. Depletion curves for solid pin UC pin NaF-ZrF_4 cooled models.....203
Figure F-12. CTC depletion behaviour for solid pin UC pin NaF-ZrF_4 cooled models 203
Figure F-13. DC depletion behaviour for solid pin UC pin NaF-ZrF_4 cooled models 204
Figure F-14. BOL CTC vs BU/e domain for solid UC pin NaF-ZrF_4 cooled models.....204
Figure F-15. BOL DC vs BU/e domain for solid UC pin NaF-ZrF_4 cooled models.....205
Figure G-1. Maximum achievable power vs SF and fuel thickness for annular pin FHRs ...206
Figure G-2. LCOE vs SF and fuel thickness for annular pin FHRs.....206
Figure G-3. Maximum achievable power vs P/D and fuel thickness for annular pin FHRs..207
Figure G-4. LCOE vs P/D and fuel thickness for annular pin FHRs.....207

List of Tables

Table 2-1. Breakdown of costs for the FOAK next generation PWRs 32
Table 3-1. Annular fuel assembly design specifications.....39
Table 3-2. Specifications for reference plate type FHR assembly designs.....41
Table 3-3. TRISO particle fuel specifications.....41
Table 3-4. Safety Criteria and limits for different coolant and fuel materials 43
Table 3-5. Specifications for the proposed solid pin FHRs 48
Table 3-6. Design specifications for 3-ring, 4-ring and 5-ring annular pin assemblies compared with reference AGR fuel assembly 50
Table 3-7. Maximum power and corresponding operating conditions for annular fuel FHRs 51
Table 4-1. Summary of recommended design details for the reference FHR.....63
Table 4-2. Sensitivity of SCOOP results to specifics of the reference reactor in CapCost 64
Table 4-3. Sensitivity of SCOOP results to the value of n_R.....65
Table 4-4. Sensitivity of SCOOP results to the values of A_R and B_R.....66
Table 5-1. Dimensions of all proposed assembly designs 68
Table 5-2. Design specifications for selected best assembly designs 84
Table 7-1. Specifications of best FLiBe cooled UC solid pin designs.....124
Table 7-2. Specifications of best FLiBe cooled FCM solid pin designs.....125
Table 7-3. Specifications of best FLiBe cooled FCM annular neutronic models.....125
Table 7-4. Specifications of best neutronic designs across all four selected design streams.127
Table 8-1. FCM fuelled annular pin FLiBe cooled designs with lowest LCOEs 140
Table 8-2. Solid pin designs with lowest LCOEs 140
Table 8-3. Best AGR-like neutronic models.....143
Table 8-4. Best thermal-hydraulic models matching the best AGR-like neutronic models ..143
Table 8-5. Best solid FCM fuel pin neutronic design with lowest P/D 144
Table 8-6. Best thermal-hydraulic design matching the best solid FCM fuel pin neutronic model with lowest P/D.....144
Table 8-7. Optimised AGR-like FHR designs 145
Table 8-8. Best PWR-like neutronic models.....148
Table 8-9. Optimised PWR-like FHR designs with solid FCM fuel pins.....148
Table 8-10. Optimised PWR-like solid UC fuel pin designs 150
Table 8-11. Projected specifics for the optimised annular FCM pin FHR.....152
Table 9-1. Thermal-hydraulic models with lowest LCOEs 161

Table 9-2. Specifications of final optimised FHRs 162
Table B-1. TH_Sol-THERMO benchmarking test case specifications 188
Table D-1. Benchmarking results for an example primary heat exchanger condition 195
Table D-2. Benchmarking results for an example heat exchanger using CO_2 195
Table E-1. Comparison of heat transfer system cost ratio and power ratio 197

Acronyms and Abbreviations

AGR	Advanced Gas-cooled Reactor
AHTR	Advanced High Temperature Reactor
BDBA	Beyond Design Basis Accident
BEIS	Department of Business, Energy & Industrial Strategy
BOL	Beginning of Life
BU	Burnup
BU/e	Burnup to Enrichment Ratio
COA	Code of Accounts
COE	Cost of Electricity
CTC	Coolant Temperature Coefficient
D&D	Decontamination and Decommissioning
DC	Doppler Coefficient
DOE	Department of Energy
DRACS	Direct Reactor Auxiliary Cooling System
EEDB	Energy Economic Data Base
EWMG	Economic Modelling Working Group
FCM	Fully Ceramic Microencapsulated
FCR	Constant Dollar Fixed Charge Rate
FHR	Fluoride Salt Cooled Reactor
FIRES	Firebrick Resistance-heated Energy Storage
FIRM	Fuel In Radial Moderator
FLiBe	$2LiF\text{-}BeF_2$
FLiNaK	LiF-NaF-KF

FOAK	First of a Kind
GFR	Gas Cooled Fast Reactor
GIF	Generation IV International Forum
HM	Heavy Metal
HTR	High Temperature Recuperator
HX1	Primary heat exchanger
HX2	Secondary heat exchanger
INL	Idaho National Laboratory
IPyC	Inner Pyro Carbon
k_∞	Neutron multiplication factor
LCC	Levelised Capital Cost
LCOE	Levelised Cost of Electricity
LEU	Low-enriched Uranium
LFR	Lead Cooled Fast Reactor
LMTD	Log Mean Temperature Difference
LTR	Low Temperature Recuperator
LWR	Light Water Reactor
MSR	Molten Salt Reactor
MSRE	Molten Salt Reactor Experiment
NACC	Nuclear Air Brayton Combined Cycle
NEA	Nuclear Energy Agency
NPP	Nuclear Power Plant
OCC	Overnight Capital Cost
O&M	Operations and Maintenance

OECD	Organisation for Economic Co-operation and Development
OPyC	Outer Pyro Carbon
ORNL	Oak Ridge National Laboratory
P&C	Predictor and Corrector
P/D	Pitch to diameter ratio
PCHE	Printed Circuit Heat Exchangers
Re	Reynolds number
sCO_2	Supercritical Carbon Dioxide
SCOOP	Search of Core Optimum Operating Parameters
SCWR	Super-Critical Water-Cooled Reactor
SFR	Sodium Cooled Fast Reactor
SiC	Silicon Carbide
SNL	Sandia National Laboratories
SODom	Search of Operating Domain
S-PRISM	Super Power Reactor Inherently Safe Module
TRISO	Tristructural Isotropic
UC	Uranium-carbide
UCB	University of California, Berkeley
UO_2	Uranium-dioxide
VHTR	Very High Temperature Reactor

Chapter 1 Introduction

The Fluoride Salt Cooled Reactor (FHR) was studied in this thesis as a way of providing a feasible solution to the requirements of the future energy market as well as meeting strategic goals of many countries. In particular, this work proposed an alternative reactor concept to the current FHR class that leverages the British Advanced Gas-cooled Reactor (AGR) technologies. This could to a great extent utilise and preserve the UK nuclear development legacy and experience from the current fleet of AGRs, while providing new opportunities to the technical challenges faced by other FHR development branches.

1.1 Generation IV Reactor Concepts – The Answer to All?

Since January 2000, the Generation IV International Forum (GIF) has been evaluating and documenting the development of the next (fourth) generation nuclear reactor technology. Six reactor concepts have been selected by GIF, namely, Very High Temperature Reactor (VHTR), Sodium Cooled Fast Reactor (SFR), Super-Critical Water-Cooled Reactor (SCWR), Gas Cooled Fast Reactor (GFR), Lead Cooled Fast Reactor (LFR), and Molten Salt Reactor (MSR). All six reactor concepts offer substantially improved safety and non-proliferation and economic features. However, Gen IV technologies are still far from being mature for near term commercialisation for them to make significant contributions before the environment problems become irreversibly severe.[1] From the latest Technology Roadmap Update [2] for Generation IV Nuclear Energy Systems published by Nuclear Energy Agency (NEA) of the Organisation for Economic Co-operation and Development (OECD) on behalf of GIF, none of the six proposed six Gen IV reactors have the potential to be ready for a large-scale commercial deployment before mid-to-long term (2030-2050) time frame. Furthermore, the problem of unstable electricity price due to mismatching of energy demand and supply in the free electricity market with large penetration of renewables remains poorly addressed by the use Gen IV technology alone.

1.2 FHR Answers to Next Generation Nuclear Technology Requirements

To meet the carbon emission reduction requirement and maintain a well-functioning and flexible energy market as soon as possible. One logical solution is to take a step back from the conceptual Gen IV technologies and exploit the experience accumulated in the past during the development of existing nuclear technologies.

Adhering to this philosophy, FHR is identified as one of the best reactor candidates for this task. FHR is envisaged to offer similar level of performance in many aspects as other advanced Gen IV reactor types. It has a shorter and therefore more manageable development schedule which makes FHR a more practical candidate compared with other Gen IV reactors to become the first fleet of next generation reactors.

1.2.1 Manageable Development Timeframe

Initially proposed by C. Forsberg (ORNL), P. Peterson (UCB) and P. Pickard (SNL) in 2003, [3] FHR, the salt-cooled solid fuel high temperature reactor, is a middle step towards the Gen IV MSR (liquid fuel) and HTGR (pebble bed with high operating temperature) technologies. Most of the technical developments needed for FHR are also needed for MSR or HTGR. This allows a smoother and more timely transition from the current LWR-dominated era to the future advanced nuclear systems.

FHR incorporates a combination of state-of-the-art and off-the-shelf technologies from recent developments, providing economic value and technological certainty. Various conceptually mature FHR designs have been proposed, all of which use high temperature Tristructural Isotropic (TRISO) coated particle fuel and molten salt coolant. TRISO particle fuel is initially developed for High Temperature Gas Cooled Reactors such as AVR. [4] Molten salt was first introduced to reactor technology as coolant and fuel carrier in Molten Salt Reactor Experiment (MSRE) in ORNL from 1964 to 1969 and was then studied in the development of Molten Salt Reactors. Extensive experiments and simulations have been carried out around the application of molten salt in reactor technology. The accumulated knowledge and experience, such as the understanding of chemistry and thermal-hydraulics of molten salt can be directly applicable to FHR. FHR operates with coolant core outlet temperature of up to 700 °C and can be coupled to high temperature power conversion cycles designed for gas-cooled reactors such as AGRs and VHTRs. Experience in high temperature Air Brayton Power Cycle and structural alloys can also be adopted from coal power plants. Off the shelf gas turbine technology can be directly coupled to FHR's high temperature power conversion cycle. [3] Also, passive decay heat removal systems such as Direct Reactor Auxiliary Cooling System (DRACS) can be adopted directly from Gen IV Liquid Metal Cooled Reactors such as General Electric's Super Power Reactor Inherently Safe Module (S-PRISM). DRACS employs a natural circulation heat-transport loop that moves the decay heat from the primary coolant pool to a heat exchanger outside the core submerged in. [5] With a similar working environment as MSRs and Liquid

Metal Reactor, FHRs can directly take advantage of the previous development on these technologies. [5~8]

1.2.2 Improved Reliability and Safety

One of the three design goals of FHR is to assure no major fuel failure occurs during Beyond Design Basis Accidents (BDBAs). [3] FHR's safety features derive from sound engineering design and inherent material properties.[7] The TRISO particle which the baseline FHR uses is a very safe form of fuel. [9] As shown in Figure 1-1, a TRISO particle contains a fuel kernel surrounded by a porous graphite buffer layer, and successive isotropic layers of dense inner pyro carbon (IPyC), chemically vapor deposited SiC and a dense outer pyro carbon (OPyC) layer. This structure allows TRISO particles to maintain integrity under high temperature and irradiation so that fission products produced in the fuel kernel are reliably trapped inside the layers. A conservative estimate for TRISO particles temperature limit for fuel failure is 1600 °C. The actual material temperature limit may well be higher. The complicated structure also exhibits non-proliferation features. [10][11]

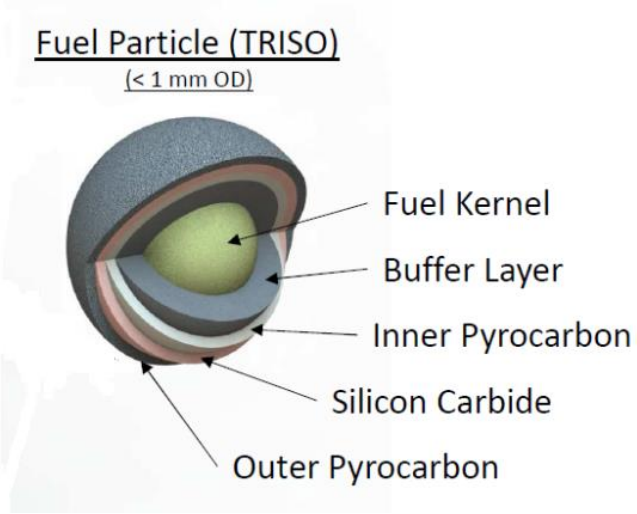

Figure 1-1. Illustration of a TRISO fuel particle [12]

Notwithstanding, FHR does not rely exclusively on TRISO fuel for its safety performance. Its inherent safety also derives from unique reactor design: the use of molten salt and graphite allows the core to have good heat transfer properties and its neutronic design with favourable reactivity feedback coefficients. FHR also incorporates both Reactor Vessel Air Cooling

System (RVACS) [9] and DRACS that allows passive natural convection-driven heat removal from the core. The molten salt coolant in FHRs also have many desirable properties: low viscosity, high density, high specific heat capacity, good conductive and convective heat transfer properties. This makes heat removal more efficient and requires less pumping effort for fixed reactor power and temperature rise across the core. In some proposed designs, the primary vessel is submerged in a pool of secondary cheap salt which serves as radiation shield and an effective heat sink. The structure implies that there are multiple layers of radioactivity containment. This also provides the core with a large thermal inertia and allows more grace time for accident management. The FHR core operates at atmospheric pressure thanks to the working temperature range of its molten salt coolant. This makes FHR operation much safer than LWRs or HTGRs which require high pressure to operate. [3][7]

1.2.3 Improved Economics

FHR has the potential to present a better investment scenario than other advanced reactor concepts do for potential investors. The economics goal of FHR under the US IRP is to increase nuclear power's revenue by 50% to 100% from the current baseload LWRs. [13]

Initial cost investment is the biggest component in the lifetime cost of a nuclear reactor, and most of the initial investment goes to the reactor construction. Having the thermal-hydraulic potential to reach high power densities, FHRs can substantially reduce the capital costs. Low operating pressure also waives the requirement for a high-performance pressure vessel. Additionally, FHR has a high coolant outlet temperature of ~ 700 °C, which allows many power conversion schemes to be applied. It is able to deliver industrial grade heat directly or coupled with advanced high temperature Brayton power cycle with significantly higher conversion efficiency compared with the current nuclear power plants or can be combined with traditional gas-fired power turbines to allow fast reaction to changing electricity grid demand. This latter concept was proposed by C. Forsberg and P. Peterson, [14] and known as the Nuclear Air Brayton Combined Cycle (NACC) and Firebrick Resistance-Heated Energy Storage (FIRES) concept. These ideas comprise a strong cost reduction argument for FHRs economic performance.

Traditional nuclear reactors are struggling to compete with other types of baseload energy forms, especially as the price of natural gas has dropped after significant investment in shale gas extraction technologies in the US. The recent increase in the deployment of renewables in the global energy portfolio has resulted in large electricity price variations. Since power turbine

in the NACC always spins at hot conditions, it allows fast response time and therefore efficient integration into energy grids with high proportion of renewables. When the demand for electricity increases, the power output could be nearly instantly increased (doubled in the case of the reference pebble bed FHR design by C. Forsberg et.al) to generate and sell electricity in periods of high electricity price. The FIRES enables an FHR power plant to buy, store and sell energy flexibly from and to the electricity market depending on its demand. When the electricity price is less than gas (or coal or other baseload energy sources, depending on local energy mix) price per unit energy, electricity would be bought from the grid to electrically heat up a large store of fire bricks (FIRES). In this case, the baseload electricity generation by FHR would also be stored to FIRES for later sales to the grid when electricity price goes up. Similar logic can be applied when the electricity price is higher than that of gas per unit energy. High temperature process heat could also be sold to industries when the price is more desirable than energy-equivalent electricity. [3][13]

1.3 Previous FHR Development

Based on the 2002 Gen VI VHTR design, the first reactor that falls under the FHR class, the Liquid Salt cooled Very High Temperature Reactor (LS-VHTR), was studied in ORNL in 2004. While being a large reactor (2400 MWt) with very high coolant outlet temperature (1000 °C), the LS-VHTR has the core configuration and complexity similar to small modular reactor S-PRISM and, therefore, benefits from both the economies of scale and high power conversion efficiency.[15] Its assembly design was mostly derived from the prismatic block variant of VHTR. A more detailed description of the LS-VHTR design is included in Appendix A. The LS-VHTR became the design basis for ORNL's subsequent Advanced High Temperature Reactor (AHTR) (2400 MWt) and its small modular version, the Small-modular Advanced High Temperature Reactor (SmAHTR) (125 MWt). [16] The SmAHTR explored many alternative assembly options during its design evolution. Some of its design variants chose the clustered-rod fuel block configuration where the fuel rods are closely packed in single large coolant channels inside a graphite block, resembling the AGR assembly. The final baseline assembly designs for the AHTR and SmAHTR both incorporate flat fuel plates in hexagonal carbon boxes, only with small differences in dimensions, fuel plate composition and assembly arrangements. The Appendix A includes a description of the AHTR and the design evolution of the SmAHTR.

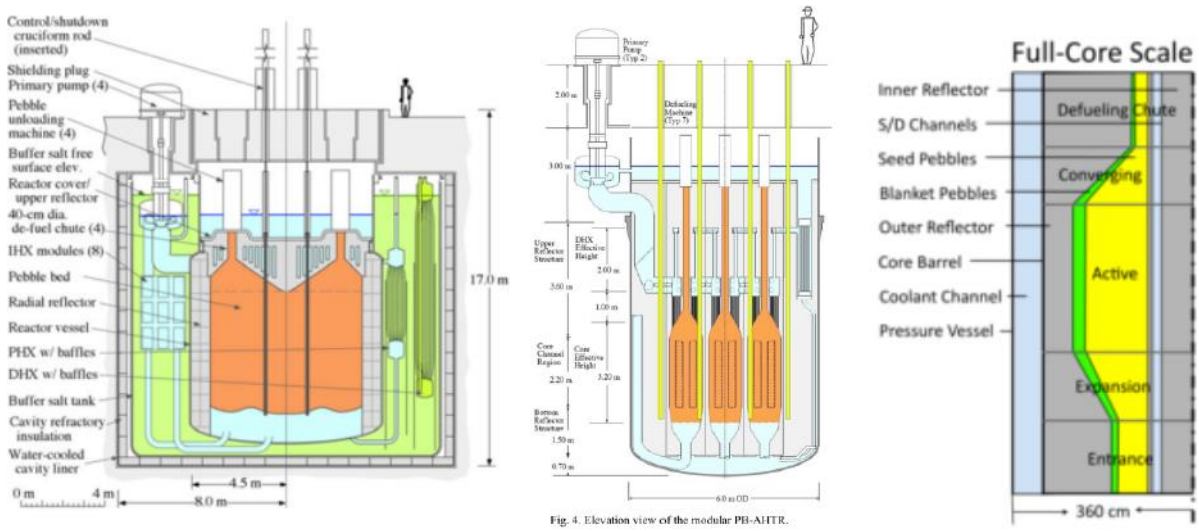

Figure 1-2. Evolution of FHR pebble bed reactors: Integral PB-AHTR(left); Modular P-AHTR; Annular PB-AHTR (right) [17]

In 2006, the pebble bed design concept was proposed by Zwaan and the FHR branched into another design stream, i.e., the pebble bed design. UC Berkeley proposed an integral pebble bed AHTR (PB-AHTR) fuelled using pebbles from the South African PBMR program in an unstructured cylindrical channelled pebble bed core. [18] Several additional design variations were later studied in the UC Berkeley PB-AHTR design branch, such as a modularised PB-AHTR, which incorporates modified pebble channel assemblies to allow higher fuel loading in pebbles and reduce spent fuel and coolant volume. [19] In 2009, PB-AHTR evolved into an annular core configuration with central and outer reflectors. [20] This configuration led to the later Mark-1 (Mk1) FHR. Mk1 FHR have since become the most mature pebble bed FHR design, and often referred to as the FHR at the time of this thesis writing. It is a small modular reactor (236 MWt, 100 MWe) with an annular shaped pebble bed core. Many desirable features of FHR described previously, such as the use of RVACS and DRACS for passive safety, NACC and FIRES for improved economic performance, were developed for the Mk-1 FHR. Figure 1-2 illustrates some core designs along the evolution of the pebble bed FHR. A more detailed description of Mk1 PB-FHR is included in Appendix A.

1.4 FHR with AGR Design Features

The pebble bed FHRs have many unique advantages such as improved safety and non-proliferation features. However, there are concerns around the inherent uncertainty of the positions of the pebbles in the core and the high cost of the pebbles. In addition, pebble online

recirculation associated problems such as reactivity control and online burnup detection and refuelling system are also new to the nuclear industry. Although previous experience with high temperature gas cooled reactors such as AVR proved the feasibility of the pebble bed, the FHR has a different core environment that requires new knowledge of fluid mechanics and chemistry.

In contrast, the prismatic block type FHR requires less technical innovation by using the more well understood assembly configuration. However, there is limited work done for the prismatic block FHR stream aside from the ORNL's research on its AHTR family, which has chosen the 'flat plate fuel in hexagonal carbon box' design. Although, some alternative assembly configurations have been studied, such as clustered fuel rods in graphite blocks in ORNL during the evolution of SmAHTRs, they were not designed for large commercial size reactors. [21]

In support of the FHR development effort, this thesis explored a new prismatic block type FHR concept with future commercialisation potential. It leverages the British AGR technology, a mature technology that has provided baseload power for the UK for over four decades. The idea of developing FHR using AGR technology was first proposed 2015 [22]. It was recognised that many of the neutronic, materials and engineering problems faced by the FHR designers' community have, to a large extent, been already dealt with during the development and operation of existing AGRs in the UK's. Some of the prismatic block type FHR designs are similar to the AGR. This is evident from the design evolutions of LS-VHTR and the AHTR pin-type fuel, as explained earlier [21] , where the coolant channels are made progressively larger and with greater clustering of fuel rods to achieve better neutronic and thermal-hydraulic performance. Such evolution of designs was driven by the requirement to increase burnup and reduce parasitic neutron absorption. This is a fundamental design strategy seen in CANDUs and AGRs: fast neutrons are born in the clustered fuel zones, moderated with minimum neutron loss to U238 resonance absorption in the moderator regions that are physically separated from the fuel zones, then, after being thermalised, migrate back to the fuel regions to sustain chain reaction. The recently developed "Fuel In Radial Moderator" (FIRM) fuel assembly concept for application in FHR test reactor evolved as a result of an optimisation process and arrived at a design that can be easily modified into an AGR-like assembly, except that the coolant channels were made into smaller individual channels arranged in a hexagonal lattice together with the fuel channels. The dimensions were also similar to AGR assembly [22]. Figure 1-3 illustrates the FIRM FHR design and the potential AGR-like FIRM design.

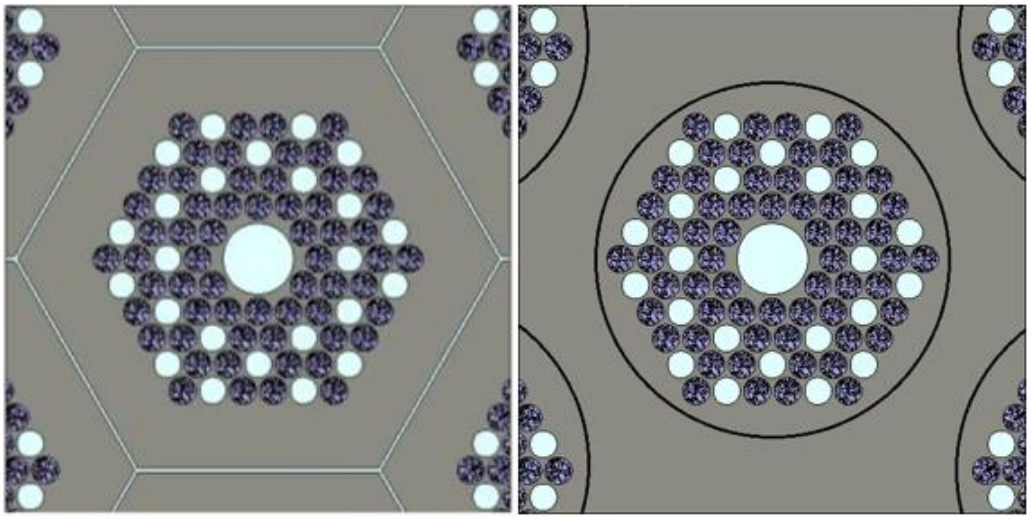

Figure 1-3. FHR FIRM test reactor assembly (top) and an AGR-like FHR (bottom) [22]

1.4.1 The Advanced Gas-Cooled Reactor (AGR)

The AGRs have operated in the UK for over four decades and evolved significantly over the years. There is great amount of valuable experience accumulated over decades of AGR design and operations that can be translated to benefit FHR development. Examples of such include understanding of material characteristics and behaviour in high temperature operation (especially graphite), graphite fabrication, spent fuel management, refuelling operations, power plant component manufacturing, etc. AGRs can operate with core outlet coolant temperatures of up to 675 ºC, the highest among all reactors in operation worldwide and therefore the most thermodynamically efficient. [23]

The core configuration of latest AGR, Torness, was adopted as the reference AGR core for this thesis. The Torness core contains 332 fuel channels inside cylindrical graphite blocks that are locked together with square graphite bars ('keys'). Each fuel assembly located in a fuel channel contains two concentric graphite sleeves, within which, there are eight fuel elements stacked axially and connected with a central stainless-steel tie bar. Each element consists of three circular rings of solid Uranium Dioxide (UO_2) pins (36 pins in total), 14.5 mm in diameter, protected with a stainless-steel cladding of 0.38 mm thick. No information was found for the dimension of the gap between the pellet and the cladding, which itself changes with fuel depletion. For all thermal-hydraulic design work in this thesis, the gap is assumed to be 0.002 cm. The fuel-containing active core is 830 cm tall, and the assemblies are 1036 cm in total

length. [23] Figure 1-4 to Figure 1-6 show the core configuration of a typical AGR, the assembly and key structure, and the cutaway view of a standard AGR fuel element.

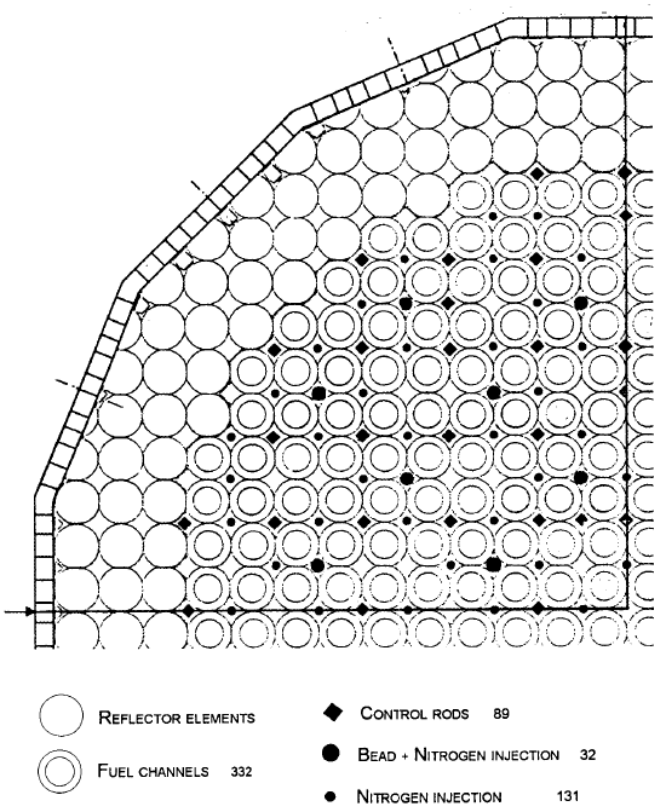

Figure 1-4. AGR core layout – nearly ¼ core symmetry [24]

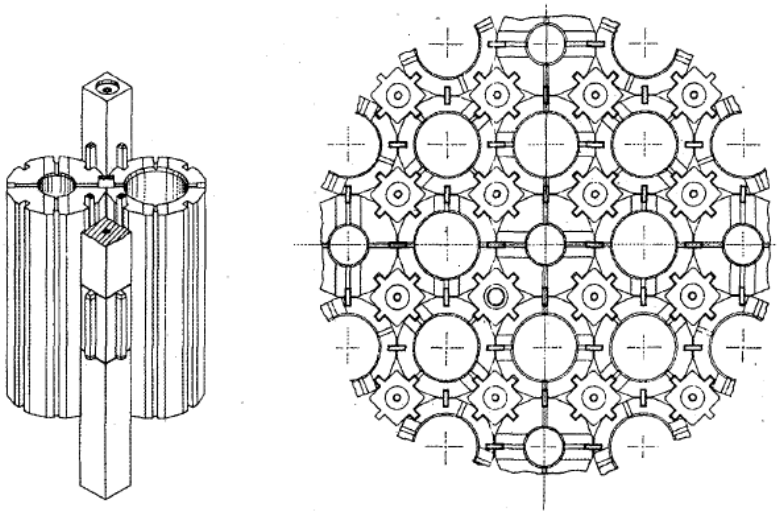

Figure 1-5. Interconnection of graphite bricks with keys [24]

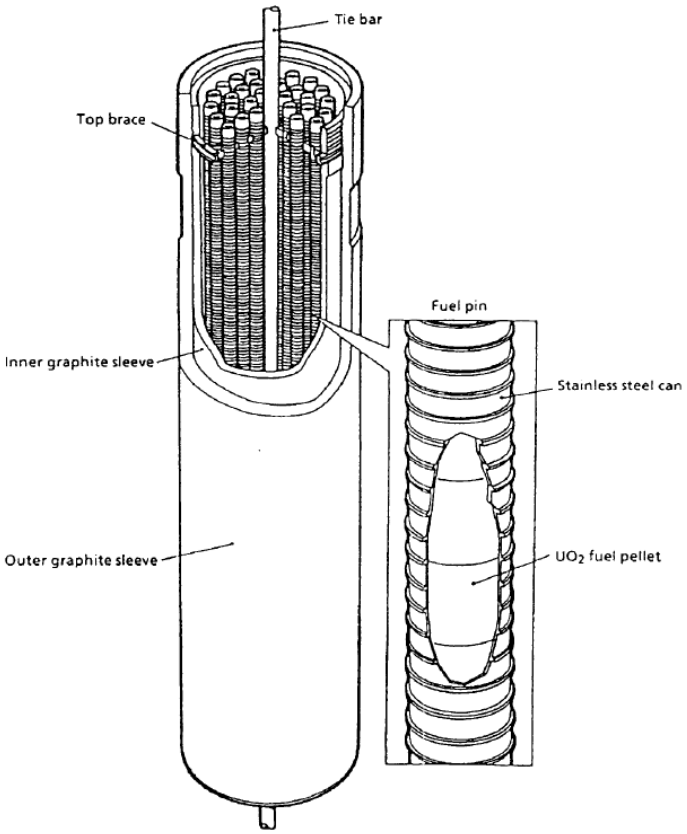

Figure 1-6. Illustration of an AGR fuel element [24]

1.4.2 Potential Improvements upon AGR with FHR Concepts

It is not intended in this thesis to borrow the physics of AGR in FHR design as unlike the AGR, the FHR is proposed as a high power density reactor with better economic features. Instead, the power plant engineering, refuelling machines, high temperature operations, experience with graphite, etc. can be adopted from AGR and applied in a high power density FHR core. The large graphite volume in AGR core allowed substantial freedom for design modification. It was speculated that after the redesigning, the FHR would not deviate significantly from the AGR dimensions, which could be easily tailored to perfectly fit into the current AGR assembly lattice by e.g., creating void or coolant channels in the core graphite structure. This way, the refuelling machinery could be directly borrowed from the current fleet of AGRs.

Weight loss of in-core graphite from progressive oxidation and the resulting cracking of the graphite was one of the most limiting concerns for AGRs as the lifetime of in-core graphite directly translates into the power plant lifetime. To mitigate the problem, the AGR injects carbon monoxide and methane to the CO_2 coolant. However, this causes carbon deposition on

the fuel pins and the heat exchangers, which limits the heat transfer capabilities. [24] Using FHR technology, much greater power density can be achieved, and very likely with much smaller graphite content. In addition, with the primary loop operating at atmospheric pressure, the FHR could allow thinner concrete pressure vessel walls (Torness operates at 45.7 bar pressure which requires 5 m thick reinforced concrete walls and a 5.4 m thick top slab). This means that the AGR-like FHR can become an SMR design with good possibilities of construction time reduction. The graphite can also be made into modularisable blocks and be removed and replaced when needed. Therefore, the graphite would not have to sit permanently inside the core, giving the core a longer operating lifetime.

Problems with the long fuel stringers were also encountered by the AGR. The cross-flow of the coolant caused by the pressure difference between the unfuelled channel and the neighbouring fuelled channel sometimes induced violent oscillatory behaviour of the fuel stringers. A more significant fault could be when the stringer fails, and the fuel element crashes into the core with high speed. In addition to uncontrolled reactivity insertion, this may also cause blockage of the coolant flow as the fuel assemblies may shatter, in which case the fuel might reach melting point in 6 to 8 minutes. [24] This was the main reason preventing AGRs from refuelling at full power. Salt in FHRs has similar density as the fuel assembly, therefore a dropped assembly in case of stringer failure would sink with low speed (or even float, in NaF-ZrF_4 for example). This can help simplify the safety case and could potentially allow the AGR-like FHR to operate with on-power refuelling and enhance fuel utilisation and economics of the reactor.

Due to the pressure difference between the steam side and gas side, the steam generator tube in AGRs may fail and cause steam and water ingress into the core. The main reason for the weakened steam generator tube is due to imperfect water chemistry combined with large temperature gradient during different water boiling regimes. [24] The Printed Circuit Heat Exchanger (PCHE), which is proposed in this thesis for the AGR-like FHR, has a robust structure and was tested to have good chemical compatibility with FLiBe at high temperatures. Also, the primary and secondary loop coolants are both high temperature liquid state salts at atmospheric pressure. This would relax the pressure and temperature gradient burden on the PCHE. The supercritical CO_2 power cycle proposed for the FHR was also proven to work well with PCHE. Even if the pressure difference between the gas power cycle and the intermediate loop causes PCHE failure, the intermediate loop in the FHR could act as a barrier for CO_2 ingress and simplify the depressurisation and isolation of the core. The steam generator failure

in AGRs also caused maintenance problems during the early AGR operations. This forced the AGR to evolve from single cavity design to multi-cavity design in Hartlepool, the first modified first generation AGR to allow easier maintenance and/or replacement of the boilers. In comparison, the PCHE in FHRs, besides being more robust, is also very compact and comes in modularised units, making the replacement much simpler and quicker. For an SMR sized FHR, the PCHE size would be even smaller.

1.5 Research Framework and Design Scope

This thesis fills the gap of some of the design space that was not yet covered by the other FHRs studies by allowing many degrees of freedom in the design process. The assembly configuration of the FHR resembles that of the AGR, consisting of the graphite channels, interlocking keys, and vertically aligned fuel elements. This ensures that much of the knowledge and experience gained from AGR can be retained and used. To explore a wide design search space, many independent design parameters were investigated and the physical envelope of the AGR design was to some extent relaxed while maintaining some level of geometrical resemblance to the AGR assembly. Firstly, the fuel channel and graphite sleeve dimensions and the number of fuel pins were changed. This was to allow a large variation in neutron spectrum by having different levels of moderator to fuel volume ratios. The top row of Figure 1-7 shows some assembly configurations with different channel radii and number of fuel pins.

The baseline FHR took the AGR solid fuel pin design as a reference. Two alternative fuel forms were also investigated to seek potential advantages over the baseline solid pin fuel in terms of thermal-hydraulics, neutronics, and economics: 1) annular pin type fuel with inner coolant channels for enhanced heat transfer, [25] and 2) plate type fuel as in the ORNL AHTR designs. Examples of these two types of fuel are included in the bottom row of Figure 1-7. [21] For the solid and annular fuel designs, three fuel materials were considered: UO_2, Uranium-carbide (UC) and Fully Ceramic Microencapsulated (FCM) fuel [21], i.e., TRISO particle fuel in graphite matrix. Both the traditional stainless-steel and the more accident tolerant SiC were considered as a cladding material for the pin-type fuels. The plate type fuel, considering manufacturability, used only FCM fuel meat sandwiched in between graphite outer cladding. [21] The subsequent part of the neutronic design space exploration went a step further, relaxing all geometrical constraints except the fuel dimension by using unit cell models with fuel pin in a homogenised coolant and moderator medium. An example of this (a unit cell model of a solid

pin using FCM fuel) is shown at the bottom right figure in Figure 1-7. For all neutronic models, fuel enrichment was varied from a 2.5 wt% to 20 wt% to identify any neutronic trade-offs of different enrichments.

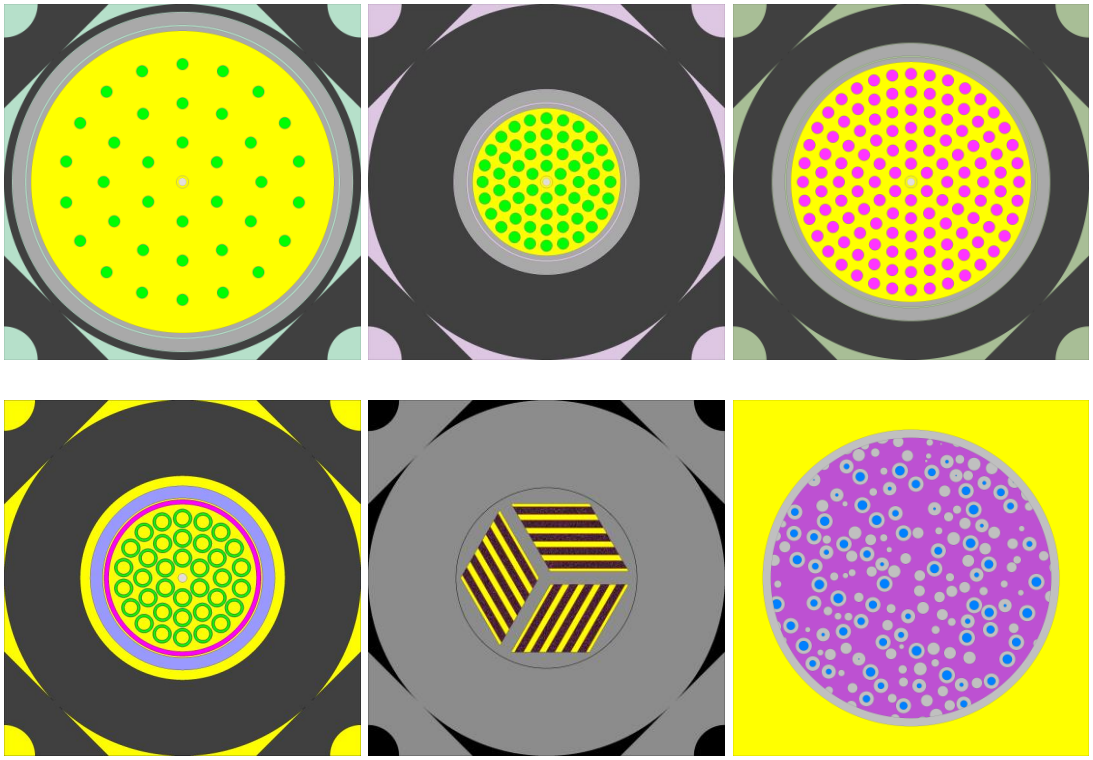

Figure 1-7. Examples of 2-D AGR-like FHR models

The choice of coolant material was another free design parameter. Three salts: $2LiF\text{-}BeF_2$ (FLiBe), LiF-NaF-KF (FLiNaK) and $NaF\text{-}ZrF_4$ were selected as coolant candidates. FLiBe has been chosen as FHR's most favourable coolant candidate due to its superior neutronic and heat transfer properties. [26] FLiNaK has similar heat transfer properties as FLiBe. It is widely used in other industries in non-radiation environments and is thus commonly used by the nuclear industry and research communities as heat transfer loop salt. Compared to the other two coolant candidates, $NaF\text{-}ZrF_4$ has less favourable but reasonably suitable heat transfer properties. However, it does not produce tritium under irradiation and is potentially the cheapest coolant salt material. [27] It could become a very good alternative coolant to FLiBe in case the removal and storage of tritium eventually prove to be major technological challenges. Within the space determined by these free design parameters, thermal-hydraulic and neutronic analyses were

conducted step by step and the designs that lied in any unfeasible domain were discarded before the next level of design domain search was performed.

1.6 Project Objectives

Several sequential research objectives were proposed for the design space exploration process. They address specific questions within the project scope defined earlier and serve as individual research milestones of this thesis. These are summarised as follows: 1) power density maximisation and development of computational toolkit, 2) system thermal-hydraulic design optimisation and development of computational toolkit, 3) neutronic design optimisation and 4) final design optimisation considering both thermal-hydraulics and neutronics. On a higher level, this thesis aimed at developing a design process along with a set of computational tools for fast and convenient preliminary reactor design space search.

1.6.1 Power Density Maximisation and Tool Development

Power density is a strong economic indicator for nuclear reactors. The FHR uses molten salt as coolant, giving the core a large thermal inertia and cooling capacity. This allows FHR to reach much higher power densities than AGRs. Also, molten salts offer stronger moderation than the almost neutron-transparent CO_2, which grants possibilities of even higher power uprates in salt-moderated epi-thermal cores with less graphite. The extent to which the power density can be increased depends on the thermal-hydraulic and material temperature limits. A code package SODom (Search of Operating Domain) was developed that can identify, for a given core configuration and coolant flow rate, the bounding operating conditions within which the reactor can operate without breaching materials temperature limits.

The thermal-hydraulic design step was carried out before neutronic work because the two alternative fuel forms, i.e., annular and plate type fuel, which constituted two-thirds of the whole design space, were primarily chosen for their potential to withstand high power due to better heat transfer. Quantifying this thermal-hydraulic advantage of the alternative fuels helped justify or nullify these design options. In addition, it is reasonable to carry out thermal-hydraulic analysis to study the design space prior to neutronic study as it is significantly computationally cheaper.

1.6.2 System Thermal-hydraulic Design Optimisation and Tool Development

LCOE of a power plant is a function of not only the reactor output, but also the fixed and variable cost and capacity factor of the power plant. Therefore, this thesis aimed to identify,

for a given FHR design, its operating condition and the corresponding operating power that can minimise the power plant's LCOE. As the basis to this analysis, a simplified FHR system power conversion layout based on previous work by Dostal et.al was proposed and illustrated in Figure 1-8. The proposed plant consisted of the reactor core, an intermediate loop of cheap heat transfer salt NaF-ZrF_4, and a supercritical Carbon-Dioxide (sCO_2) recompression power conversion cycle. This is described in more detail in Chapter 4.

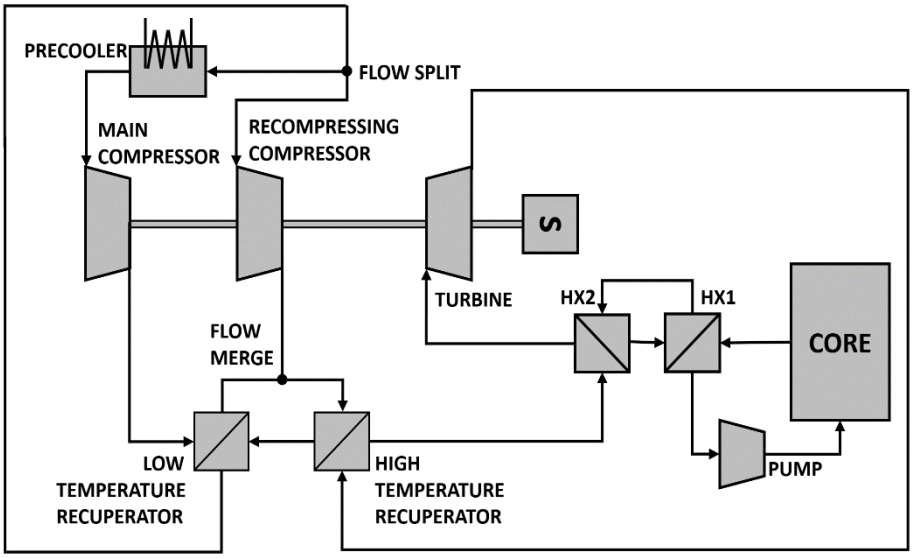

Figure 1-8. Proposed simplified FHR plant layout

A python code, Search of Core Optimum Operating Parameters (SCOOP), was built around SODom to meet this objective. For any FHR configuration, a range of pressure drop values were fed into SODom to produce the maximised core powers and the corresponding coolant temperature conditions. SCOOP then performed heat transfer system cost estimations using a system design optimisation module (OptSys). Lastly SCOOP estimated the power plant's LCOE using a simple capital cost scaling rule, assuming that the variable components and parts of the fixed components of the power plant's cost scale with the cost of heat exchanger and pumping system according to widely accepted Capital Cost Scaling Rule. The optimised core operating condition was the one that minimises the plant's LCOE. A power plant cost estimation module (CapCost) was developed for this task.

1.6.3 Neutronic Design Optimisation

Burnup to enrichment ratio (BU/e) is a strong indicator of fuel cycle economics: fuel cycle cost is almost linearly proportional to the enrichment for low enriched uranium and the discharge burnup translates directly to energy generation from the core. [28] Reactivity feedback is crucial to ensure inherent safety and stable operation. Also, the lifetime of fuel material is limited by the radiation damage the fuel can tolerate. The neutronic design optimisation sought for designs that can maximise the BU/e while keeping the core average reactivity coefficients, i.e., coolant temperature reactivity coefficient (CTC) and Doppler coefficient (DC) reasonably negative throughout depletion and a reasonable burnup.

1.6.4 Coupled Neutronic and Thermal-hydraulic Design Optimisation

Thermal-hydraulic calculations were performed for the design streams selected from the neutronic design optimisation for coupled analysis. AGR-like assembly models with relaxed dimensional constraints were used to cover the as much design space as allowed by the AGR envelope. A mapping technique was applied to convert the AGR-like thermal-hydraulic space to the non-AGR-like space to match some of the neutronic models that did not possess AGR design features. The final optimisation aimed at minimising the reactor's LCOE while having competitive neutronic performance.

1.7 Organisation of the Thesis

Following this introduction chapter, Chapter 2 introduces the core computational solvers used in later chapters. CapCost is introduced in Chapter 2. Chapter 3 details the models and assumptions behind SODom and applies it to several preliminary designs. Chapter 4 introduces OptSys and applies it to a reference FHR design. Chapter 5 performs preliminary neutronic space exploration at the BOL on some of the most thermal-hydraulically desirable design streams. A homogeneous unit cell model is introduced in the chapter to represent the heterogeneous assembly level models. Using the unit cell model, Chapter 6 searches through a wider BOL neutronic design space and produced a few well-performing design streams. Depletion analyses are carried out for these design streams and reported in Chapter 7. The results are used to perform neutronic design optimisation. Chapter 8 revisits thermal-hydraulics for the most neutronically desirable models and performs the final design optimisation considering both neutronics and thermal-hydraulics. Chapter 9 provides a comprehensive summary of this thesis and discussion on the important findings and some recommendations of future work.

Chapter 2 Computational Tools

The methods used in this thesis spanned across thermal-hydraulics and neutronics. The thermal-hydraulics part was carried out with the code package SCOOP, which incorporated an in-core thermal-hydraulic design module (SODom), a system thermal-hydraulic design module (optSys) and a power plant cost estimation module (CapCost). The neutronics part used Monte Carlo code Serpent [29] to simulate FHRs on both unit cell and assembly levels to identify the allowable core configuration domain from the neutronic point of view.

2.1 Thermal-hydraulic Modelling Tools

To perform thermal-hydraulic modelling, a python code package SCOOP was developed. The function of SCOOP was split into three modules. All three modules can be used stand-alone or coupled to the other modules in SCOOP. The first module, SODom (Search of Operating Domain), was developed to identify the bounding operating conditions within which the reactor can operate given a specified coolant flow pressure drop across the core. The core solvers implemented in SODom perform sub-channel thermal-hydraulic and heat transfer calculations. The second module of SCOOP is optSys, which takes the output of SODom, i.e., coolant temperature condition and maximum achievable power as inputs and produces the optimum heat transfer system design that minimises the heat exchanger and pump system cost. The core solver used in optSys is a heat exchanger and pump modelling solver, calcHX. The final module in SCOOP, CapCost, takes the outputs of SODom and optSys, i.e., the core power and heat transfer system costs, and, using a capital cost scaling rule, estimates the LCOE of the reactor. A wrapper function was created in SCOOP to feed different pressure drop inputs to the three main modules and finally identify the LCOE-minimising operating condition for the reactor. The power cycle thermodynamic efficiency is required in the estimation of LCOE. SCOOP assumed the 'Advanced Design' recompression s-CO_2 power cycle proposed by Dostal et.al as the power cycle for the power conversion cycle for the AGR-like FHR design. Implementing a power cycle design and optimisation module in SCOOP can be a topic for future work. Figure 2-1 shows the modules and how they are coupled together in SCOOP. The following sub-sections describe the fundamental solvers created in SCOOP, i.e., the sub-channel solvers, calcHX and CapCost. The details of the use of these solvers and algorithms with which the sub-channel solvers and calcHX are implemented in the SODom and optSys modules of SCOOP for different specific design tasks are described in the corresponding sections of the subsequent chapters.

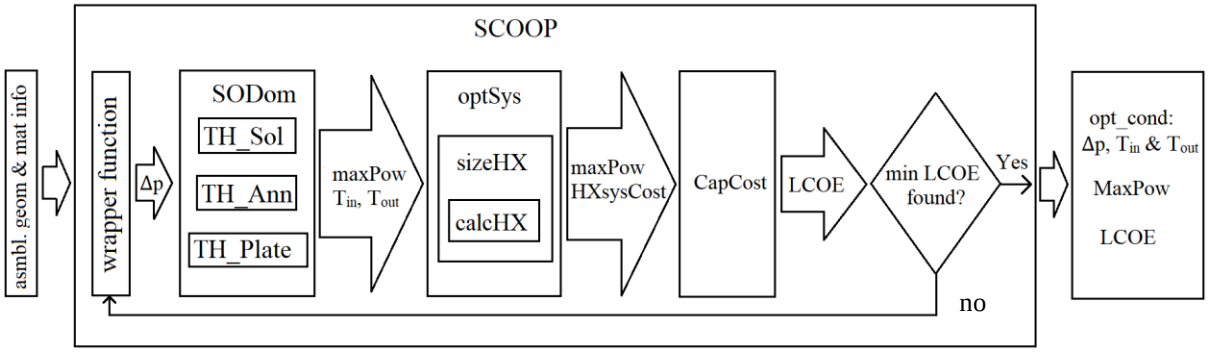

Figure 2-1. Flow chart for SCOOP

2.1.1 Sub-Channel Thermal-hydraulic and Heat Transfer Solvers in SODom

Three one-dimensional single channel steady state forced convection thermal-hydraulic analysis solvers (TH_Sol, TH_Ann and TH_Plate) were created using python to cover the design space proposed for the AGR-like FHR: solid fuel pellet, internally and externally cooled annular fuel and plate-type fuel. The thermophysical properties for graphite, fuel, and cladding materials used were taken from IAEA report. [26] Torness AGR core dimensions were taken as the reference geometry input used in all sub-channel calculations. [24] The hot channel was modelled assuming a reactor core radial power peaking factor of 1.3, which is reasonable and rather conservative for a large core such as AGR. The axial power profile was obtained from coupled neutronic (Serpent) and thermal-hydraulic (THERMO) [30] calculations. Physical properties of molten salt were taken from recently published reports. [27][31][32] For all TRISO in carbon matrix fuel types, the maximum fuel temperature was obtained by superimposing the temperature difference across a TRISO particle on top of the central line temperature of the plate type fuel calculated using effective thermal conductivity of the FCM fuel estimated using Vegard's Law. Temperature drop across a TRISO particle was calculated by analytically solving heat conduction equation in spherical geometry. For the prediction of maximum fuel temperature to be conservative, the fuel kernel was assumed to be UO_2 which has lower thermal conductivity than the UC fuel form. Several simplifying and conservative assumptions were made in in the sub-channel solvers. Firstly, radial heat conduction in the fuel dominates, thus axial conduction was neglected in the heat transfer calculations. Secondly, all fission power from the core was assumed to be deposited in fuel, meaning that 1) the solver treats a steady state problem where no heat is accumulated anywhere in the core, and 2) gamma and neutron scattering heating in core components such as graphite and coolant was neglected.

The thermal-hydraulic solvers divide the assembly into 50 axial nodes, each with a 20.75 cm height. The 40 nodes (830 cm) in the middle represented the active core, leaving the five nodes at the top and five at the bottom with zero power. For each node, the solvers calculate the temperature distribution in coolant, cladding and fuel meat. The solvers also calculate frictional pressure and gravitational pressure drop of the coolant across the core. Shock pressure loss at the inlet and outlet were not included in this model as they typically comprise a small contribution to the total coolant pressure drop. This observation was made from studying the results of modelling a test case with THERMO, the thermal-hydraulic model in BGCore. [30] The coolant pressure and radial temperature distribution in assembly components at each axial level was assumed to be the same across all channels. In an AGR, the coolant flows upwards through the fuel channels. However, after exiting the gas circulators, part of the coolant flow is diverted to flow downward through the graphite cooling channels inside and around the interlocking graphite keys to cool the graphite and then merges back with the coolant entering the fuel channels at the bottom of the core. The downward re-entrant coolant flow stream was not considered in the three solvers: all coolant was assumed to flow upwards from the bottom of the core only with no lateral flow. It was noted that this simplification brings about some small error in the coolant temperature distribution. A benchmark work of TH_Sol was carried out against BGCore and summarised in Appendix B. The benchmarking case of TH_Ann was done against the test case with analytical solution reported in Nuclear Systems II – Elements of Thermal Hydraulic Design, [33] and TH_Plate as verified against an AHTR thermal-hydraulic study. [34]

An iterative method, i.e., the traditional 'iteration till convergence' algorithm was implemented in all subchannel solvers to account for temperature dependent material properties. An initial guess of the temperature gives the initial material thermal conductivity, with which the material temperature is re-estimated. The new temperature updates the material properties which is used in a new round of heat transfer calculation. This process continues until the error between the material temperatures from two subsequent iterations is below a certain threshold.

For all three sub-channel solvers, the heat convection in the vertical direction in the coolant in each axial node was calculated using the following energy balance equation:

$$Q = C_p \dot{m} \Delta T \tag{2.1}$$

where Q is the amount of heat carried away by the coolant in the axial node under examination. Under the assumptions laid out earlier, this energy was equal to all the thermal energy produced

by fission reaction in that node; $\dot{m}$ is the coolant mass flow rate in the vertical direction in one fuel channel; C_p is the specific heat capacity of the coolant; and ΔT is the bulk coolant temperature rise across the node. The axial temperature distribution in the bulk coolant over the entire assembly is obtained by cumulatively adding ΔT of each axial node to the temperature of the node below.

The heat transfer by convection in the radial direction in the coolant in each node from the cladding surface to the bulk coolant temperature was solved by the following energy balance equation:

$$h(T_w - T_{cool}) = q'' \tag{2.2}$$

where q" is the heat flux through the outer cladding surface. The direction of this heat flux points outwards from fuel to the coolant. Assuming no heat flux in the axial direction, the magnitude of this heat flux is equal to the total fission energy generated in the node divided by the surface of heat transfer; T_{cool} is the bulk coolant temperature of the node; T_w is the outer cladding temperature in the node and h is the heat transfer coefficient of the coolant in the node. From this equation, the radial temperature distribution of outer cladding surface (T_w) could be obtained given the radial temperature distribution of bulk coolant (T_{cool}) obtained previously.

The heat transfer coefficient was calculated using the following set of equations:

$$h = k\frac{Nu}{D_h} \tag{2.3}$$

$$D_h = 4\frac{A}{S} \tag{2.4}$$

where k is the thermal conductivity of the coolant; Nu is the Nusselt number of the coolant; and D_h is the hydraulic diameter; A is the flow area of the coolant in the channel; and S is the wetted perimeter in the fuel channel.

In the development of TH_Sol, the calculation of Nusselt Number in each node was firstly attempted using two empirical correlations that are commonly used for internal flow forced convection, namely Dittus Boelter and Gnielinski correlations. [35] After completing

development of the model, a test case (the benchmarking case with THERMO, presented in Appendix B) was analysed to compare the results obtained from the two different correlations. Errors in the range from 0.2 K to 0.15 K were observed. For the benchmark case, Dittus-Boelter correlation was eventually chosen for TH_Sol and TH_Ann:

$$Nu = 0.023Re^{0.8}Pr^{0.4} \tag{2.5}$$

$$Re = \frac{\rho V D_h}{\mu} \tag{2.6}$$

$$Pr = \frac{C_p \mu}{k} \tag{2.7}$$

where Re and Pr are the Reynolds and Prandtl number respectively; ρ is the density of the coolant; V is the velocity of the coolant; μ is the dynamic viscosity of the coolant; all these quantities are calculated individually for each node.

The gravitational (ΔP_g) and frictional pressure drop (ΔP_f) in the coolant flowing vertically across each node were calculated using the following equations respectively:

$$\Delta P_g = \rho g h \tag{2.8}$$

$$\Delta P_f = \frac{1}{2}\rho V^2 f \frac{h}{D_w} \tag{2.9}$$

where g is the gravitational acceleration, h is the height of each node, f is the friction factor in that node. Note that the S in the formula for D_w here is not the heated perimeter as defined earlier, it is the wetted perimeter of the coolant channel.

The gravitational pressure drop if taken in the upward direction would be significant. However, in a confined primary loop, the upward flow pressure loss will be compensated by the downward flow pressure loss with the net Δp being zero if there is no heating/cooling. In case the gravitational pressure loss of up flow (which is lighter) would be more than compensated

by heavier downflow pressure loss, thus resulting in total negative gravitational pressure loss – i.e., helping the pump. Therefore, neglecting the gravitational Δp would be conservative. In the calculations of the pumping power requirements, the gravitational Δp was not considered.

The friction factor was calculated in TH_Sol and TH_Ann using the correlation for turbulent flow as follows: [35]

$$f = 0.184Re^{-0.2} \tag{2.10}$$

TH_Ann used Fanning friction factor $f = 0.046 \times Re^{-0.2}$, suggested by Taitel and Dukler in 1976, and TH_Plate used Blasius's Fanning friction factor of $0.0791 \times \mathrm{Re}^{-0.25}$ [35] to calculate friction factor.

For TH_Sol and TH_Ann, the heat conduction from the fuel outer surface, i.e., cladding inner surface, to the inner fuel were calculated differently in TH_sol and TH_Ann as the heat transfer physics is different for the two different fuel geometries.

The heat conduction from the cladding outer to cladding inner surface in TH_Sol was calculated using the following equation: [35]

$$T_{ci} - T_{co} = \frac{q'}{2\pi k_c} \cdot ln\left(\frac{R_{co}}{R_{ci}}\right) \tag{2.11}$$

where R_{co} is the radius of the outer cladding; R_{ci} is the radius of the inner cladding; q' is the total linear heat rating in the node under examination; k_c is the thermal conductivity of the cladding material. k_c was assumed to be constant as the cladding layer was very thin. The heat transfer across the gap between the fuel and the cladding was calculated in a similar manner.

In TH_Sol, the following equation [35] gives the relation between temperature (T_0) at a specific point in the fuel pellet (R_0) and the outer surface temperature (T_{fo}), the local conductivity of the fuel as a function of temperature,$k_f(T)$, the radius of the fuel outer radius (R_{fo}) and the power density q''' in the fuel ring encircled by the fuel outer radius and the radius of the specific point. Temperature dependency of the thermal conductivity was accounted for using iterative method.

$$\int_{T_{fo}}^{T_0} k_f(T)dT = \frac{q'''}{4}\left(R_{fo}^2 - R_0^2\right) \tag{2.12}$$

There are two cladding layers around an annular fuel pellet, one on the outside and one on the inside channel. The heat conduction across the claddings was calculated in the same way as in TH_Sol, only with some adjustments to the radii and heat flux used (the differences are described later). The heat conduction across the fuel in TH_Ann, however, was more difficult to model than that for TH_Sol. For the annular fuel pellet with internal cooling model, the maximum fuel temperature is not in the centre of the fuel ring, and the heat transferred to the internal coolant channel and the outer channel is not equal. The radius of the point where fuel temperature reaches maximum value (R_0) and the heat conduction from the maximum fuel temperature T_{R0} to the fuel inner surface temperature T_v were determined using the following equations. [35]

$$R_0 = \sqrt{\frac{\left[\int_{T_v}^{T_{fo}} k dT + \frac{q'''}{4}\left(R_{fo}^2 - R_v^2\right)\right]^2}{q''' \ln\left(R_{fo}/R_v\right)}} \tag{2.13}$$

$$\int_{T_v}^{T_{Ro}} k dT = \frac{q'}{4\pi}\left(\frac{R_v^2 - R_o^2}{R_{fo}^2 - R_v^2}\right) + \left[\left(\int_{T_v}^{T_{fo}} k dT\right) + \frac{q'}{4\pi}\right]\frac{\ln\left(R_o/R_v\right)}{\ln\left(R_{fo}/R_v\right)} \tag{2.14}$$

where T_v and R_v are the temperature and radius of the inner surface of the annular fuel pellet, T_{fo} is the temperature of the outer surface of the fuel pellet, k is the temperature dependent thermal conductivity of the fuel material, q' and q''' are the linear heat rating and power density of the fuel, and R_{fo} and R_v are the radii of the fuel outer surface and the fuel inner surface respectively. By applying the iterative method on Equations 2.13 and Equations 2.14, TH_Ann calculates the value (T_{R0}) and the position (R_0) of maximum fuel temperature. The temperature drops across the inner and outer gaps were calculated by TH_Ann in a similar fashion as described in Equation 2.11.

TH_Plate modelled simple heat transfer by conduction through the plate geometry (same configuration as the ORNL AHTR fuel plate illustrated in Appendix A), as well as convective heat transfer in the coolant salt using equivalent hydraulic diameter of the coolant channel. The spacer ridges were assumed to be semi-circular with a radius equal to the width of the coolant channel. Uniform heat flux normal to the plate surface and zero axial heat conduction were assumed here as well.

A model verification study using TH_Plate on the AHTR fuel assembly design specifications was performed comparing the results against data published in a recent ORNL study. [21] The ORNL calculations assumed a cosine axial power profile and ignored the effect of the spacer ridges on the coolant flow and heat transfer. Using the same conditions, TH_Plate results agreed reasonably well on maximum fuel temperature (846°C by TH_Plate vs 854°C from ORNL), average coolant velocity (1.96m/s by TH_Plate vs 1.93m/s from ORNL), and coolant frictional pressure drop (0.55 bar by TH_Plate vs 0.58 bar from ORNL).

2.1.1 Heat Exchanger and Pump Solvers in optSys

PCHE, which is introduced in more detail in Chapter 4.1, was proposed for AGR-like FHR heat transfer system. To model a heat exchanger of a given duty, Log Mean Temperature Difference (LMTD) and flow area, a lumped parameter heat exchanger routine calcHX was created in the optSys module of SCOOP. calcHX used the LMTD method expressed in Equation 2.15 to model a heat exchanger. A counter current flow design was assumed in calcHX in calculating the LMTD.

$$Q = U \cdot A \cdot LMTD \tag{2.15}$$

where Q is the heat exchanger duty, U is the overall heat transfer coefficient and A is the total heat transfer area. Molten salt heat transfer properties were taken from INL's Engineering Database of Liquid Salt Thermophysical and Thermochemical Properties. [32] The Fanning friction factor and the Nusselt number were calculated using Hesselgreaves universal correlations (2001) for PCHE. [36] Several assumptions were made in calcHX: 1) based on conservative estimations by Dostal et al., [37] the heat transfer effectiveness of PCHE heat exchangers was assumed to be 98%, and pump efficiency was assumed to be 89%, 2) equal numbers of hot channels and cold channels was assumed, 3) A minimum approach temperature

of 15 °C was assumed for both heat exchanger units' hot ends, [38] 4) the channels in the PCHE were assumed to have zero waviness, i.e. straight channels, and 5) a single PCHE unit was assumed for each heat transfer stage. The pressure drop of the coolant through the PCHE was calculated in calcHX using the same equations as in the sub-channel solvers. The pumping power requirement was calculated as follows:

$$pumping\ power = \frac{\dot{m}\Delta p}{\rho\mu} \tag{2.15}$$

where $\dot{m}$, ρ and Δp are the mass flow rate, density and pressure loss of the coolant, and μ is the efficiency of the pump. The annual cost of the pumps was calculated by multiplying the annual pumping power required (assuming a 90% capacity factor of the reactor) by the nuclear power LCOE of 96 £/MWh suggested by the Department of Business, Energy & Industrial Strategy (BEIS) in the *Electricity Generation Costs* report. [39] The total levelised annual cost of a heat transfer unit was the sum of the annual heat exchanger cost and the annual pumping power cost. The heat exchanger simulation sub-routine calcHX considered only frictional pressure loss of fluid in heat exchangers with a fouling factor of 1 when calculating required pumping power. calcHX would slightly under-predict the pumping cost of the reactor as there are, although relatively smaller in magnitudes, pressure losses of other types in other components of the power system.

A heat exchanger sizing routine sizeHX was built in optSys that used calcHX as its core solver to identify the best size and aspect ratio of a PCHE for a given duty and temperature condition. When sizing a heat exchanger, a trade-off exists between the cost of heat exchangers and the cost of pumps. The aspect ratio of the heat exchanger plays an important role in this trade-off. For a given duty and LMTD, the smaller the flow area is, the larger the flow velocity and the Reynolds number (Re) becomes, which results in a larger U and a smaller total size of the heat exchanger. However, it also means that a larger pumping power is required. sizeHX was created to address this trade-off. The heat exchanger upfront capital cost was calculated by multiplying the material cost converted to 2019 currency by a fabrication cost factor of 6.5. [40] A levelised annual heat exchanger capital cost was then calculated assuming a constant annual cash payment over the assumed PCHE service life of 20 years with an interest rate of 5% using the following equation. [41]

$$A = P\left(\frac{i(1+i)^n}{(1+i)^n - 1}\right) \tag{2.16}$$

where A is the amount of equal annual cash instalments, P is the initial investment, n is the number of service years and i is the discount rate.

sizeHX iteratively calls calcHX with different total flow areas to identify the heat exchanger aspect ratio and size that required the minimum total levelised annual cost. Figure 2-2 shows an example of the effect of heat exchanger aspect ratio on the total annual cost of the heat transfer unit. The figure was produced for the primary heat exchanger with an example duty of 6000 MWt and an example LMTD of 36.7°C.

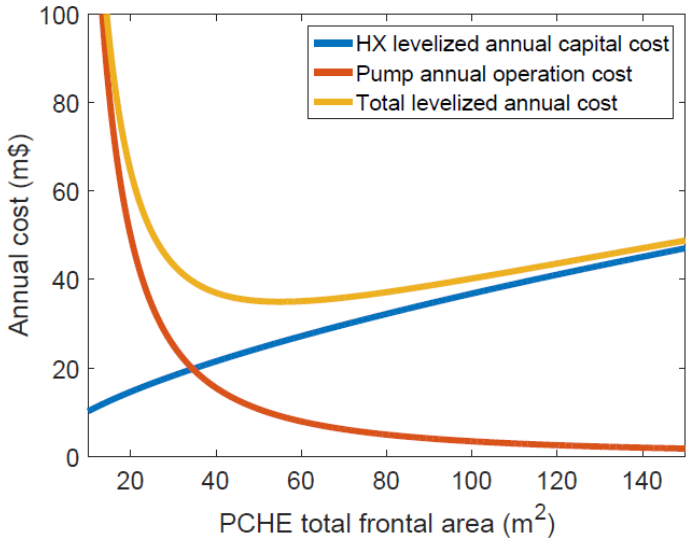

Figure 2-2. Effect of heat exchanger frontal area on the cost of heat transfer unit.

As can be seen from Figure 2-2, for a given duty and LMTD, the heat exchanger cost decreased with the increase of total frontal area, while the pumping cost increased. The optimum aspect ratio that minimised the annual cost of the heat exchanger could be identified after a complete search of sizeHX.

calcHX and sizeHX were verified before being applied in this thesis. Using the same PCHE design specifications, operating conditions and coolant salt as in the INL study, [38] calcHX successfully reproduced the data published in the INL study report. The benchmarking study

results are included in Appendix C. E. S. Kim et al. described a simplified printed circuit heat exchanger sizing optimisation code based on cost of heat exchanger and pumps, i.e., the same optimisation parameters as those adopted for sizeHX. [40] A benchmark study between sizeHX and the work by E. S. Kim et al. were performed and included in Appendix D.

2.1.2 LCOE Estimation – Capital Cost Scaling Rule in CapCost

The final module of SCOOP is CapCost – a simplified economic module which takes the power and the cost of the heat exchanger and pump system of a reactor to estimate its LCOE.

Generation IV Economic Modelling Working Group (EMWG) IAEA 2007 reported on the *Cost Estimation Guidelines for Generation IV Nuclear Energy Systems*. [41] However, it was impossible to collect sufficient data or make realistic assumptions for the conceptual-stage FHRs to fill in the parameters space required of the EMWG guidelines. Such a cost estimation necessitates detailed design descriptions, benchmark studies, experimental, industrial, and up-to-date commercial data, licencing and siting progress, etc. This was outside the scope of this study and would be more appropriately placed in latter stages of the FHR project.

However, incorporating some form of economic evaluation in SCOOP was important as only to capture the non-linear power vs. cost trends resulting from the relative thermal-hydraulic performance of alternative designs. CapCost was created for this purpose. It estimates costs by simple and fast methods, while delivering results that can suggest, with reasonable level of confidence, the comparative performance, or classification and ranking of reactor designs.

CapCost was created following the concept of the ‘Modelling’ method of the ‘Simplified Top-Down’ approach suggested in the EWMG guidelines with some simplifications and assumptions. The ‘Modelling’ method takes a reference power plant with known cost and its breakdowns and determines the differences between the design of interest and the reference to construct a model mimicking the variations of the cost elements. The top-down technique estimates costs of different cost elements of an NPP and GIF provides a full Code of Accounts (COA) structure, programming the cost components into four-digit codes for this purpose. Lacking information on the final NPP details at this stage, CapCost took only the highest-level cost classification scheme (grouped by the first digit of COAs):

10 – Capitalised Pre-Construction Costs

20 – Capitalised Direct Costs

30 – Capitalised Indirect Services Costs

40 – Capitalised Owner's Costs

50 – Capitalised Supplementary Costs

60 – Capitalised Financial Costs

70 – Annualised O&M Cots

80 – Annualised Fuel Cost

90 – Annualised Financial Cost

NPPs are capital-heavy projects, i.e., Capital Cost forms the biggest component in an NPP's Cost of Electricity (COE). Overnight Capital Cost (OCC) consists of major components of 10 to 60 COAs, among which COAs 20 (Capital Direct Cost) is the most dominant. CapCost started first by studying COAs 20. It is suggested in the EWMG guidelines that the cost of process equipment or complete process systems (Accounts in COAs 20) can be split into two components, i.e., fixed and variable, as expressed as follows: [41]

$$C = \{A + (B \times P^n)\} \tag{2.17}$$

where

C = the cost of the subject plant element or processing system

A = fixed component of the reference plant cost

B = variable component of the reference plant cost

P = ratio of subject plant to reference plant component parameter value

n = exponent that reflects the size benefit of rating for the component (<1)

P^n = equivalent to a cost factor for ratio of parameters between the subject and reference plant data

In conventional top-down economic models for NPPs, such as ones explored by Carelli et.al., the cost taken from a reference plant are scaled in relation to power output only. [42] This is widely accepted in the industry as the power density of current fleet of reactors is of similar order of magnitude. In this thesis, however, significant power density uprate was expected while the physical size of the FHR was fixed. Therefore, a scaling law of the form of Equation 2.17 better describes the capital cost behaviour for such a project: some parts of the capital cost

that scale in relation to the physical size of the NPP should be fixed (A), while the power scaling of other parts shall be captured (B). Therefore, CapCost borrowed the form of cost scaling from Equation 2.17 to estimate the capital cost of the whole NPP. Lacking detailed design and cost data to extract the scaling behaviour of each cost element, CapCost conglomerated all capital cost components (COAs 10 to 60) into one simplified model to estimate OCC as follows:

$$OCC_s = \left\{A_r + \ (B_r \times {P_r}^{n_r}) + C_r \times (\frac{Q_s}{Q_r})^{n_r}\right\} \tag{2.18}$$

where

OCC_s = OCC of the subject NPP

A_r = fixed capital cost of the reference NPP

B_r = variable capital cost of the reference NPP that scales with heat transfer system

C_r = variable capital cost of the reference NPP that scales with reactor power

P_r = ratio of heat exchanger system costs of the subject plant and reference plant

n_r = exponent that reflects the size benefit of rating for all variable components of a power plant (n<1)

Q_r = power output of the reference plant

Q_s = power output of the subject plant

CapCost assumed that the cost of fixed components (A_r) to be the sum of all fixed OCC that do not vary with power output. Examples of such elements include pressure vessel, core structure, containment buildings, etc. The parameter B_r is a size-penalty term, i.e., elements in OCC that have the power law behaviour with the heat transfer system costs. Examples of such include heat exchangers, pumps, turbomachinery, etc. The parameter P_r should describe the scaling of all such variable costs. SCOOP has a heat transfer system cost estimation module and CapCost assumed that the power scaling coefficient P_r can be effectively represented by the ratio of heat transfer system costs. The parameter C_r is another size-penalty term. It describes the cost elements (such as piping and heat sinks) that scale with power output of a reactor. It was shown (see Appendix E) that the scaling of heat exchanger agrees very well with that of the power. Therefore, CapCost represented all variable costs by one term (B_r) that is scaled with P_r (heat transfer system cost ratio). For simplicity, CapCost assumed one fixed scaling exponent for all such Accounts. Due to lack of cost data for components in large FHRs, a value of 0.64 as

suggested by Carelli et.al. in an economic study for small-to-medium size reactors was used for the exponent n_r for the First of a Kind (FOAK) FHR. [42]

The reference FHR chosen for calculation of Q_r in Equation 2.18 was an AGR-sized three-ring solid pin UC fuelled SiC cladded reactor that used FLiBe as primary coolant, NaF-ZrF_4 as intermediate loop heat transfer fluid and a sCO_2 power cycle. Adopting the design data of the large size commercial scale AHTR reactor, the reference FHR was assumed to have a power of 3400 MWt, i.e. Q_r = 3400 MWt, a coolant inlet temperature of 650 °C, a coolant outlet temperature of 700 °C. TH_sol and optSys calculations were performed for this reference reactor and found an optimal coolant pressure drop for that system to be 28 kPa and a total annual heat exchange system cost £39.9 million, which was subsequently used as the denominator of the variable P_r. The power output of the subject reactor, Q_s, was taken from the output of SODom, i.e., the maximum achievable power for the given pressure drop.

The EWMG guidelines suggests that Levelized Capital Cost (LCC) is expressed as follows:

$$LCC = (FCR \times OCC)/E \tag{2.19}$$

where, FCR = constant dollar fixed charge rate (%), which represents financial capital discounting covering the operational or regulatory life of a plant, OCC = Overnight Capital Cost in constant dollars ($ or £) and E = power × mean hours of full power operation per year, i.e., annual electric energy generation (MWh) of the NPP.

Substituting OCC of the subject and reference plant using Equation 2.18 (with B_r representing all variable costs) into Equation 2.19, and assuming constant average capacity factor and operating power level so that the ratio of E and be represented by the ratio of power, and with some derivation, the LCC of the subject plant can be estimated using the reference plant data as follows:

$$LCC_s = \{A_r + (B_r \times {P_r}^{n_r})\} \times FCR\ /E_r \times \frac{Q_r}{Q_s} \tag{2.20}$$

where LCC_s represents the LCC of the subject reactor and E_r is the annual electric energy generation (MWh) of the reference NPP.

Operations and Maintenance (O&M) and Decontamination and Decommissioning (D&D) along with electricity production information, yield the contributions of the non-fuel costs to the overall COE. Further adding Fuel and capital discounting of all the cost elements of COE, the LCOE can be then estimated. [41] CapCost made some assumptions to simplify this formulation. Firstly, fuel cost scales almost linearly with e/BU. [43] However, for some of the reactor designs proposed in this thesis, fuel types or fuel services are not yet commercially available. Due to lack of data describing the cost behaviour, CapCost assumed that cost of fuel per unit energy produced (£/MWh) to be fixed. Although different reactors may have different e/BU, it was assumed that the cost variation introduced by this difference would be small. Secondly, according to the EWMG guidelines, other non-capital costs (such as O&M and D&D) are either fixed for per unit of electricity output or are related to power output. Therefore, CapCost assumed that all non-fuel COE contribute to either A_r or B_r or both in Equation 2.20.

Finally, CapCost assumed that the cost behaviour with power is the same across all FHRs explored, including the reference FHR. This means that all FHRs 1) have the same fixed cost as the reference FHR as they have the almost identical physical size, 2) have variable costs that scale from the reference design in the same manner and 3) same fuel cost per unit of output. With these assumptions, CapCost multiplied through A_r and B_r by FCR/E_r in Equation 2.20 to obtain A_R and B_R, which now represent the fixed and variable components of the non-fuel part of the LCOE. Adding levelised fuel cost to model, CapCost computed the LCOE of a subject FHR as follows:

$$LCOE = \{A_R + (B_R \times {P_R}^{n_R})\} \times \frac{Q_r}{Q_s} + F \tag{2.21}$$

where

LCOE = the LCOE of the subject plant element

A_R = fixed components of the non-fuel part of LCOE of the reference plant

B_R = variable components of the non-fuel part of LCOE of the reference plant

P_R = ratio of heat exchanger system costs of the subject plant and reference plant

n_R = exponent that reflects the size benefit of rating for all variable components of a power plant

$P_R^{n_R}$ = equivalent to the cost factor for ratio of power output between the subject and reference plant

F = levelised fuel cost of the reference plant

Q_r = power output of the reference plant

Q_s = power output of the subject plant

According to the "*Electricity Generation Costs*" report by BEIS, the cost of the next generation FOAK PWR can be broken down into several components: the pre-development costs, construction costs, O&M costs, fuel costs, decommissioning and waste or D&D costs. [39] Table 2-1 presents the breakdown of these components. CapCost assumed that the FOAK reference FHR would have the same cost breakdown as the next generation FOAK PWR.

Table 2-1. Breakdown of costs for the FOAK next generation PWRs [39]

Pre-development costs	7	£/MWh
Construction costs	66	£/MWh
O&M	16	£/MWh
Fuel Costs	5	£/MWh
Decommissioning/Waste	2	£/MWh
total	96	£/MWh

Based on the table, the LCOE of the reference FHR was assumed to be 96 £/MWh, and fuel cost F in Equation 2.21 was assumed to be 5 £/MWh. Parameters A_R and B_R in Equation 2.21 represent the fixed and variable elements of all COAs for the reference plant except fuel cost (totalling 91 £/MWh). Accurately estimating the values for A_R and B_R, however, was nearly impossible: A_R and B_R should be derived from historical data using regression or other forms of statistical learning methods. However, it would require sufficient and detailed historical reactor cost data covering a wide range of power outputs for any statistical analysis to have statistical robustness. Detailed cost information was obtained for several NPPs from Energy Economic Data Base (EEDB); [44] however, past power reactors have rather a small ranges of power outputs, far too small to reach the potential power levels of the any optimised FHRs from the thesis, as will be shown later. Furthermore, LCOE scaling behaviour is very sensitive to many factors including total construction site size, material volume, construction duration,

experience, modularisation, onsite manufacturing vs offsite manufacturing and online assembling, logistics, etc. [45] The technological advancements and transfer of experience from other reactor projects would certainly help reduce the size-penalty effect ($B_R \times {P_R}^{n_R}$), but the engineering and manufacturing uncertainly of an FOAK reactor might do otherwise. More accurate predictions of A_R and B_R can only be obtained as more large-size NPP projects are carried out.

CapCost therefore attempted to make reasonably conservative assumptions to derive the values for A_R and B_R. The conservatism comes from adding more weights to parameter B_R. When there is a power increase from the reference plant, the parameter P_R would be greater than one, and since the exponent n is greater than 0 for all common components or systems, [41] the coefficient for B_R is always greater than one, whereas the coefficient for A is set to one. This means that when there is a power uprate, the larger the parameter B (and therefore the smaller the parameter A_R) is, the greater the cost of the plant element would be.

Adhering to the EWMG suggestion that O&M and pre-development costs are linear with power output and their power law component is rather small, CapCost assumed that these two cost components contribute to parameter A_R only. Construction, which includes the manufacturing costs of equipment, comprises most of the components of COAs 20 and, therefore, OCC. D&D (COA 58) also exhibits both linear and power law behaviour. Therefore, they should contribute to both A_R and B_R. For conservatism, CapCost assumed a 1:3 split between the two terms for Construction and D&D. Under these assumptions, A_R = 7 + 16 + (66+2) ×1/4 = 40 £/MWh and B_R = (66+2) ×3/4 = 51 £/MWh. With all the variables obtained, the LCOE of the subject reactor could be calculated by CapCost using Equation 2.21.

The AGR-like FHR is a new reactor concept. Therefore, no accurate estimations of these independent variables or the cost estimation method could be obtained yet. The assumptions made in CapCost should not be regarded as a guideline for FHR cost estimations. The most important intent was that consistent assumptions and cost models are applied across all cases in the design space during design optimisation, including the reference plant, so that the relative economic performance could be compared, and the optimisation could be carried out in a consistent manner. In Chapter 4.4.1, a sensitivity study is presented to investigate how the choices of some of these variables affect the results of CapCost and SCOOP. As will be shown in Chapter 4.4.1, LCOE from CapCost is most sensitive to the choice of the reference reactor, i.e., parameter Q_r. With the growing research interest and based on the recommendations from

this work, future studies should refine the designs and the corresponding cost models as design details and cost-relevant data become available.

2.2 Neutronic Modelling

After defining the operating domain and the optimum operating condition for each assembly configuration under thermal-hydraulic limits, neutronic analysis was carried out to further identify the design space defined by neutronic limits. In this study, Serpent was used to perform neutronic calculations. Serpent is a continuous energy stochastic Monte Carlo neutron transport reactor physics code developed by Leppänen et al. at VTT Technical Research Centre of Finland. [29] The Monte Carlo method simulates a series of particle collisions using known laws of physics and track events such as creation from neutron source, fission, scattering, absorption and escape for individual particles. The behaviour of simulated particles is averaged to derive macroscopic behaviour of the system as a whole. Serpent performs depletion calculations by solving Bateman equations for all isotopes under investigation. Serpent version 2.1.23, which offers parallel calculation modes using both MPI and OMP parallelisation was used for this work. Continuous-energy cross-section data library ENDF-7 with thermal scattering for graphite was implemented and power density was used for flux normalisation.

The Monte Carlo method possesses many advantages over deterministic method that are very valuable for this specific work. These advantages more than make up for Serpent's requirement for high computational resource. This project searched across a wide range of design options that cover all types of neutron spectrum (from fast to thermal). Monte Carlo method can model designs with different energy spectra without a need for any setup modifications. Contrarily, deterministic codes require pre-processed multi-group cross-section library for specific neutron spectra in different applications. These libraries are very well established for LWRs. However, in the design search for FHR, majority of the designs would require new cross-section libraries to be prepared. Furthermore, the FHR design space covered very different fuel materials, forms, and geometries (some very exotic, requiring full double heterogeneity for fuel with TRISO particles in carbon matrix). Monte Carlo code Serpent has greater flexibility and accuracy in modelling these exotic designs. Also, Serpent's Woodcock delta-tracking method and unionised energy grid method for continuous-energy cross-section storage make the modelling of full double heterogeneity only marginally more computationally expensive than traditional fuel. [46][47] On the other hand, accurately modelling double heterogeneity is a challenge for deterministic codes. Although successful benchmarking cases between WIMS (deterministic)

and Serpent (Monte Carlo) has been performed for both prismatic and pebble bed type FHRs with double heterogeneity in their fuel, the calculation routines in WIMS are extensively tailored for those two specific reactors for the benchmark to work and are therefore not applicable to other FHR designs.

In the first design stage of this project, 2D assembly models with reflective boundary conditions were created for four different assembly configurations: solid pin in AGR assembly; annular pin in AGR assembly; plate type fuel in AGR assembly and enlarged plate type fuel in an AGR assembly with no graphite sleeve. Designs using UC and UO_2 fuel were modelled in Serpent with 10 equal-volume rings to capture the spatial shelf-shielding effect caused by the different absorption rates of U238 in the fuel. This 'onion peel' model also ensured the accuracy of the model in case of the later use of burnable poisons. Models using TRISO particles were modelled explicitly in 3D models capturing the actual geometry of the fuel layers and dispersion of the particles in the carbon matrix using Serpent's random particle dispersion capability. The later stage neutronic studies involved homogenising the assembly designs into a representative unit cell models with reflective boundary conditions to speed up the calculations and to cover greater design space outside of the AGR physical constraint. The Serpent simulation setups were the same across all models for consistency. Neutron histories in all Serpent simulations were selected such that the Monte Carlo uncertainties were kept under 30 pcm. This was considered acceptable for preliminary design space exploration and design optimisation studies that evaluate rough reactor designs that have rather significant differences (on the order of thousands of pcms) in neutronic performance.

Chapter 3 Preliminary Thermal-hydraulic Design Space Exploration

This chapter presents the initial stage thermal-hydraulic design space exploration for the AGR-like FHR. A numerical modelling tool, SODom, is introduced and applied to several FHR designs based on AGR fuel element to report on their thermal-hydraulic operating domains and maximum allowable power levels. The objective of the exercise is to 1) develop computational tools that can aid the subsequent thermal-hydraulic design after the neutronic design choices are made, 2) perform a proof-of-concept study to investigate whether salt coolant could indeed deliver superior thermal-hydraulic performance than gas with minimal modifications to AGR design and 3) develop initial understanding of the AGR-like FHR thermal-hydraulic design trade-offs and narrow down the design space by screening out design options with the inferior thermal-hydraulic performance.

3.1 Preliminary AGR-like FHR Design Options

In this chapter, three fuel designs were considered: 1) traditional AGR solid pin fuel, 2) annular fuel pin from the pin type SmAHTR and 2) plate type fuel from AHTR. For solid and annular pins, three fuel material options were considered: 1) UO_2 2) UC and 3) FCM. Considering manufacturability, plate type fuel considered only FCM fuel meat. Cladding choices for UO_2 fuel and UC fuel rods included stainless-steel and SiC. All design modifications to the AGR were limited to the fuel channel and assumed the nominal fuel temperature of Torness AGR. This was to allow a direct and consistent comparison between the FHRs and the AGR, for which thermal-hydraulic conditions data was available. Also, by doing so, many of AGRs technologies such as refuelling machines could be borrowed with minimal modifications. If successful, this exercise could produce a number of baseline AGR-like FHR design options with minimum technology development requirements. As will be shown later in this thesis however, global design space optimisations studies will suggest designs that fall outside the preliminary design space study results presented in this Chapter.

3.1.1 Reference FHR Design – Sold Pin Fuel

The reference AGR-like FHR assembly inherited the Torness AGR assembly design with three concentric rings of standard solid fuel pellet in a circular lattice and replaced the CO_2 coolant with molten salt. Following this reference layout, a design with four rings of solid fuel pins was also studied. For favourable corrosion resistance in molten salt environment at high

temperature, Hastelloy N was chosen to be the core structural material, although Hastelloy N is beyond AGR material experience and is more costly than steel. Figure 3-1 shows cross-sectional views of 3-ring and 4-ring reference assembly designs modelled with Monte-Carlo code Serpent. The graphite is shown in grey and the central coolant is in yellow. The 4-ring design on the right of Figure 3-1. has two shades of colour to represent coolants: grey for the coolant outside the channel and yellow for the coolant inside the channel. This model is used when the inner channel and outer channel coolants are modelled to have different temperature (and thus density) for calculating coolant temperature coefficients. There is a central tie bar that links the eight vertically stacked elements. The gap between the cylindrical graphite core block structure and the square graphite keys are for down-coming coolant gas, for cooling the graphite blocks. The channels within each graphite key are reserved for control rods, boron beads or nitrogen injection (used only for emergency shutdown).

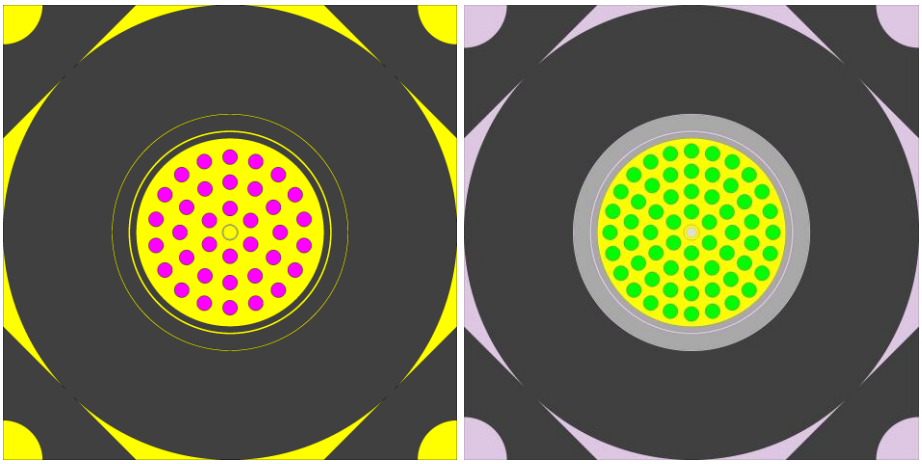

Figure 3-1. 2-D Serpent models for 3-ring and 4-ring AGR-like FHR designs

3.1.2 Alternative FHR Assembly Designs – Annular Pin Fuel

Annular fuel rods were proposed to be arranged in a circular lattice in the same fashion as the reference design. Material choices were also same as the solid pin designs. Three assembly configurations were studied, namely the 3-, 4- and 5-ring arrangements.

The annular fuel rod outer radius was first determined such that the rods could fit into the graphite sleeve with a gap between fuel rods of at least 1mm. The inner radius of the fuel rods was then determined such that the temperature of coolant inside and outside of the rods were equal, to maximise the thermal-hydraulic benefit of annular fuel. Since inner and outer channels

share the same upper and lower plena, the flow rate will be distributed such that there is no pressure difference between the inner and outer channel at any levitation along the assembly. Therefore, assuming same coolant temperature distribution and thus same gravitational pressure loss, frictional pressure loss must be the same inside and outside of the fuel ring:

$$\left(\frac{\rho v^2}{2} \times \frac{L}{D} \times f\right)_{inner} = \left(\frac{\rho v^2}{2} \times \frac{L}{D} \times f\right)_{outer} \tag{3.1}$$

where the subscript *inner* represents coolant in the channel inside the fuel, while the subscript *outer* represents coolant between the fuel rods, ρ is the coolant density, v is the coolant velocity, L is the length of the channel, D is the hydraulic diameter, and friction factor f can be taken to be proportional to $Re^{-0.2}$. Assuming same internal and external coolant temperature, coolant density was assumed to be the same. Expanding the equation 3.1 and noting that $Re = \rho v D/\mu$ and the channels have the same length, it can be shown that:

$$\left(\frac{v_{inner}}{v_{outer}}\right)^{1.8} = \left(\frac{D_{inner}}{D_{outer}}\right)^{2.2} \tag{3.2}$$

To have equal inner and outer coolant temperatures, the following equation must be satisfied:

$$K A_{inner} v_{inner} = A_{outer} v_{outer} \tag{3.3}$$

where A is the coolant flow area, and K is a correction factor to account for the difference in heat flux to internal and external coolant channels. Substituting Equation 3.3 into Equation 3.2:

$$K \left(\frac{A_{outer}}{A_{inner}}\right)^{1.8} = \left(\frac{D_{inner}}{D_{outer}}\right)^{2.2} \tag{3.4}$$

All variables in Equation 3.4 are functions of inner and outer radius of fuel rods only. After determining fuel rod outer radius for each of the three designs, inner radius was then determined for each design using Equation 3.4. The correction factor *K* was iteratively determined, and inner radius was updated for each *K* value such that the resulting internal and external coolant temperatures were the same. The cladding thickness is assumed to be 0.0635 cm. Table 3-1 summarises specifications of the three considered configurations. Figure 3-2 illustrates representative assembly designs using three and four rings of annular fuel pins modelled and analysed with Serpent. With the same colour scheme as in Figure 3-1, the shade of purple on the assembly sleeve represents a trial design variation where SiC is chosen as sleeve material. This material choice and assembly dimension are only shown for illustrative purposes.

Table 3-1. Annular fuel assembly design specifications

Specifications	*3-ring*	*4-ring*	*5-ring*
Number of fuel pins	36	60	90
Rod inner radius (cm)	0.8255	0.5413	0.4705
Fuel inner radius (cm)	0.889	0.6048	0.534
Fuel outer radius (cm)	1.1575	0.9415	0.7505
Rod outer radius (cm)	1.221	1.005	0.814
Correction factor K	1.0945	1.2678	1.1449

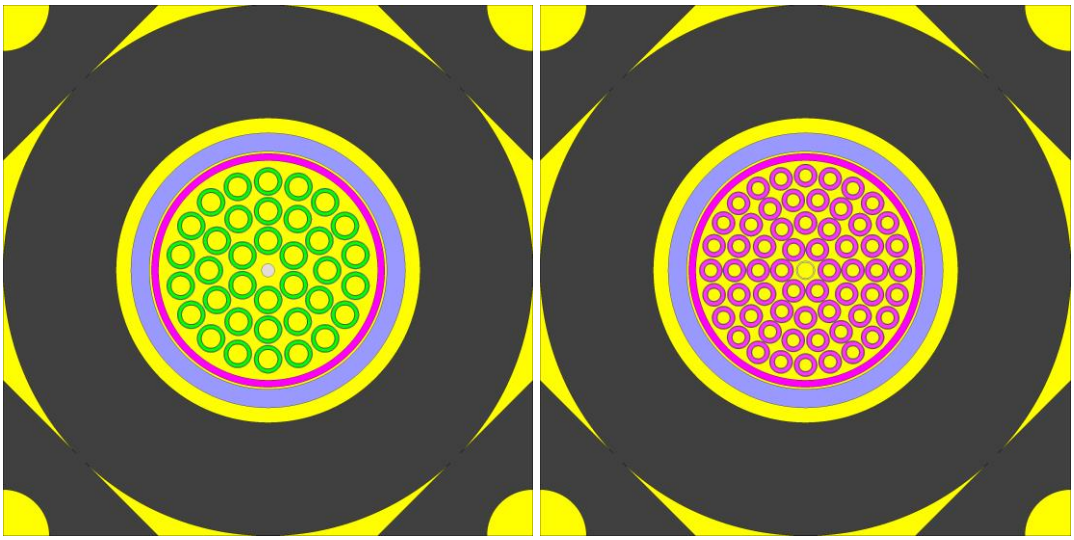

Figure 3-2. 2D Serpent models for 3-ring and 4-ring annular fuel AGR-like FHR designs

3.1.3 Alternative FHR Assembly Design – Plate Type Fuel

The plate type assembly design was adopted from the ORNL AHTR's plate type fuel assembly. [21] The assemblies are boxed in hexagonal C-C composite walls of 1mm thick. Within each hexagonal prismatic box, there are three symmetric parallelogram channels separated by a Y-shaped structure made of C-C composite, originally serving as a control rod follower. In each of the three regions, there are several equidistantly spaced fuel plates supported by the Y-shaped structure and the C-C assembly box. The coolant channels adjacent to the walls have half the width of the coolant channels between the fuel plates. In the AHTR design, the control elements are Y shaped blades that are inserted into the Y-shaped structure. Control rods in AGRs are inserted into the control rod channels in the graphite keys that lock the cylindrical graphite blocks in place. This frees up the control blade channel space in Y-shape structure and allows its thickness to be reduced allow larger fuel loading and coolant flow. The thicknesses of the Y-shape structure and the carbon wall for the FHR assembly were assumed to be 1.7 cm and 0.5 cm, respectively.

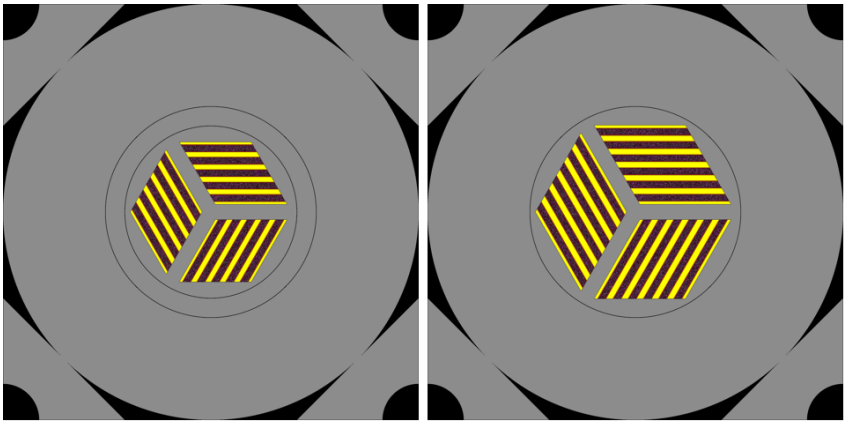

Figure 3-3. Serpent models for 5-plate Sleeved assembly (left) and 6-plate No-Sleeve assembly (right)

Two parallel assembly design options were proposed for the plate type fuel: 1) Sleeved design (S), i.e., assembly that fits within the inner graphite sleeve and 2) No-Sleeve (N/S), i.e., a single-piece (no sleeve) assembly that fits into the space of an AGR fuel channel. The Sleeved assembly design had a flat-to-flat diameter of 16.45 cm and a fuel plate length of 7.94 cm; the No-Sleeve design had a flat-to-flat diameter of 21.18 cm and a fuel plate length of 10.09 cm. The specifications of the reference plate type fuel designs are presented in Table 3-2. For all reference designs, the fuel volume and thus the coolant flow area were similar for designs with

different number of plates. Figure 3-2 shows Serpent models of Sleeved and No-Sleeve assembly designs with 5 and 6 plates, respectively. FCM fuel plates were modelled with Serpent's randomly dispersed particle function.

Table 3-2. Specifications for reference plate type FHR assembly designs

Type	*#Plates*	*Plate thickness*	*Cool. chan. width*	*Asmbl. fuel vol*	*Core HM*
Sleeved	3	1.2 cm	0.892 cm	0.0712 m^3	3933 kg
Sleeved	4	0.82 cm	0.7 cm	0.0648 m^3	3580 kg
Sleeved	5	0.62 cm	0.555 cm	0.0613 m^3	3387 kg
No-Sleeve	3	1.4 cm	1.313 cm	0.1055 m^3	5831 kg
No-Sleeve	4	1.1 cm	0.885 cm	0.1105 m^3	6109 kg
No-Sleeve	5	0.8 cm	0.747 cm	0.1005 m^3	5553 kg
No-Sleeve	6	0.62 cm	0.637 cm	0.0935 m^3	5164 kg

Table 3-3. TRISO particle fuel specifications

Region	*Parameter*	*Parameter value (μm)*	*Material*	*Density (g/cm^3)*
Kernel	diameter	427	UCO	10.9
Buffer	thickness	100	Porous graphite	1
IPyC	thickness	35	Pyrolitic graphite	1.9
SiC	thickness	35	SiC	3.2
OPyC	thickness	40	Pyrolitic graphite	1.87
	Particle diameter	847		
matrix	–	–	Carbon material	1.59

The fuel plate designs were also adopted from the SmAHTR. [48] The FCM fuel meat contains tightly packed (40% volume fraction) TRISO particles in graphite matrix and is separated from the coolant salt by a thin (1mm thick) sheath of carbonaceous material. On each fuel plate, there are two unfuelled semi-circular 'spacer ridges' that run on one side of the fuel plate to provide mechanical rigidity and prevent flow-induced vibration. [21] The dimension and material specifications of the TRISO particles used in this study were from the AGR-2 experiment described in recent studies. [49-51] The kernel of the TRISO is composed of a

Uranium Oxycarbide (UCO), which is a mixture of UO_2, UC and $UC_{1.86}$ with molar fractions of 71.4%, 16.4% and 12.3%. [51] Table 3-3 lists the specifications of the FCM fuel used.

3.1.4 Coolant Salt Options

There are many coolant salt candidates considered by the FHR design community. In 2006, ORNL reported on the assessment of more than ten fluoride and fluoroborate salt candidates (e.g., FLiBe, FLiNaK, NaF-BeF_2, LiF-NaF-BeF_2, Li-ZrF_4, NaF-ZrF_4, KF-ZrF_4, Rb-ZrF_4, etc.) for its AHTR in terms of thermochemical properties, fluid transport properties, heat transfer capacities, nuclear properties, cost and chemical considerations [27]. It was commented in the report that 1) ZrF_4- salts have the potential for low cost and special properties, among which NaF-ZrF_4 is potentially the least expensive; 2) BeF_2- salts have superior neutronic properties and heat-transfer properties, with FLiBe having the lowest activation and 3) further experimental work shall be undertaken to examine the chemistry of NaF-ZrF_4 and related ternary mixtures with the Alkali fluoride salt, FLiNaK, being the reference salt for corrosion response. [27] Other studies also considered alternative chloride salt (e.g., LiCl-KCl, LiCl-RbCl, NaCl-$MgCl_2$, etc.) for heat transfer in nuclear reactors. [27] However, it was concluded that these alternative salt classes display poorer heat-transfer performance than fluorides and most fluoroborates.

Based on recommendations from previous studies, this thesis selected three salt candidates for design evaluation: 1) FLiBe 2) FLiNaK and 3) tritium-free NaF-ZrF_4. FLiBe has the best neutronic and thermal-hydraulic performance among all known molten salts and large amount of experience has been accumulated around it over decades of MSR and FHR research. However, the Lithium and Beryllium inside FLiBe absorb neutrons and produce tritium, which is radioactive and can permeate through almost any material at high temperature. Li-6 has a large absorption cross-section. Therefore, the FLiBe has to be enriched in Li-7 to reduce parasitic absorption and tritium production. This makes FLiBe not only toxic but also expensive. Although extensive work has been done to deal with tritium problem, both effectiveness of removal and costs of these newly proposed tritium removal systems are still uncertain and remain a subject of investigation. [52][53] FLiNaK is widely accepted as the best alternative salt to FLiBe. It is cheaper and has reasonably good thermal-hydraulic properties. It is often used as the heat transfer fluid in the secondary loop of FHRs. However, it also produces tritium and therefore also requires Li-7 enrichment and tritium removal system. The third salt candidate, NaF-ZrF_4, although with relatively less favourable neutronic and thermal-

hydraulic properties, is considered the most affordable salt candidate. It contains neither Beryllium nor Lithium and therefore does not produce tritium. It is also readily available for purchase from current nuclear-grade suppliers. NaF-ZrF_4 could be a very good alternative candidate to the tritium producing salts should tritium removal technologies prove to be prohibitively complex and expensive.

3.2 Nominal State Safety Limits

Table 3-4. Safety Criteria and limits for different coolant and fuel materials

Design criteria	*Limits*	*Physical Constraints*
1. Min bulk $T_{coolant}$	559°C for FLiBe 554°C for FLiNaK 600°C for NaF-ZrF_4	FLiBe freezing at 459°C LiNaK freezing at 454°C NaF-ZrF_4 freezing at 500°C
2. Max bulk $T_{coolant}$	700°C	Hastelloy N allows 730°C
3. Max local $T_{coolant}$	1230°C for FLiBe 1370°C for FLiNaK 1150°C for NaF-ZrF_4	FLiBe boiling at 1430°C FLiNaK boiling at 1570°C NaF-ZrF_4 boiling at 1350°C
4. Max T_{clad}	1200°C for SiC 800°C for s-steel	Material failure
5. Max T_{fuel}	1250°C for TRISO 1350 °C for UC and UO_2	good performance under 1250°C UO_2 melting at 2865°C UC melting at 2365°C AGR nominal Max T_{fuel} = 1430°C
6. Min local Re	4000	Ensure turbulent flow regime

To ensure safe operation, the allowable operating domain was bounded by a number of design constraints. There were six design constraints chosen for the AGR-like FHR such that there were reasonable margins on the limiting parameters to allow for a safety case under reactor transient during normal operation. [54] These criteria, which in this application are also referred to as Limiting Safety System Settings (LSSSs) are summarised in Table 3-4. These LSSSs only

considered thermal-hydraulic limits on temperature and flow conditions. Neutronic, material, engineering and manufacturing considerations, etc., will necessarily impose more limits on the achievable power domain. For example, fuel loading requirements to ensure reasonable cycle length could become limiting since it would require larger fuel volume and thus impact the core power density. Mechanical properties of reactor vessel at high temperature and transients, and Wigner energy temperature limits of the core graphite may impose additional safety requirements. However, under steady state operation they are less-limiting requirements than the six considered in Table 3-4. Large thermal inertia of the core also helps to avoid the drastic temperature changes.

Criterion 1 in Table 3-4 defines the minimum temperature for bulk coolant inlet temperature. This makes sure that the coolant could stay above the melting temperature, with a minimum 100 °C margin. Criterion 2 states that the maximum bulk coolant temperature at the outlet of the core is 700 °C. This criterion was derived from the properties of the chosen FHR primary loop structural material Hastelloy N, which was demonstrated to have a maximum working temperature 730 °C. [55] A 30 °C margin was given to ensure the structural material integrity in anticipated transients. Criterion 3 limits the maximum local coolant temperature to stay below its boiling point with a 200 °C margin. This should also to great extent prevent the critical heat flux (burnout) scenarios. The cladding material chosen for FHR included stainless-steel, which starts to fail at above ~800°C and SiC which fails at above ~1200°C. These are addressed in Criterion 4. Criterion 5 set the maximum fuel local temperature so that there is a large margin to fuel melting. The limit for FCM fuel was selected based on the Idaho's AGR-2 experiment. [50][51] In the chapter, the limits for the two ceramic fuels were derived from the Torness AGR nominal operating condition: assuming a core radial power peaking factor of 1.3, the maximum fuel temperature of Torness AGR was calculated to be 1420 °C, thus the maximum fuel temperature for the proposed FHRs under nominal operating condition was limited to 1350 °C to allow some margin for the analysis uncertainties. By choosing the temperature limit from nominal operating condition of Torness, the FHR thermal-hydraulic result can be compared to the published AGR data. In later stage, this limit can be relaxed to actual material limits to fully exploit the benefit of using salt coolant. Criterion 6 introduced a limit on minimum local Re to assure turbulent flow and heat transfer regime. Coolant salt velocity should also be limiting a factor as large coolant flow might cause problems such as flow induced vibration or abrasion of the cladding and structural material. However, the limit must be experimentally established, which shall be addressed in future work.

To show how these constraints were applied to define the maximum allowable power, Figure 3-4 illustrates schematically the hot channel temperature distribution of a hypothetical FHR. The relative magnitudes of the temperatures are not to scale and are exaggerated to give clearer presentation and therefore not representative of the actual temperature profiles. In this example, temperatures of all other components are below their corresponding limits, therefore, the maximum amount of power that this hypothetical design can produce safely is limited by the maximum fuel temperature constraint.

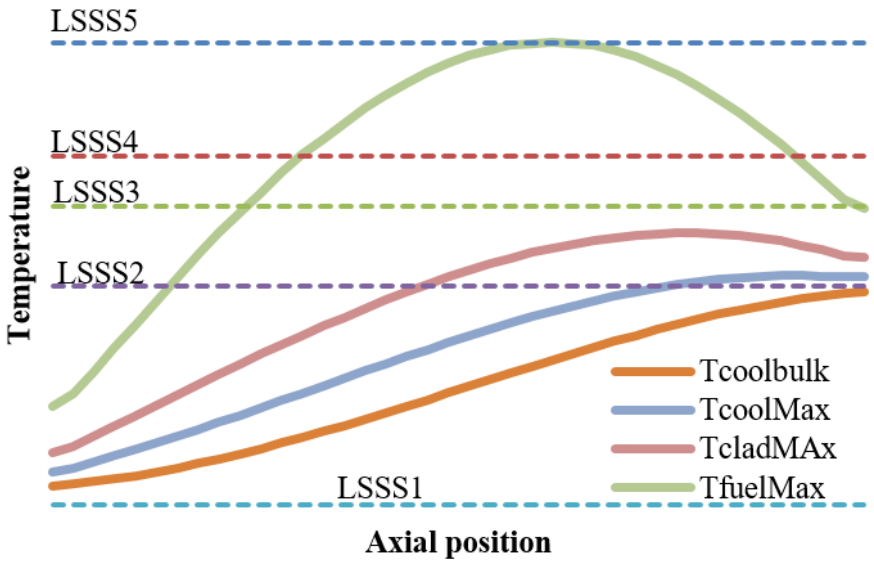

Figure 3-4. Schematic plot of hot channel core component temperatures and LSSS limits

3.3 Search for Operating Domain

The SODom code iteratively calls the sub-channel thermal-hydraulic solvers given a specified coolant pressure drop to identify the power level that breech each of the six LSSSs defined. These power output levels and their corresponding temperature conditions can be plotted on a graph to define the allowable operating domain of an FHR. Figure 3-5 shows an illustration of the operating domain for a hypothetical FHR.

The operating domain (green region) is bounded by three lines: 1) the blue line that bounds the left side of the domain is the ‘inlet coolant temperature line’; 2) the vertical red line bounding the right side of the domain is the ‘outlet coolant temperature line’; 3) the line bounding the

domain from the top is the line joining the most limiting cases from the ‘inlet line’ and the ‘outlet line’. The ‘inlet line’ is determined by fixing the bulk coolant inlet temperature to design constraint criterion 1, i.e., minimum bulk coolant temperature. To ensure turbulent heat transfer regime, Re was targeted to be greater than 4000 in any position along the coolant channel. Since Re increases with coolant temperature for a given mass flow rate and coolant channel geometry as viscosities of salts are strongly temperature dependent, in some cases the Re limit might become more restrictive than the minimum coolant inlet temperature limit. Therefore, the bottom left corner of the operating domain and thus the ‘inlet line’ is determined by considering both design constraint 1 and 6. Starting from zero power, in which case there is no coolant temperature difference between inlet and outlet (bottom left corner of the domain), the bulk coolant outlet temperature increases with reactor power.

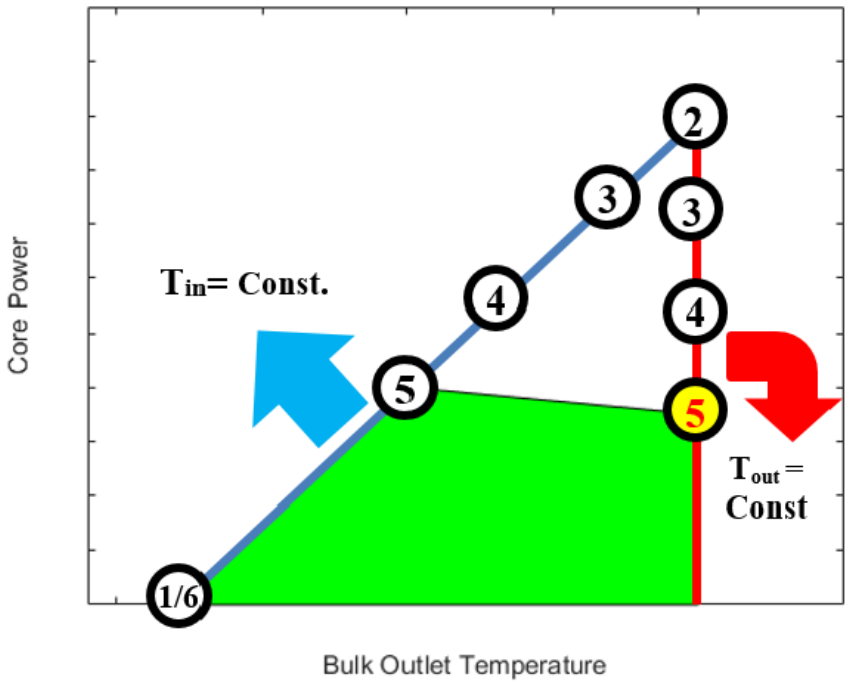

Figure 3-5. Schematic plot of operating domain of an example FHR.

The ‘outlet line’ is determined by fixing the bulk coolant outlet temperature to design constraint criterion 2, i.e., the maximum bulk coolant temperature. With increasing power, the inlet coolant temperature decreases along the ‘outlet line’. The circled points on the ‘inlet line’ and the ‘outlet line’ represent cases where each of the design constraint criteria is violated under

fixed inlet temperature or fixed outlet temperature conditions, and the numbers in these circles represent the number of the constraint being violated. The line connecting the point 5 in yellow and point 5 in white in Figure 3-5 is the design space 'maximum power boundary'. Any point along this line represents the maximum allowed power for each specific set of operating conditions (coolant inlet and outlet temperatures, and coolant flow rate). Since a higher outlet temperature would result in a higher thermal efficiency, the maximum power allowable in this example would be taken from the outlet temperature line, i.e., point 5 in yellow. Figure 3-5 illustrates a situation where the inlet and outlet temperature conditions are the least limiting factors. This was shown to be true for most solid pellet fuelled FHR designs. In cases where allowable window for coolant temperature rise is the most limiting factor, the allowable operating domain becomes triangular shaped, bound by the 'outlet line' and the 'inlet line', i.e., points 1/6 and 2 on from Figure 3-5.

3.4 Operating Domain Search Results

The operating domain results presented in this chapter were all obtained assuming a core coolant pressure of 150 kPa (excluding gravitational pressure drop). This condition was derived from the AHTR design: Assuming no spacer ridges between fuel plates, the coolant pressure drop of AHTR was predicted to be 55.3 kPa by TH_Plate, which was consistent with the value reported by ORNL. [56] However, when considering the effect of the spacer ridges, TH_Plate predicted the frictional coolant pressure loss of AHTR to be 76.8 kPa. Scaling the value with reactor height, the FHR would have ~150 kPa pressure drop. Identification of the optimum core pressure drop for a certain FHR design is presented in the next chapter.

3.4.1 Operating Domain for the Reference Design

SODom was applied to the reference designs with three and four rings of fuel rods, in combination with three fuel materials, three salt coolants and two claddings. A total of 36 designs were analysed. The maximum allowable powers and the corresponding limiting LSSSs and other specifics for the analysed FHR models are summarised in Table 3-5. All models were reported with a coolant outlet temperature of 700 °C. In the cases where two results are reported, the two values represent results for SiC and stainless-steel cladded reactors respectively. It firstly was noticed that for all UC and FCM fuelled designs that used stainless-steel cladding, cladding temperature became the most limiting constraint and forced the reactor to operate at much lower power than would be allowed if SiC cladding is used. On the contrary, all SiC cladded designs apart from the 4-ring UC fuelled and NaF-ZrF_4 cooled design, fuel temperature

limit was the most restrictive LSSS. This suggested that cladding and fuel choice played major roles in determining the operating domain boundaries and maximum allowable power for the reference designs: SiC worked well with all three fuel candidates, whereas stainless-steel worked better with UO_2 only; UC and FCM fuels offered much larger operating domain compared to UO_2, with UC slightly outperforming FCM. Therefore, it can be concluded that, in general, stainless-steel is a less attractive cladding material in terms of thermal-hydraulic performance compared with SiC. As a result, stainless steel was excluded from consideration as cladding material in later stages of this project for solid pin FHRs. The choice of coolant, on the other hand, did not affect the maximum allowable power significantly.

Table 3-5. Specifications for the proposed solid pin FHRs

#rings	*fuel mat*	*coolant mat*	*Maximum allowable power (MWt)*	*Most limiting parameter*	*Coolant inlet T (°C)*
3	UO_2	FLiBe	1142/1131	Max T_{fuel}	693
3	UO_2	FLiNaK	1152/1140	Max T_{fuel}	692
3	UO_2	$NaF\text{-}ZrF_4$	1089/1083	Max T_{fuel}	690
3	UC	FLiBe	4565/2336	Max T_{fuel}/T_{clad}	674/686
3	UC	FLiNaK	4708/2573	Max T_{fuel}/T_{clad}	669/683
3	UC	$NaF\text{-}ZrF_4$	3880/1540	Max T_{fuel}/T_{clad}	664/686
3	FCM	FLiBe	3499/2336	Max T_{fuel}/T_{clad}	680/686
3	FCM	FLiNaK	3588/2573	Max T_{fuel}/T_{clad}	676/683
3	FCM	$NaF\text{-}ZrF_4$	3049/1540	Max T_{fuel}/T_{clad}	672/686
4	UO_2	FLiBe	1899/1879	Max T_{fuel}	679
4	UO_2	FLiNaK	1910/1898	Max T_{fuel}	676
4	UO_2	$NaF\text{-}ZrF_4$	1814/1796	Max T_{fuel}	668
4	UC	FLiBe	7535/3739	Max T_{fuel}/T_{clad}	616/659
4	UC	FLiNaK	7793/4123	Max T_{fuel}/T_{clad}	599/647
4	UC	$NaF\ ZrF_4$	5556/2398	Min T_{in}/T_{clad}	600/657
4	FCM	FLiBe	5797/3739	Max T_{fuel}/T_{clad}	635/659
4	FCM	FLiNaK	5967/4123	Max T_{fuel}/T_{clad}	623/647
4	FCM	$NaF\text{-}ZrF_4$	5014/2398	Max T_{fuel}/T_{clad}	611/658

An interesting finding was that directly replacing CO_2 in an AGR with salt coolant did not allow any power uprate. This is because the specific heat capacity and density of the salts are much higher than CO_2, therefore the average core temperature is much higher in salt cooled

environments, leaving smaller margin for fuel temperature rise before breaching the maximum fuel temperature limit. This observation also partly explains why FLiNaK cooled designs allow slightly higher power than FLiBe. Additionally, although FLiBe has higher thermal conductivity and Pr number, under the same pressure drop, FLiNaK has greater flow velocity and Re number and, therefore, has higher heat transfer coefficient than FLiBe. Comparing the 3-ring models with the 4-ring models, competing effects were found that determine the power uprate potential of the two. With more fuel rods in an assembly, there is less coolant flow area and poorer heat removal efficiency. On the other hand, the power is distributed across larger number of fuel rods and linear heat rating is reduced for each rod. The 4-ring model offered larger operating domain and achieved greater power, suggesting that the reduction in linear power effect won over the reduced coolant flow area effect. The 4-ring UC fuelled FLiNaK cooled FHR had the greatest power uprate to 4708 MWt (~ 2.9 times power uprate from AGR level). It is expected that greater power can be achieved by the FHR by increasing the number of fuel pins per assembly and pumping power. This may require larger coolant channels.

It was also noted that the operating domain for the $NaF\text{-}ZrF_4$ cooled 4-ring UC fuel model became triangular, suggesting that it was no longer limited by the maximum fuel temperature constraint. Instead, the coolant temperature rise window for $NaF\text{-}ZrF_4$ became more restrictive limit. This is because $NaF\text{-}ZrF_4$ has the poorest specific heat capacity and largest density and viscosity among the three salt candidates and therefore require greater temperature rise to carry the same amount of heat.

3.4.2 Operating Domain for Annular Pin Designs

Table 3-6 summarises the flow areas and hydraulic diameters for the three annular fuel designs. The SiC cladded 4-ring and 5-ring designs had almost identical allowable operating domains. It was observed that compared with the 4-ring design, 5-ring design had larger flow area for both internal and external coolant, which allowed higher mass flow rate for a given frictional pressure loss, and thus allowing higher power before breaking coolant temperature limits. However, the 5-ring design also had smaller hydraulic diameters for both internal and external coolant, which means less mass flow rate was allowed for a fixed pressure drop, thus allowing less power. As a result, the case with 5-rings had similar operating domain as the 4-ring design. The 3-ring design, on the other hand, had larger flow area and hydraulic diameters, and thus allowed a larger operating domain than the other two designs.

The 5-ring annular fuel design had the largest surface area to volume ratio, more than tripling that of the reference solid fuel design. This means that its shelf-shielding effect would be weaker. A large fuel surface area also means more cladding material is required per volume of fuel. The cladding will become a competitor for neutrons absorption, further reducing reactivity. Moreover, although having 30 more fuel rods than the 4-ring design, the 5-ring design can only accommodate 0.065 m^3 of fuel per assembly, 80% of the 4-ring design's fuel loading (0.082 m^3). Having the less favourable fuel utilisation and hydraulic performance, the 5-ring annular ring design offers no advantage and, therefore, it is not included in subsequent analyses.

Table 3-6. Design specifications for 3-ring, 4-ring and 5-ring annular pin assemblies compared with reference AGR fuel assembly

Assembly specifications	*3-ring*	*4-ring*	*5-ring*	*Ref. AGR*
Inner A_{flow} (cm^2)	77.07	55.23	62.59	*NA*
Outer A_{flow} (cm^2)	110.2	89.97	94.1	215.9
Inner Dh (cm)	1.65	1.08	0.94	*NA*
Outer Dh (cm)	1.28	0.81	0.72	3.6
Fuel loading (m^3)	0.055	0.082	0.065	0.049
Surface/Volume(/cm)	6.93	5.94	9.24	2.76

Table 3-7 lists the maximum powers and the operating conditions of the annular models. Again, in the cases where two values are reported, the two represent results for SiC and stainless-steel cladded reactors respectively. All SiC cladded designs were constrained by the minimum coolant inlet temperature limit or the or minimum Re limit. These designs had maximum allowable power (top vertex of the triangular operating domain illustrated in Figure 3-5) represented the case where the coolant enters the core with minimum bulk coolant temperature allowed by coolant freezing point/Re limit and exits the core at maximum bulk coolant temperature allowed by structural material integrity. This showed that cooling of annular fuel was significantly better than that of solid fuel as the fuel temperature limit becomes less restrictive than the coolant temperature limit. whereas all 3-ring designs using stainless-steel were limited by stainless-steel failure. Stainless-steel cladding again became the most limiting

constraint in some cases (all 3-ring designs), pushing them to lower power output significantly or use SiC instead. Therefore, stainless-steel was excluded from consideration as cladding candidate in later stages of this project.

Table 3-7. Maximum power and corresponding operating conditions for annular fuel FHRs

#rings	*fuel mat*	*coolant mat*	*Maximum allowable power (MWt)*	*Most limiting parameter*	*Coolant inlet T (°C)*
3	UO_2	FLiBe	11254/5517	Min T_{in} /T_{clad}	562/633
3	UO_2	FLiNaK	10116/6157	Min T_{in} /T_{clad}	556/614
3	UO_2	NaF-ZrF_4	4964/3584	Min T_{in} /T_{clad}	603/630
3	UC	FLiBe	11252/5710	Min T_{in} /T_{clad}	563/631
3	UC	FLiNaK	10181/6193	Min T_{in} /T_{clad}	556/613
3	UC	NaF-ZrF_4	4968/3682	Min T_{in} /T_{clad}	603/628
3	FCM	FLiBe	11251/5648	Min T_{in} /T_{clad}	563/632
3	FCM	FLiNaK	10123/6161	Min T_{in} /T_{clad}	558/614
3	FCM	NaF-ZrF_4	4954/3706	Min T_{in} /T_{clad}	603/628
4	UO_2	FLiBe	3531/3531	Max Re	624/624
4	UO_2	FLiNaK	5771/5718	Min T_{in}	556/557
4	UO_2	NaF-ZrF_4	2830/2830	Min T_{in}	603/603
4	UC	FLiBe	3532/3550	Max Re	625/624
4	UC	FLiNaK	5687/5711	Min T_{in}	558/557
4	UC	NaF ZrF_4	2848/2845	Min T_{in}	603/603
4	FCM	FLiBe	3536/3644	Max Re	624/624
4	FCM	FLiNaK	5688/5683	Min T_{in}	558/558
4	FCM	NaF-ZrF_4	2837/2850	Min T_{in}	603/603

Since fuel temperature was no longer a design limit for SiC cladded designs. The choice of fuel material did not affect the thermal-hydraulic operating domain and maximum allowed power for these reactors. Instead, the combination of coolant salt and the assembly configuration determined this. FLiBe has the best heat transfer properties followed by NaF-ZrF_4, and the 3-rings design offers greater coolant flow area than the 4-ring design; therefore, for most cases, FLiBe outperformed FLiNaK and NaF-ZrF_4 in terms of power uprate, and all 3-ring designs outperformed 4-ring designs when using the same salt. The 3-ring annular design had very little difference in operating domain when using FLiBe and FLiNaK, achieving the highest powers among all models explored. However, FLiNaK became a better coolant option than FLiBe in

all 4-ring annular fuel designs. FLiBe cooled 4-ring designs were most limited by the Maximum Re constraint. Since Re for salts increases with temperature, the coolant inlet temperature was therefore increased to ensure a turbulent flow at core inlet. As a result, the maximum allowable powers for these designs were dramatically reduced.

3.4.3 Operating Domain for Plate Type Designs

The results obtained from SODom calculations for plate type fuel designs are plotted in Figure 3-6. The No-Sleeve assembly designs allowed significantly higher power than Sleeved assemblies as expected. The number of plates in the assembly had relatively small effect on the power for reactors using FLiNaK and NaF-ZrF_4. There are, however, dramatic power reductions with the increase in the number of plates in FLiBe cooled Sleeved designs and in No-Sleeve designs with more than 4 plates.

For FLiBe cooled 3-plate No-Sleeve assembly design, Re at inlet was greater than the 4000 limit at an inlet temperature of 559 °C with 150 kPa pressure drop. FLiBe reached the Re limit of 4000 at 559 °C in the reference 4-plate design. When further increasing the number of plates, coolant inlet temperature must be increased to satisfy the Re constraint. FLiBe cooled Sleeved assembly designs saw similar behaviour starting from three plates. Therefore, sharp reductions in achievable power were seen with the increase in the number of fuel plates. For all designs using FLiNaK and NaF-ZrF_4, the Re limit was not breached at their specified minimum inlet temperature. Therefore, no significant power change with number of plates was observed.

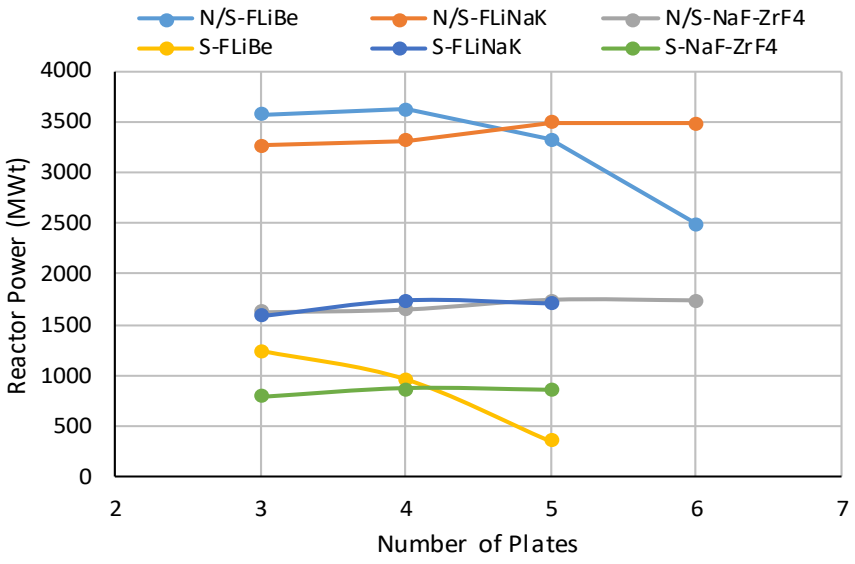

Figure 3-6. Allowable Reactor Power for different reference plate type fuel designs

In general, the notable reduction in achievable power with the number of fuel plate was a result of decreased temperature difference across the core due to the Re constraint. At the same coolant inlet temperature, the Re at reactor inlet decreased with number of plates. This is because with more plates, the wetted surface area is larger and therefore same pressure drop allows less coolant mass flow rate. For the same design, FLiNaK had the largest Re among the three candidate salts, which was almost twice as large as FLiBe in the temperature range of the proposed FHR. Viscosity of FLiBe is largest among the three salts (twice that of FLiNaK) and FLiBe and FLiNaK has similar densities. Therefore, FLiBe had the lowest Re for same design and pressure drop. NaF-ZrF_4 had Re in between those of FLiBe and FLiNaK, which was large enough for the designs proposed without needing to increase coolant inlet temperature from the limit of 600 °C. However, with the smallest temperature increase window restricted by the high melting point and much smaller heat capacity, the NaF-ZrF_4 cooled reactor could only achieve much lower powers than the designs with the other two salts.

3.4.3.1 Sensitivity to Fuel Plate Thickness

The plate type fuel uses FCM fuel meat and therefore fuel loading is a major concern for this design stream. By using thicker fuel plates, the reactor can have larger fuel loading, but this may come at a cost of reduced power output. Four design streams were chosen to study the sensitivity of reactor output to fuel plate thickness, namely: 1) No-Sleeve designs with FLiBe, 2) No-Sleeve designs with FLiNaK, 3) No-Sleeve designs with NaF-ZrF_4 and 4) Sleeved assembly designs with FLiNaK. All design streams considered four to six fuel plates. The Sleeved assembly designs with FLiBe and NaF-ZrF_4 performed notably worse than the reference Torness AGR and were not investigated further. In varying plate thickness, the minimum thickness of fuel plate and coolant channel width were both limited to 5 mm. The fuel plate thickness was varied for each design within the parallelogram channel envelope width (6.88 cm for Sleeved assemblies and 8.74 cm for No-Sleeve assemblies).

Figure 3-7 plots the maximum allowable power against heavy metal (HM) loading for the different plate type fuel FHRs. In this figure, the upper right corner is the most desirable design region, i.e., large HM loading and large power achievable. The plate type FHR operating domain in terms of fuel loading is bounded by FLiBe cooled No-Sleeve designs with three, four and five plates. At low fuel loading range (4860 kg HM), 5-plate design allowed highest power output (greater than 4350 MWt, or specific powers higher than 895 W/g). At intermediate fuel loading range, i.e., 4860 to 6664 kg HM, the 4-plate design allowed highest

power (2996 MWt to 4350 MWt, or specific power from 895 W/g to 450 W/g); and at high fuel loading range, i.e., higher than 6664 kg HM, 3 plate design cooled with FLiBe won over all others by allowing power of 2798 MWt to 2996 MWt, or specific power of 395 W/g to 450 W/g. The curves for 3-plate designs were relatively insensitive to plate thickness and thus to HM loading for all three coolants. This means that the 3-plate design had greater potential for larger fuel loading without sacrificing too much power output. Sleeved assembly designs (as circled) can potentially achieve higher power than AGR, but only at very low HM loading (around 3600 kg), compared to a typical AGR core has 14600 kg of uranium loading. [24]

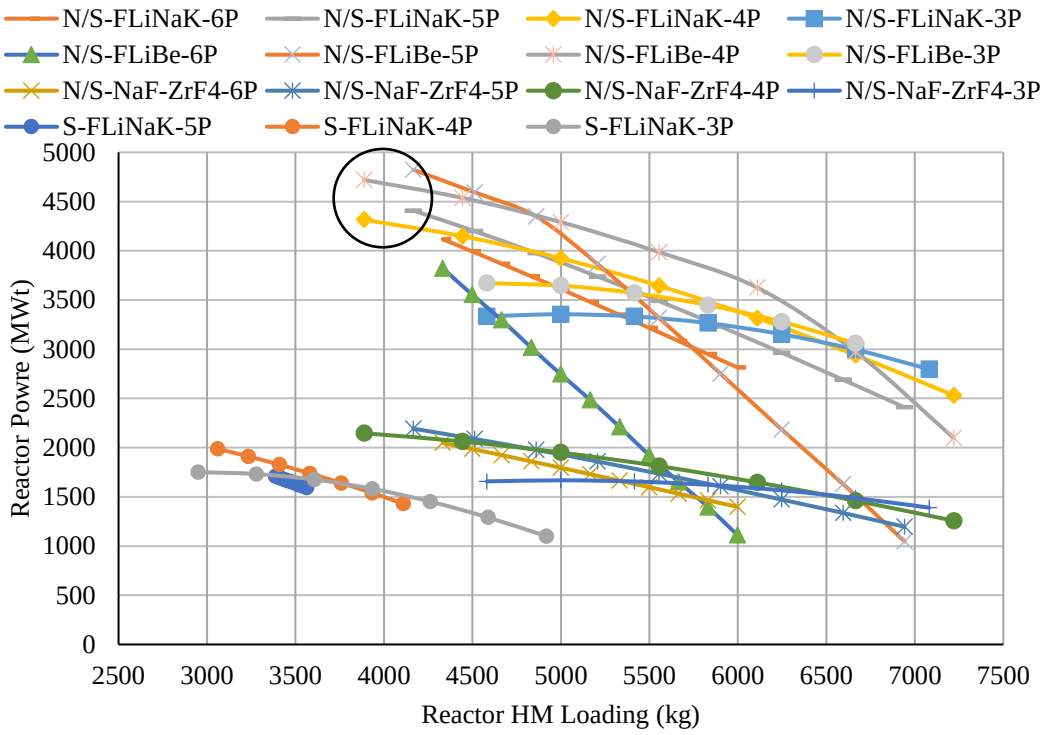

Figure 3-7. Trade-off between power output and reactor heavy metal loading

Chapter 4 System Thermal-hydraulic Optimisation

This chapter establishes methods necessary to identify the optimum core and heat transfer system operating condition from economic point of view. It firstly proposes a power conversion plant layout for the AGR-like FHR, based on which this chapter presents the heat transfer system design optimisation problem. It then introduces the optSys module of SCOOP, which is used to perform the optimisation task, and a wrapper function in SCOOP for identifying the optimum core operating condition. With all three main modules of SCOOP (SODom, optSys and CapCost) and the wrapper function ready, the code package is applied to a reference AGR-like FHR to demonstrate its capability. The last part of the chapter presents a sensitivity study to investigate how the assumptions used in SCOOP affect the LCOE reported and how this may affect SCOOP's application in future FHR design work.

4.1 AGR-like FHR Power Plant Layout

The proposed reference power conversion system for the AGR-like FHR consists of the reactor core, primary coolant pumps and heat exchangers, intermediate coolant loop pumps and heat exchangers and a supercritical CO_2 (sCO_2) recompression power cycle. [37] The sCO_2 recompression cycle offers one of the highest efficiencies at core outlet temperature in the region of 700 °C and has relatively high technology readiness level among all advanced power cycles. [37] The power cycle has also attracted much attention in industries outside of nuclear power, such as solar power, fuel cells, gas turbine exhaust heat recovery systems etc. [57] Studies have also been carried out to improve sCO_2 recompression cycle efficiency and safety. [58] There are many variations of the sCO_2 power cycle. At the preliminary design stage of the FHR, the 'Advanced Design' recompression sCO_2 power cycle proposed by Dostal et.al was considered because of its high efficiency (45.27% at 650 °C core outlet temperature), simplicity, and good compatibility with the proposed FHR temperature conditions. [37]

Figure 4-1 illustrates the power plant layout for the FHR. The thermal power generated from the reactor core is first carried by the reactor coolant to the primary heat exchanger (HX1) in which the heat is transferred to a secondary coolant, assumed to be the potentially cheapest heat transfer salt, $NaF\text{-}ZrF_4$. The secondary coolant brought the heat to the power cycle via a secondary heat exchanger (HX2). The components of the sCO2 recompression power cycle included the secondary heat exchanger, a turbine, a main compressor, two recuperators, namely, high temperature recuperator (HTR) and low temperature recuperator (LTR), a heat sink and a compressor. After producing work in the turbine, the hot exhaust CO_2 is directed into both

recuperators. The flow of CO_2 is then split into two: one stream goes through the precooler and cold channels of the LTR and recombines with the other stream before going through the HTR. In the Dostal's cycle design, the sCO2 enters the turbine at a pressure of 19.8MPa and a temperature of 650°C. The main compressor has an inlet pressure of 7.7MPa and an inlet temperature of 32°C. This served as the reference plant layout for this thesis on which the optimisation was performed. Other power cycles and plant layouts are potentially possible for FHRs and can be analysed using the same logic and development framework.

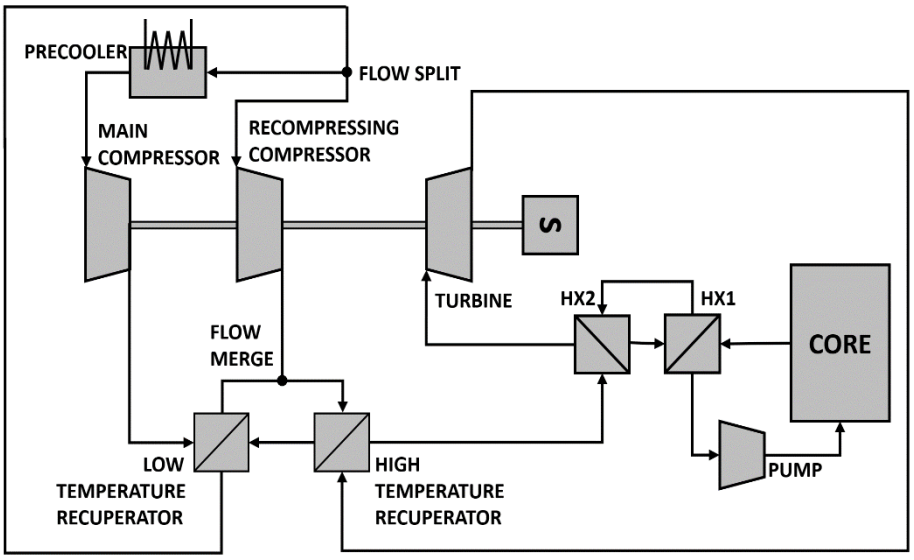

Figure 4-1. Proposed FHR plant layout

PCHEs were proposed for the recompression sCO_2 cycles. In this work, PCHE was also chosen as the heat exchangers between the primary loop, intermediate loop and the power conversion cycle. PCHE is a commercially available from HEATRIC. [59] The heat exchanger is made with Hastelloy N plates carrying etched channels joined together by diffusion welding to form all-metal modules. Hastelloy N shows very good resistance to corrosion at high temperatures and can operate at up to 750°C and thus often chosen as material for molten salt environment. [55] A thermal soaking period during the diffusion welding process allows grain growth that gives the PCHE core the strength of its base metal, high pressure containment capability and avoidance of corrosion cells. Also, flow induced vibration problems that happen to traditional shell and tube heat exchangers can also be avoided. [36] Figure 4-2 illustrates the cross-section of an example PCHE. [59] The plate thickness and channel width can range from 0.5mm to

5mm. The plates with etched channels can be placed on top of each other with zero or 90° angle to allow concurrent flow, counter current flow or cross flow. In the Idaho National Laboratory's (INL) feasibility study of secondary heat exchanger concepts for the Advanced High Temperature Reactor (AHTR), [38] a PCHE design was proposed to have a channel width of 3 mm, channel pitch of 3.3mm and a plate thickness of 3.17mm. These specifications were adopted in this thesis.

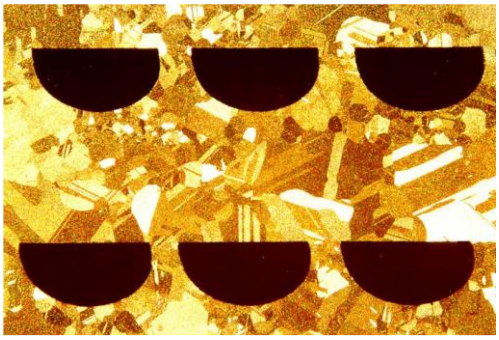

Figure 4-2. Cross-sectional view of an example PCHE [38]

4.2 Understanding the Optimisation Problem

Based on the plant layout presented, there was a complicated network of interdependencies among the design parameters, and all of them affect plant economics in competing ways. Optimising one parameter would necessarily bring negative effect(s) to the other(s). Figure 4-3 schematically plots the temperature-entropy (T-S) diagram for the proposed AGR-like FHR plant layout to help illustrate the heat transfer system design space and identify the design trade-offs of the system thermal-hydraulic design. The relative positions of the points on the graph are not to scale and are exaggerated for demonstration purposes. The top triangle bounded by points A, B and C in Figure 4-3 represents the reactor core. Coolant enters the core from point B, absorbs nuclear heat as it passes through the channels and exits the core from point A at a higher temperature. The coolant then goes through the primary heat exchanger (HX1) where heat is transferred to the secondary loop heat transfer salt. The primary loop coolant exits the cold leg of the heat exchanger at point C and is pumped back into the core at point B. The second triangle bounded by points D, E and F represents the intermediate heat transfer loop. The salt in the intermediate loop runs at a slightly lower temperature than the primary coolant to allow heat transfer. The same process discussed for the primary loop takes

place in the intermediate loop. The heat source becomes the primary loop coolant and the heat sink becomes the working fluid in the power conversion cycle, in this case, CO_2 from point H to G. The triangular-shaped TS diagram for the reactor and the intermediate loop shows that the heat transfer process is non-isobaric and the compression (pumping) process is non-isentropic. The sCO_2 recompression cycle is not fully shown in the T-S diagram. Only the part where the working fluid absorbs heat from the intermediate loop and transfers the thermal energy to kinetic energy through expansion is shown.

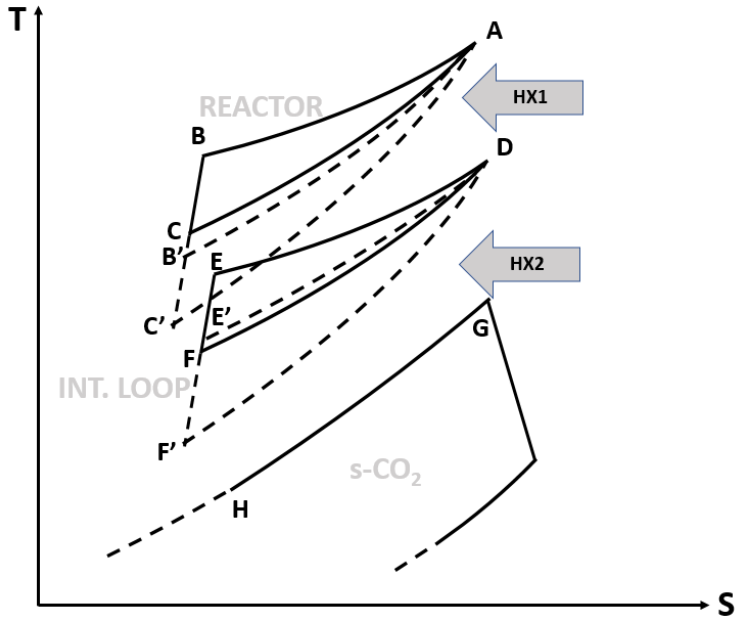

Figure 4-3. Schematic T-S diagram for the FHR.

Figure 4-3 also shows some dashed lines linking points marked with apostrophes. This demonstrates the degrees of freedom in the heat transfer system design. Line G-H can in principle move up and down depending on further design judgement on the trade-off between power cycle efficiency and the cost of HX2. Under the scope of this study, points G and H of the power cycle were assumed to be fixed. Points A and D, G and H were also fixed, whereas other points on the graph could be varied. In order to maximise power conversion efficiency, the reactor coolant outlet temperature (point A) was maximised under the materials safety limit (700 °C). The temperature and pressure conditions of the turbine inlet of the sCO_2 cycle, point G, (as well as other points in the sCO_2 cycle) were fixed assuming specific pressure losses

along the power cycle. Assuming a fixed minimum approach temperature of 15 °C for all heat exchangers, the intermediate loop salt maximum temperature, point D was also fixed.

For a given core power and coolant pressure drop, relative positions of the reactor inlet (point B) and primary heat exchanger hot channel outlet (point C) on the T-S diagram is fixed. Same analysis is applied to the intermediate loop. In fact, the difference between B and C (and between E and F) under any reasonable reactor power level is so minimal that when plotted on the T-S diagram to scale, the two points would almost overlap. Therefore, for a given power level, there are two points on the T-S diagram that needed to be optimised in the power conversion system, namely point B, the reactor coolant inlet point, and point E, the exit point from the hot leg of the secondary heat exchanger. The condition of the reactor loop (point B and C) determines the allowable ranges of Log Mean Temperature Differences (LMTDs) of the primary and secondary heat exchangers, while the intermediate loop condition (relative position of point E and F with C and H) determines the balance of heat transfer efficiencies of both the primary and the secondary heat exchanger. For a given core power, when the coolant passes through the core at a lower mass flow rate, the temperature rise of the coolant increases. For a fixed core outlet design temperature, this means that the reactor coolant entered the core at a lower temperature, i.e., point B moves to B' and point C moves to C'. On one hand, less pumping power would be required in this case; on the other hand, the reactor thermal power is transferred across the heat exchangers less efficiently and thus more heat transfer surface area in the primary heat exchanger is required to carry the same heat exchange duty. Likewise, points E and F on the intermediate loop are also subject to similar analysis considerations.

The interdependencies between the design parameters in the heat transfer system are summarised in the Figure 4-4. Assuming all other capital costs apart from heat exchangers being held constant with the heat transfer system design, three major contributors to the plant economics are illustrated in Figure 4-4: 1) power density (powDens), 2) heat exchanger capital cost (HXcost) 3) pump operating cost (PumpCost). Δp_{cool} and ΔT_{cool} are the heat transfer fluid pressure drop and the temperature increase respectively, and the subscripts 1 and 2 represent the primary and the intermediate loops. HX1size and HX2size represent the sizes of the primary and secondary heat exchangers respectively. The blue arrows in the figure represent positive correlations between the two linked parameters and the red arrows represent inverse relationships. For example, Δp_{cool1} points to powDens with a blue arrow and points to ΔT_{cool1} with a red arrow. This shows that with increasing coolant pressure drop, greater power is allowed, and the primary coolant would have smaller temperature increase across the core.

From the colours of the arrows, it can be seen that there is no particular independent design variable that can be increased (or decreased) to lead directly to improved plant economics without sacrificing performance in other aspects.

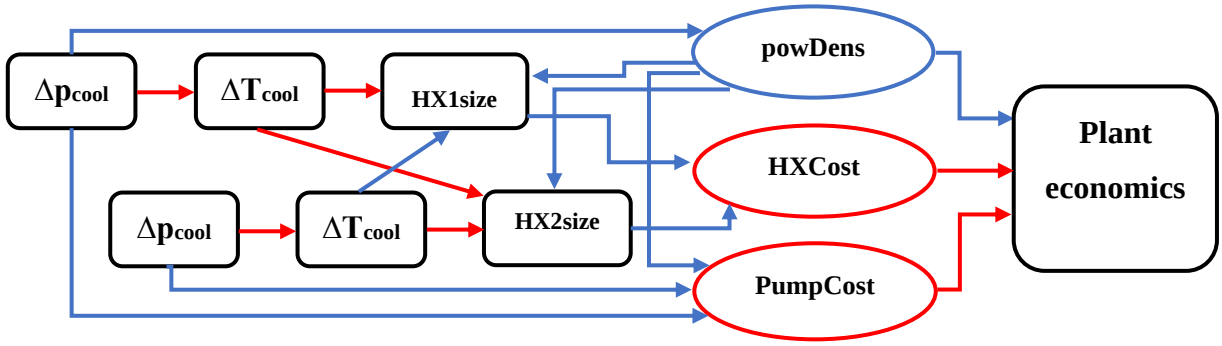

Figure 4-4. Interdependencies of operating conditions with power density, heat exchanger cost and pump cost

This trade-off described is essentially a three-way trade-off between power density, heat exchanger capital cost and the pumping cost: 1) for a certain reactor power level, the greater the pumping cost, the lower the heat exchanger costs, and vice versa. 2) with increased core power, greater cost must be expended on both the heat exchangers and the pumps. Therefore, the optimum design must satisfy two conditions: 1) marginal benefit of pumping power equals marginal benefit of heat exchangers, and 2) marginal benefit of an increase in core power, which is enabled by an increased pressure drop, equals the marginal cost incurred by the power plant, e.g., greater pumping power requirements and heat exchanger sizes. To optimise the design, these trade-offs must be quantified.

4.3 System Thermal-hydraulic Design Optimisation with sysOpt

This section introduces a module in SCOOP, optSys, which quantifies the trade-offs illustrated in Figure 4-4 and optimises the system thermal-hydraulic design, i.e., the positions of points E and F on Figure 4-3. First, SCOOP calls the SODom sub-routine to identify the maximum allowable power and the corresponding coolant temperature conditions for the subject reactor at a given pressure drop. The pressure drop is fed to SODom by a wrapper function, which is described later. Then, SCOOP feeds the power from SODom to optSys, which uses a standard gradient descent optimisation algorithm to identify the optimum primary and secondary loop temperature conditions for a given core design. optSys begins by calling sizeHX twice for the primary and secondary heat exchanger respectively to obtain the minimised heat exchanger

system cost using the core power and temperature conditions from SODom and an initial guess for the temperature difference across the cold leg of the primary heat exchanger, i.e., ΔT between points C and F in Figure 4-3. The core coolant pressure drop is accounted for in the pumping cost calculations for the primary loop. Then, a small perturbation is made to the temperature condition, i.e., perturbing the positions of points E and F in Figure 4-3 and the sizeHX calculations are performed again to update the heat exchanger system cost. The negative value of the rate of change, i.e., the gradient, of the cost with the temperature perturbation is scaled by a 'gradient descent step size factor' and used as the size of the temperature perturbation of the next round of sizeHX calculations for the primary and secondary heat exchangers. This routine is continued until the absolute value of the gradient becomes smaller than a chosen threshold, meaning that the target parameter, i.e., the heat exchanger system cost in this case, had reached its minimum value. The final secondary loop temperature conditions, i.e., the positions of points E and F and the heat exchanger designs are then reported by optSys.

In this routine, the initial guess of temperature condition and the gradient descent step size factor had large impacts on the speed of calculation convergence. It was found that approximately 0.5 is a suitable value for the step size factor and a good guess for the temperature at point F is the mid-point between the temperatures at points C and H. Since a minimum approach temperature of 15 °C was chosen for the heat exchanger design, optSys is performing a bounded optimisation problem. If the final optimised operating condition reported by optSys violates this condition, the boundary conditions, i.e., the one where the cold leg of the primary heat exchanger has a temperature difference of 15 °C and the one where the cold leg of the secondary heat exchanger has a temperature difference of 15 °C, are tested and the one that had lower heat exchanger system cost would be reported as the optimum system operating condition for the reactor. This is only a theoretical possibility and it was not encountered in the optSys calculations for any of the proposed FHR designs. The result of optSys, i.e., the cost of the heat exchanger system, is used to calculate the variable P_R in Equation 2.21. It is then fed to CapCost together with the result of SODom, i.e., the maximum achievable power Q_s in Equation 2.21, to estimate the LCOE of the subject reactor at a given coolant pressure drop across the core.

4.4 Identifying the Optimum Core and System Operating Parameters with SCOOP

A simple wrapper function was created to feed different core coolant pressure drop values to the three main modules in SCOOP. For each pressure drop value, SCOOP calculates 1) the maximum achievable power and primary coolant temperature conditions (from SODom), 2) the optimum secondary loop fluid temperature conditions and primary and secondary designs (from optSys) and 3) the LCOE of the power plant (from CapCost). The core pressure drop that minimised the LCOE of the plant would be identified as the optimum core operating condition.

To demonstrate the functions of SCOOP, the code package was applied to an example FHR design, i.e., the 3-ring solid pin FHR with UC fuel, SiC cladding, FLiBe coolant and NaF-ZrF_4 intermediate loop heat transfer fluid. It should be noted that this 'example FHR' was different from the 'reference FHR' chosen for CapCost, which was assumed to have an LCOE of 96 £/MWh. Pressure drops ranging from 50 kPa to 1000 kPa were tested. The final SCOOP results, i.e., the optimised core and system operating parameters, are summarised in Table 4-1. The design specifications of the power cycle are adopted from Dostal's 'advanced supercritical CO_2' design. [37] However, power conversion efficiencies would be different for different core temperature operating ranges. For a fixed outlet temperature, a higher coolant inlet temperature would increase the average heat transfer temperature to the secondary loop and power conversion cycle, increasing the thermodynamic efficiencies of the cycle. By how much the inlet temperature affects the overall power efficiency and the resulting power output should be investigated in future studies.

It must be acknowledged that it is not suggested to rely on SCOOP for accurate prediction of the LCOE of a reactor since the assumptions made in SCOOP are hard to justify due to lack of data. Therefore, LCOE reported by SCOOP should always be taken in context of the assumptions made in SCOOP. Furthermore, the neutronic calculation requires core power and temperature as an input when coupled with thermal-hydraulic calculations. It would therefore be a concern for SCOOP if the resulting optimum operating condition and the corresponding power are affected by the assumptions made. However, it is expected that these variables would not be significantly affected by the assumptions made. The following sub-section examines the sensitivity of SCOOP results to its assumptions.

Table 4-1. Summary of recommended design details for the reference FHR

Plant Design		**Primary HX and Pump**	
Reactor Type	FHR	Total volume	19.3 m^3
Thermal output	6520 MWe	Total frontal area	13.4 m^2
Electrical output	2837 MWe	Heat exchanger length	1.4 m
Net efficiency	43.5 %	Pumping power	17 MWe
LCOE	65.7 £/MWh	Annual HX & pump cost	£ 36.1 mil
Core Design		**Secondary HX and Pump**	
Fuel material	UC	Total volume	25.9 m^3
Moderator material	Graphite	Total frontal area	10.3 m^3
Coolant material	FLiBe	Heat exchanger length	2.5 m
Mean inlet temperature	662 °C	Pumping power	10.3 MWe
Mean outlet temperature	700 °C	Annual HX & pump cost	£ 38.9 mil
Core coolant pressure drop	150 kPa		
		s-CO2 Power Cycle Design	
Intermediate Loop Design		Turbine inlet temperature	670 °C
Coolant material	$NaF-ZrF_4$	Turbine inlet pressure	19793 kPa
Mean hot leg temperature	685 °C	Compressor inlet temperature	32 °C
Mean cold leg temperature	562 °C	Compressor inlet pressure	7692 kPa
		Net efficiency	45.3 %

4.4.1 Sensitivity Studies of the Capital Cost Scaling Model

Firstly, among all the assumptions made in CapCost, the choice of the reference design in CapCost was expected to have the biggest influence on SCOOP's results. If a different reactor (especially one with a different power output level) was chosen as the reference for cost calculation, the LCOE of any subject reactor to SCOOP assumptions would be calculated differently since the LCOE changed with the reference power output Q_s and the ratio of subject reactor to reference reactor heat exchanger system cost, P_R. It can be argued that the current choice of the reference FHR for cost estimations is reasonable as the reactor has similar power output (3400 MWt) as most of the large size next generation reactors. Although larger in physical size, the reference FHR also had higher power plant thermodynamic efficiencies

thanks to having a significantly higher turbine inlet temperature. However, it was impossible to justify the choice of the reference FHR used in CapCost at the time of this thesis writing. To examine how this assumption may affect SCOOP results, the choice of the reference plant was parameterised into Q_s and P_R in Equation 2.21 to perform the sensitivity study using the example reactor in Table 4-1. Five different reference reactor parameter sets were implemented in CapCost, all of which kept the core design and the coolant inlet and outlet temperatures unchanged, only the power output and the resulting heat exchanger system costs were perturbed. Table 4-2 lists the sensitivity study results. The top three rows list the Q_s, the heat exchanger system costs for the five different reference FHRs and the corresponding P_R values calculated for the example FHR from Table 4-1. The bottom four rows present the LCOE, coolant pressure drop, core inlet temperature and the power of the example FHR calculated by SCOOP using five reference FHRs in CapCost. It was found that the optimum core and secondary loop (although not shown in Table 4-2) operating conditions were not affected by the choice of the reference FHR used in CapCost. This suggests that the uncertainty in the choice of reference power plant would not cause a major concern for SCOOP when coupling with neutronic calculations, which requires only the core power and temperature as inputs from thermal-hydraulic modules. The LCOE reported, on the other hand, increased with the power of the reference reactor, which was expected.

Table 4-2. Sensitivity of SCOOP results to specifics of the reference reactor in CapCost

Qs	*(MWt)*	*2600*	*3000*	*3400*	*4200*	*4600*
HXsysCosts	*(mil £/yr)*	*30.32*	*35.07*	*39.86*	*49.6*	*54.56*
P_R		*2.47*	*2.13*	*1.88*	*1.51*	*1.37*
LCOE	(£/MWh)	57.2	61.6	65.7	73.5	77.3
Core Δp	(kPa)	150	150	150	150	150
Coolant inlet T	(°C)	662	662	662	662	662
Core power	MWt)	6520	6520	6520	6520	6520

The scaling exponent n_R determines how the variable component of the plant's total cost scales with the cost of the primary and secondary loop heat exchanger and pumping costs. To investigate the sensitivity of LCOE and optimum operating condition to the value of n_R, Table 4-3 describes five cases analysed with SCOOP for representative FHR using increasing values

of n_R. The optimum operating conditions of the example reactors were not affected by the value of n_R except with the lowest n_R tested, for which case the LCOEs with 150 kPa pressure drop (63.7 £/MWh) and 200 kPa pressure drop (63.6 £/MWh) had a minute difference. The LCOE did change somewhat with n_R, but by much smaller factor comparing to the previous test.

Table 4-3. Sensitivity of SCOOP results to the value of n_R

n_R		*0.56*	*0.6*	*0.64*	*0.68*	*0.72*
LCOE	(£/MWh)	63.6	64.7	65.7	66.7	67.8
Core Δp	(kPa)	200	150	150	150	150
Coolant inlet T	(°C)	667	662	662	662	662
Core power	(MWt)	6672	6520	6520	6520	6520

The values of A_R and B_R in Equation 2.21 represent the split between the fixed and the variable components of the power plant cost. They were chosen based on some assumptions and cost breakdowns of the FOAK next generation LWRs. However, it is uncertain whether the FOAK AGR-like FHR would have similar cost distribution across different components as LWRs and/or the assumptions of fixed vs variable cost breakdown of different cost elements made in CapCost were near accurate. To test the sensitivity of SCOOP to this assumption, Table 4-4 depicts five scenarios: 1) very high fixed cost, 2) high fixed costs, 3) the reference CapCost setting, 4) low fixed costs and 5) very low fixed costs. The optimum operating condition of the subject reactor was changed slightly by the value of A_R and B_R in the first two scenarios. With larger A_R and smaller B_R, the extra variable cost incurred from having greater power output was reduced, and therefore the overall plant economics was enhanced by having increased pressure drop and power. Again, the original optimum core operating condition, i.e., 150 kPa pressure drop and 6520 MWt power, were only slightly inferior to the optimised design in scenarios 1 and 2, having LCOEs of 61.4 £/MWh and 63.6 £/MWh respectively. For this example FHR, LCOE increased with the value of B_R (or decreased with the value of A_R). This was expected as lower fixed costs and higher variable costs means weaker sizing benefit from a power uprate. Again, the change in LCOE was not significant comparing with the first test.

Table 4-4. Sensitivity of SCOOP results to the values of A_R and B_R

A_R		*56*	*48*	*40*	*32*	*24*
B_R		*35*	*43*	*51*	*59*	*67*
LCOE	(£/MWh)	61.3	63.5	65.7	67.8	69.8
Core Δp	(kPa)	200	200	150	150	150
Coolant inlet T	(°C)	667	667	662	662	662
Core power	(MWt)	6672	6672	6520	6520	6520

The fuel cost variable F in Equation 2.21 was assumed to be fixed to 5 £/MWh in CapCost. This would not true if the fuel type, material, enrichment or BU/e were changed. However, without neutronic design, it was meaningless to make further assumptions on the fuel. The effect of F on the LCOE was linear and would not affect the optimum operating condition. Therefore, sensitivity study of SCOOP to F was not performed. There are other assumptions that could affect the estimation of LCOE, such as power peaking factor of the core, maximum bulk coolant temperature limit, fuel enrichment cost, fabrication cost for different fuel forms, etc. However, justifying these assumptions would require future experimental tests.

In summary, the LCOE was indeed sensitive to the assumptions in the CapCost module of SCOOP. Therefore, LCOE from SCOOP should always be used in reference to the assumptions made, especially the choice of the reference reactor. In contrary, the optimum operating condition produced by SCOOP was not significantly sensitive to its assumptions. Only in cases where the reactor had large power output or expensive heat exchanger systems, the optimum core power and pressure drop from SCOOP might be slightly underpredicted if the actual value of B_R and/or n_R was much smaller than the current CapCost setting, which is unlikely based on past experience with NPPs. Therefore, it should not be a concern for SCOOP when coupling with neutronic calculations, which take operating conditions as inputs.

Chapter 5 Preliminary Neutronic Design Space Search

Based on the thermal-hydraulic recommendations in the previous chapters, this chapter firstly explores the AGR-like FHR assembly level neutronic designs space limited by the physical envelope bounded by the AGR assembly graphite keys. The solid pin type design was taken as the basis of this study. Since Monte Carlo simulations performed were very demanding in terms of computational resource, only BOL calculation was performed. The feasible design space defined at this stage was bounded by two simple requirements on reactor BOL neutronic performance: 1) critical core configuration must be assured at the BOL, and 2) CTC must not be positive at the BOL. After the initial assembly level design investigation, a decision was made to move to simpler unit cell neutronic models to allow more degrees of freedom in design optimisation and greater simulation speeds. A comparison of assembly models and unit cell neutronic models was carried out before transitioning to the next chapter's neutronic design which were all performed on unit cell level.

5.1 Assembly-Level Neutronic Design Space

This stage of the project explored a range of designs without making commitments or preferences to any design option. The solid pin type design was chosen as a reference design in this step to develop initial understanding of trade-offs between assembly design options with reasonable computational cost. This design was one of the best performing designs suggested by previous thermal-hydraulic analyses and requires minimum amount of technological innovation. Two fuel candidates with fuel enrichments varying from 2.5 wt% to 12.5 wt% and three different coolant candidates were considered. The lithium components in FLiBe and FLiNaK were assumed to be 99.995 wt% enriched in Li-7 for both salts. This was the standard lithium composition used in the FLiBe coolant of other more mature FHR designs. [3][11] The zirconium component in NaF-ZrF_4 was assumed to have natural zirconium isotopic composition at this stage of the study.

To cover the entire possible geometrical design space allowed by the AGR core configuration, the radius of the inner and outer graphite sleeve and the number of fuel pins were systematically varied to allow for more degrees of freedom in terms of the proportions of graphite, coolant, and fuel. From the Torness AGR dimensions (assembly sleeve inner radius = 9.52 cm), the assembly radius was increased stepwise by 2 cm for each variation until the assembly sleeve inner radius reached 19.52 cm, which was the largest assembly sleeve dimension allowed by the AGR graphite keys which lock the assembly channels together. Six values of the radius

were studied. For each assembly radius, the number of fuel pins inside the assembly sleeve was varied by increasing the number of fuel pin rings in the circular fuel pin lattice. A range of 36 pins to 330 pins as covered by changing the number of rings in the fuel assembly array. Each ring of fuel pins was evenly spaced from the centre tie rod to the inner radius of assembly sleeve. The spacing from the outermost ring of fuel pins to the assembly sleeve was kept the same as the spacing between the fuel rings (and tie rod). The minimum distance between two adjacent rings of fuel pins was limited to 0.2 cm. This limit was chosen empirically based on current LWR designs to prevent possible thermal-hydraulic design failures where extreme frictional pressure and flow induced vibration might occur.

A total of 960 design options were studied in this chapter. Table 5-1 summarises the assembly dimensions allowed by the geometrical constraints of AGR. Figure 5-1 shows some of the aforementioned design options modelled with Serpent. The yellow part represents the coolant channel salt, which was perturbed in isolation from the coolant (shown in different colours chosen by Serpent) that fills the gaps between assembly channels. The two shades of grey represent graphite channels (dark grey) and the SiC assembly sleeve (light grey) respectively. The fuel pins are shown in either green or purple representing UC or UO_2, respectively. A Python script was created to systematically generate Serpent input files for all the design options considered. All simulations were performed with Serpent using 2-D geometry and reflective boundary condition and no depletion was performed at this stage.

Table 5-1. Dimensions of all proposed assembly designs

	Minimum gap between fuel rods (cm)							
sleeve outer radius (cm)	*3-ring*	*4-ring*	*5-ring*	*6-ring*	*7-ring*	*8-ring*	*9-ring*	*10-ring*
9.52	1.026	0.513						
11.52	1.526	0.913	0.505	0.214				
13.52	2.026	1.313	0.839	0.499	0.245			
15.52	2.526	1.713	1.172	0.785	0.495	0.269		
17.52	3.026	2.113	1.505	1.071	0.745	0.492	0.289	
19.52	3.526	2.513	1.839	1.356	0.995	0.714	0.489	0.305

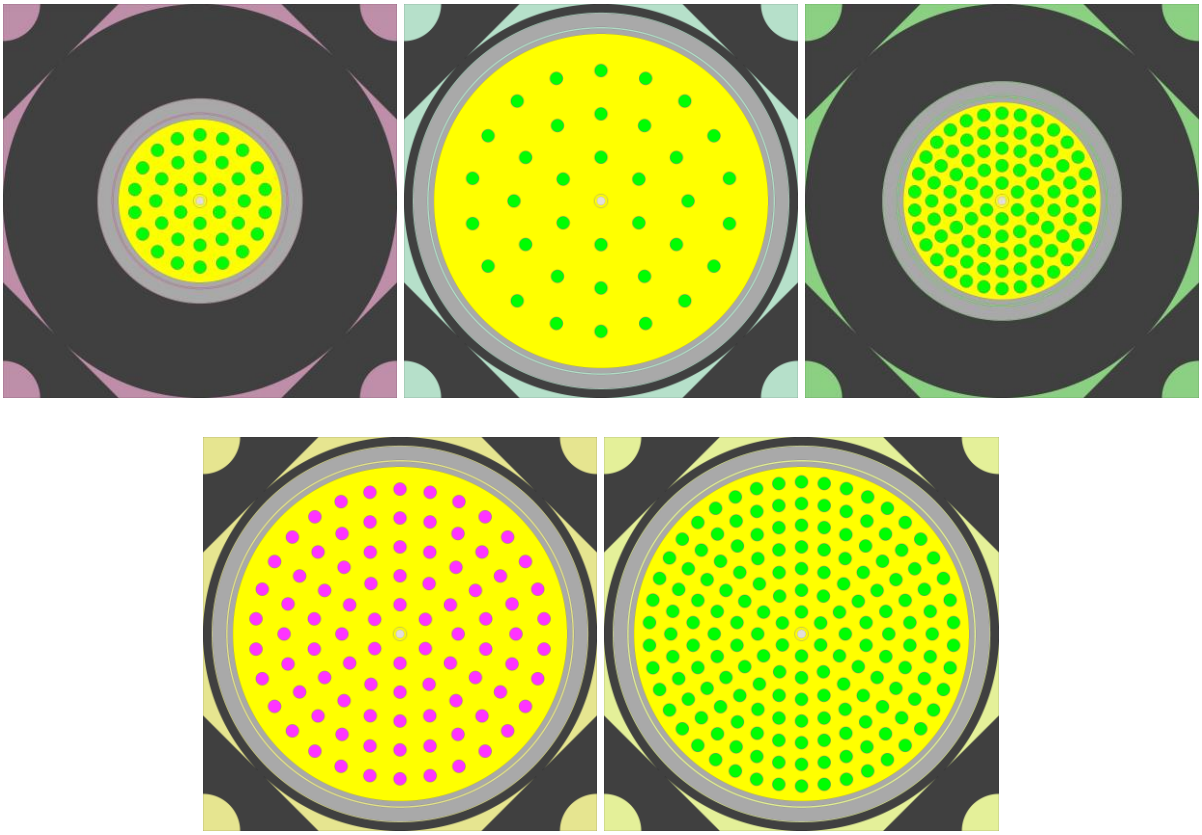

Figure 5-1. Examples 2-D Serpent models of proposed FHR assembly designs

Two BOL neutronic performance parameters were chosen as the design targets, i.e., k_∞ and CTC. Criticality eigenvalue must be greater than unity at the BOL since the AGR-like FHR was not envisaged to be a breeder reactor. Coolant temperature coefficient shall be kept negative for safety reasons. However, with the use of salt as coolant, which has notably higher absorption cross-sections than water or CO_2, the coolant temperature coefficient could potentially become positive. Coolant temperature coefficient was defined as the change in reactivity introduced per unit change in coolant temperature and was calculated using the following equation:

$$\alpha_{\text{coolant}} = \frac{k_\infty(T_{c2}) - k_\infty(T_{c1})}{k_\infty(T_{c2}) \times k_\infty(T_{c1}) \times (T_{c2} - T_{c1})} \times 10^5 \text{ pcm/K} \qquad (5.1)$$

where T_{c1} and T_{c2} are the perturbed and the nominal coolant temperatures and $k_\infty(T_{c2})$ and $k_\infty(T_{c1})$ are the corresponding infinite multiplication factors. The Serpent models neglected the gap

between the fuel and the cladding and assume zero leakage and an infinitely long fuel pin, i.e., 2-dimensional models with reflective boundary condition. Leakage introduces negative contribution to the core because as temperature rises, the spectrum hardens, and the macroscopic collision cross-sections decrease. As a result, more neutrons leak out of the core. The neutronic models used will therefore slightly overpredict k_∞ and over-predict the CTC (bias towards more positive values) because leakage effect is neglected.

To calculate the coolant temperature coefficients, for each of the considered assembly designs, a nominal state simulation assumed coolant temperature to be 900 K and at perturbed state simulation the coolant temperature was increased to 1000 K. Only the coolant inside the fuel channel was perturbed. This large temperature difference between the nominal and perturbed states was used to reduce the uncertainty in CTC from propagation of error in Equation 5.1.

5.1.1 General Discussion on Neutron Spectrum and CTC

There are several factors that affect reactivity when coolant temperature is perturbed, and the levels of contribution to CTC from these factors vary with reactor design. When the temperature of coolant increases, the reduction in salt density results in the hardening of the neutron spectrum and less absorption in salt (positive contribution to CTC). Resonance absorption in U238 will also be affected because of the spectral shift (could be negative or positive contribution to CTC), depending on the balance between thermal and resonance neutrons in the core. Spectrum hardening will result in smaller U235 fission cross-section (negative contribution to CTC), less absorption in burnable poisons and some fission products (positive contribution to CTC), less absorption in lower energy resonances of Pu240 (positive contribution to CTC), and more fast fissions in U238 if the spectrum is sufficiently hard (positive contribution to CTC). There are also a number of other effects on CTC such as increasing neutron leakage with spectrum hardening which will depend on the size and geometry of the system. The assembly sleeves in the AGR can in principle be replaced with SiC for its greater durability at high temperature and high radiation tolerance.

Most current FHR designs operate in thermal spectrum to take advantage of large U235 fission cross-sections. This requires large amount of moderating material in the core. The mainstream FHR fuel, Fully Ceramic Micro-encapsulated (FCM) fuel particles, have a fuel kernel volume fraction of only ~12.8%, with the rest being occupied by carbon or carbide material. The fuel particles are then dispersed in graphite matrix and packed into pebble, pin or plate forms. Therefore, most of the moderation in these FHRs comes from graphite while the Fluoride salt

has a primary function of cooling the core. Compared with graphite, FLiBe is much less moderating and also much more absorbing, especially its Li6 component. FLiNaK and NaF-ZrF_4 also have large absorption cross-section due to their Li and Zr components. When relying heavily on graphite for moderation, the core can potentially have much less negative or even positive CTC as the marginal moderation reduction with reducing salt density is small in this case and the absorption reduction is strong as the spectrum is soft due to graphite moderation. By introducing more salt and less graphite into the core, the dependence on salt for moderation increases, therefore the negative contribution to CTC from loss of moderation would be enhanced; the spectrum would harden with weaker moderation from salt, and the absorption cross-section of salt would be reduced, potentially weakening the positive effect on CTC from loss of salt absorption. However, the overall positive contribution to CTC from loss of absorption could also increase with larger salt volume. In addition, the hardened spectrum can result in lower reactivity and burnup.

5.2 Initial Neutronic design Space Search Results

Figure 5-2 plots k_∞ and CTC of the entire population of 960 surveyed assembly designs grouped by the coolant material. To ensure a critical core, the value of the k_∞ at BOL should be greater than one to allow for leakage, control rod and other parasitic absorption and reactivity loss due to burnup. In terms of reactivity coefficient, a negative value was targeted to ensure inherent safety and stability. When selecting the origin of the plot as the point where $k_\infty = 1$ and CTC = 0 pcm/K, the fourth quadrant of Figure 5-2 represents the neutronically feasible design domain at BOL, where the core is critical and inherently safe against coolant temperature perturbations. Only 26 out of 960 models searched fell within the feasible design space, which made the neutronic design of the AGR-like FHR challenging but also emphasised its importance. The upper boundary line for each coolant option (the black dashed line for FLiNaK cooled designs) in Figure 5-2 connects the designs with the smallest fuel volume fractions and salt volume fractions among all surveyed assembly designs. These were cases with the small assembly sleeve radii (i.e., large graphite block) and small number of fuel pins. These designs had the greatest graphite content per unit of fuel volume and had the weakest dependence on salt for moderation. With an increase in coolant temperature, the positive reactivity feedback from the reduced salt density and reduction in absorption in salt dominated over the negative reactivity feedback from the loss in moderation in salt, thereby increasing the reactivity of the core. On the other hand, when studying the shapes of the ‘clusters’ of points in Figure 5-2, it was found that the designs were bounded by a lower boundary (shown in blue

dashed line). This lower boundary line connects the designs with the largest fuel and salt volume fractions. With a harder spectrum and a heavier dependence on salt for moderation, the loss of moderation from salt when the coolant temperature was raised would play a greater role in affecting the reactivity level, therefore resulting in lower or negative CTCs.

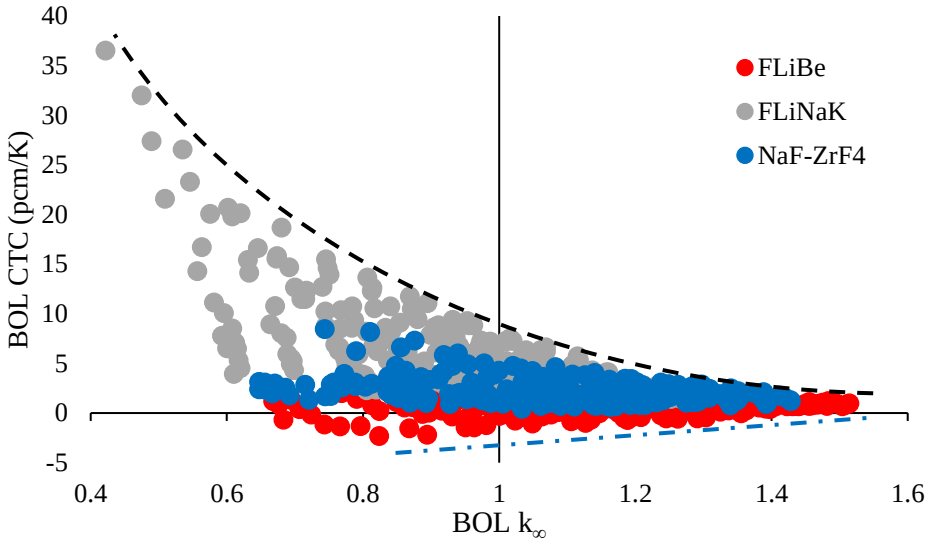

Figure 5-2. BOL CTC vs BOL k_∞ performance domain for all searched assembly designs

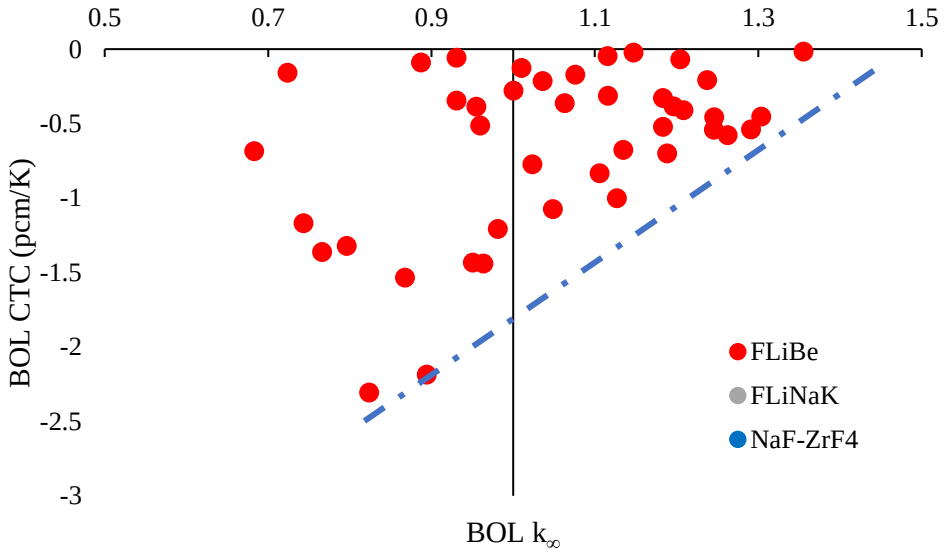

Figure 5-3. Non-positive BOL CTC part of the BOL CTC vs BOL k_∞ performance domain

Designs using FLiBe as coolant were more neutronically favourable than the ones using the other two salts, allowing greater BOL k_∞ value and more negative BOL CTC. All 26 cases that lied in the fourth (lower right) quadrant all used FLiBe as coolant, which is shown in Figure 5-3. FLiNaK appeared to be the least favourable coolant candidate in Figure 5-2 as it had the most positive CTCs, reaching more than 35 pcm/K and smallest BOL k_∞. Designs with NaF-ZrF_4 lied marginally above the axis where CTC = 0. Both Figure 5-2 and Figure 5-3 show that the lower boundary for the FLiBe cooled designs was an upward sloping curve when plotting the designs' k_∞ values against their CTCs. Targeting for greater BOL k_∞ and more negative BOL CTC in the preliminary design process, this lower boundary line in Figure 5-2 and Figure 5-3 connected the best assembly designs among all 960 searched and forms the 'optimum frontier'. Along this frontier, a trade-off existed between the reactor's neutron economy and inherent safety, where one parameter must be sacrificed for any improvement in the other.

To understand how different designs had such different neutronic characteristics and to identify which designs perform the best and what design patterns they have in common to land near the 'optimum frontier', the next sections present the effects of design parameters on k_∞ and CTC for the solid pin type assembly. Some preliminary design recommendations are then derived from the following analysis.

5.2.1 Effect of Material Choices on k_∞ and CTC

Coolant choice had very significant effect on the reactor's k_∞ and CTC values. FLiBe had the highest k_∞ and the most negative CTC; NaF-ZrF_4 was slightly worse in terms of CTC and FLiNaK is the worst among all three. In this setup, FLiBe was the only feasible coolant option as the other two salts could not make an AGR-like FHR core critical while having a negative CTC at BOL.

The choice of fuel material, i.e., UC or UO_2 did not affect the neutronic performance significantly, especially in terms of the k_∞. When keeping other design parameters fixed, around 0.94% difference was seen between the two fuel options on average, with UC fuelled designs having slightly greater k_∞. There were two competing factors that affected the reactivity levels of UC fuelled reactors in comparison with UO_2 fuelled. UC had roughly 50% higher heavy metal density. Therefore, with the same fuel dimensions, UC fuelled reactor would have greater fuel content. However, at the same time there is extra carbon present inside the UC fuel. These two factors could balance out and the ratio of the moderator to fuel could be maintained at a similar level as suggested by the k_∞ results from the two fuels. CTC was slightly more

sensitive to the choice of fuel material, with an average difference (15% outliers excluded since CTC results are statically twice as noisy as k_∞ values, and some of this statistical error turns out to be rather large) of about 9%, with UO_2 fuelled designs having more positive CTCs. However, majority of this difference came from FLiNaK and NaF-ZrF_4 cooled designs that have large and positive CTCs, i.e., the upper boundary of the k_∞ vs CTC space for these two salts. These designs were to be screened out because of their reactivity feedbacks and therefore their sensitivity to the fuel choice was irrelevant to the analysis. When examining the FLiBe cooled designs only, the difference in CTC between the two fuel options became 1.39%; while the CTC values for NaF-ZrF_4 cooled designs were within 7.45 % between the two fuel options.

5.2.2 Effect of Assembly Configuration on k_∞

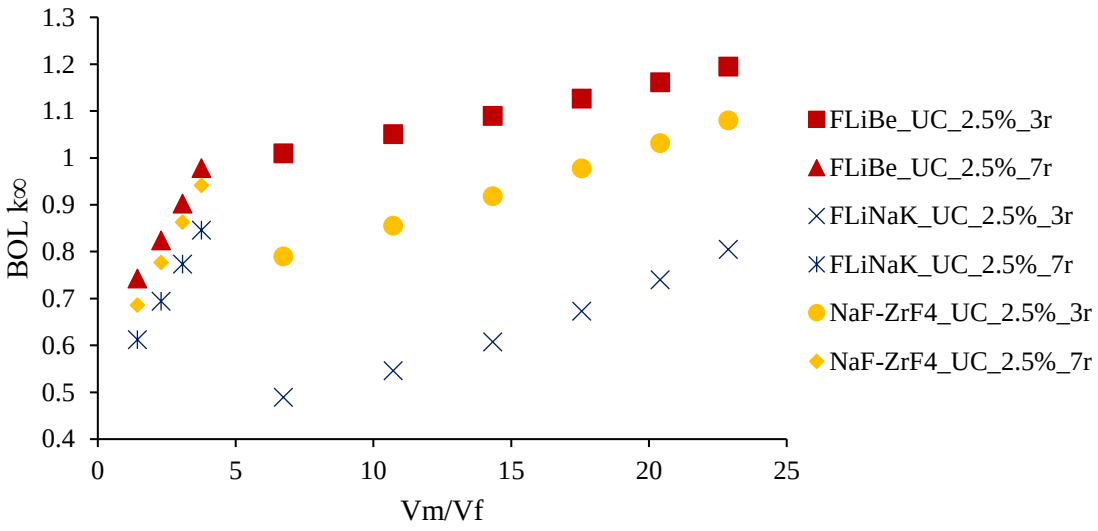

Figure 5-4. Vm/Vf effects on BOL k_∞ for different coolants and channel radii

Figure 5-4 shows how the moderator to fuel volume ratio (V_m/V_f) affects the k_∞ of different designs. The volume of moderator used in this ratio considered only the graphite and does not include the salt volume. The assembly sleeves' volume was not included although they are also moderating. This would lead to underestimation of moderation. However, taking only graphite volume as moderator volume could still give a good representation of the studied trends as the offset in neutronic results would be consistent across all models. The plot shows only the designs using UC as fuel with an enrichment of 2.5 wt% to screen out the effects of fuel choice

and enrichment on k_∞. Designs with UO_2 fuel demonstrated very similar trends as in Figure 5-4.

Each point on the plot represents a single assembly design at BOL. All dark red markers on the plot are designs cooled with FLiBe; orange-coloured markers represent FLiNaK cooled designs and blue markers are designs using $NaF\text{-}ZrF_4$. When plotting k_∞ values against their V_m/V_f, all designs showed a clear upward sloping trend, as expected. This suggests that all these designs were benefiting from more moderation to achieve greater reactivity. The magnitude in which V_m/V_f increased the reactivity however varied. In Figure 5-4, there are two groups of points showing different slopes. The group on the left of the plot represents designs using seven rings of fuel pins. The fuel occupied large space in the assembly and therefore the V_m/V_f for these 7-ring designs was limited to a small range and the fuel pin pitch was also varied within relatively small range. The group of points at the centre of the plot represent designs with three rings of fuel pins. More space was left for salt and graphite and therefore a greater range of V_m/V_f and pitch values were covered by these designs.

The k_∞ of the 7-ring designs responded more to a changing V_m/V_f compared with the 3-ring designs, as can be seen from the difference in their slopes. In addition, the 7-ring designs were much less sensitive to the choice of coolant. This suggests that the arrangement, i.e., pitch, of the fuel pins in the 7-ring designs are better suited to take advantage of moderation from graphite and was less sensitive to parasitic absorption in the coolant. This is because in the 7-ring designs, fuel pins are very closely packed and the distances between fuel pins are very small. This closely clustered design made the fuel pins behave collectively similar to one single big 'pin' of fuel, only diluted with some salt. The neutrons were moderated in the outer graphite and returned to the assembly packed with pins to trigger fission reactions. The small amount of coolant inside the assembly reduced the parasitic absorption in the coolant. The large gradients in k_∞ vs V_m/V_f plot for the 7-ring designs also means that these designs were far from optimum V_m/V_f level. With increased V_m/V_f, the marginal increase in k_∞ would be expected to decrease and the k_∞ vs V_m/V_f curve should plateau as the moderation saturates. Normally, reactors are designed to be slightly under-moderated. These 7-ring designs were under-moderated and exhibit greater potential to achieve higher reactivity than the 3-ring designs with the same amount of fuel if more moderation can be introduced. This would however require changes to the AGR core configuration to allow more room for graphite. In addition, insufficient cooling could be a problem for these designs and further increase in moderation

could potentially expose the difference in absorption in different salts as they are all thermal absorbers.

There is a discontinuity in the k_∞ vs V_m/V_f curve when transitioning from 7-ring designs to 3-ring designs, especially in FLiNaK and NaF-ZrF_4 cooled cases. With FLiNaK as coolant, 3-ring cases underperformed all 7-ring designs despite having much greater moderation (higher V_m/V_f). NaF-ZrF_4 cooled 3-ring designs were slightly better than the 7-ring ones. This is because with the same V_m/V_f, the 3-ring designs has only 3/7 of the graphite volume as in the 7-ring designs. Therefore, the total coolant volume in the 3-ring designs is much larger than in the 7-ring designs with the same V_m/V_f. In terms of actual assembly configuration, the 3-ring designs has relatively large pitch to diameter ratios (P/D) so that there is large amount of coolant between pins. The fuel pins behaved more like individual pins instead of effectively being lumped into one big fuel pin. The additional salt content allowed by the large P/D introduced both absorption and moderation to the core. The discontinuity in Figure 5-4 therefore suggests that FLiBe was more moderating than absorbing whereas the contrary was true for the other two salts. Compared with the 7-ring designs, the 3-ring designs were, for the same reason, very sensitive to the choice of coolant. Such substantial performance difference between different salts seen in 3-ring designs again confirms that FLiNaK and NaF-ZrF_4 are strongly absorbing, whereas FLiBe is slightly more moderating than absorbing.

Increasing V_m/V_f had weaker effects on the reactivity for these 3-ring designs, especially the FLiBe cooled ones. When using FLiBe as coolant, all 3-ring designs outperformed 7-ring designs and could reach k_∞ values of up to 1.19 with $V_m/V_f = 22.88$. With the smallest V_m/V_f surveyed (6.73), the FLiBe cooled 3-ring UC fuelled design achieved k_∞ of 1.01. This is because in 3-ring designs, V_m/V_f was greater and moderation effect was more saturated so that absorption in salt started to affect the neutron balance more. Thermal-hydraulically, the advantage for these 3-ring designs is that they were cooled much more efficiently. However, if they were most restricted by maximum fuel temperature limit, the small number of fuel pins would not help as greater linear power rating must be provided by each fuel pin to reach the same reactor power.

The above analysis for the 3-ring vs 7-ring designs could be generalised to a discussion of trade-offs for using small number of pins and large number of pins when designing the AGR-like FHR. More closely packed assembly with more fuel pins can potentially achieve better neutron economy than the ones with small number of fuel pins that are more loosely spaced

and filled with large amount of coolant in between. Thermal-hydraulically, on the other hand, the designs with large coolant volume per fuel pin might be more favourable in some cases.

5.2.3 Effect of Assembly Configuration on CTC

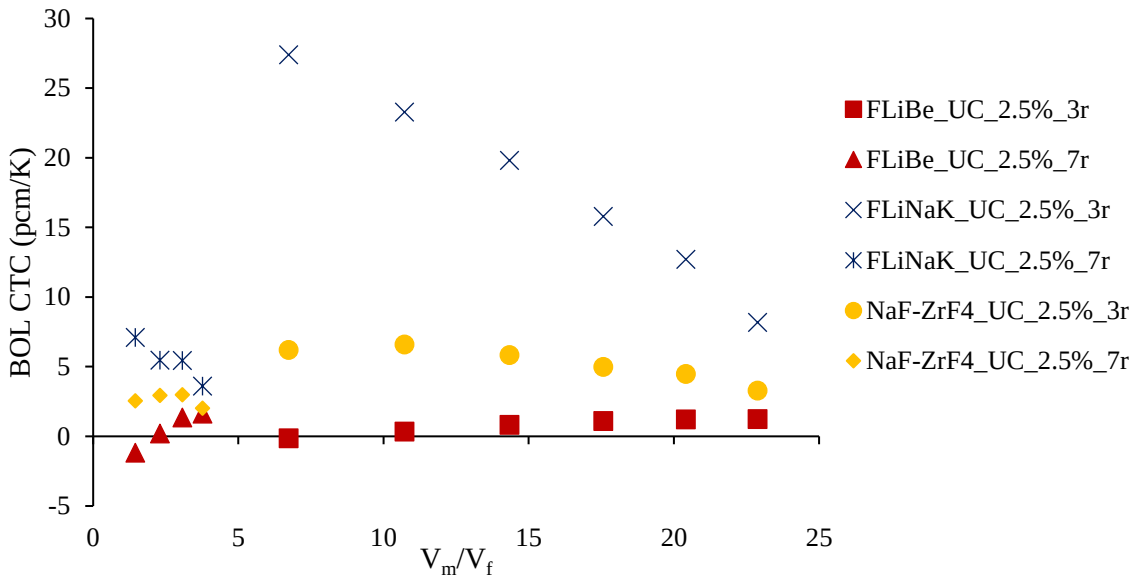

Figure 5-5. V_m/V_f effects on BOL CTC for different coolants and channel radii

Figure 5-5 plots how CTC of the AGR-like FHR varied with the V_m/V_f and how CTC values of different designs responded to changing V_m/V_f. The same designs from Figure 5-4 were used in this figure. When increasing moderator volume relative to that of fuel, the coolant volume fraction in the core decreased, and therefore the overall effect (of absorption and moderation) that the coolant has on the neutronics was weakened. That is, CTC would become less positive if the coolant were more absorbing than moderating, and vice versa. It was found that, contrary to the trend shown for k_∞ in Figure 5-4, CTCs for designs using different coolant options responded differently to increasing V_m/V_f. For example, FLiBe cooled designs had increasing CTCs with increasing V_m/V_f; whereas for FLiNaK cooled ones, CTCs decreased with V_m/V_f. This again proved that the balance of absorption and moderation effects from the three salts were different: FLiBe's moderating power outweighed its absorption and FLiNaK's absorption outweighed its moderating power, and by large amount, as shown by the large negative gradient of the curve.

Examining Figure 5-4 and Figure 5-5 together, it can be seen that there was a clear trade-off between k_∞ and CTC. Figure 5-4 showed that with greater V_m/V_f, k_∞ increased for all cases and that the FLiBe cooled designs with large V_m/V_f had the most potential for good neutron economy. Figure 5-5, however, showed that FLiBe cooled 7-ring designs could only achieve negative CTC at low V_m/V_f and then the CTC increased with V_m/V_f and became positive. The same was also true for FLiBe 3-ring designs. In fact, all other designs shown in Figure 5-4 did not have negative CTC, except the FLiBe cooled 3-ring and 7-ring cases at their lowest possible V_m/V_f values. Therefore, to obtain negative CTC, the performance in k_∞ (neutron economy) must be sacrificed. In essence, this is a trade-off between reactor economics and reactor safety. FLiNaK cooled showed a coherent trend in the performance in k_∞ and CTC when changing V_m/V_f: with increasing V_m/V_f, FLiNaK cooled designs had increasing k_∞ and decreasing CTC. However, the k_∞ was still too low to reach criticality and CTC was still too positive. The CTC trend with different V_m/V_f of NaF-ZrF_4 was similar to that of FLiNaK and the performance of NaF-ZrF_4 cooled designs were always in between that of FLiBe and FLiNaK with respect to both neutronic parameters of interest.

Figure 5-5 plots CTC on the same axis as in Figure 5-4 to demonstrate more clearly the trade-off between k_∞ and CTC. However, the large discontinuity in the CTC vs V_m/V_f curve between the 3-ring and the 7-ring designs did not help explaining what determined the trend of CTC. It was obvious from the discontinuity that the spectrum of a reactor was not the only contributor to its CTC. Instead, the change in coolant density when its temperature changed accounts for the most change in reactivity. The two designs had significantly different fuel volumes; therefore, for a fixed assembly volume, the V_m/V_f ratio did not translate to the amount of coolant being perturbed in temperature, which directly contributed to the CTC.

Figure 5-6 plots CTC against the volumetric ratio of the coolant (inside the assembly channel) and fuel (V_{cool_c}/V_f). In this plot, the 3-ring and 7-ring designs have more consistent CTCs at the same V_{cool_c}/V_f value, with only the FLiBe cooled designs showing some discontinuity between the two cases. This shows that CTC in FLiBe cooled reactors were more sensitive to how the fuel pins were arranged than the other two salts. The 7-ring vs 3-ring comparison of the CTC's behaviour for different assembly configurations can also demonstrate how different number of fuel pins affect the CTC of the designs. When using FLiNaK or NaF-ZrF_4 as coolant, CTC was not very sensitive to the number of fuel pins and how the pins were arranged; instead, it was mainly determined by the volume of coolant (being perturbed under transient) per unit volume of fuel. FLiBe cooled designs were more sensitive to the heterogeneity of the assembly

design because FLiBe is a better moderator and therefore the self-shielding effect was amplified. More negative CTC could be achieved by using more fuel pins with larger V_{cool_c}/V_f. Having more pins means greater surface area and resonance absorption in U238 which becomes more absorbing with spectrum hardening. Therefore, CTC would be more negative if the salt has stronger moderation.

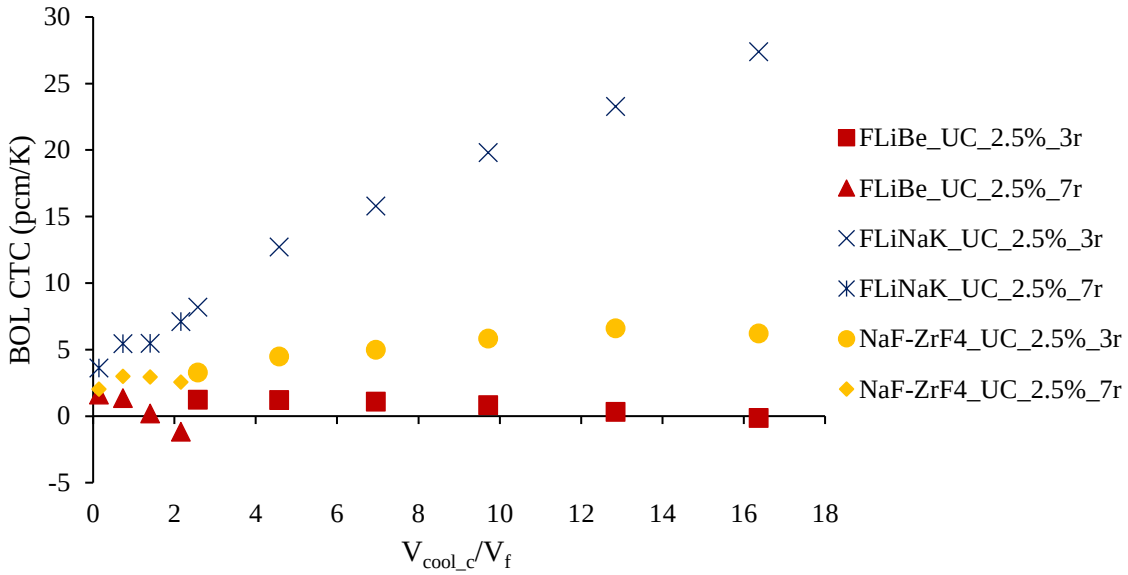

Figure 5-6. V_{cool_c}/V_f effects on BOL CTC for different coolants and channel radii

5.2.4 Effect of Fuel Enrichment on k_∞ and CTC

To study how fuel enrichment affects the k_∞ of an FHR, Figure 5-7 plots the BOL k_∞ against fuel enrichment of several FLiBe cooled solid UC pin models. FLiNaK and NaF-ZrF_4 were not included in this test, and it was expected that the physics seen in FLiBe cooled models were universal in other coolant materials. Enrichments below 20 wt% was commonly accepted for Low Enriched Uranium (LEU) fuel, however due to limitations of the computational resources, five different enrichment levels were used in this preliminary design search, ranging from 2.5 wt% to 12.5 wt%. The solid filled orange markers in Figure 5-7 represent designs with the largest channel diameter (inner graphite sleeve radius = 19.52 cm), whereas the red markers with no fill represent designs with the second smallest assembly channel size (inner graphite sleeve radius = 11.52 cm). Different shapes of markers represent designs with different number of fuel rings.

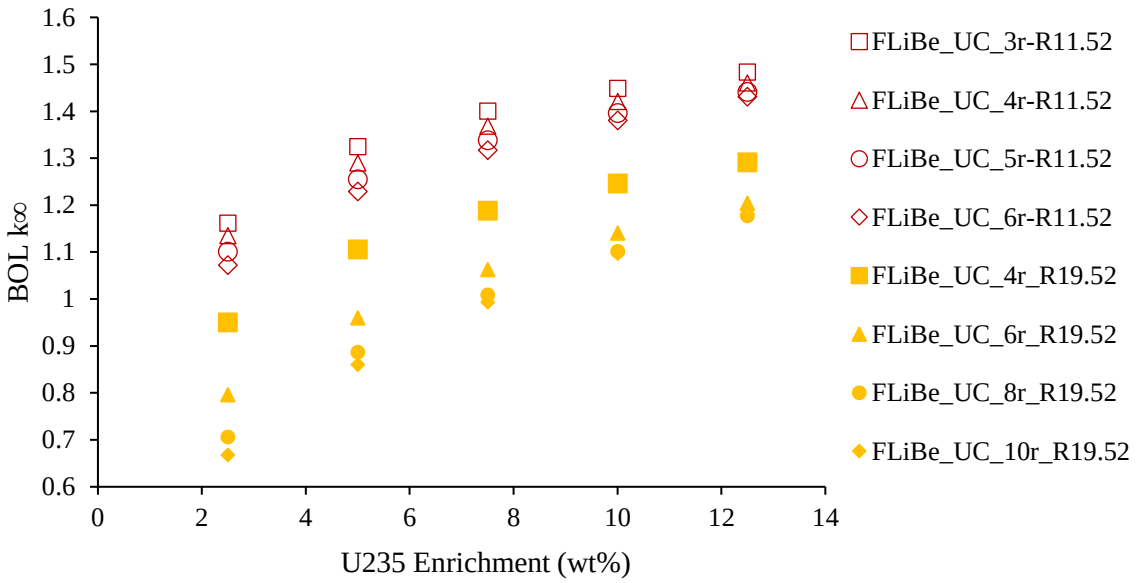

Figure 5-7. Effects of U235 enrichment on BOL k_∞ for different number fuel rings and channel radii with FLiBe coolant

For all designs, k_∞ increased with fuel enrichment as expected. However, the marginal increase in k_∞ diminished with increasing enrichment, as can be seen from the reducing gradient of the curves. Since fuel cycle cost is roughly linearly proportional to the fuel enrichment for LEU fuels, this finding suggests that further increase in enrichment might not be necessary when the marginal gain in reactivity was offset by the marginal cost of fuel cycle. The magnitude of improvement on k_∞ by increasing enrichment for the designs with larger assembly channels were slightly greater than the ones with smaller channels. However, these designs had much smaller reactivity level compared with the small-channelled ones. Also, it could be deduced from the plot that, with increasing fuel enrichment, the designs became less sensitive to the number of fuel pins.

Figure 5-8 plots the BOL CTC against the enrichment of the same designs from the previous figure. Unlike k_∞, CTCs of these designs responded differently to changing enrichment. All small-channelled designs (inner graphite sleeve radius = 11.52 cm) had positive CTC of similar values, which all slightly decreased with increasing enrichment and started to increase slightly when enrichment became greater than 10 wt%. The designs with a larger channel diameter (19.52 cm), had a wider range of CTC values and their behaviour with changing enrichment

were also different. This was because the total absorption and moderation effect of the coolant were both stronger due to a larger coolant volume, therefore a slight shift in spectrum from an enrichment change would favour one effect over the other to a greater extend, causing a larger perturbation in CTC. For the 10-ring design, the CTC behaviour was very similar to that of the small-channelled designs. As the number of fuel pins reduced, the CTC moved in the negative direction and started to become slightly more positive with increasing enrichment. Designs that had intermediate assembly channel radii demonstrated the same behaviour patterns as the two shown in Figure 5-5.

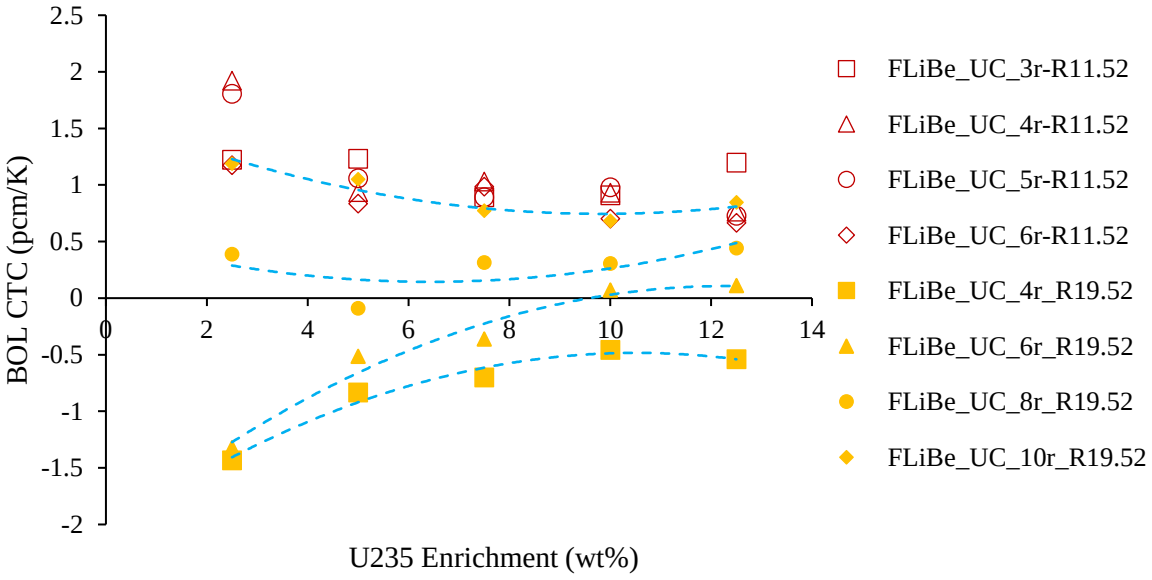

Figure 5-8. Effects of U235 enrichment on BOL CTC for different number fuel rings and channel radii with FLiBe coolant

Also, the CTC of designs with higher fuel enrichment were less sensitive to assembly configuration than the ones with lower enrichments. This is because with increasing enrichment the spectrum hardened, and the parasitic absorption in the salt would decrease, reducing the magnitude of coolant temperature reactivity feedback. In conclusion, to have a negative CTC, the reactor should have relatively few pins inside a large assembly channel. However, it might mean that the neutron economy would be compromised. A low enrichment helped achieve more negative CTC but could very possibly make the core sub-critical.

5.2.5 Summary of Assembly Model Neutronics

The fuel choice between UC or UO_2 did not have a notable effect on the neutronic performance whereas the coolant choice did affect the neutronics significantly. FLiBe was the best option in terms of achieving both high k_∞ and negative CTC, and FLiNaK was the worst. Fuel enrichment directly affected the reactivity but had relatively small impact on the CTC. The assembly configuration, i.e., the volume fraction and the arrangement of the fuel, graphite and salt also played an important role in determining the reactor's physics. A greater moderator content per unit of fuel meant higher, k_∞, but, at the same time, it also drove CTC of FLiBe cooled designs to the positive direction, as the better moderated reactor relied less on the salt for moderation. The absorption in salt was marginally affected by the graphite volume: a smaller coolant volume fraction meant less parasitic absorption but the thermal spectrum as a result of greater graphite volume would lead to larger absorption cross-sections and these two contradicting effects balanced out in most cases. V_m/V_f was used to characterise the proportion of salt, graphite and fuel to generalise the analysis. This ratio was determined by two factors: 1) the number of fuel pins in the assembly and 2) the radius of the assembly channel. It was found that the second factor was the more dominant factor that determined whether a design was neutronically feasible.

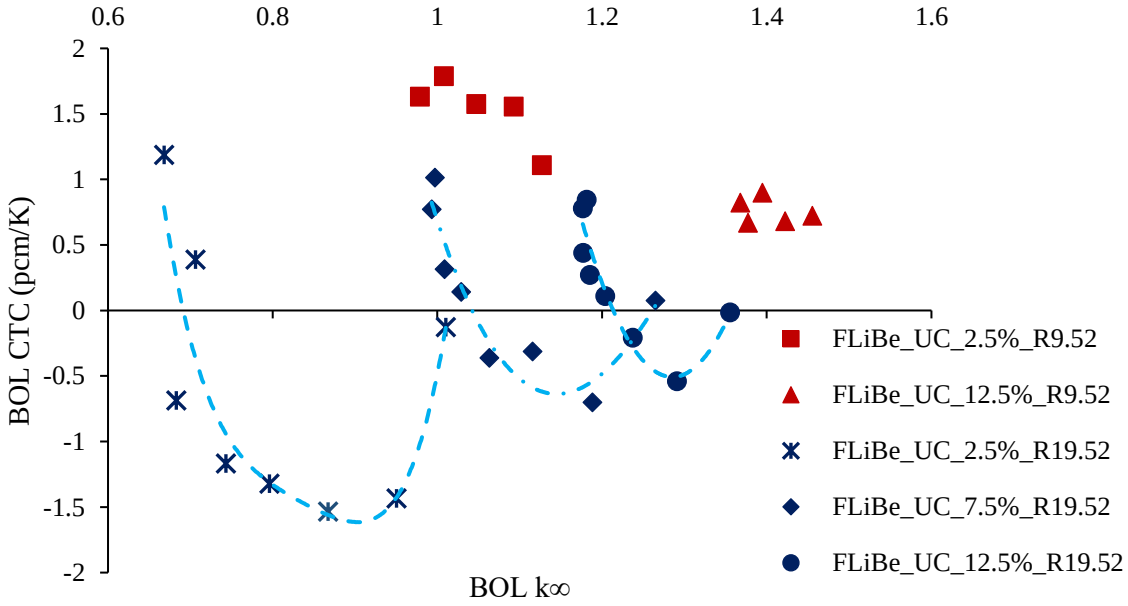

Figure 5-9. BOL CTC vs k_∞ performance trade-off for FLiBe cooled FHRs with different radii and U235 enrichments

Figure 5-9 plots k_∞ against BOL CTC for some of the FLiBe cooled UC solid pin fuelled designs. The dark blue markers represent cases with an assembly sleeve inner diameter of 19.52 cm and the red ones are designs with the smallest sleeve inner diameter, 9.52 cm. The different marker shapes represent different enrichments, and marker colours represent designs with different channel radii. The small-channel designs had greater k_∞ but struggled to reach negative CTC. Also, the effect of enrichment and number of fuel pins on the k_∞ vs CTC curve was roughly linear. With fewer fuel pins and higher enrichment, both CTC and k_∞ linearly increased.

As the inner graphite sleeve diameter increase (assemblies with intermediate diameter values not shown on the graph), the designs moved in the lower left direction, i.e., smaller k_∞ but more negative CTC. Also, CTC started to respond to changing fuel volume fraction and enrichment in a non-linear fashion. When the inner graphite sleeve radius reached its largest value (19.52 cm), as depicted by the blue markers, the CTC became very sensitive to enrichment and fuel volume fraction. Designs with each enrichment level formed a U-shaped curve on the k_∞ vs CTC plot. The height of the U-shaped curve, i.e., the range of CTCs of the designs, increased with decreasing enrichment, and the position of the curve shifted to the left (smaller k_∞) as the enrichment decreased. The fuel volume, i.e., the number of rings of fuel, determined where on the U-shaped curve the design lands. At the left of the U-curve, the reactor with large number of fuel pins (10 rings, 330 fuel pins per assembly) had a low k_∞ and a large and positive CTC value. As the number of fuel pins decreased, the k_∞ decreased and the CTC became more negative (going down to the right along the U-curve). The marginal decrease in CTC diminished with decreasing fuel volume. At some point, the k_∞ vs CTC curve started to go up as k_∞ continued to increase and CTC became more and more positive. This suggests that the fuel enrichment for these designs set the trade-offs between k_∞ and CTC, i.e., the position and the size of the U-curve in the k_∞ vs CTC plot: with higher enrichment, a greater k_∞ could be achieved, but the CTC would be less negative, even for the designs at the bottom of the U-curve. The enrichment level however could not be too low unless there was sufficient fuel loading to maintain the chain reaction and a reasonable fuel cycle length. These recommendations are consistent with the analyses in previous sections.

Figure 5-10 plots all the designs on the ‘optimum frontier’ identified earlier. There were in total eight designs that made the list. These designs were considered the best performing where no modification within the assembly level design space could achieve simultaneous improvements in both k_∞ and CTC. The specifications and performance characteristics of these

designs are summarised in Table 5-2. All of these best performing designs had the largest channel diameter possible and a small number of rings of fuel pins (3 to 5). The fuel enrichment largely determined where along the k_∞ vs CTC trade-off the reactor operates.

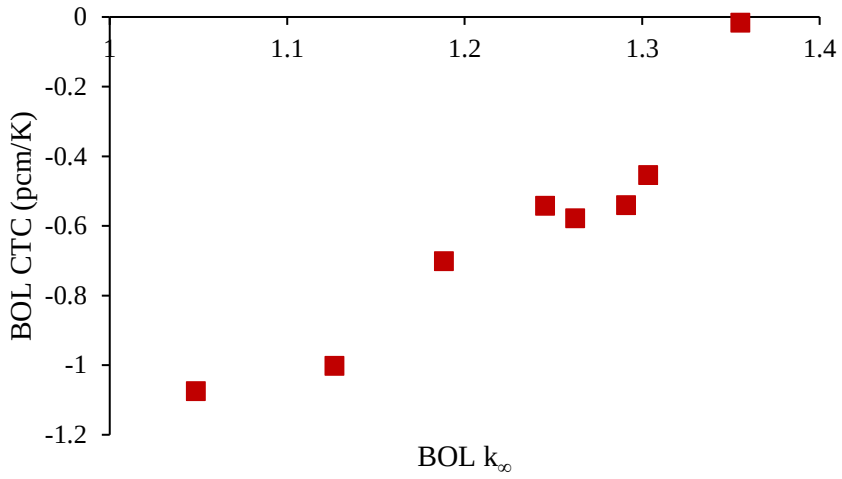

Figure 5-10. BOL CTC vs k_∞ performance for selected best assembly designs

Table 5-2. Design specifications for selected best assembly designs

#rings	*chan R (cm)*	*fuel*	*cool*	*Enri. (wt%)*	*Vm/Vf*	*Vc_c/Vf*	k_∞	*CTC (pcm/K)*
3	19.52	UC	FLiBe	12.5	6.73	16.37	1.36	-0.02
4	19.52	UO_2	FLiBe	12.5	4.04	9.13	1.30	-0.45
4	19.52	UC	FLiBe	12.5	4.04	9.13	1.29	-0.54
4	19.52	UO_2	FLiBe	10	4.04	9.13	1.26	-0.58
5	19.52	UO_2	FLiBe	12.5	2.69	5.51	1.25	-0.54
4	19.52	UC	FLiBe	7.5	4.04	9.13	1.19	-0.70
4	19.52	UO_2	FLiBe	5	4.04	9.13	1.13	-1.00
5	19.52	UO_2	FLiBe	5	2.69	5.51	1.05	-1.07

5.3 Single Pin Unit Cell Model

Many parameters come into consideration when redesigning the AGR core to operate as an FHR. Dimensions, material composition and relative volume fractions of each component in

an AGR assembly, including the fuel material, fuel form, cladding, assembly sleeves dimension, coolant choice, assembly channel and control rod channels (keys) and many more features could be subject to redesign and fine-tuning. In the previous section, only a small part of the design space was explored. Investigation of all other design parameters were impractical due to limited computational resource. Also, strictly constraining the design with the envelope of an AGR core could potentially miss the discovery of superior designs. For example, previous analysis suggested that some of the designs could benefit neutronically from a larger assembly with more graphite content. Furthermore, only BOL neutronic calculations were performed in previous sections. The behaviour of CTC (and also fuel temperature coefficient) with depletion and the achievable burnup (as a measure of fuel cycle economics) would also be different for different designs. These are important metrics in terms of both economics and safety of the reactor and should be investigated by performing depletion calculations. Therefore, to simplify and generalise the preliminary design process and expand the design domain search, while capturing the fundamental physics of the prismatic FHR design with fairly quick Monte Carlo calculations, this sub-section introduces a homogeneous single pin unit cell model.

The unit cell models should be representative of the assembly designs. It was shown that relative fractions of the materials are important in determining the reactor performance. The unit cell model must be set up to account for different ratios of fuel, moderator and coolant in a systematic way. In addition, it was found in the assembly level neutronic simulations that there were discontinuities in the curves of k_∞ vs V_m/V_f, and CTC vs V_{cool_c}/V_f when transitioning from 7-ring to 3-ring designs. Even with very similar V_m/V_f values, the 7-ring and 3-ring designs (especially when using FLiNaK and NaF-ZrF_4) did not have matching k_∞ values; with similar V_{ccol_c}/V_f values, the FLiBe cooled 3-ring and 7-ring designs did not have perfectly matching CTC values either. This showed that in addition to the material composition of the core, the heterogeneity, i.e., how the fuel, moderator and coolant were arranged in the assembly, also played an important role in determining neutronic performance. This should also be captured as much as possible in the unit cell model.

Figure 5-11 shows the proposed unit cell model. This model will be used for all subsequent neutronic calculations presented in the remainder of this thesis. To capture the wide range of neutron spectra, physical design space, and account for some degree of heterogeneity, three design parameters of the unit cell were systematically varied: 1) P/D, 2) salt mass fraction (SF) in the salt and carbon homogeneous mixture in the simplified unit cell model, and 3) the U235 enrichment of the fuel. P/D represents the geometrical envelope (and some level of

heterogeneity) of the model and was varied from 1.2 to 8 with 0.4 increment. SF represents the mass ratio of salt to the salt and carbon mixture and was varied from 20 w% to 100 w% with 20 w% increment. Fuel enrichment was varied from 2.5 wt% to 20 wt% with 2.5 wt% increment. The same coolant temperature perturbation as considered in the assembly design search was used in the pin models for calculation of coolant temperature reactivity coefficient. A simplification was made where the temperature of the graphite and coolant is perturbed together. When perturbing the density of the mixture, only the mass density of the salt portion of the mixture was perturbed whereas the carbon mass density is kept constant. All calculations used 6.12 million neutron histories per simulation cycle, ensuring reasonably high accuracy. Although when increasing P/D, the number of neutron interactions per history was affected: statistical error of k_∞ predictions is affected slightly as well: for example, the error in k_∞ at BOL increased from 13.8 pcm to 20 pcm when P/D was increased from 1.2 to 4.4, this was still considered to be an acceptable error range.

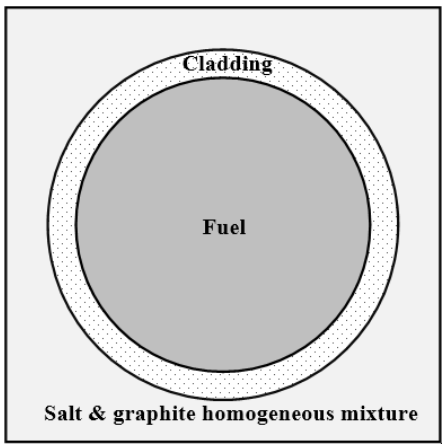

Figure 5-11. Unit cell model of FHR (not to scale)

Same as the assembly design, the unit cell models used SiC as cladding with Torness AGR pin dimensions. The gap between the fuel and the cladding was ignored and the models were built in infinite 2-D lattice in Serpent. The graphite and molten salt components were modelled using a simplified salt and carbon homogeneous mixture. It was intended that the physics of fuel assembly could be approximately captured without the need for design specifics, and the conclusions obtained from these models could be translated into future, more detailed, FHR designs of various types. This was a reasonable strategy since most of the physics was

determined by the relative amounts of fuel, coolant and moderator, all of which could be preserved and made exactly equivalent to the heterogeneous cases. Some heterogeneity-related effects such as self-shielding would be lost, but not entirely, as the pin diameter and the pitch can still be varied to capture some of the effect.

From the previous assembly-level study results, NaF-ZrF_4 allowed a UC or UO_2 fuelled AGR-like FHR assemblies to reach higher reactivity values and lower CTCs than FLiNaK did for designs with same design specifications. However, none of the designs with NaF-ZrF_4 had negative coolant temperature reactivity feedback, failing to meet the design requirement. Inspired by the work done in Klydon (Pty) Ltd, [60][61] a modification was made to NaF-ZrF_4 to improve its neutronic attractiveness in later design studies in this thesis: the Zr in the NaF-ZrF_4 coolant was assumed to be isotopically enriched to 99wt% in Zr-90 to reduce neutron absorption in the salt, while improving its moderating power slightly. It was hoped that cores with the modified NaF-ZrF_4 could achieve negative CTCs and even higher reactivity, while taking advantage of the fact that it was not tritium-producing and therefore eliminating the need for tritium capture and storage of all current FHR designs.

5.3.1 Comparison of Assembly and Unit Cell Models

This section compares the behaviour of neutronic parameters, i.e., BOL k_∞ and BOL CTC, predicted by the unit cell and assembly models. FLiNaK cooled designs were chosen to perform the benchmark study because they had greater sensitivity in k_∞ and CTC to design parameters. It was also found in the earlier analyses that these cases had the greatest statistical uncertainties in the results for the same number of neutron histories and model geometry, possibly because of a different balance between moderating and absorbing properties of this salt compared with the alternatives. The same material compositions and salt density dependence on temperature were used in the pin cell models as in the assembly models.

However, there were inconsistences in the representation of the design parameters two models: unlike the unit cell models, the assembly geometry models were created by systematically changing the number of fuel pins and channel diameters. Also, all assembly models had graphite on the periphery that surrounds the fuel channel, which had only fuel and coolant inside. This means that the fuel pin, graphite and coolant were not evenly distributed in the assembly. In addition, although only the coolant inside the assembly fuel channel was perturbed in temperature when calculating CTC, SFs of the assembly designs were calculated as the mass ratio of all salt coolant (inside and outside the fuel channel) to the total amount of graphite and

coolant mass. Therefore, some discrepancies between the unit cell and assembly models were expected, especially when the level of heterogeneity is high in the assembly model (for example, the designs that had tightly packed pins surrounded by a thick layer of graphite).

To make consistent comparison of the two models, same set of design parameters must be used. Results from both assembly and pin models with the same enrichment levels were used. Pitch to diameter ratios were calculated for the assembly models by assuming that all the components of the assembly were lumped into one homogenised region containing several fuel pins that were evenly spaced in an infinite square lattice.

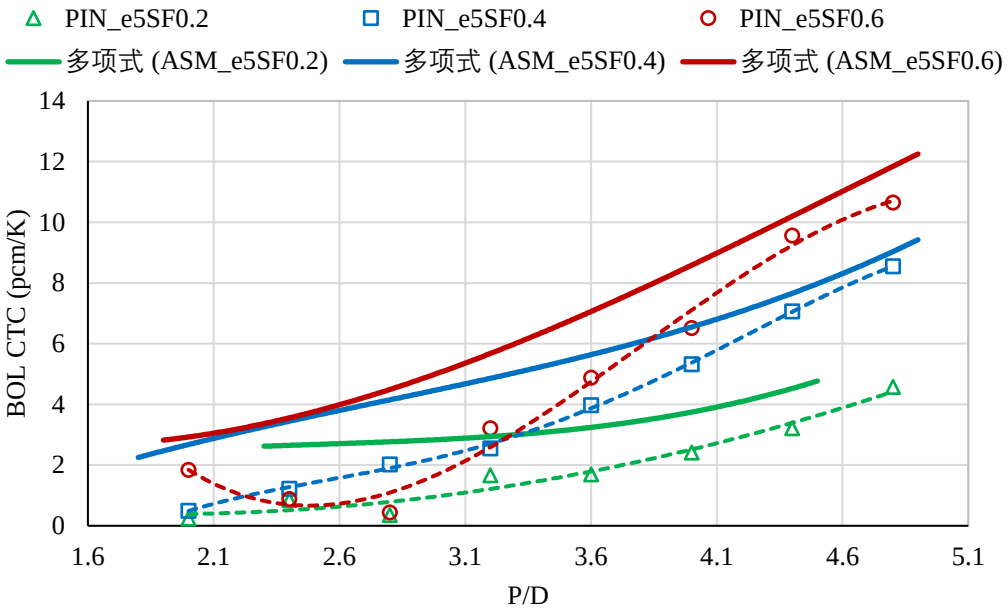

Figure 5-12. Comparison of BOL CTC variation with P/D in pin and assembly models

The pin model parameter variation process searched through the design space using evenly spaced grid of values for P/D, SF and enrichment, whereas the assembly level P/D and SF values were not evenly spaced. As a result, there was no one-to-one correspondence between P/D and SF values of the designs studied using the pin and assembly models, i.e., the points were positioned on different (P/D, SF, enrichment) grids. To be able to compare the results directly, the k_∞ and CTC values in assembly models at each enrichment level were interpolated and projected onto a fine three-dimensional (P/D, SF, and k_∞ or P/D, SF and CTC) grid that included the P/D, SF, and enrichment levels used in the pin models. On the projected 3-D

surface that represented the assembly models, k_∞ (or CTC) that corresponded to the specific P/D and SF values could then be predicted. Using this method, Figure 5-12 compares the effects of P/D on BOL CTC calculated using pin and assembly models for a fuel (UC) enrichment of 5 wt% and salt fractions of 20 wt%, 40 wt% and 60 wt%. The polynomial fit lines are used to present the assembly model data, whereas the data from single pin models is represented by marker points with dashed polynomial fit lines to help visualising the differences.

Both models predicted that the CTC increased with increasing P/D and was more sensitive to P/D at larger salt fractions. The basic physics appeared to be captured reasonably well by the two models: with larger P/D (more salt and graphite volume per unit volume of fuel) and therefore a softer spectrum, CTC became more positive as the marginal moderation effect from the salt diminished while the marginal absorption effect stayed the same. Although the CTC curves using pin model results showed slightly different gradient and shape compared to those of assembly models, the range of CTC values predicted by both models was in a reasonably good agreement: e.g., for a salt fraction of 60 wt%, the pin model predicted that CTC increased from 1.84 pcm/K at P/D = 2 to 10.66 pcm/K at P/D = 4.8, and the assembly model predicted that the CTC increased from 3 pcm/K to 11.95 pcm/K. The slight difference in the CTC curves from both models is possibly caused by the fact that the assembly model was much more heterogeneous: all the fuel pins were grouped in the centre of the assembly and were surrounded by a channel of graphite. Therefore, a fission neutron had a greater probability of escaping the fuel cluster and experiencing first collisions in graphite than in neighbouring pins, reducing the chances of resonance absorption in U238. Also, the outer ring of fuel pins shielded the inner fuel pins from resonance energy neutrons diffusing back from the graphite into the fuel region. Therefore, the spectral shift caused by the same salt density perturbation would have different magnitude of change in U238 resonance capture in the assembly and single pin models, resulting in different CTCs. For the same reason, the CTC curves approach each other as P/D increased and the spectrum softens. In a softer spectrum core, the contribution of resonance capture to reactivity became weaker therefore the difference between the two models reduces.

Figure 5-13 plots BOL k_∞ of the same set of designs shown in Figure 5-12. Again, reasonably similar range of the k_∞ values were predicted for the same enrichment and salt fraction. However, there were some discrepancies between the unit cell and assembly models: At low P/D values, the assembly models had greater k_∞ than the unit cell models. As P/D increased, the differences in k_∞ between the assembly and the unit cell models began to decrease, until

the two models predicted the same k_∞, after which the unit cell models started to predict greater k_∞ values than the assembly models.

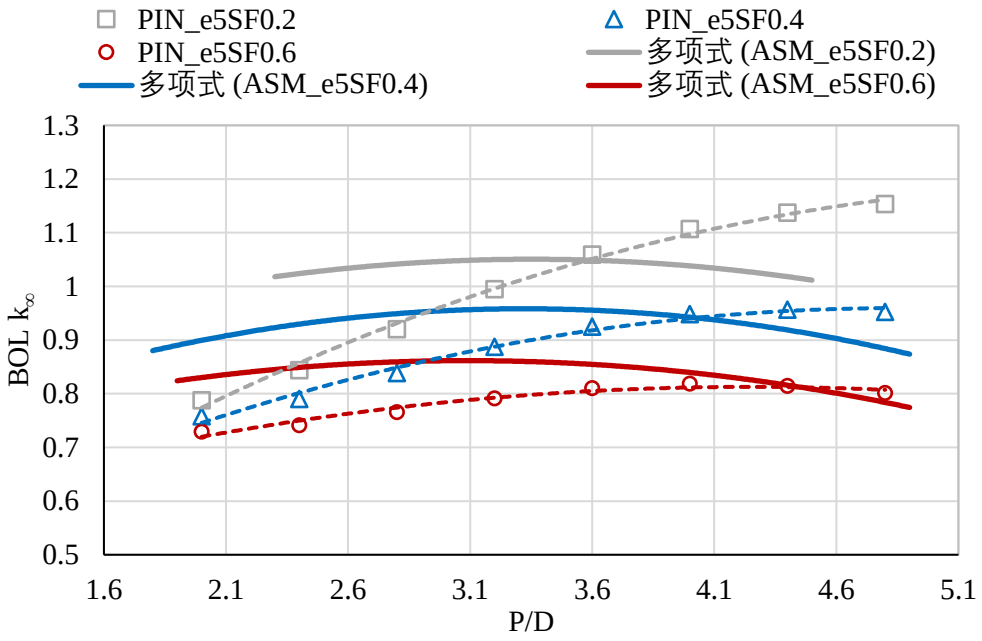

Figure 5-13. Comparison of BOL k_∞ variation with P/D in pin and assembly models

There was a complicated interplay of competing effects that causes this difference. On one hand, the heterogeneity of the assembly models provided fuel lumping effect and improved the neutron economy by increasing self-shielding and reducing resonance absorption: The fuel pins were densely packed together at the centre of the assembly channel. This means that the assemblies behaved similar to large fuel pins spaced apart by the assembly pitch (46 cm), which was very similar to the neutron migration length in carbon (~56.8 cm). This spatial self-shielding effected from the close packing of the fuel pins also helped with the reactivity at BOL. The unit cell models, however, failed to capture these effects and therefore generally predicted lower k_∞ values. On the other hand, heterogeneity of the assembly models could also have negative impact on the neutron economy: with increasing P/D, less fuel was placed evenly inside each assembly channel and all the coolant salt flowed between the fuel pins and the graphite. Therefore, more parasitic absorption happened in these designs as the thermalised neutrons reach the salt before the fuel pins. In the unit cell models, the salt and graphite were smeared so that the neutrons travelled through the homogeneous mixture and got thermalised (or absorbed with lower probability compared with the heterogeneous model) along the way.

This lumping effect of salt and graphite in the assembly model weakened the neutron economy when compared to the unit cell model.

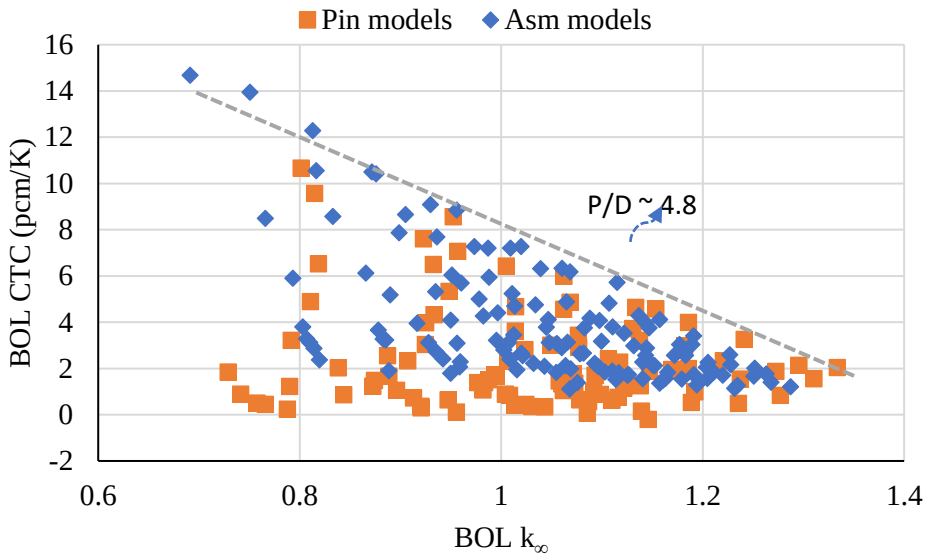

Figure 5-14. Comparison of BOL neutronic performance space of pin and assembly models

Despite some discrepancies in the k_∞ of the unit cell and assembly model, the two types of models did exhibit very similar trends in neutronic responses to changing design parameters, especially when examining how the global material composition affects the results of the two models. Figure 5-14 plots the k_∞ vs CTC space for both the pin and assembly models for a similar range of P/D (1.6 to 4.8), SF (20 wt% to 60 wt%) and fuel enrichment (5wt% to 12.5wt%). Although agreeing with the previous analysis in that the assembly models predict slightly greater minimum BOL CTCs, in general, similar performance was predicted by both models with similar design parameters: e.g., the upper boundaries of both design spaces overlapped and were bounded by designs with P/D ~ 4.8. This, again, confirmed that the pin models could be reasonably representative of heterogeneous assembly models.

Chapter 6 Unit Cell Model Neutronic Design

Following the work from the previous chapter, the homogeneous unit cell model is adopted in this chapter and applied to search through a much wider design space, covering solid fuel pin, annular fuel pin and plate type fuel using UC and FCM fuel. This chapter first presents discussions on design considerations based on the BOL results of the solid fuel pin models with FLiBe and NaF-ZrF_4 with isotopically enriched Zr. This is potentially the most attractive family of FHR designs covered in this thesis in terms of both thermal-hydraulics and technology readiness among all those considered. The chapter then investigates the BOL neutronic performance of the alternative design options. The most promising design options at BOL are selected for the next analysis stage where depletion calculations are performed.

6.1 Unit Cell Level Neutronic Design Space

Some of the previously proposed design options were screened out in the following unit cell neutronic modelling. Chapter 3 suggested that UO_2 fuelled reactors had significantly lower power density and would have higher LCOE than UC fuelled ones. This was especially significant for cases where fuel temperature was the most limiting constraint (which is true for almost all solid pin designs). However, this was not to reject UO_2 as a good FHR fuel candidate: it is the most known and commercially available nuclear fuel material. Due to limited computational resource, time, and the fact that the choice of UO_2 and UC had almost no effect on the neutronics of the reactor, as suggested in Chapter 5.2.1, UO_2 was not considered in later neutronic design studies. The neutronic performance of UO_2 fuelled FHRs could be largely inferred from that of UC designs. FLiNaK was excluded from later studies because all models with FLiNaK as coolant had very strongly positive CTCs which would complicate the reactor safety case and make it unstable in response to perturbations under nominal operating conditions. Again, the NaF-ZrF_4 used in this chapter had its Zr component isotopically enriched to 99% in Zr-90 due to its weaker neutron absorption.

Due to manufacturability, plate type fuel only considered FCM fuel. It was shown in the thermal-hydraulic analysis that the plate type fuel allowed some moderate power uprate from AGR level. This power uprate was achieved at the price of very limited fuel loading due to the structure of the FCM fuel. It was still decided to investigate this option because it might achieve better neutronic performance with NaF-ZrF_4, in which case the design can be a good back up option for tritium-producing FLiBe cooled systems.

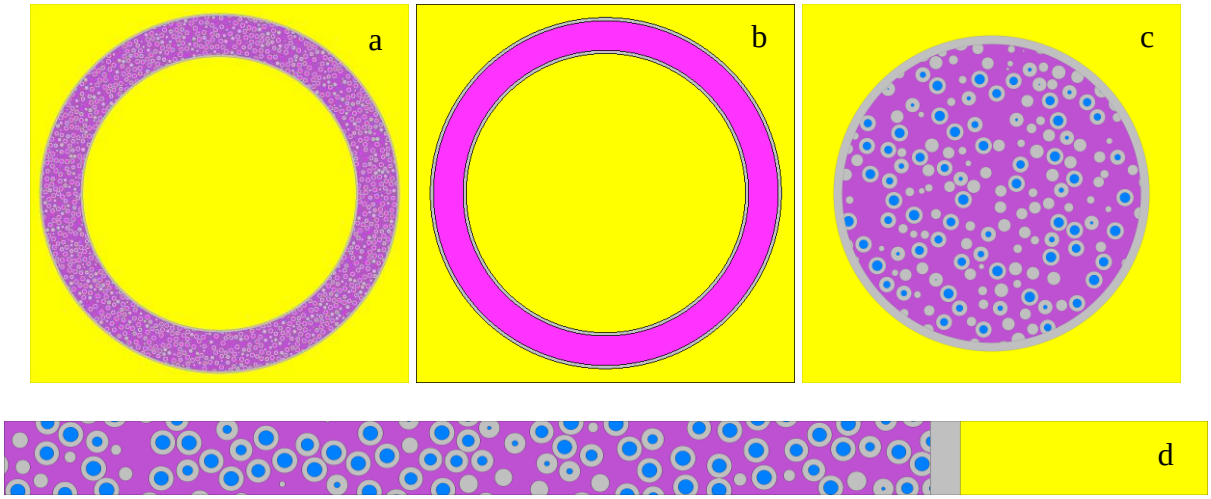

Figure 6-1. a) annular fuel model with FCM fuel, 2) annular fuel with UC fuel, 3) solid pin model with FCM fuel and d) plate type fuel model (x-z cross-section) with FCM fuel.

The unit cell level FHR design space was refined at this point to include: 1) solid UC or FCM pin fuel cooled with FLiBe or NaF-ZrF_4, 2) annular UC or FCM pin fuel with FLiBe or NaF-ZrF_4 and 3) plate type FCM fuel using NaF-ZrF_4 coolant. Similar to the unit cell model described for the solid pin designs, homogenised unit cell models with reflective boundary conditions were also created for the alternative fuel options. Leakage and control rods were again ignored in these models. Therefore, the k_∞ values would be slightly overestimated. Figure 6-1 shows some examples of the annular and plate type fuel unit cell models built in Serpent. 2-D models using UC as fuel are created, whereas the FCM fuelled models were built in 3D with a height of 1 cm to capture the 3-dimensional structure and random distribution of the TRISO fuel particles. The FCM fuel was modelled using Serpent's explicit random particle dispersion capability with a packing fraction of 40%. The TRISO particle dimensions were taken from AHTR [21] fuel and the fuel kernel material compositions were taken from Advanced Gas Reactor Irradiation Test Type 2 (AGR-2) fuel. [50][51] The TRISO geometry was simplified to have two layers in the Serpent models: the UCO (UO_2-$UC_{1.86}$-UC with mole fractions of 71.4%-12.3%-16.4%) fuel kernel with a radius of 0.025cm and all carbon layers were homogenised into one 'TRISO-layer' with a radius of 0.4235cm. The particles are dispersed in a carbon matrix which constitutes the fuel meat of the plate.

For both annular pin and plate type fuel forms, P/D, SF and fuel enrichment were used as design parameters. P/D was calculated by taking the AGR fuel pellet dimension; SF and fuel enrichment were treated in the same way as in the solid pin models. Two more design

parameters were used to characterise the annular pin unit cell models: fuel pin inner radius and fuel pin outer radius. For each P/D value, the outer radius of the annular pin was step-wise (with steps of 20% of the AGR fuel pin radius) reduced from the half pitch of the unit cell (maximum value). The fuel inner radius was then calculated for using a simplified version of Equation 3.4, where the correction factor was assumed to be unity and the coolant channel was assumed to occupy the entire space around fuel (ignoring the graphite content). When the fuel volume was smaller than that of the AGR fuel pin, the dimension search stops at that P/D and the process was repeated for the next P/D. The cladding thickness was assumed to be the same as the reference AGR.

The plate type fuel unit cell model included half of the plate and half of the coolant channel with reflective boundary conditions. The half plate thickness was used as a design parameter in addition to P/D, SF and enrichment. For each pitch value, the half plate thickness was systematically varied with a step change of 20% of the pitch, from a maximum thickness of 80% of the half pitch to the smallest thickness where the fuel plate volume was smaller or equal to that of an AGR pin. The fuel plate cladding/sleeve thickness was kept the same as that of the AHTR fuel plate. It shall be noted that most of the effect of the heterogeneous arrangements of the fuel, coolant and graphite was lost in these models. Unit cell models capture some of the effect by varying P/D. However, annular pins, compared with solid pins, had large surface to volume ratio, which affected resonance absorption and thus contributes to part of the heterogeneity of the model. The imbalance of information on heterogeneity captured by annular and solid pin models might cause some inconsistencies in representativeness of the models, the degree of which was uncertain. The same effect also applied to the plate type fuels, although to a lesser degree. This should be kept in mind when cross-comparing the results of different fuel designs.

6.2 BOL Neutronic Sensitivities Studies - Solid Pin Model

The following sub-sections firstly study BOL neutronic results of the UC fuelled FLiBe cooled solid pin unit cell models. A complete neutronic performance domain result for the solid pin models covering NaF-ZrF_4 coolant and FCM fuel was then presented and compared. It was envisaged that this understanding of the physics discovered from the solid pin design studies would also be applicable to designs with annular and plate type fuel forms.

6.2.1 Effect of P/D, Salt Fraction and Enrichment on BOL k_∞

Figure 6-2 plots the k_∞ values at BOL against fuel rod P/D for the FLiBe cooled solid UC pin cell models with U235 enrichments of 5 wt% and 12.5 wt% and SFs ranging from 20% to 100%. The results for models with 7.5% wt and 10 wt% enriched fuel were not shown in Figure 6-2. They lied in between the two curve groups plotted representing 5 wt % (brown lines with green markers) and 12% wt (blue lines with red markers) enrichment and showed similar behaviour with varying P/D as the data illustrated in the figure.

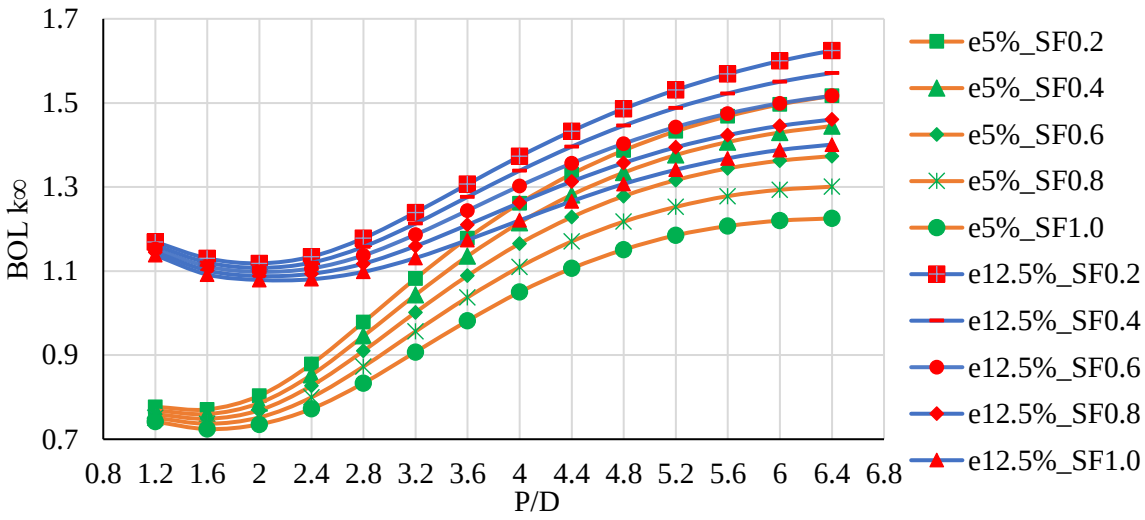

Figure 6-2. Effects of P/D on BOL k_∞ for FLiBe cooled unit cell models (5 wt% and 12.5 wt% enrichments)

Cases with the smallest lattice pitch had weak moderation, resulting in hard neutron spectra. Achieving criticality was challenging at these levels of moderation when the enrichment was lower than 12.5 wt%. As P/D increased from 1.2, the k_∞ of all designs slightly decreased initially, possibly due to fewer neutrons released per fission and smaller contribution of fast fission in U238. The sensitivity of k_∞ to changes in P/D in these hard neutron spectra increased with fuel enrichment. This was because the higher enrichments further hardened the spectrum and shifted more neutrons to energies higher than the resonance region of U238. Therefore, as more moderation was introduced with increasing P/D, larger increase in resonance absorption in U238 would be observed in designs with higher enrichments. After P/D increased to a threshold value (e.g., P/D = 2.4 for 12.5wt% enriched designs), k_∞ started to increase with P/D.

This indicates that the moderation effect began to dominate. This would lead to increased U235 fission cross-section and reduced U238 absorption cross-section. The positive gradient of the curves suggests that reactors operating at these regions could be vulnerable to over-cooling accidents associated with excessive heat removal from the primary loop. Although total volume of salt increased with larger pitch and the total parasitic absorption in salt would increase with increasing coolant volume, the increasing k_∞ suggests that the increase in U235 fission cross section won over the total effect of negative reactivity feedback from the increase in absorption in U238 and salt. In addition, with a softer spectrum, neutrons migration length shortened, and the pin lattice became more heterogeneous, therefore, enhancing self-shielding effect.

Figure 6-2 shows that k_∞ increases monotonically with decreasing SF ratios (more graphite and therefore stronger moderation) and increasing U235 enrichments. This could be better understood from the fact that the k_∞ vs P/D curves for different enrichments, but fixed SF, did not intersect, and curves of designs with different SF but fixed enrichments did not intersect. Even in hard spectrum with low P/D, this phenomenon was also observed, suggesting that U235 fission was still the dominating contributor to the changes in the multiplication factor. It suggested that at any P/D ratio, greater reactivity could always be achieved by choosing a higher enrichment and a lower salt fraction. For a reactor designer, this means that for a fixed reactor core volume and fuel loading requirement, to maintain a reasonably large BOL k_∞ and therefore a potentially greater achievable burnup, one could use high fuel enrichment and more graphite relative to coolant in the core. This method, however, would result in greater fuel cost and weaken the heat transfer capability and achievable power density, which negatively affects the economics of the reactor.

On the other hand, k_∞ vs P/D curves did intersect when they had different SF and different enrichment. This means that a well-chosen P/D could drive a low-enriched reactor with small graphite proportion up in reactivity to a greater extent than high enrichments and graphite fractions. It could be seen from Figure 6-2 that k_∞ was more sensitive to P/D ratio (steeper slope) at lower enrichments when the salt fraction was held constant. The one-group U235 fission cross-section also increased more with P/D at lower enrichments. This is because for the same amount of moderation, low enriched fuel would have softer spectrum, and therefore benefited more from the increased U235 fission cross-section with neutron energy at thermal range. For the same reason, k_∞ was more sensitive to salt fraction at larger P/D which had stronger moderation. k_∞ was also more sensitive to P/D at lower salt fractions when enrichment was fixed. Lower salt fraction means greater marginal increase in moderation from graphite

from a unit of increment in cell dimension, resulting in a larger increase in U235 fission cross-section, which is larger on its own compared with designs with higher salt fractions. The greater response to any increase in P/D at low enrichment level and salt fraction enabled a low enriched fuel to achieve higher k_∞ than a fuel with higher enrichment.

It was also noted that the slope of the curve in Figure 6-2 could be thought of as an indicator CTC: the magnitude of the gradient estimated the relative magnitude of the CTC, which had the opposite sign as the slope of the curve. For all designs, there was a 'valley' in the k_∞ vs. P/D curve. These valley points suggested that any event that results in perturbation in the moderation of the system, e.g., any mismatch between grid load and core thermal power, would introduce positive reactivity insertion to the core. This made these designs undesirable in terms of reactivity feedback. In addition, it could be seen from Figure 6-2 that k_∞ was more sensitive to lattice pitch than to salt fraction, suggesting that increasing pitch was a better way to improve neutronic efficiency. Similar to k_∞ vs Hydrogen/HM curves for light water reactors, a peak could be expected in the k_∞ vs P/D curves for FHR pin lattice designs because salt was also both moderating and absorbing. Designs operating near the peak would be desirable in terms of multiplication factor or neutron economy. However, since the moderating power of FLiBe is much weaker than that of hydrogen and carbon has very low absorption cross section, the saturation of moderation occurred at much higher P/D (above 6.8) than LWRs.

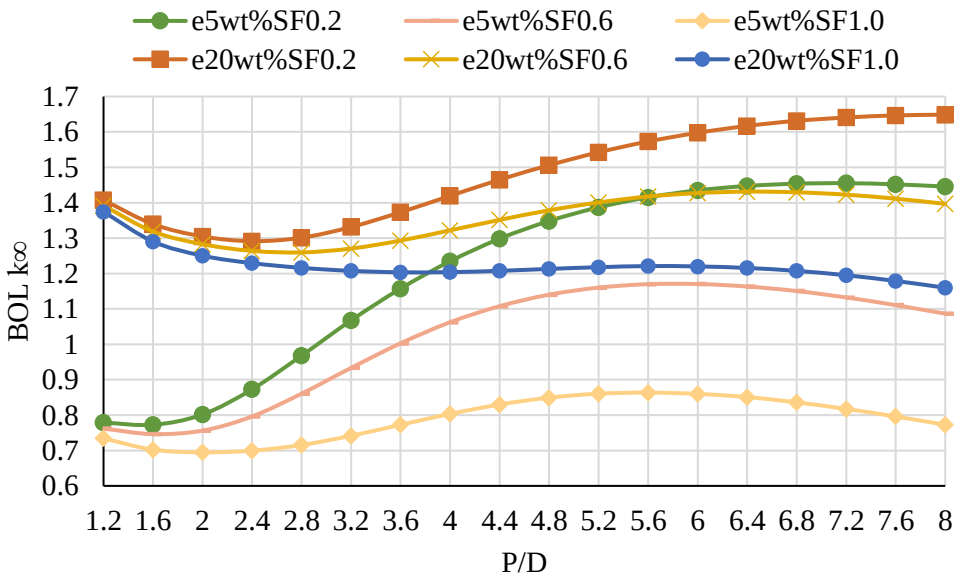

Figure 6-3 Effects of P/D on BOL k_∞ for NaF-ZrF_4 cooled unit cell models (5 wt% and 20 wt% enrichments)

Studies using NaF-ZrF4 as coolant candidate showed very similar behaviour of k∞ when changing the P/D, SF and enrichment. Therefore, the analysis presented earlier for FLiBe could also be applied to NaF-ZrF4 cooled designs. The magnitude of the gradients, the value of k∞ reached and the P/D values where the 'valleys' and the 'peaks' occurred differed from the FLiBe cooled designs, however. This is shown in Figure 6-3 where k∞ vs P/D is plotted for the NaF-ZrF4 cooled UC (5 wt% and 20 wt% enriched) solid fuel pin design. The figure suggests that the 'peaks' in the k∞ vs P/D curve appeared at P/Ds from 5 to 8. This large lattice pitch would result in either lower power density or shorter cycle length, negatively affecting the economics of the reactor. On the other hand, greater heat removal was allowed by the large P/D which could potentially increase the power density and make up for the loss.

6.2.2 Effect of Pitch to Diameter ratio on CTC

It is important to understand how CTC behaves with different neutron spectra resulted from different combination of P/Ds, salt fractions and fuel enrichments. Figure 6-4 illustrates the effect of lattice pitch on CTC for FLiBe cooled reactors with 7.5wt% enriched fuel and varying salt fraction. For all salt fractions, CTC curves initially decreased from a positive value with increasing pitch, then increased with P/D after P/D reached a valley point (e.g., P/D = 3.6 for the design with 7.5wt% enriched fuel and 100% salt fraction). The positive CTC could be caused by reduction in energy dependent fission neutrons yield and in fast fission in U238 as they become important contributors to the reactivity. CTC then became more negative with increasing P/D. This is possibly due to neutrons becoming more and more thermalised, and CTC being predominately determined by the relative level of change in moderation compared with absorption from the coolant. When P/D increased initially from a low value, the marginal increase in moderation effect contributed by salt was large. Therefore, there was a stronger negative coolant temperature reactivity feedback as lattice pitch increased. As the volume of the coolant continued to increase to a level where the core was well moderated, and any further addition of salt introduced only limited moderation but proportionally larger absorption to the core, the coolant temperature reactivity feedback would eventually become positive. To ensure a negative CTC, the core fuelled with 7.5 wt% enriched UC should be designed with a P/D greater than 2.0 and less than 6.4. Designs with different level of enrichments showed very similar pattern. This confirmed that although a very large pitch can be preferable in terms of reactivity (neutron economy), the constraint on reactivity feedback, in addition to the thermal-hydraulic and economic concerns, would put a limit on the maximum P/D an FHR can be designed with.

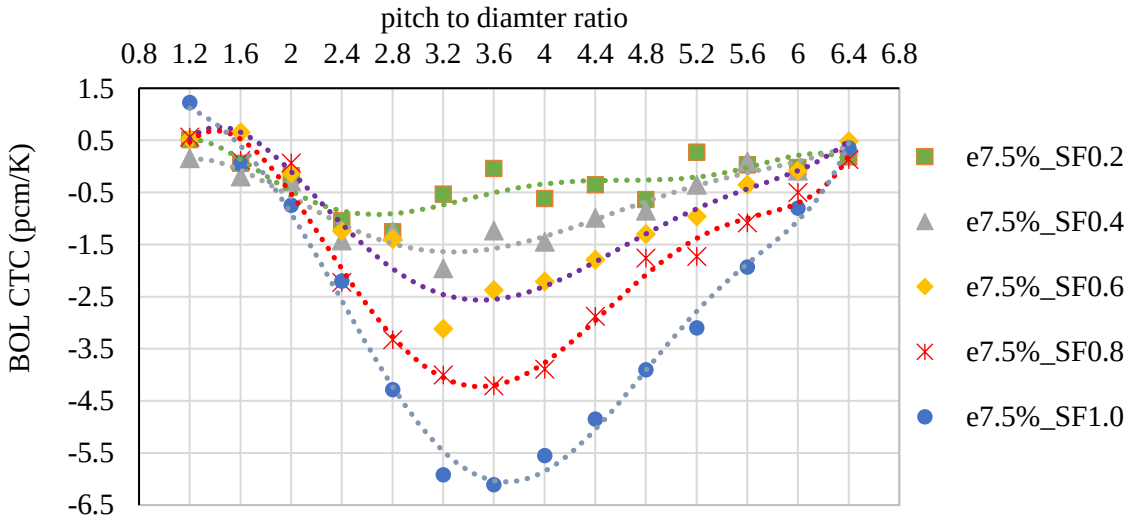

Figure 6-4 Effects of P/D on BOL CTC for FLiBe cooled models (7.5 wt% enrichment)

Increasing the salt fraction, on the other hand, caused almost monotonic decreasing effect on CTC of the FLiBe cooled core, and the effect was strongest when P/D was 3.6. As more salt and less graphite was put into the core, the moderation was reduced, therefore the core relied more on salt and less on graphite for moderation. This would make the marginal moderation from salt stronger per unit rise in salt fraction, achieving in more negative CTCs. This phenomenon would be observed until the moderation effect from salt was saturated.

NaF-ZrF_4 cooled models showed similar general behaviour patterns as the FLiBe cooled models. However, the sensitivity of the neutronic performance to the three independent design parameters were slightly different from the FLiBe cooled ones. Figure 6-5 shows the BOL CTC vs P/D plot for NaF-ZrF_4 cooled designs with 5 wt% and 20 wt% enrichments and 20% and 100% salt fractions. Out of the four designs shown, only the one with 5 wt% enrichment and 100% salt showed relatively high sensitivity to P/D and reached a notably negative CTC around a P/D value of 4. The other three did not show much change in CTC with P/D. In other words, there were threshold values for fuel enrichment and salt fraction beyond (or below) which the CTCs became insensitive to P/D. Designs with lower enrichment had greater CTC sensitivity to variations in P/D because less enrichment meant a softer spectrum and the relative moderating and absorbing effects of salt increased. This figure also shows that NaF-ZrF_4 cooled designs were much more sensitive to salt fraction than FLiBe cooled designs. This suggests that the moderating power of NaF-ZrF_4 was much weaker compared with FLiBe. Also,

when put inside a graphite moderated environment, NaF-ZrF_4's moderating power came into effect only when there is very little moderation from graphite (or no graphite at all). Therefore, to have negative CTCs for designs using NaF-ZrF_4 coolant, very little or zero graphite was to be used in the core. This would negatively affect the neutron economy of the core.

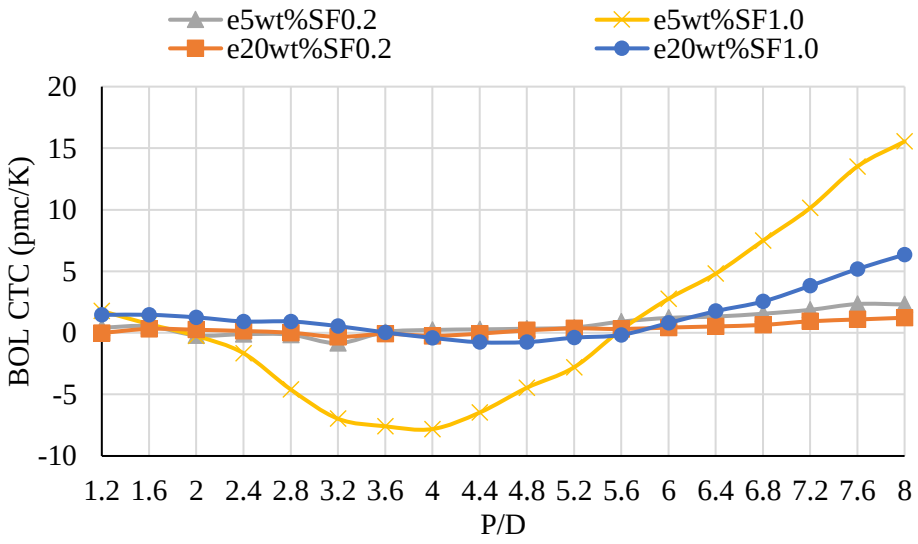

Figure 6-5 Effects of P/D on BOL CTC for NaF-ZrF_4 cooled unit cell models (5 wt% and 20 wt% enrichments)

6.2.3 Effect of Salt Fraction on CTC

To further analyse the effect of salt fraction on CTC, Figure 6-6 plots CTC against the salt fraction for the design using 7.5wt% enriched fuel at different P/D ratios. The coolant choice used in these designs is FLiBe. In agreement with the results shown in Figure 6-4, Figure 6-6 shows that at small P/D values, CTC for the 7.5wt% enriched design was positive and was not sensitive to the salt fraction in the core, increasing very slightly towards more positive values with increasing salt fraction. As the salt fraction of the designs with low P/D ratios increased, the spectrum became even harder and the positive contribution to CTC from fast fission in U238 marginally overweighed the negative contribution from resonance absorption in U238. Therefore, CTC increased slightly with salt fraction at low P/D. Beyond a certain point (P/D = 2.4 for the case illustrated in Figure 6.5), the slope of the curve became negative and the curves started to diverge, suggesting that more neutrons were thermalised. The CTC values for these thermal cores would be dominated by the coolant's moderation and absorption effect. As a

result, a larger salt fraction would increase the negative contribution from loss of moderation in coolant, making the CTC more negative. However, as P/D was greater than 6, the CTC curve became insensitive to salt fraction again. These curves represent the designs that are well moderated and therefore the difference in salt fractions did not have a large effect on CTC.

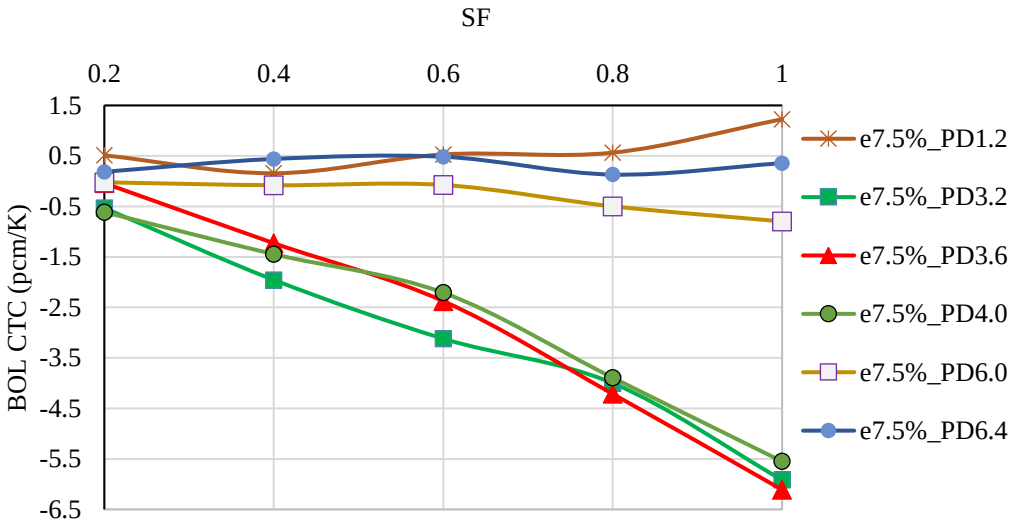

Figure 6-6. Effects of SF on BOL CTC for FLiBe cooled unit cell models (7.5 wt% enrichment)

$NaF\text{-}ZrF_4$ cooled designs exhibited similar patterns in CTC's behaviour with changing SF at different P/D values. Figure 6-7 plots the same graph as Figure 6-6 for designs with 7.5 wt% enriched UC fuel using NaF-ZrF4 as coolant. It shows that CTCs of the designs with low P/D also stay relatively constant with changing salt fraction. Agreeing with previous conclusion from analysing Figure 6-4, negative CTCs for a $NaF\text{-}ZrF_4$ cooled FHR could only be achieved when P/D was roughly between 3.6 to 4.4 with very large salt fractions (beyond 80%). With P/Ds greater than 4.4, the reactor began to have increasingly more positive CTCs with increasing salt fractions. This was when the absorption won over the moderation effect of the $NaF\text{-}ZrF_4$. Unlike Figure 6-6, where all CTC vs SF curves had roughly zero or negative slopes, Figure 6-7 shows upward sloping curves. This suggests that $NaF\text{-}ZrF_4$ was much more absorbing and less moderating than FLiBe. The range of P/Ds that could give negative CTCs was rather similar when using either salt, with $NaF\text{-}ZrF_4$ requiring slightly larger pitch than FLiBe. However, this suggests a different range of P/D from the range of P/D that optimised neutron economy for designs using the two salts.

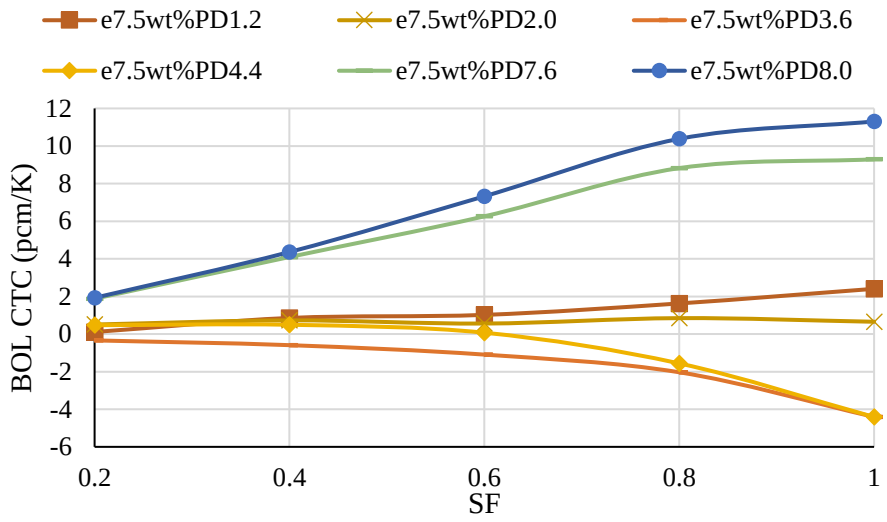

Figure 6-7. Effects of SF on BOL CTC for NaF-ZrF_4 cooled unit cell models (7.5wt% enrichments)

In addition to changing the energy spectrum of the core, the salt fraction in the salt-graphite mixture affected the non-fuel absorption and pin-to-pin collision probability. As mentioned earlier, larger optical thickness of coolant region (shorter neutron migration length) made the lattice appear more heterogeneous to neutrons, and this reduced the lattice shadowing effect (increase the fuel lump escape probability) and enhanced the geometrical self-shielding effect in U238, which could be illustrated by observing a reduction in one group U238 absorption cross-section. To demonstrate this lattice effect caused by varying salt fraction on neutronics, Figure 6-8 plots the one-group absorption cross-section of U238 for different salt fractions against pitch to diameter ratio for the FLiBe cooled designs. Similar behaviours were also seen when using NaF-ZrF_4 as coolant.

For designs with small lattice pitch, U238 absorption cross-section increased with increasing P/D. This indicates that the fuel pin escape probability increased (self-shielding decreased). Also, increased moderation would result in an increase of thermal U238 captures. These effects eventually saturated, leading to levelling-off of the curves. Similar logic could be applied to explain the increase in U238 cross section with increasing salt volume fraction. Being much more absorbing than graphite, increasing the salt fraction for a given P/D, would reduce the probability of neutrons escaping from a fuel pin to experience first collision in a neighbouring pin, effectively increasing the fuel pin (and U238 resonance) escape probability, weakening the spatial self-shielding and increasing the U238 capture cross section. This effect may also

(at least partially) explain why CTC was positive at pitch to diameter ratios greater than 6.4 while the curves shown in Figure 6-5 still have upward trend.

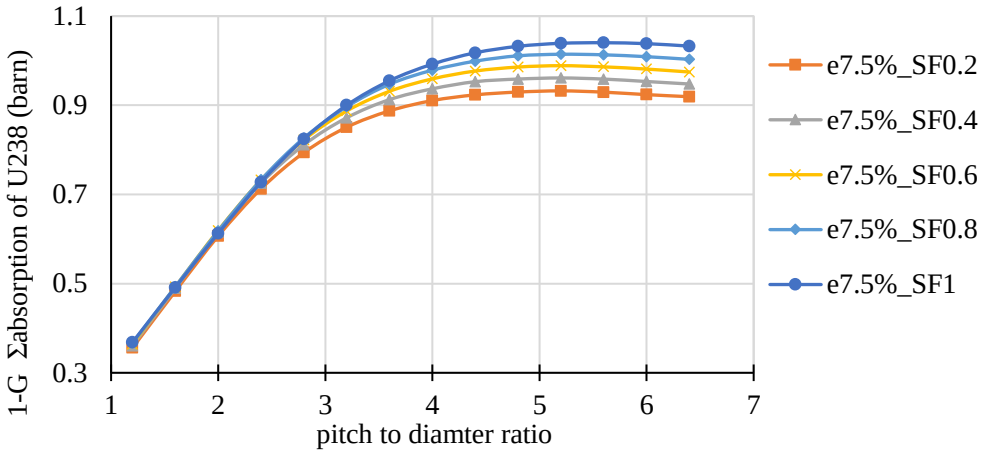

Figure 6-8. One-group U238 absorption XS vs. P/D (7.5 wt% enrichment)

6.2.4 Effect of Fuel Enrichment on CTC

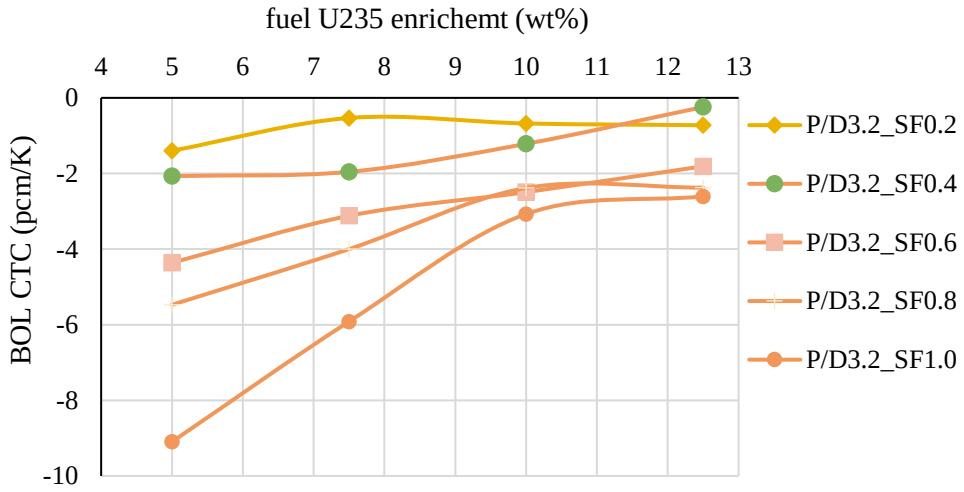

Figure 6-9. Effects of fuel enrichment on BOL CTC for FLiBe cooled FHR (P/D = 3.2)

Figure 6-9 plots the coolant temperature coefficient against the fuel enrichments for designs with a lattice pitch to diameter ratio of 3.2 and different salt fractions. Apart from the design with lowest salt fraction, CTC became less negative with increasing fuel enrichment and the

rate of change was greater with larger fractions of salt in the salt-graphite mixture. Since the U235 fission cross-section is inversely proportional to neutron velocity, for the same shift in neutron energy caused by a coolant temperature perturbation, the negative contribution to CTC from fission in U235 became weaker at a higher enrichment, which gave a harder spectrum. For the same reason, CTC was more sensitive to fuel enrichment at higher salt fractions: higher salt fractions resulted in weaker moderation per unit of fuel; therefore, for the same increase in fuel enrichment, designs with larger salt fractions would experience greater spectral shift to higher energies, exhibiting less negative CTCs. Very similar trend was also observed in NaF-ZrF_4 cooled unit cell models.

6.2.5 BOL Neutronic Performance Optimum Frontier

Figure 6-10 plots the cases within the theoretically feasible BOL design neutronic performance domain (k_∞ greater than 1 and negative CTC) in the k_∞-CTC space. Designs outside of the domain were excluded in Figure 6-10. The points with greater distance from the origin were better designs with more negative CTC and greater BOL k_∞. They form an 'optimum frontier' (the red curve) that was comprised of best performing cases among all surveyed designs. This frontier indicates that there was no single best design that can outperform others at BOL in both CTC and k_∞. Moving along the frontier means sacrificing the CTC to achieve better neutron economy, or vice versa. The points in Figure 6-10 are grouped by a) fuel enrichment and b) salt fraction to better understand how these two parameters affect the trade-off between CTC and k_∞.

Figure 6-10 a) shows that designs with lower enrichment (5wt% and 7.5wt%) were less likely to appear on the optimum frontier, and when they did, they were at the bottom left portion of the domain, meaning strongly negative CTC but small excess reactivity at BOL. The designs with higher enrichments, on the other hand, often had less negative CTC, all roughly above -4 pcm/K. Figure 6-10 b) shows that while designs with different salt fractions were equally able to achieve large excess reactivity, CTC below -2 pcm/K could only be achieved with salt fractions greater than 40 wt%. However, it should be noted again that the k_∞ values in Figure 6-10 were estimated without considering neutron leakage, parasitic absorption, etc. This could become a non-negligible factor, especially for the cases with high salt fractions where the reactor essentially becomes an epithermal or even a fast reactor. Therefore, all points on Figure 6-10 would be shifted left in realistic scenarios, with the ones with higher salt fractions moving

further, making the actual feasible domain a smaller and shorter triangle than depicted in Figure 6-10.

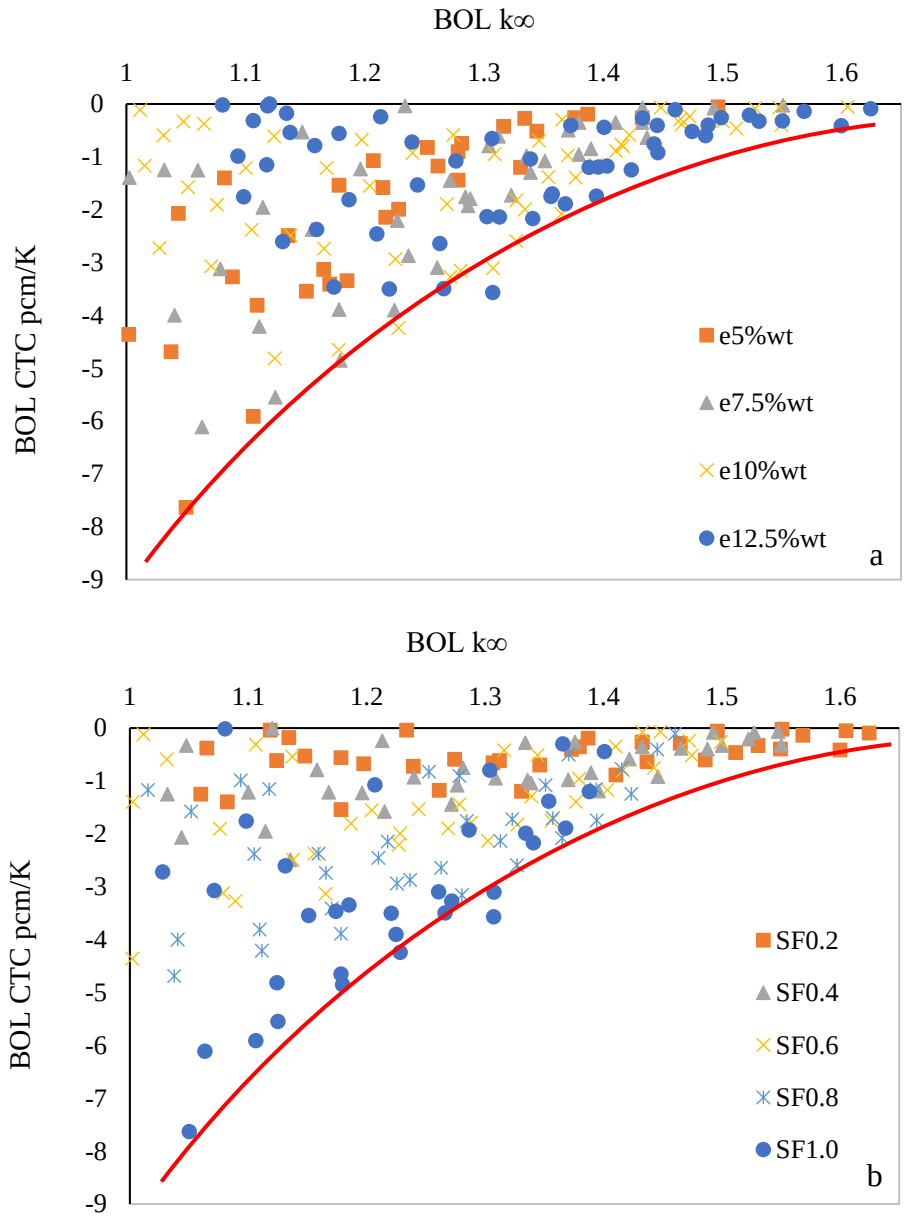

Figure 6-10. BOL CTC vs k_∞ performance domain a) grouped by enrichment b) grouped by SF for FLiBe cooled FHR

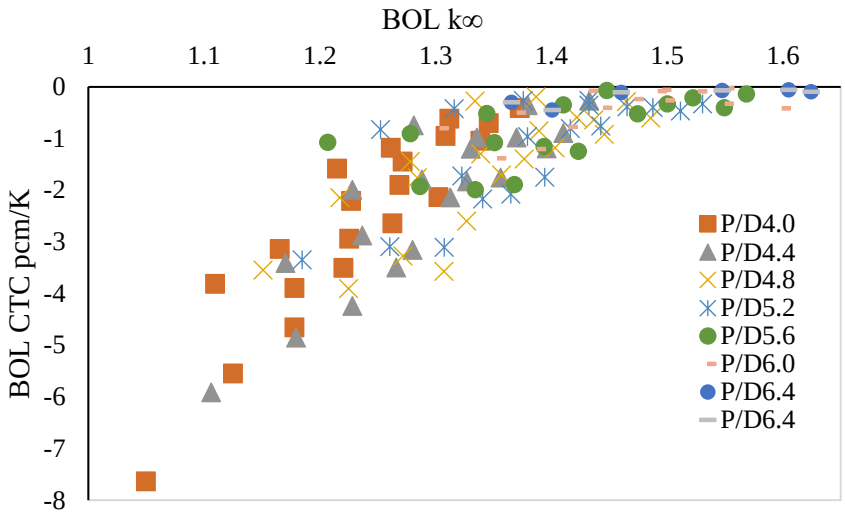

Figure 6-11. BOL CTC vs k_∞ grouped by P/D for $4 \leq P/D \leq 6.4$ for FLiBe cooled FHR

When examining the effect of P/D on the design's location in the k_∞-CTC space, it was found that P/D was the most decisive factor that determines whether an FHR can reach the optimum design frontier. Figure 6-11 shows models with P/Ds from 4.0 to 6.4 in the CTC- k_∞ space. The points moved away from the optimum frontier towards the origin as their P/D was decreased (or potentially when increased, as greater P/Ds are not yet covered in the design space search). These were considered to be less efficient and therefore not shown in the figure. In other words, the optimum frontier for the UC solid fuel FLiBe cooled FHR consists of designs with P/Ds ranging from 4 to 6.4.

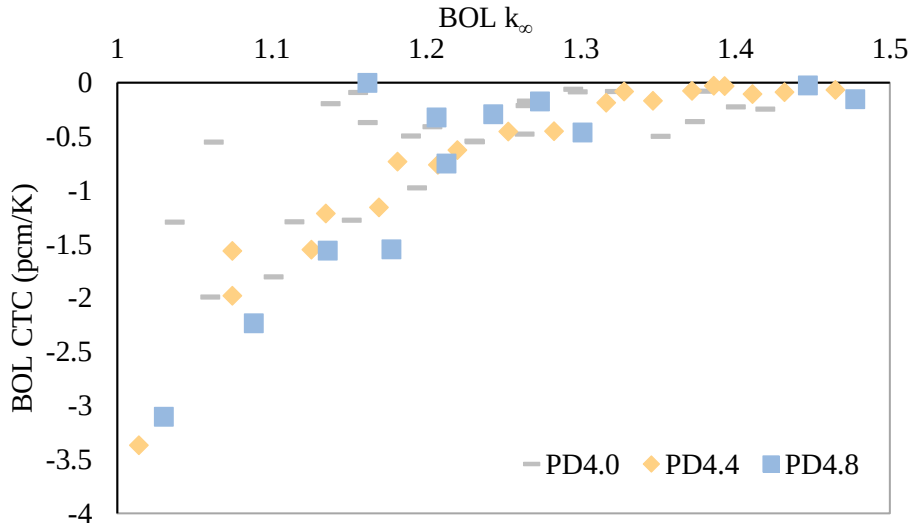

Figure 6-12. BOL CTC vs k_∞ grouped by P/D for $4 \leq P/D \leq 6.4$ for NaF-ZrF_4 cooled FHR

The same analysis when applied to the NaF-ZrF_4 cooled designs revealed very similar findings: P/D of a core determined how close the design as to the optimum frontier; whereas the SF and enrichment determined its position along the optimum frontier (if the design reached the frontier). Figure 6-12 shows the UC solid pin cell models using NaF-ZrF_4 as coolant with P/Ds from 4.0 to 4.8. Designs with this range of P/Ds values essentially composed the achievable optimum frontier in the CTC- k_∞ space. It was also noted that the unit cell model using isotopically enriched Zr in NaF-ZrF_4 achieved very significant improvements in terms of both BOL k_∞ and CTC from the assembly models using NaF-ZrF_4 with natural Zr. The isotopic separation of Zr would unavoidably make the salt more expensive, but the cost reduction from not having to deal with tritium can potentially make the enriched NaF-ZrF_4 a very attractive coolant option for FHRs.

6.2.6 BOL Neutronic Performance Domain Sensitivities

Figure 6-13 plots the BOL neutronic performance spaces (CTC- k_∞ space) of the solid UC and FCM fuelled models cooled with FLiBe (Figure 6-13-a) and FLiNaK (Figure 6-13-b) respectively on the same scale. Out of 910 FLiBe cooled designs covered, 300 fell into the feasible neutronic performance domain, of which 213 used UC as fuel and 87 used FCM. With the same number of designs modelled using NaF-ZrF_4 as coolant, 149 reached the feasible domain with 134 using UC and 15 using FCM fuel.

Both Figure 6-13 a) and b) suggest that for the solid pin designs, UC was clearly the better fuel choice in terms of neutronics (also in terms of thermal-hydraulics as shown in earlier chapters). Comparing Figure 6-13a) with b), it was found that FLiBe outperformed NaF-ZrF_4 in terms of both k_∞ and CTC. The FLiBe cooled solid pin designs could reach a maximum BOL k_∞ of 1.6584 ± 0.0002, and a most negative CTC of -7.6 ± 0.1 pcm/K; whereas NaF-ZrF_4 cooled designs only reached 1.4777 ± 0.0002 BOL k_∞ and -3.4 ± 0.1 pcm/K CTC.

Another finding which agreed with previous observations was that the P/D was indeed the most significant design parameter that drove the performance of a reactor into the feasible domain towards the optimum frontier. Although a very large range of P/D values was covered (1.2 to 6.4) when creating the unit cell models, only P/D values in a particular range led to a critical core with a negative CTC at BOL. UC fuelled designs required P/Ds ranging from 4 to 6.4 when using FLiBe, and P/Ds ranging from 4 to 4.8 when using NaF-ZrF_4; FCM fuels need much smaller P/D as the carbon inside the fuel meat provides rather large strong moderation already: feasible FLiBe cooled FCM models had P/D values between 1.2 to 3.2 and NaF-ZrF_4

cooled designs had P/D ranging from 1.6 to 2.4. For both fuel materials, NaF-ZrF_4 cooled FHRs had fewer degrees of freedom in terms of fuel pin pitch than FLiBe to meet the k_∞ and CTC targets. With P/D being the strongest variable in determining the performance of a solid pin FHR, salt fraction and enrichment had notable effects on the reactor's CTC-k_∞ performance domain as explained in earlier sections for UC fuelled solid pin designs. Similar behaviour was observed for both coolant salts in FCM fuel solid pin models.

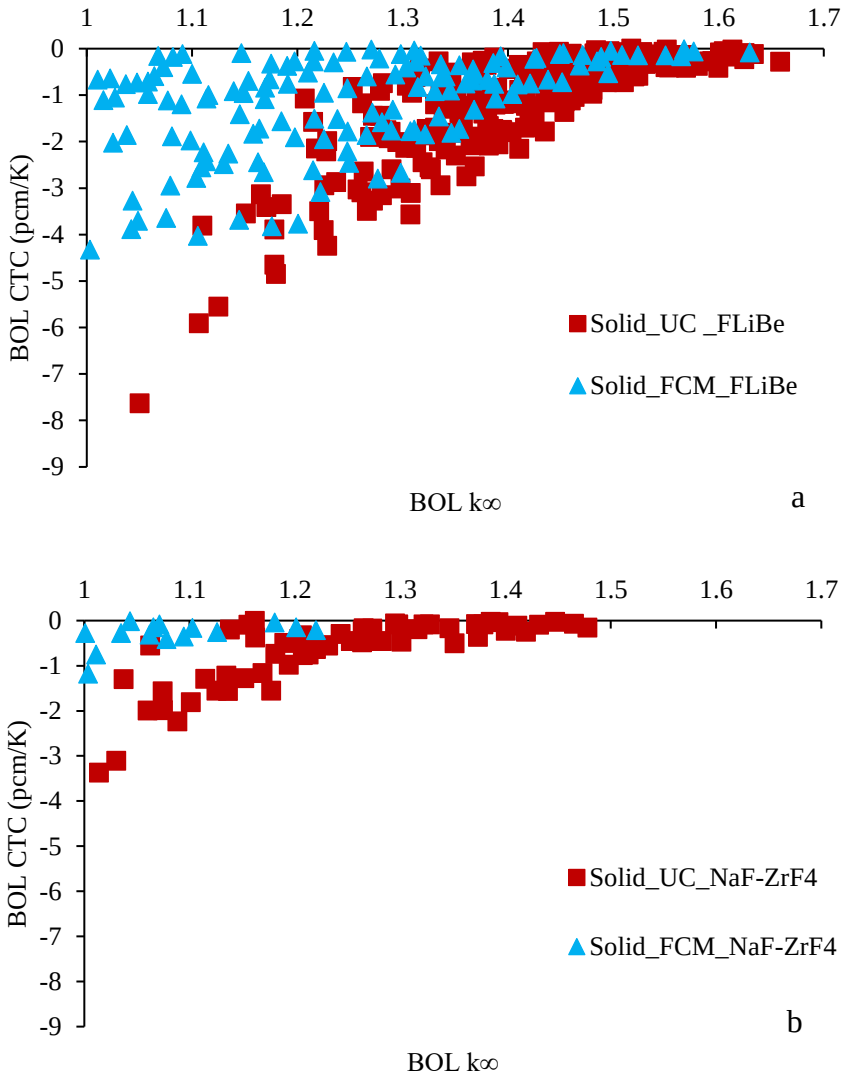

Figure 6-13. BOL CTC vs k_∞ performance domains for solid pin type FLiBe (a) and NaF-ZrF4 (b) cooled FHR

6.3 BOL Neutronic Performance Domains for Alternative Designs

6.3.1 Annular Pin Fuel Designs

Starting from 1400 fuel pin dimensions, 5600 annular pin unit cell models were created using FCM and UC rods in combination with FLiBe and NaF-ZrF_4. When using UC fuel, 165 cases were neutronically feasible. Among these, 118 used FLiBe and 47 used NaF-ZrF_4 as coolant. When using FCM fuel, 499 models were neutronically feasible, with 420 models cooled with FLiBe and the 79 with NaF-ZrF_4.

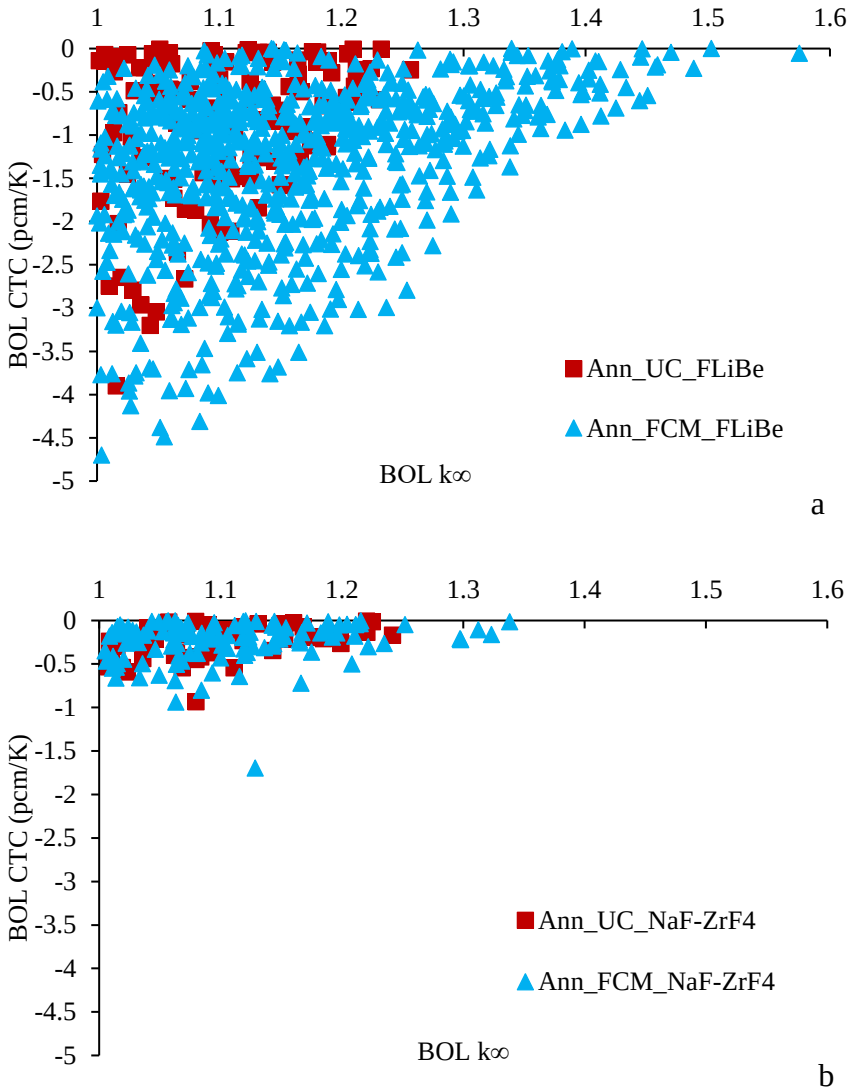

Figure 6-14. BOL CTC vs k_∞ performance domains for annular pin type FLiBe (a) and NaF-ZrF_4 (b) cooled FHR

Figure 6-14 plots the feasible BOL neutronic performance domains of the annular pin models using two coolant options on the same scale: Figure 6-14 a) shows designs using FLiBe and Figure 6-14 b) shows designs using NaF-ZrF_4. Same as in solid pin FHRs, FLiBe was clearly the better coolant choice using annular fuel pin. The FLiBe cooled annular pin designs could reach a maximum BOL k_∞ of 1.5749 ± 0.0002, and a most negative CTC of -4.4 ± 0.1 pcm/K; whereas NaF-ZrF_4 cooled designs only reached 1.3384 ± 0.0002 BOL k_∞ and -0.9 ± 0.1 pcm/K.

However, contrary to the solid pin models, the annular fuel pin models performed significantly better neutronically at BOL when using FCM instead of UC. This was true for both coolant options. In addition, when P/D was greater than 2.8, there was much weaker relationship between a model's P/D and its proximity to the optimum frontier in the CTC- k_∞ space. All points were scattered without clearly identifiable pattern.

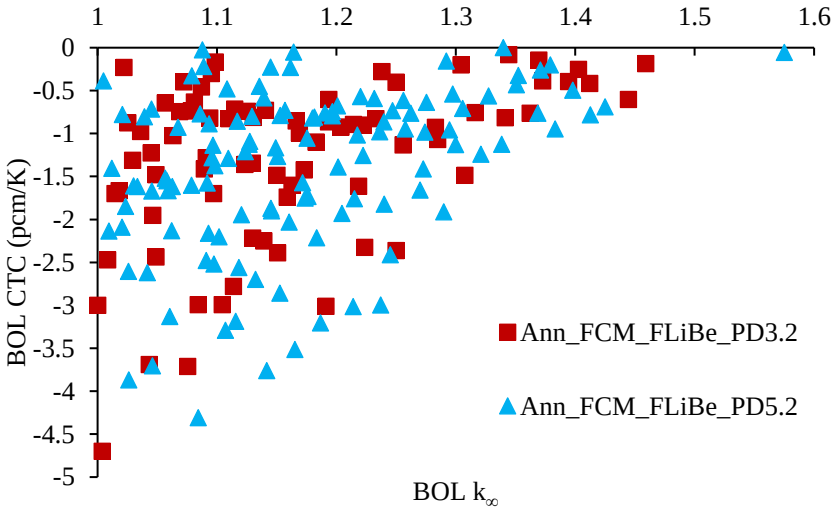

Figure 6-15. BOL CTC vs k_∞ domain for annular pin FCM fuel FLiBe cooled FHR

Figure 6-15 plots FLiBe cooled annular FCM fuel models with P/Ds of 3.2 and 5.2 on the same graph. No clear trends were observed between the designs with the two P/D values. This was possibly because the relationship between the moderator to fuel volume ratio and the P/D for annular pin models was complicated. The inner and outer radii of the pellet were not fixed but calculated for each individual P/D value to satisfy thermal-hydraulic constraints. Unlike in the solid pin models where larger P/D meant greater moderator per unit volume of fuel, in an annular model, a larger P/D could require a larger or thicker fuel ring to achieve the required

coolant flow rate conditions on both sides of the fuel. The variation in size and thickness of the annular fuel rods resulted in substantial variation in self-shielding and resonance absorption effects which were superimposed on top of the P/D variation effect. It was found that for a specific P/D value, the larger but thinner the annular pin was, the closer the core design was to the optimum frontier.

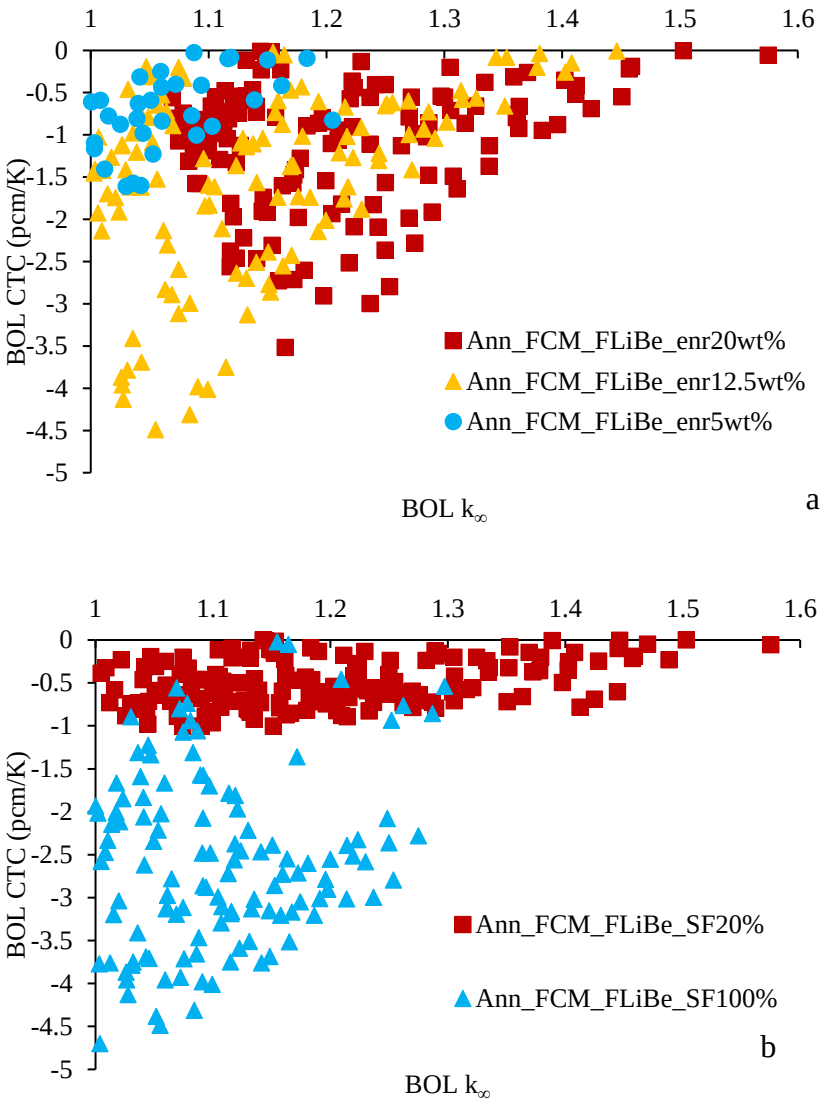

Figure 6-16. BOL CTC vs k_∞ performance domain a) (up) grouped by enrichment b) (down) grouped by SF for annular FCM pin FLiBe cooled FHR

Similar to previous discussions for solid pin unit cell models, salt fraction and fuel enrichment of an annular fuel FHR determined the trade-off between its CTC and k_∞, although the

magnitude of the sensitivity to these parameters was slightly different from the solid UC fuel unit cell models. To illustrate this, Figure 6-16 a) plots the FLiBe cooled annular FCM pin models with 100 wt% and 20 wt% salt fractions, and b) shows 5 wt%, 12.5 wt% and 20 wt% enriched FLiBe cooled annular FCM pin models. Designs with small salt fractions (e.g., 20 wt%) lied in the upper region of the triangular performance domain (higher k_∞ but less negative CTC), whereas larger salt fractions moved the designs downward to the region where CTC was more negative but k_∞ became smaller. The same analysis laid out earlier for solid pin designs regarding the effect of leakage on k_∞ also applies here.

The effect of enrichment on the performance of an FHR was not straightforward. At low enrichment (around 5 wt%), the designs tend to have low k_∞ and small magnitude of CTC. Then, the performance improved in both k_∞ and CTC as enrichment increased (at about 12.5 wt%). At higher enrichments (up to 20 wt%), the core performance improved further with some cases becoming close to the optimum frontier but the effect on further CTC improvement saturated. In summary, the optimum frontier of the annular fuel FHR was composed of designs with thin annular fuel rings with P/D values greater than 2.8, and enrichment levels greater than 12.5 wt%. Salt fraction determined where along the optimum frontier the reactor was positioned.

6.3.2 Plate Type Fuel Designs

4842 plate type FCM fuel unit cell cases using NaF-ZrF_4 coolant were simulated with Serpent. The BOL CTC- k_∞ performance domain of the plate type model was again formed triangle, with a maximum k_∞ value of 1.40263 ± 0.0002 and a most negative CTC of -2.0 ± 0.1 pcm/K. There were 926 designs in this domain. P/D was again determined proximity of a case to the optimum frontier. However, having the right P/D value was a necessary but insufficient condition for a plate type FHR design to reach the frontier. The combined effect of enrichment, SF and plate thickness also played an important role in determining the core performance. Figure 6-17 plots the CTC-k_∞ performance domain for the plate type fuel unit cell models with P/D ranging from 3.6 to 5.2, fuel meat half thickness smaller than 1.23 cm with the smallest considered value being 0.46 cm, and enrichment levels between 17.5 wt% and 20 wt%. Models outside of this range fall outside the feasible domain and are therefore not shown.

Similar to pin type FHR, plate type models with different salt fractions occupied different regions of the performance domain: small salt fraction pushed the reactors to the left boundary of the domain and large salt fractions drove the designs up towards the upper right corner. This

is seen in Figure 6-17 a). Also, similar to the annular type designs, the plate type FHR unit cell models did not show significant performance sensitivity to P/D as long as it was greater than 3.6. On the other hand, unlike the pin type FHRs, the plate type designs reached the optimum frontier only when fuel enrichment was above 17.5 wt%. No significant difference in neutronic performance was observed between 17.5 wt% and 20 wt% enriched models, as can be seen from Figure 6-17 b).

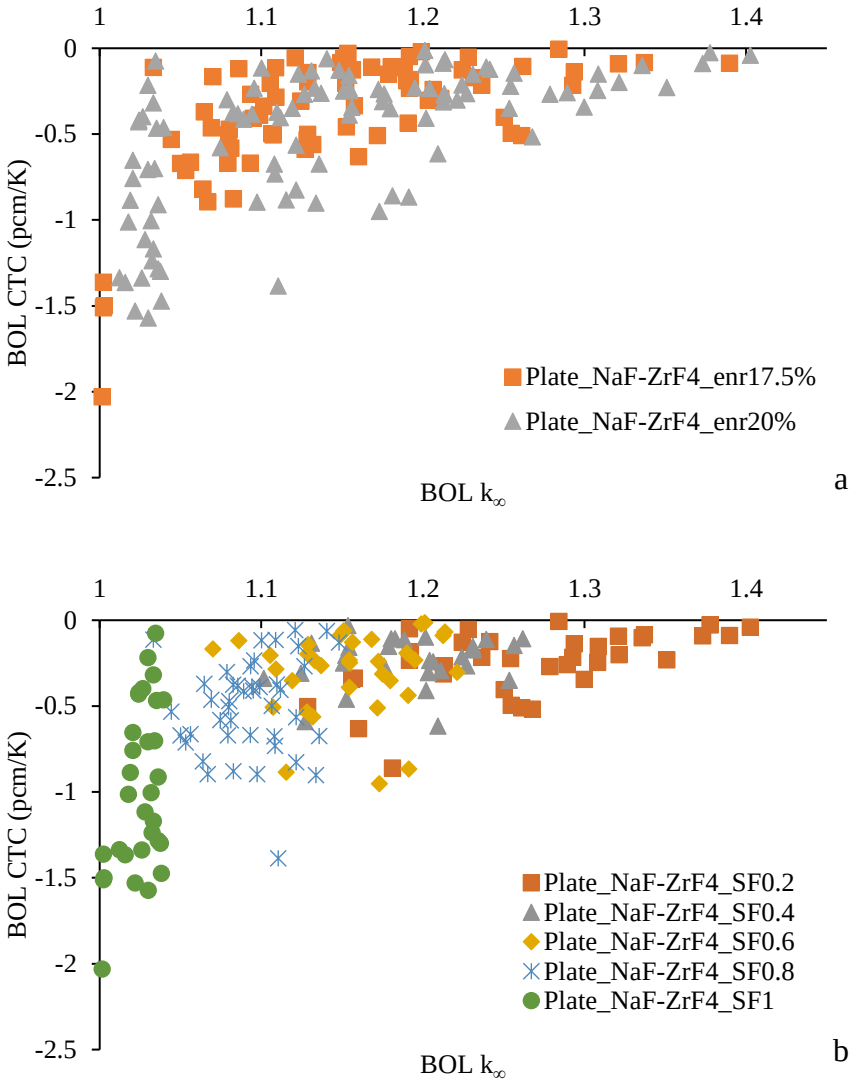

Figure 6-17. BOL CTC vs k_∞ performance domain a) (up) grouped by enrichment b) (down) grouped by SF for Plate FCM fuel NaF-ZrF_4 cooled FHR

6.4 Unit Cell Models Neutronic Performance Domain Summary

For solid pin models, regardless of the fuel and coolant material choice, the neutronic performance had greatest sensitivity to P/D: designs within specific ranges of P/D values performed the best in maximising k_∞ and minimising CTC and form the optimum frontiers. This is because the fuel pin dimension was fixed in the solid pin models, and the P/D directly translated to the moderator to fuel volume ratio. This, on the other hand, was not true for annular pin and plate type fuel designs, where fuel dimensions varied for each P/D. Therefore, for these models, there was no strong or clearly identifiable relationship between the models' P/Ds and their neutronic performance. Instead, the combined effect of P/D and fuel dimensions (which translated to moderator to fuel volume ratio) determined the performance.

For all models, a trade-off between k_∞ and CTC was clearly observed, which was predominantly governed by the models' SF. Fuel enrichment also affected the CTC-k_∞ performance of a design, although this dependence was slightly weaker. It also varied for different fuel forms: solid pin designs saw more negative CTCs with lower reactivity when using lower fuel enrichments, and greater k_∞ values were seen with less negative CTCs only when using higher enrichments. In fact, fuel enrichment of a solid pin model had very similar effect on the core performance as salt fraction. For annular pin and plate type fuel models, the enrichment moved the points in the CTC-k_∞ space collectively: only relatively higher enrichments allowed the designs to fall within the neutronically feasible domain.

For all models, the feasible CTC-k_∞ domains were triangular shaped, and the optimum frontier for each was a curve that connected the design with the most negative CTC (lower left corner of the space) and the design having the highest k_∞ (upper right corner of the space). The degree of curvature of these frontiers was relatively small and, given the level of tolerable errors of the results reported here, could be approximately represented by a straight line. To better illustrate the relative positions of the different models in the CTC-k_∞ space, Figure 6-18 plots the representative optimum frontiers for all design streams. Again, it shall be noted that if considering leakage and other neutron losses, these dashed lines would shift leftwards. Dashed lines in Figure 6-18 connecting solid markers were the approximated optimum frontiers for solid pin models; annular pin models were represented by hollow markers and the plate type FHR was represented using a solid '-' marker. The figure shows that FLiBe allowed the designs to achieve higher k_∞ and more negative CTCs compared with FLiNaK for all models and fuel materials, and FCM only outperformed UC in models using annular pins. Comparing the nine

different design streams, UC and FCM solid pin models with FLiBe coolant outperformed the rest, whereas the annular pin models with UC and FCM fuel, and solid FCM fuel pin models showed the worst performance among all when using NaF-ZrF_4 coolant.

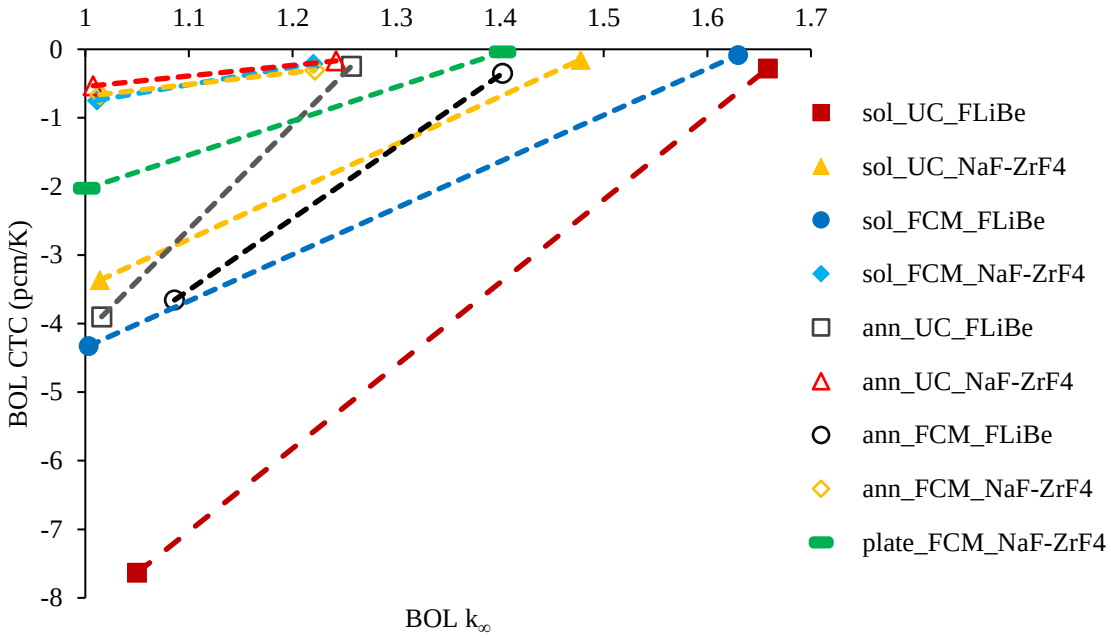

Figure 6-18. BOL CTC vs k_∞ performance optimum frontiers for all selected design streams

By examining Figure 6-18, four design families were selected for further analysis. Firstly, the best overall design streams among the nine studied, the solid UC fuel with FLiBe coolant was selected. Secondly, the best FCM fuel model, the FLiBe cooled solid FCM pin was selected because of the robustness of the fuel form and associated safety benefits. Thirdly, the best annular fuel design, the annular FCM FHR cooled with FLiBe was selected because it showed promising thermal-hydraulic performance and allowed higher power uprate. Although UC fuel could potentially grant the annular pin FHRs even greater power uprate, it was discovered that all neutronically feasible UC fuelled annular pin FHRs (i.e., k_∞ greater than one and negative CTC and BC throughout burnup cycle) had very small fuel thickness of 0.1 to 0.2 cm. The manufacturability and structural integrity of such thin fuel is uncertain and therefore the design option was abandoned at this stage. Finally, the best performing NaF-ZrF_4 design, the one with solid UC pin was selected as a backup option to the mainstream FLiBe cooled FHRs.

Chapter 7 Unit Cell Model Depletion Analysis

Depletion calculations are performed for the four selected designs in this chapter to obtain their discharge burnup and evolution of the two reactivity coefficients, i.e., CTC and DC, with burnup. With the depletion data obtained, instead of maximising BOL k_∞ and minimising CTC, this chapter seeks to maximise the BU/e, which correlates well with fuel cycle costs, [28][43] Limits on CTC, DC and discharge burnup are imposed during the design optimisation.

7.1 Unit Cell Models Depletion Analysis

Without depletion analysis, judgements on the reactor's economic and safety performance would be incomplete and unconvincing. To incorporate the fuel cycle economic considerations into the analysis, BU/e was adopted as a performance metrics. This ratio represents the amount of economic gain from the reactor's electricity production (which is proportional to burnup) per unit of fuel cost (which is approximately proportional to fuel enrichment) and should therefore be maximised. The assembly (represented by unit cell models) CTC and DC were obtained at several stages along the depletion. Reactivity coefficients should be kept below zero throughout the cycle were therefore used as designs constraints, while the BU/e was the optimisation objective. Besides the reactivity coefficients, a limit on burnup was imposed as fuel and cladding materials could only withstand certain amount of irradiation before their mechanical properties deteriorate significantly.

All burnup calculations were performed in Serpent with eleven depletion time-steps. A linear power rating of 18000 w/cm, which is roughly three times that of the Torness AGR, was used. The power rating value was conservatively selected as the previous thermal-hydraulic analyses showed that the solid pin design could achieve much greater power uprate from AGR' power level. All models were depleted up to 80 MWd/kg. The predictor corrector option in Serpent was turned on for better accuracy in calculation of the number densities of the materials at each burnup step. The first four steps were chosen to be short (0 MWd/kg, 0.5 MWd/kg, 1 MWd/kg and 2 MWd/kg) to correctly capture the Xenon build up at reactor start up. The k_∞ and CTC at each step were obtained by perturbing the coolant temperature and density around their nominal values. The reactivity (ρ) at each point was calculated from the k_∞ value. To save computational cost, the DC of the reactors were calculated at 6 depletion steps, i.e., at every other burnup step of the nominal condition depletion calculation. In order to obtain BU/e, the discharge burnup must be calculated for all models. Assuming an on-power refuelling scheme for the FHR, the discharge burnup of the reactor would be the twice that of a once depleted core according to

Linear Reactivity Model (LRM) [62]. However, the depletion curve for each FHR had different shapes (could be concave or convex), especially when using different fuel and salt materials. LRM might therefore overpredict or underpredict the actual discharge burnup. The discharge burnup values were estimated as follows: for each design, second order polynomial regression was performed on the k∞ vs reactivity data using the numpy.polyfit function in Python. When fitting the curves, the first three points were discarded since the Xenon build-up distorts the beginning of the depletion curve and would introduce large errors in the fitted polynomial if included. Then, secondary derivative of the fitted polynomial was calculated. A positive secondary derivative suggested that the curve was convex (or concave upwards), and a negative secondary derivative suggested a concave (concave downwards) depletion curve. To be conservative, the discharge burnup for reactors with convex depletion curves were estimated by doubling the burnup of a single-batch core. This underestimated the discharge burnup as the fuel reactivity loss became progressively smaller with burnup in these reactors. The designs with concave depletion curves had progressively larger reactivity loss with burnup. For these FHRs, an integration was performed for the fitted depletion polynomial curve. The discharge burnup of the fuel was calculated as the point at which the core net excess of neutrons became zero, i.e., negative reactivity in the depleted fuel was fully compensated by the positive reactivity of less depleted fuel in the core.

It must be pointed out again that all Serpent models assumed zero leakage and the absence of control rods. Therefore, all reactivity values reported in this thesis would be overestimated. Caution must be taken to analyse any value that lies around the zero-reactivity boundary.

7.1.1 Solid UC pin FLiBe Cooled FHR

The previous chapter suggested that the solid UC pin models with FLiBe coolant reached the BOL optimum frontier with P/D values ranging from 4 to 6.4. Although realizing that leakage and parasitic absorption would impose further penalty on the reported reactivity values, without performing calculations with real whole core models, all designs that had negative BOL CTCs and positive BOL reactivity values (156 in total) are analysed in this chapter for conservative reasons, to perform depletion calculations in Serpent. Figure 7-1 plots the depletion curves (ρ vs burnup) for all these designs. The number of neutron histories used for each depletion step were kept the same as in the BOL analysis presented earlier, resulting in similar ranges of statistical errors of ~ ± 20 pcm on k_∞. Majority of the designs had convex depletion curves. The curvatures for these curves were not significant and the gradients for all were very similar.

This suggested that the BOL k_∞ was indeed a good indicator for discharge burnup and that selecting the designs from the BOL optimum frontier was a reasonably good approach to narrow down the design domain.

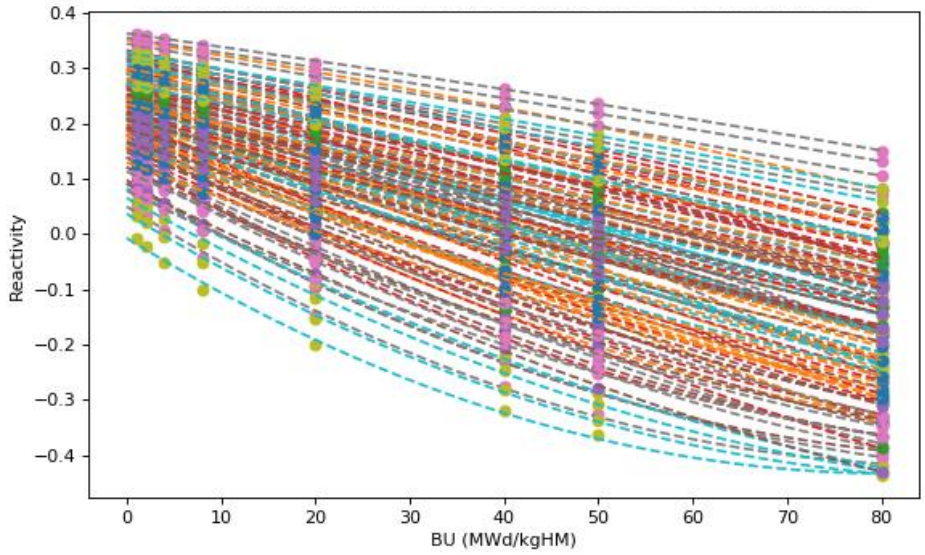

Figure 7-1. Depletion curves for all selected solid UC pin FLiBe cooled unit cell models

It was noted that the models with convex depletion curves were those that had lower BOL k_∞ values and the ones with greater BOL k_∞ have linear or slightly concave depletions curves. The cases with low BOL k_∞ had smaller enrichment and weak moderation (large salt fraction), which resulted in a faster spectrum and the excess reactivity was lost at a faster rate due to smaller U235 fission cross-sections in these spectra. However, Pu in these cases was built up more rapidly due to stronger resonance absorption in U238 with the spectrum hardening. This introduced positive reactivity (slows down the reactivity loss with burnup) at later stages of fuel burnup. The same argument could be applied in reverse to explain why the well thermalised designs with high BOL k_∞ values have linear or concave depletion curves.

The FHR was proposed to be refuelled on-power, so the core will contain a mix of assemblies at different stages of depletion. The core CTC should then be equal to the weighted average of the reactivity feedback effects of all the fuel assemblies. As discussed earlier, this means that an increasing CTC with burnup would pose more stringent requirements on the BOL CTC as

the high burnup assemblies would push the core average CTC to be less negative (or even positive) than the assembly BOL CTC value. On the other hand, if the CTC decreases with burnup, the BOL CTC requirement can be relaxed as the depleted fuel would make the core CTC more negative than the BOL CTC of individual assembly. In this case, a small-magnitude positive CTC of fresh fuel assemblies can be allowed.

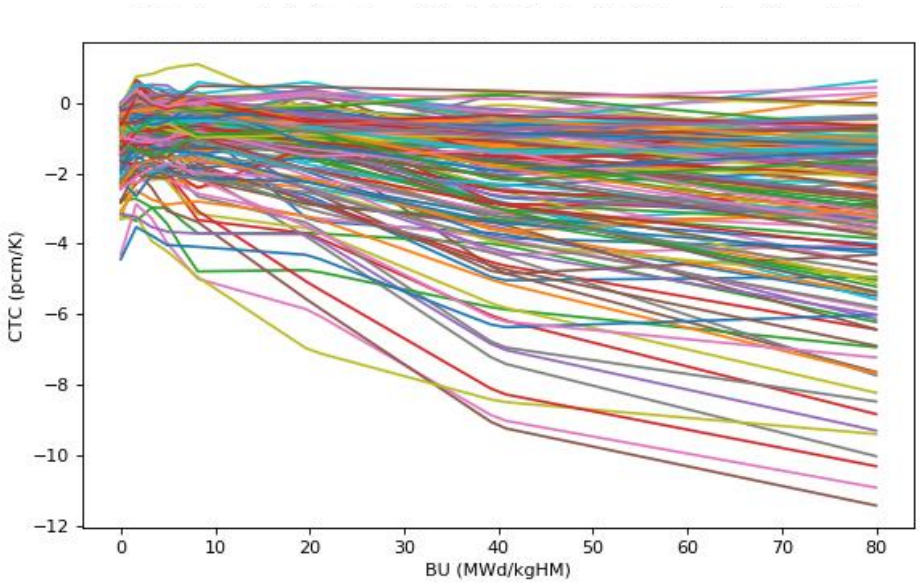

Figure 7-2. CTC behaviour with depletion for solid UC pin FLiBe cooled unit cell models

Figure 7-2 shows how CTC behaved with depletion for solid UC pin FLiBe cooled reactors. Despite some statistical fluctuations (on the order of 0.1 pcm/K compared to a second order polynomial fit of the curves, excluding the first few points during Xenon build up), a general decreasing trend was seen. This was possibly because neutron spectrum became softer with burnup, and there was greater U238 resonance absorption with spectrum softening since there were more thermal neutrons to be shifted to the resonance range when moderation was lost. Resonance absorption in Pu isotopes may also contribute to this effect. However, 60 out of the 156 analysed cases showed positive marginally CTCs at some point along the burnup and some designs showed increasing CTCs as it reached 80 MWd/kg. Therefore, without explicitly calculating the core average CTC for each design, a margin should be added to the BOL CTC constraint.

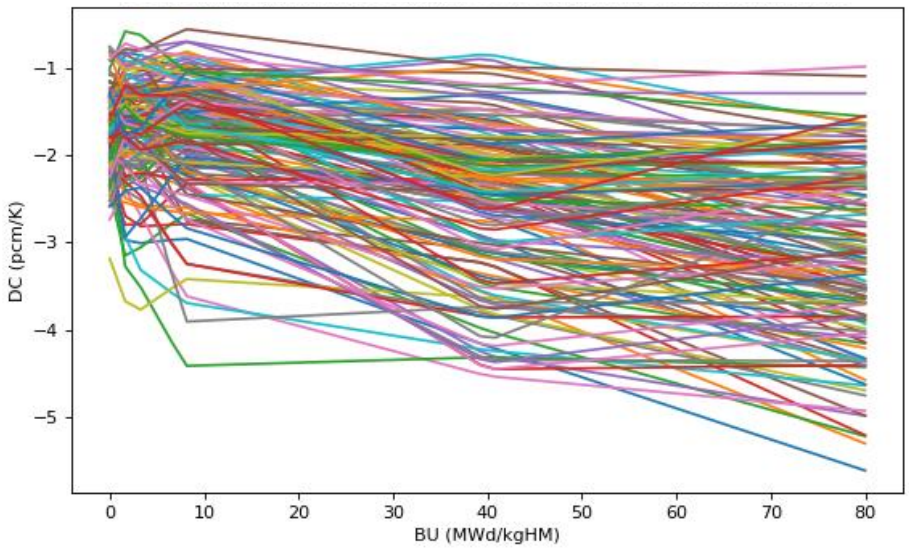

Figure 7-3. DC behaviour with depletion for solid UC pin FLiBe cooled unit cell models

The depletion behaviour of DCs with burnup for the 147 designs, as plotted in Figure 7-3 also showed decreasing trend starting from negative BOL DC values. This is because at later stages of the cycle, absorption of neutrons by U238 was increased, due to reduced competition with gradually depleting U235. No design among those analysed was found to have positive DC at any point through the cycle. However, some designs showed increasing DC trend after 40 MWd/kg burnup. Therefore, a margin was also imposed on BOL DC requirement in the later design optimisation for conservatism.

Figure 7-4 plots the BOL CTC against BU/e. This figure resembles the CTC- k_∞ plots shown in the previous section, again confirming that the BOL k_∞ is a good indicator of the reactor's BU/e. On this plot an optimum frontier can be identified that connects the designs with the largest BU/e and negative CTCs. When moving along the frontier, better fuel cycle economics could only be reached by sacrificing the safety performance. It was found that near the upper right region of the plot, the optimum frontier was relatively flat, meaning that a small increase in CTC could result in a significant economic performance enhancement. Unfortunately, these cases had only marginally negative CTCs. As discussed earlier, a margin on CTC limit was imposed, which is illustrated by the dashed blue line on Figure 7-4. Similar relationship between a reactor's DC and BU/e was observed as shown in Figure 7-5. The design with maximum BU/e that lie on or just below the limiting lines of CTC and DC were selected as the

best neutronic design. The CTC limit was more restrictive than DC limit. A chosen constraint of -1 pcm/K on BOL CTC suggested a best design (blue marker) reaching a BU/e value of 12.8 MWd/kg. The limit of -1 pcm/K, while not being too conservative, left a reasonable margin to accommodate statistical errors on the core average CTC and DC, which was on the order of ~0.2 pcm/K, and account for occasional positive trends of CTCs with burnup, all of which did not exceed 0.4 pcm/K) as shown in Figure 7-2.

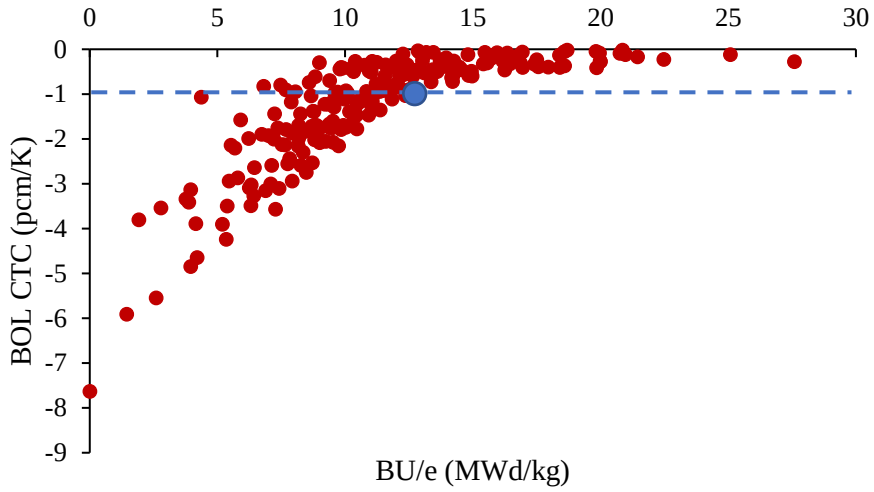

Figure 7-4. BOL CTC vs BU/e performance domain for solid UC pin FLiBe cooled models

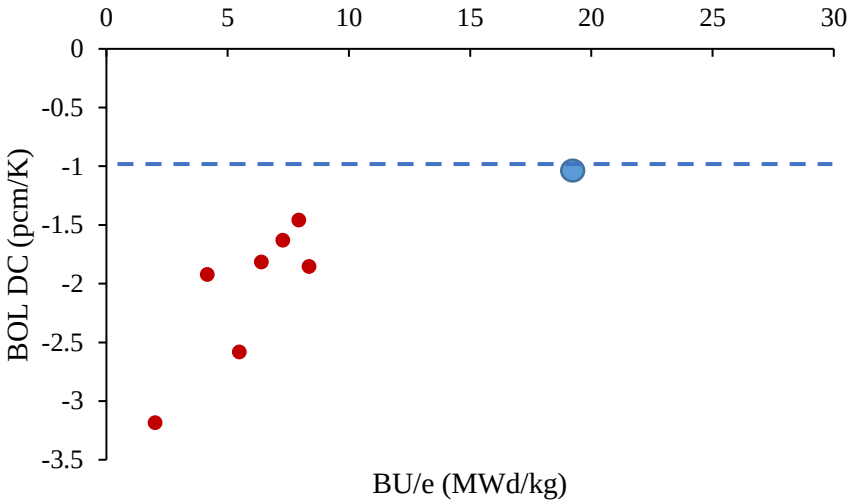

Figure 7-5. BOL DC vs BU/e performance domain for solid UC pin FLiBe cooled models

Figure 7-6 plots the BU/e ratio for the analysed cases against their discharge burnups. Designs with different enrichment levels are marked with different coloured markers. As expected, higher enrichments led to greater discharge burnups. The achievable BU/e also showed an increasing trend with higher enrichment levels. The 5 wt% enriched design reached a maximum of 92.9 MWd/kg burnup with a BU/e of 18.6 MWd/kg, whereas the 20 wt% enriched case can reach an incredibly high burnup of 552MWd/kg with BU/e of 27.6 MWd/kg. Therefore, by choosing a higher enrichment level, better theoretical economic performance can be achieved considering only the BU/e as a performance metric.

Unrealistically high burnups were predicted for some of the designs (up to ~ 500 MWd/kg). These values were obtained using extrapolation from the 0 to 80 MWd/kg depletion data and therefore unreliable. Also, the in-core time of the fuel is often limited by the fuel and/or the cladding's material integrity under irradiation. High burnup could result in deformation of the pellet, fission gas release, loss of the cladding ductility etc. The current nuclear reactors in the U.S. are limited to a peak burnup of 62 MWd/kg. Efforts have been made by the nuclear industry to raise the limit to 75 MWd/kg for traditional fuels. [63] Although FCM fuels were designed to accommodate more irradiation damage, the actual burnup limit is yet to be experimentally confirmed. UC, like UO_2, is also a ceramic, and such a high level of burnup is likely to be unachievable for these fuels even if SiC cladding is used.

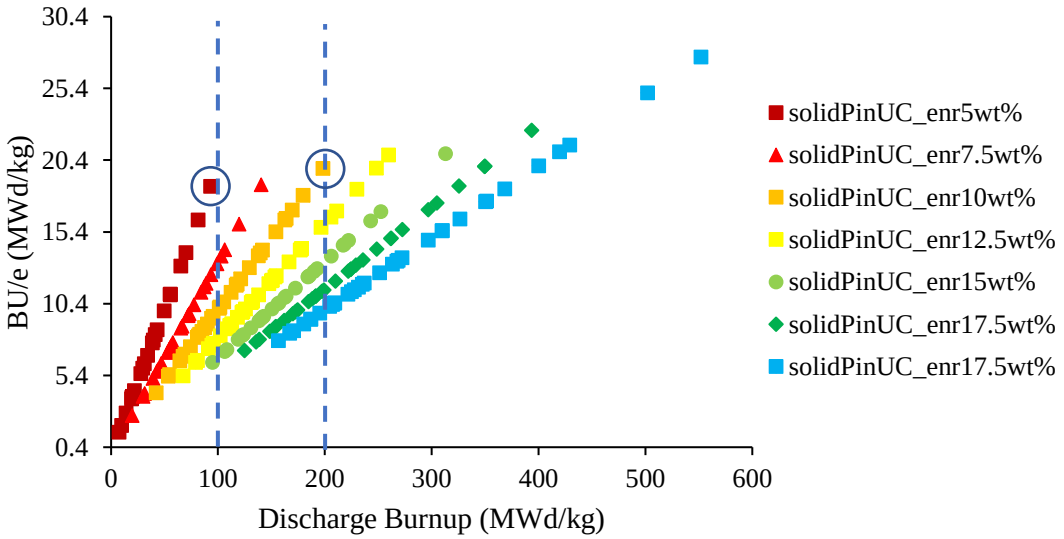

Figure 7-6. BU/e vs burnup for solid UC pin FLiBe cooled FHR with different enrichments

Several vertical dotted lines are shown in Figure 7-6 to demonstrate how possible fuel material burnup limitations can impact the design decisions. The designs that lie on or left side of these lines are considered practical under the corresponding assumption of maximum burnup constraint. For the five hypothetical burnup constraints, the corresponding best designs are circled in Figure 7-6. For example, if the fuel could tolerate up to 100 MWd/kg burnup, a 5 wt% U235 enrichment shall be used to achieve the best fuel cycle economics. Increasing enrichments beyond current AGR and LWR level would seem unnecessary if aiming only for maximised BU/e. One could argue that the BU/e vs BU curves for each enrichment level could be theoretically extended by choosing a larger geometrical design space, in which case a lower enrichment should be chosen for a certain burnup limit. For example, assuming a 200 MWd/kg burnup limit, the 7.5 wt% enriched FHR could potentially reach greatest BU/e than the circled 10 wt% enriched FHR with orange square marker. However, this is unlikely since the design space covered in this project is already large enough covering up to P/D ratios of 6.4. Again, depletion calculations were carried out assuming zero leakage and neutron loss to control rods, etc. Therefore, discharge burnup values as well as BU/e were all overestimated. The leakage effect would be more significant for less moderated cores (points near the origin) where neutrons have greater energy and thus longer mean free path. It would be somewhat compensated however by generally smaller parasitic absorption. In realistic cases, all points on Figure 7-6 would likely to be shifted towards the origin.

The three constraints (CTC, DC and BU) worked collectively to narrow down the design domain. Assuming a limit of -1 pcm/K on both CTC and DC and a burnup limit of 100 MWd/kg for the UC fuel, five best designs are tabulated in Table 7-1 in order of decreasing BU/e. For all five, CTC showed downward trends with depletion, therefore the -1 pcm/K limit was conservative. It was noted that the fifth best design had 100 wt% SF, which is essentially PWR-like. It also found that relaxing the BOL CTC constraint to -0.5 pcm/K allowed only a small increase in BU/e to 11.83 MWd/kg, as the burnup became the more restrictive constraint. The selected five solid pin designs delivered similar level of fuel cycle economics compared with the current fleet of LWR, which normally achieves BU/e of around 10 MWd/kg.

In addition to the best overall design stream of UC solid pin case with FLiBe coolant, three alternative designs streams were selected in the previous chapter: 1) solid FCM pin with FLiBe, 2) annular FCM pin with FLiBe and 3) solid UC pin with NaF-ZrF_4 coolant. All three alternative design streams were found to share similar characteristics of depletion behaviour with the UC fuelled FHRs discussed earlier. Although with different performance levels,

almost identical trends as those presented in Figure 7-1 to Figure 7-5 were seen for the three alternative FHR designs. To avoid repetition and confusion, these figures are included in Appendix F.

Table 7-1. Specifications of best FLiBe cooled UC solid pin designs

Ue5 (wt%)	*P/D*	*SF (wt%)*	*BU/e (MWd/kg)*	*BU (MWd/kg)*
5	4.4	20	11.1	55
7.5	5.6	80	9.7	73
7.5	4.8	60	9.6	72
10	5.2	80	9.5	95
10	6	100	8.7	87

7.1.2 Alternative Design - Solid FCM pin FLiBe cooled FHR

The solid FCM pin case had very similar depletion behaviour only with slightly poorer overall performance compared with UC fuel cases. Optimum frontiers were similarly identified in CTC-BU/e space and the DC-BU/e space. Considering the limits of -1 pcm/K on both BOL reactivity coefficients, the maximum achievable BU/e was 9.5 MWd/kg, which was again restricted by the CTC limit. The BU/e vs BU plot also shows that different fuel burnup limits could lead to different fuel enrichment choices. For example, ignoring the CTC and DC limits, with a hypothetical burnup limit of 200 MWd/kg, which is potentially achievable for FCM fuels, the best design had an enrichment of 20 wt%, reaching a discharge burnup of 326 MWd/kg with a BU/e of 16.8 MWd/kg. A smaller burnup limit of 200 MWd/kg suggested a best design reaching a BU/e of 12.6 MWd/kg with an enrichment of 15 wt%.

Combining all three design limits: -1 pcm/K for both CTC and DC and an allowable burnup of 200 MWd/kg for the FCM fuel, five best designs are summarised in the Table 7-2. For all five selected best designs, the CTC showed downward trend with depletion, therefore the -1 pcm/K was conservative. Again, two out of the five designs required zero graphite, becoming a PWR-like reactor. The highest discharge burnup of the five was 166 MWd/kg suggesting that the CTC was a more restrictive constraint on the design.

Table 7-2. Specifications of best FLiBe cooled FCM solid pin designs

Ue5 (wt%)	*P/D*	*SF (wt%)*	*BU/e (MWd/kg)*	*BU (MWd/kg)*
17.5	2.4	60	9.5	166
15	2.4	60	9.4	141
20	2.8	100	8.8	175
17.5	2.8	100	8.5	149
20	2.4	80	8.1	163

7.1.3 Alternative Design - Annular FCM pin FLiBe Cooled FHR

Unlike the previous two solid pin design streams, the annular FCM pin fuel had concave depletion curves. This was possibly due to more efficient Pu build up and thus slower U235 depletion in the early stages of burnup. The annular pins had large surface to volume ratios; therefore, the self-shielding effect was weaker. The Pu build-up rate was much faster at BOL, and a relatively flat depletion curve was observed at early burnup. Later depletion stage saw increasing reactivity loss with burnup as fissile nuclides were depleted while Pu build-up was not sufficiently fast. CTC and DC all showed generally decreasing trends with burnup.

Table 7-3. Specifications of best FLiBe cooled FCM annular neutronic models

Ue5 (wt%)	*P/D*	*SF (wt%)*	*BU/e (MWd/kg)*	*BU (MWd/kg)*
20	5.2	80	3.9	77
17.5	5.2	80	3.4	60
20	4.8	100	3.2	65
20	5.2	100	3.1	61
15	5.2	80	2.9	44

By imposing the same limits of -1 pcm/K on both BOL reactivity coefficients, the maximum achievable BU/e value was identified to be 6.7 MWd/kg for the annular FCM pin with FLiBe coolant. This was again more restricted by the limit on CTC. The maximum discharge burnup achieved for this design stream was 246 MWd/kg, which is potentially achievable for FCM fuels. Considering a burnup limit of 200 MWd/kg without the reactivity limits, the best design was a 15 wt% enriched reactor reaching a BU/e of 11.9 MWd/kg. In addition to the three

constraints, a minimum fuel meat thickness of 0.5 cm was chosen for the annular pin FHRs. Considering all constraints together, the design recommendations are summarised Table 7-3. Five best designs are reported. All five had very large salt content, of which two has 100% salt fraction.

7.1.4 Alternative Design - Solid UC pin NaF-ZrF4 Cooled FHR

The solid UC pin with NaF-ZrF_4 showed similarly shaped depletion curves as the two solid pin designs: majority of the curves were convex with only few exceptions. DC also showed decreasing trend with depletion, but CTC for this design stream increased slightly with depletion. Out of the 45 analysed designs with best BOL performance, only 13 had negative CTCs up to 80 MWd/kg of burnup. Therefore, a larger margin must be imposed on the BOL CTC. With a more stringent constraint on the BOL CTC, the achievable BU/e was limited to very small values: a -2 pcm/K limit on the BOL allows the best design (12.5 wt% U235 enrichment) achieving only a BU/e of 2.3 MWd/kg with a discharge burnup of 29 MWd/kg. The burnup and the DC design constraints were both less limiting than the CTC constraint.

7.2 Unit Cell Depletion Analysis Summary

In summary, the solid UC pin with FLiBe coolant design stream had the best performance in terms of BU/e. the BOL CTC limit was the most restrictive among the three applied. With a relatively conservative limit of a -1 pcm/K on CTC, the UC solid pin FHR with FLiBe reached a BU/e of 11.06 MWd/kg, the highest among the four selected design streams and comparable to contemporary LWR fuel. The solid FCM pin design was selected in the previous chapter for its better accident-tolerance and potential for achieving higher burnup. Unfortunately, it was proven that the CTC constraint was more limiting than the burnup for these designs. A -1 pcm/K limit on the BOL CTC allowed the best case to achieve a BU/e of 9.5 MWd/kg, reaching a burnup of 166 MWd/kg. The annular pin design option using the FCM fuel was shown to have an attractive performance in terms of power uprate but it did not offer any advantage over the other three options in terms of neutronics. It reached a smaller BU/e (6.74 MWd/kg) compared with the solid FCM pin option under the same design constraints. However, thermal-hydraulic analysis suggested that it may achieve higher power densities and low capital cost which might compensate for its inferior fuel cycle economics. The best NaF-Zr_4 cooled design (with solid UC fuel pins) still underperformed the other three designs options using FLiBe: reaching only a BU/e of 2.3 MWd/kg with a discharge burnup of 29 MWd/kg. Nevertheless, NaF-ZrF_4 does not produce tritium and the discharge burnup was comparable to the current

fleet of AGRs so this design option had its strategic value. The top five best performing designs among all considered options are summarised in the Table 7-4 in which ranks them according to BU/e. The inner and outer radii of the annular fuel designs are omitted in this table.

Table 7-4. Specifications of best neutronic designs across all four selected design streams

type	*fuel*	*coolant*	*Ue5 (wt%)*	*P/D*	*SF (wt%)*	*BU/e (MWd/kg)*	*BU (MWd/kg)*
sol	UC	FLiBe	5	4.4	20	11.1	55
sol	UC	FLiBe	7.5	5.6	80	9.7	73
sol	UC	FLiBe	7.5	4.8	60	9.6	72
sol	FCM	FLiBe	17.5	2.4	60	9.5	166
sol	UC	FLiBe	10	5.2	80	9.5	95
sol	FCM	FLiBe	15	2.4	60	9.4	141
sol	FCM	FLiBe	20	2.8	100	8.8	175
sol	UC	FLiBe	10	6	100	8.7	87
sol	FCM	FLiBe	17.5	2.8	100	8.5	149
sol	FCM	FLiBe	20	2.4	80	8.1	163
ann	FCM	FLiBe	20	5.2	80	3.9	77
ann	FCM	FLiBe	17.5	5.2	80	3.4	60
ann	FCM	FLiBe	20	4.8	100	3.2	65
ann	FCM	FLiBe	20	5.2	100	3.1	61
ann	FCM	FLiBe	15	5.2	80	2.9	44
sol	UC	NaF- ZrF_4	12.5	4.8	100	2.3	29

One finding from Table 7-4 was that except the NaF-ZrF_4 cooled FHR, other selected reactors had rather high discharge burnups (44 MWd/kg ~ 175 MWd/kg) comparing with AGR: up to five-folds from AGR's discharge burnup. Unless these reactors operate at much higher levels of power than AGRs, on-load refuelling seemed unnecessary. Fortunately, power uprate can be fairly significant for these proposed FHRs. Also, it was found that solid FCM pin fuelled reactors required much smaller P/D than the rest. This could further give the design option an edge in terms of power maximisation and capital cost reduction.

Another interesting finding from the final design recommendation is that many of the best performing designs effectively had no graphite and rely entirely on salt coolant for moderation, i.e., a PWR-like, only with salt coolant. This opened up more design possibilities for the FHR, which had always been assumed to require some form of solid moderator. Although BU/e might not be directly comparable across different fuel options, as the fuel fabrication and post-processing costs would be different, the figure still conveys information about relative economic performance within each design option.

Chapter 8 Bringing Together Thermal-hydraulics and Neutronics

This chapter reports the results of SCOOP calculations for the design streams recommended from the neutronic analysis using relaxed dimensional constraints. The effects of P/D, SF and pressure drop on the reactor's maximum achievable power and LCOE is discussed using the data generated for the extended thermal-hydraulic design space to better understand ways to optimise the designs. The last part of this chapter suggests several optimised FHR designs that minimised LCOE by coupling thermal-hydraulics and neutronics. For the designs resembling less of an AGR, but rather being more PWR-like with 80 wt% or more salt fraction, a mapping of the thermal-hydraulic results to the PWR-like design space was also performed.

8.1 Revisiting Thermal-hydraulics with Extended Design Space

Homogenising the previous AGR-like thermal-hydraulic assembly models reported in Chapter 3, P/Ds of only 3.9 and 5 were covered with SF ranging from 18 wt% to 25 wt%, covering merely 30.6% of the P/D and 8.75% of the SF range in the neutronic models. To arrive at a more comprehensive design recommendations, the AGR-like FHR must have an overlapping neutronic and thermal-hydraulic design space. Ideally, same models used in the neutronic design search shall be used to perform thermal-hydraulic tests. However, the homogeneous unit cell model cannot be analysed with the subchannel solvers, which require detailed geometrical information to perform thermal-hydraulic and heat transfer calculations. Therefore, to ensure greater design space is covered without losing heterogeneity, assembly level model was again used with relaxed dimensional constraints. The new physical boundary was chosen to be area bounded by the graphite keys. By doing so, the volume of core graphite became an additional degree of freedom and a greater range of coolant-to-fuel-to-graphite ratio could be covered. Such models were created for the four strategically selected design streams.

Same as the models in Chapter 5.1, the assembly inner graphite sleeve radius ranged from 9.52 cm to 19.52 cm, exploring the entire possible volume between the graphite keys. A finer mesh of 0.5 cm was applied to the parameter space thanks to fast SCOOP calculations, producing models with 20 different inner graphite sleeve radii. For each fuel channel dimension, different numbers of fuel pins were assigned following the same rule described in Chapter 5.1: the fuel pins were arranged evenly in a circular lattice inside the fuel channel around the central tie rod. Starting from a minimum value of three, the number of rings of fuel pins was increased until

the gap between the adjacent fuel pins becomes less than 0.2 cm. The solid fuel pin preserved the AGR fuel dimensions, i.e., pin diameter of 1.45 cm with a cladding thickness of 0.038 cm and a gap thickness of 0.002 cm. The annular fuel pin dimensions were recalculated for each model: the outer radius of the pin firstly took the AGR solid pin dimension and increased gradually with a step of 0.02 cm until the gap between the pins became smaller than 0.5 cm. The fuel pin inner radius was then calculated using Equation 3.4 with an estimated K value of 1.1 so that the resulting annular fuel pin design would have similar internal and external coolant axial temperature rise. The gap and cladding dimensions were assumed to be the same as the solid pin fuel. If the inner radius calculated was greater than the outer radius, i.e., the design is physically impossible, or the resulting annular fuel ring had a thickness below 0.5 cm, the design was discarded. For each model, the core frictional pressure drop input for SCOOP's wrapper function increased from 50 kPa to 1000 kPa with a step of 50 kPa to identify the optimum operating condition.

For SODom calculations, the same set of LSSSs described in Table 3-4 was used apart from the maximum temperature limit for UC fuel. The previous fuel temperature limit imposed on the FHR was derived from the fuel temperature of the AGR under nominal operating condition. However, this is well below the maximum fuel temperature in current LWRs and the material temperature tolerance of the fuel is not fully taken advantage of in a low power density core like an AGR. Therefore, in the subsequent calculations, to further exploit the power uprate potential of the AGR-like FHR, higher temperature limits were chosen for UC fuel where a 500 °C margin was reserved below the material melting temperatures: the UC temperature limit was increased to 1875 °C (UC melting at 2375 °C). FCM fuel temperature limit was kept the same (1250°C) as in Table 3-4 as it was already limited by TRISO particle material performance. It was expected that the new LSSS would increase the allowable power for reactors that are most limited by UC fuel melting, which was mostly true when using solid pin fuel form.

It was realised that not all designs in the extended design space could produce physically meaningful SODom results. To illustrate this, the schematic plot of the operating domain is shown again in Figure 8-1. For better power conversion efficiency, point 5 on the constant T_{out} line in Figure 8-1 would be selected as the best design that offers maximised core power. This means that the reactor operates at a coolant outlet temperature of 700 °C. However, for a reactor with very large coolant volume and very small fuel volume operating at very small coolant flow rate might not be able to reach the coolant Re limit of 4000 even if the bulk coolant

temperature rise across the core is fixed at the target outlet temperature of 700 °C, which is the highest possible bulk coolant temperature considering the integrity of the structural components. This is essentially a zero-power reactor. Any increase in power would increase the coolant temperature difference across the core, further reducing the local Re number at reactor inlet. These designs, therefore, do not offer any thermal-hydraulic value and were excluded from the design space. To screen out such designs, a simple solver was introduced to SCOOP prior to exercising SODom to pre-estimate the minimum Re number assuming a very low core power of 50 MWt. If the resulting Re number was greater than 4000, the reactor can potentially reach a reasonable the power, and SODom calculation and system thermal-hydraulic design was carried out for the model; otherwise, the model was marked as a failed design, i.e., one that offers almost zero thermal power, and no further calculation was performed.

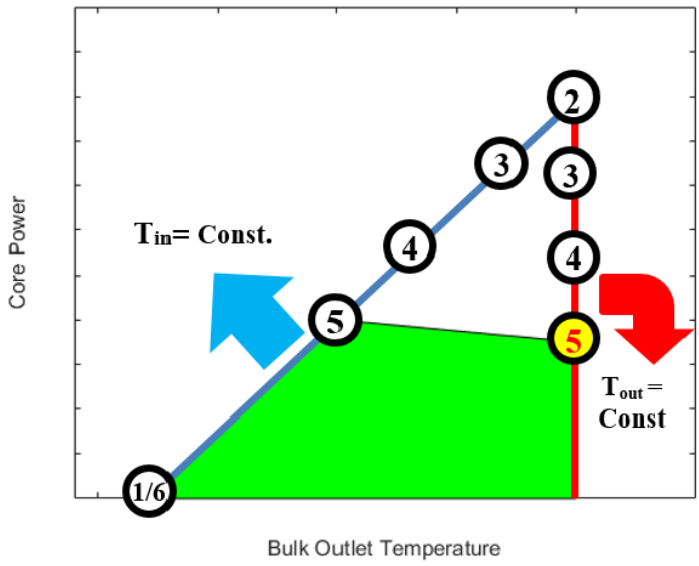

Figure 8-1. Schematic plot of operating domain using safety constraints.

Following the new geometrical and coolant flow constraints, SCOOP created and tested a total of 291 valid solid pin models with 5819 test cases (different operating conditions), and 288 valid annular pin models with 5760 test cases. As intended, the new thermal-hydraulic results covered a much bigger P/D and SF space. The solid pin models covered P/D ranging from 1.9 to 5.3 and SF ranging from 17 wt% to 74 wt%. The annular pin models covered a smaller P/D

space of (from 3.3 to 5.3) and SF ranging from 21 wt% to 61 wt%. Due to the presence of some fixed core graphite structures of the AGR, i.e., the graphite keys and channels, there was a theoretical upper limit of achievable SF. However, some of the neutronic models required SFs of greater than 80 wt%. To reach this level of SFs, the reactor needs to forgo the graphite keys and channels. Analysis of this possibility is laid out in last sub-section of this chapter.

8.2 Thermal-hydraulic Results in the Extended Design Space

SCOOP results for the new assembly level thermal-hydraulic models showed that the AGR-like FHR indeed proved to be economically desirable: all FHR models achieved power uprate from AGR level. The solid pin type FHR could reach power levels from 2555 MWt up to 56109 MWt. The solid pin type FHR had LCOEs as low as 28.6 £/MWh. The annular pin type FHR had power levels from 2853 MWt to 62344 MWt. The lowest LCOE seen for the annular pin type FHR was 28 £/MWh. The following subsections take the best neutronic design stream, i.e., the UC fuelled solid pin type FHR as a reference to study how the reactor design and operating condition affect the reactor's thermal-hydraulic performance and the resulting LCOE of the plant. It is expected that the analysis for the reference design can also be applied to other design streams. Similarities and differences between them are also discussed.

8.2.1 Effect of P/D and SF on Maximum Achievable Power

Figure 8-2 plots the maximum allowable power against P/D for the FLiBe cooled solid UC pin FHR with three different inner graphite sleeve radii at pressure drops of 50 kPa and 350 kPa. It was noticed that there is an asymptotic line for each coolant flow condition: at a pressure drop of 350 kPa, all three curves for different inner graphite sleeve radii almost overlapped across the whole P/D range; at 50 kPa, the curves showed a peaked shape: the reactor started at a smaller power level, which rose with P/D and eventually joined the other designs and forms one descending curve. This behaviour was seen across the whole design space. It was discovered that the points on the descending asymptotic curve represented reactors constrained by the maximum fuel temperature limit. These designs had very similar maximum allowable power despite having different assembly channel radii, or in other words, SF. For these reactors, using more fuel pins to reduce the average fuel temperature was the most effective way to achieve higher power. The ascending parts of the power vs P/D curves represent cases where the most restrictive safety limit was the minimum coolant inlet temperature limit, i.e., the coolant freezing or minimum Re limit. Since the temperature rise of the coolant was fixed for these reactors, with increasing pitch to diameter ratio, more power could be extracted as greater

coolant mass was used to carry the heat with larger coolant velocity. Increasing the graphite sleeve radius had similar effects. These reactors also benefited from greater coolant pressure drop to increase the maximum allowable power until the fuel temperature constraint became the most limiting, after which only small increase in maximum achievable power was seen with higher pressure drop.

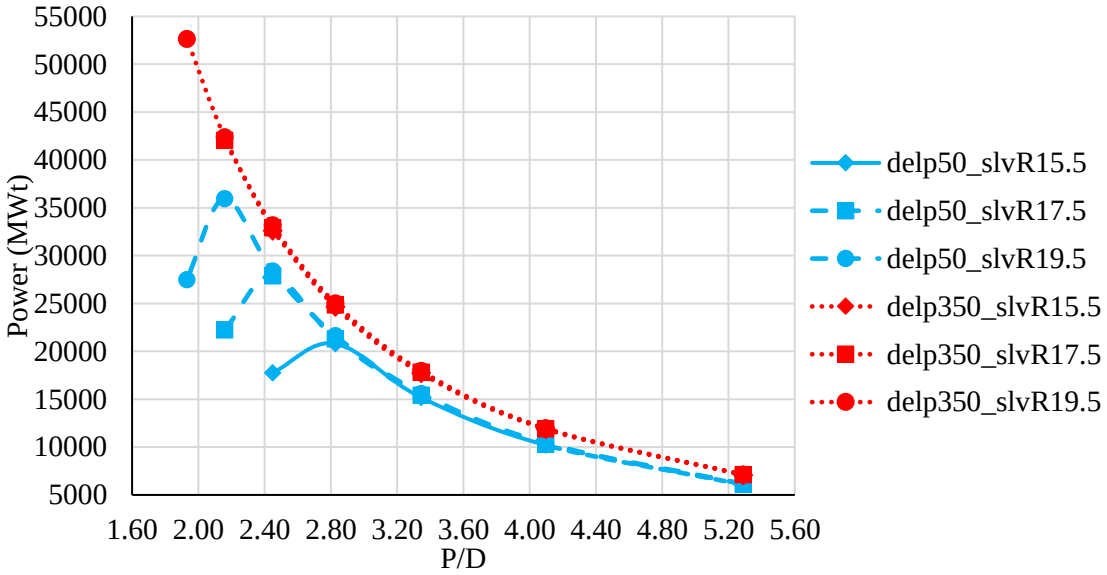

Figure 8-2. Effect of P/D on maximum allowable power for FLiBe cooled solid UC pin FHR

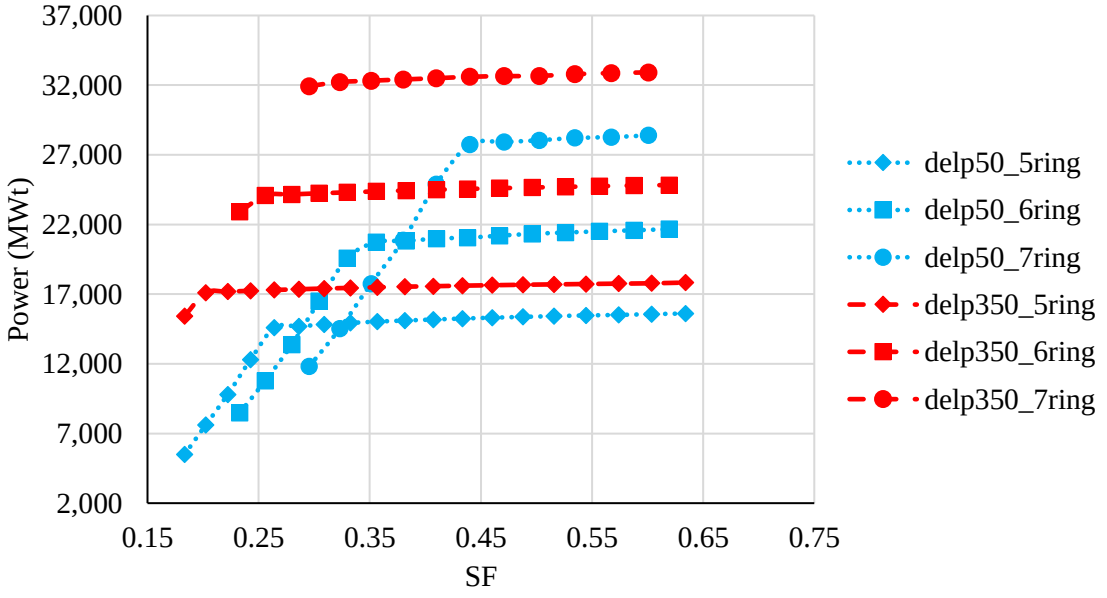

Figure 8-3. Effect of SF on maximum allowable power for FLiBe cooled solid UC pin FHR

Figure 8-3 plots the maximum allowable power for the 5, 6 and 7-ring solid pin FHRs (representing different SFs) at 50 kPa and 350 kPa respectively. The maximum allowable power for the FHR increased with SF and then plateaued. The initial increase in power level with increasing SF corresponds to designs that were limited by the minimum coolant inlet temperature. When the power increase resulted in the reactor reaching its maximum fuel temperature limit, greater coolant mass, i.e., larger SF, no longer helped with power uprate.

FCM fuelled solid pin FHRs had very similar behaviour of maximum power against changing P/D and SF as the UC fuelled reactors. However, for the same design and operating conditions, significantly lower power level was allowed by FCM fuel and the turning point at which the fuel temperature constraint started to limit the reactor occurred at much smaller P/Ds and SFs for FCM fuelled reactors. This is because the FCM fuel has much more limiting fuel temperature constraint and poorer heat transfer properties.

Unlike the solid pin fuel, which had fixed fuel dimensions across the entire design space, annular fuel pins were individually designed for each assembly configuration. This introduced an additional degree of freedom, i.e., the fuel pin thickness, which represented the thermal-resistance across the fuel pin. It was found that the majority of the annular pin designs were limited by the maximum fuel temperature constraint. For these reactors, the fuel plate thickness is a very crucial parameter in determining the maximum power achievable: with larger fuel plate thickness, less power is allowed and vice versa. Figures of how maximum allowable power behaves with changing P/D and SF and fuel ring thickness are included in Appendix G.

8.2.2 Effect of P/D and SF on LCOE

Figure 8-4 plots the LCOE of the same designs as those presented in Figure 8-2 against their P/Ds. Comparing with the power vs P/D curves in Figure 8-2, the LCOE vs P/D curves in Figure 8-4 show an opposite trend, confirming that greater powers indeed translated to lower LCOEs. Although more expensive heat transfer and pumping system was needed for greater power output, it is seen from the figure that the LCOE reduction effect from increased power outweighed the resulting increased variable cost. Another finding is that, unlike the maximum allowable power, which had very weak dependence on the inner graphite sleeve radii, i.e., the salt fraction, the LCOE of all reactors limited by the fuel temperature constraint changed with the inner graphite sleeve radii, which can also be seen in Figure 8-5. This demonstrates how, in addition to power level, the cost of pumping and heat transfer system contributes to the

LCOE of the power plant. The plot also suggests that it is worthwhile investing in larger pumps only when P/D is small.

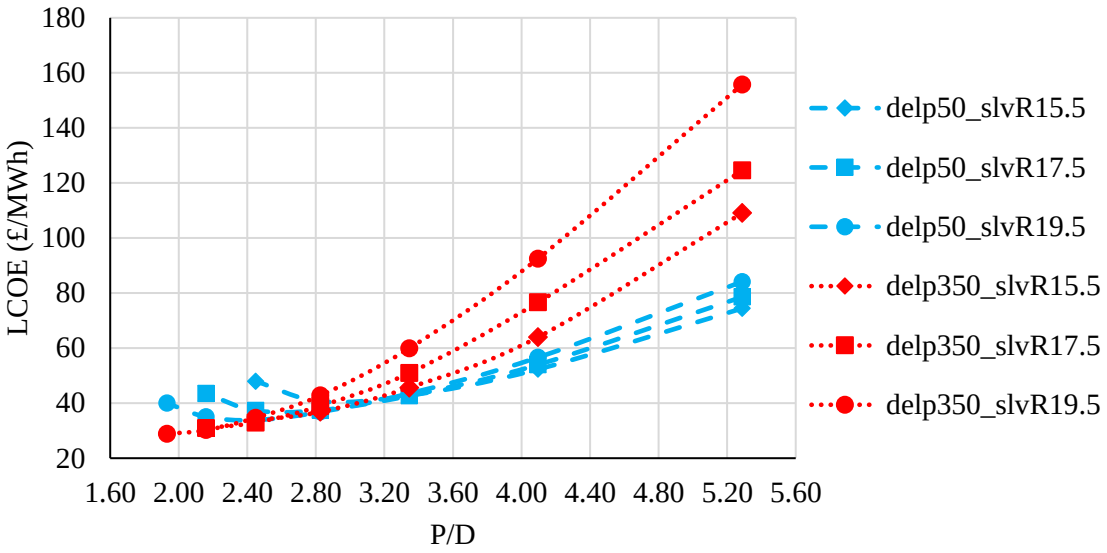

Figure 8-4. Effect of P/D on LCOE for FLiBe cooled solid UC pin FHR

Figure 8-5 plots the LCOE for the same designs as those presented in Figure 8-3, which had P/Ds (2.4 to 3.3) corresponding to the middle part of Figure 8-2 and Figure 8-4, for the entire SF range. For the reactors operating at 350 kPa, the LCOE firstly decreased with salt fraction and then levelled off and started to rise. Referring to the curves in Figure 8-2, the initial lowering of LCOE corresponded to power increase with SF for designs that were limited by coolant temperature constraint. However, as the maximum achievable power levelled off after the maximum fuel temperature limit was reached, the LCOE continued to fall with SF before the trend was reversed. This behaviour was more pronounced for the designs with more fuel pins, i.e., smaller P/D. As the number of fuel pin increased, e.g., from 5 to 7, the decreasing trend of LCOE stopped at a larger SF, then the LCOE increased more gradually. For designs operating at a lower pressure drop (50 kPa), reduction in LCOE was seen across the entire SF range up to ~0.75, although the rate of cost reduction was decreased with increasing SF. Again, similar to the curves with 350 kPa pressure drop, the trend of cost reduction with increasing SF continued after the reactor power levelled off. The reactors with more fuel pins (smaller P/D), e.g., the 7-ring design, saw a stronger cost reduction and eventually reached lower LCOEs than ones with fewer fuel pins, e.g., the 5-ring design. For these designs, it could be expected that further increase in SF might result in even lower LCOEs. For reactors with greater P/Ds, one

could expect that the cost reduction, similar to the ones with higher pressure drop, would level off and an increasing trend with SF would be seen. It was further found that for designs with the largest P/D explored (~4.5), the LCOE started to increase with SF at very small SF values, and the rate of increase with SF was very high. Therefore, how SF affected the LCOE depended on the P/D and pressure drop of the reactor.

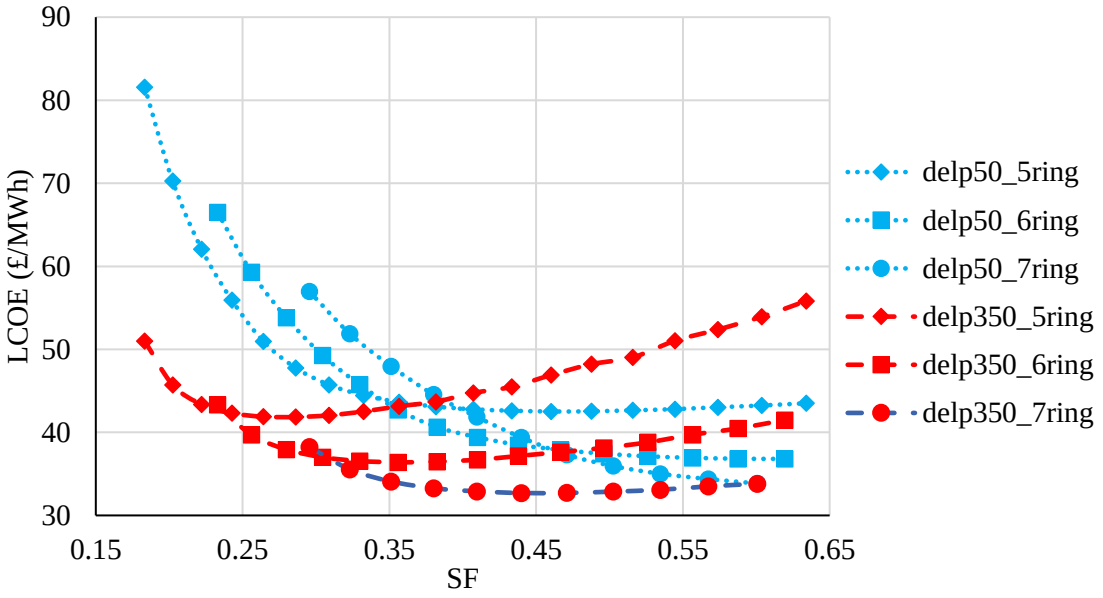

Figure 8-5. Effect of SF on LCOE for FLiBe cooled solid UC pin FHR

There are competing factors to explain the behaviour of LCOE with SF. When the reactor design is limited by the coolant inlet temperature, which normally happens at small P/D, small pressure drop and/or small SF, increasing SF results in the reactor reaching higher power since more coolant mass could be pumped through the core with the same coolant pressure drop and temperature difference. Higher power contributes to the reduction of LCOE, while higher pumping power and heat transfer area is required to pump the coolant and transfer the heat. It is apparent from Figure 8-5 that for the designs most limited by coolant inlet temperature or minimum Re limit, the cost reduction effect from power uprate dominated the increased heat exchanger and pump cost and drove down the LCOE.

After coolant inlet temperature limit was no longer at play and the fuel temperature limit dominates, which could be achieved by increasing P/D, or more effectively by increasing the SF and/or pressure drop, the power hardly increased with SF, but the coolant temperature

difference across the core started to decrease. Since the core outlet temperature was fixed at 700 ºC, the core average temperature rose with SF. On one hand, this means that heat was transferred from the primary loop to the intermediate loop at a higher average temperature, thereby reducing the required heat exchanger size and cost. On the other hand, the margin left for fuel temperature rise was smaller, limiting or even lowering the power uprate and cost reduction potential. Also, the pumping power requirement continued to increase with SF. This is because at a given power level, with the reduction of coolant temperature difference across the core, the coolant mass flow rate increases since the specific heat capacity of the salt has only weak temperature dependence, and the pumping power is proportional to mass flow rate and pressure drop, which was fixed for each curve.

The LCOE of the FCM fuelled solid pin designs also showed similar behaviour with changing P/D and SF to its UC fuelled counterparts, although being much higher due to less power output allowed by the FCM fuel. For the annular type FHRs, again, the LCOE also depended heavily on the fuel thickness: smaller fuel thickness allowed the reactor to achieve greater power and, therefore, lower LCOE. The effects of P/D and SF on LCOE were similar to those found for solid pin FHRs but were relatively weaker comparing with the effect of fuel thickness on LCOE for these reactors. Figures showing how LCOE of annular pin FHRs changes with P/D, SF and fuel thickness are included in Appendix G.

8.2.3 Effect of Core Pressure Drop on Maximum Achievable Power and LCOE

SCOOP reported the optimum core pressure drop for a given design that minimised its LCOE, and a large range of operating conditions was tested for the reactors while doing so. This data provided very useful information on how the Δp affects the reactor's economic performance. Figure 8-6 and Figure 8-7 plot the maximum achievable power and LCOE against different pressure drops for the solid pin 5, 6, and 7-ring FHRs with two inner graphite sleeve radii of 14.5 cm and 19.5 cm. Comparing with Figure 8-3 and Figure 8-5, it was found that the maximum allowable power and LCOE respond to changing pressure drop in very similar way as to a change in SF. This suggests that the coolant pressure drop had similar effect on the reactor as the salt fraction: both affect the convective heat transfer within the coolant. When the reactor was restricted by the coolant inlet temperature or minimum Re limit, more power could be allowed by enhancing convective heat transfer. This could be achieved through increasing either SF or coolant pressure drop. After the maximum fuel temperature became the dominating constraint, increasing pressure drop allowed very small power-uprate and changing

coolant volume had almost no effect on the maximum power output. In comparison, increasing the number of fuel pins per assembly, i.e., reducing the P/D, would be a more preferable choice for achieving greater power.

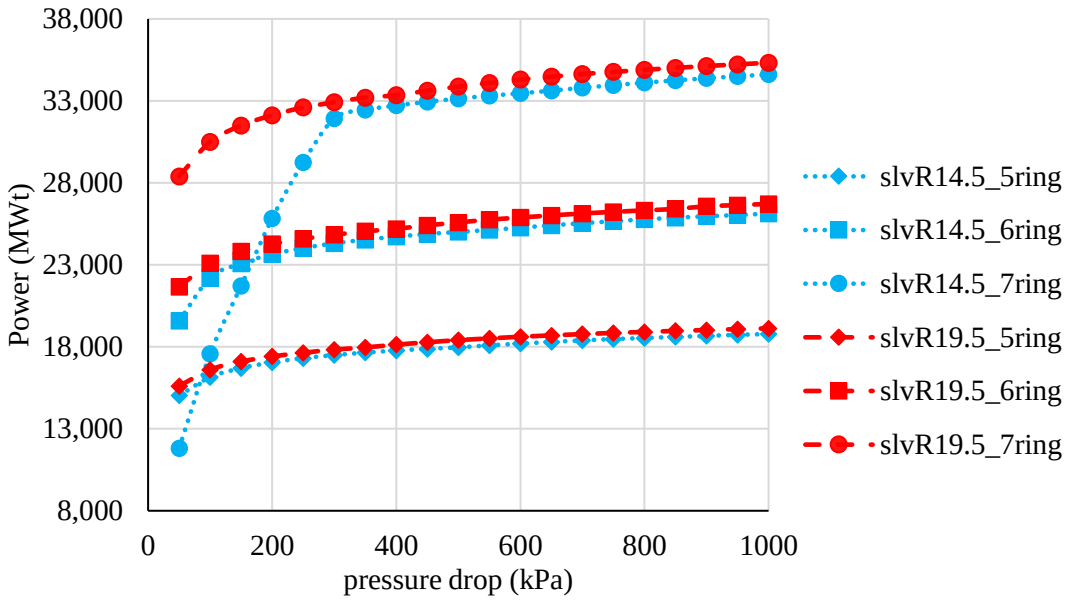

Figure 8-6. Effect of coolant pressure drop on maximum allowable power for FLiBe cooled solid UC pin FHR

Same as increasing SF, increasing pressure drop affected the reactor's LCOE in four competing ways: 1) allowed power uprate to reduce LCOE, especially when the reactor design was limited by coolant inlet temperature or minimum Re constraint, 2) required greater pumping power which increased operating cost, 3) increased average coolant temperature and thereby reduced the heat exchanger cost and 4) the higher core average temperature limited or even reduced the power uprate. Figure 8-7 shows the effect of coolant pressure drop on LCOE for FLiBe cooled solid UC pin FHR. The decreasing trend of LCOE in Figure 8-7 was due to the power uprate allowed by greater pressure drop or the cost reduction of heat exchangers from higher average hot side coolant temperature; the part where LCOE increased with pressure drop corresponds to the cases that were limited by fuel temperature constraint: the benefit of power uprate from better convective heat transfer diminished and the cost increase from pumps dominated the cost reduction in heat exchangers. In some cases, power was reduced since core average temperature rose with pressure drop, leaving smaller power margin to fuel melting. Comparing with SF, core pressure drop affected the pumping cost more directly, therefore the LCOE increase with pressure drop was more pronounced comparing with Figure 8-5. Also seen in Figure 8-7, the

optimum pressure drop occurred at smaller values for the designs with less fuel pins per assembly, i.e., smaller P/D and SF. Similar effects of operating condition on LCOE and maximum achievable power were seen for the alternative design streams.

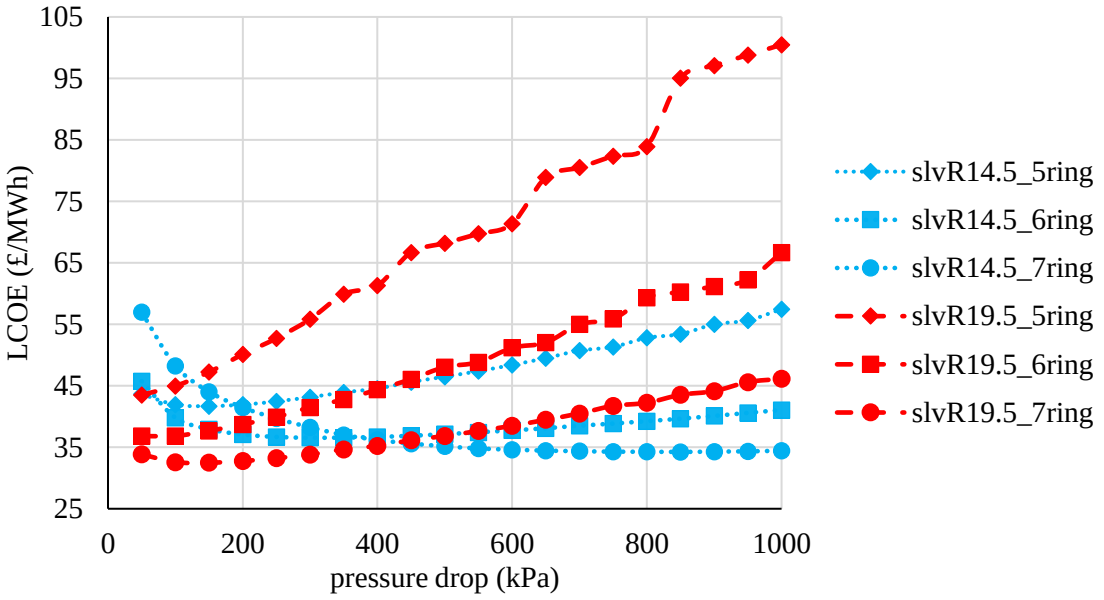

Figure 8-7. Effect of coolant pressure drop on LCOE for FLiBe cooled solid UC pin FHR

8.2.4 Discussion of Thermal-hydraulic Results

Table 8-1 and Table 8-2 present the specifics of the top five designs with the lowest LCOE for each of the selected annular and solid pin design streams respectively, ranked in ascending order of LCOE. In the extended thermal-hydraulic design space, all selected design streams had the potential to achieve much lower LCOE than the strike price for the Hinkley Point C power plant (92.5 £/MWh). [64] The main driver behind the cost reduction was the significant power uprate. Annular FCM pin designs were only marginally superior in this regard. The best annular fuel FHRs all had very small fuel thicknesses, nearly approaching the chosen limit of 0.5cm. This way the reactors benefited from good heat removal capacity and small temperature rise across the fuel meat. All reactors had large inner graphite sleeve radii, but the solid pin designs used many more fuel pins per assembly, so that the reactors could reach greater power by splitting the power duty between the fuel pins. These reactors had small P/Ds (1.93 to 2.16). For the designs with the largest possible SF and largest possible number of fuel pins in AGR physical boundary, i.e., the inner graphite sleeve of 19.5 cm and 9 rings of fuel pins, greater

power and lower LCOE could potentially be achieved if the design space can be extended beyond the AGR envelope.

Table 8-1. FCM fuelled annular pin FLiBe cooled designs with lowest LCOEs

slvR (cm)	*#rings*	R_{in} *(cm)*	R_{out} *(cm)*	*P/D*	*SF (wt%)*	T_{in} *(°C)*	Δp *(kPa)*	*Pow (MWt)*	*LCOE (£/MWh)*
19.5	5	1.02	1.67	3.34	58	619	600	59685	28.0
19	5	0.99	1.63	3.34	55	618	650	58762	28.3
18.5	5	0.96	1.59	3.34	52	615	700	57686	28.6
19.5	4	1.34	1.99	4.10	59	640	400	48135	29.1
19	4	1.28	1.95	4.10	56	636	400	46220	29.5

Table 8-2. Solid pin designs with lowest LCOEs

slvR (cm)	*#rings*	*P/D*	*SF (wt%)*	T_{in} *(°C)*	Δp *(kPa)*	*Pow (MWt)*	*LCOE (£/MWh)*
Solid UC fuel with FLiBe coolant							
19.5	9	1.93	55	625	500	53687	28.6
19	9	1.93	51	623	650	54484	28.8
18.5	9	1.93	47	616	750	54900	29.2
19.5	8	2.16	58	640	250	41575	29.9
19	8	2.16	54	638	300	41948	30.0
Solid UC fuel with $NaF\text{-}ZrF_4$ coolant							
19.5	9	1.93	65	608	750	51365	31.8
19	9	1.93	61	603	900	51693	32.2
19.5	8	2.16	68	620	300	38591	33.0
19	8	2.16	64	625	450	39830	33.1
18.5	8	2.16	61	618	500	40038	33.3
Solid FCM fuel with FLiBe coolant							
19.5	9	1.93	55	642	250	28037	34.4
19	9	1.93	51	639	300	28355	34.4
18.5	9	1.93	47	638	400	28861	34.6
18.5	8	2.16	51	653	200	22095	37.4
18	8	2.16	47	651	250	22427	37.4

It must be stressed again that the results reported in Table 8-1 and Table 8-2 shall not be taken as accurate predictions of LCOE and final design recommendations. Firstly, the assumptions

made in CapCost module of SCOOP, which could not be justified, had non-negligible impact on the final LCOE reported. In addition, the LCOE was also very sensitive to the assumptions made in SODom, i.e., the material temperature limits, which affected the maximum allowable power, as all of the well performing designs are limited by their fuel temperature constraints. In the current setting, the reactors operated at a fuel temperature with 500 °C margin to the material failure point and result of this was that reported reactors have extremely large power outputs. If more conservative fuel temperature limits were chosen in SODom, smaller core power and therefore larger LCOE would be reported by SCOOP. Choosing the design limit involves a complex network of engineering, economic and safety trade-offs. The exact safety limits should be determined by comprehensive safety analyses, taking into account the whole range of operations and anticipated transient scenarios as well as accidents. Results reported here can serve as a demonstration of the FHR's potential for power uprate and cost reduction. Furthermore, the coolant velocity, which was not considered in the models, might become a limiting factor: flow induced vibration and abrasion of the fuel clad, etc. could hinder the reactor's safety performance. The effect of large coolant velocity must be further investigated to establish more realistic design limits. If coolant velocity indeed proves to be a limiting factor for the FHR, a smaller pressure drop must be enforced which would increase the reactor's LCOE. Studies addressing these concerns is recommended for future studies.

Studying the data for all FHR cases explored, it was discovered that a reactor can achieve greater power and lower LCOE when the fuel temperature constraint dominates. If the design goal is to minimise LCOE by fully exploiting the reactor's power uprate potential, several design recommendations can be followed: 1) design the reactor with sufficient, but not too large, SF and pressure drop to ensure that the coolant enters the core with a temperature and Re number above the design limits, 2) select a fuel material with high thermal conductivity, 3) select a fuel with high melting temperature and 4) use more fuel pins per assembly to reduce linear power rating for each pin and thus the peak fuel temperature.

8.3 FHR Design Accounting for both Neutronics and Thermal-hydraulics

With the thermal-hydraulic design space extended, the data was sufficient to apply to the earlier neutronics results. The last part of this chapter presents the most important findings of this thesis: discussions and final design recommendations for the new FHR concept applying both thermal-hydraulics and neutronic constraints.

A good FHR design is expected to have low LCOE and high BU/e. If trade-offs exit between the neutronic (BU/e) and thermal-hydraulic (LCOE) figures-of-merit, some neutronic performance can be compromised without jeopardising the reactor's safety for lower LCOE, as it quantifies the economics of the whole power plant, whereas BU/e quantifies the fuel cycle economics which typically constitutes a small part of the NPP economics. The coupling step sought to identify, adhering to this design optimisation philosophy, the best design from the overlapping region of the thermal-hydraulic and neutronic design space.

The feasible neutronic design space after applying the reactivity coefficients and fuel burnup constraints was rather small and neutronic performance (BU/e and burnup) of the reactors that were included in the feasible domain varied significantly, therefore it was much easier to identify good neutronic designs. On the contrary, the feasible thermal-hydraulic design space was very large and had very fine variation for each design parameter and thus many reactors had very similar thermal-hydraulic performance. Considering the uncertainties in the thermal-hydraulic modules, it was difficult to identify with confidence the absolute best thermal-hydraulic design. Therefore, the coupling strategy applied was to first identify for each of the selected best neutronic unit cell design options, if any, the best corresponding assembly level thermal-hydraulic designs that have lowest LCOE. After this, attempts were made to see if perturbations can be made to these designs to further lower its LCOE without rendering these reactors' neutronics undesirable.

8.3.1 AGR-like FHR Design

Studying the best neutronic designs in Table 7-4, it was found that these FHRs could be categorised into AGR-like and non-AGR-like design streams: the AGR-like FHRs were the reactors with SFs between ~18% and ~75% and P/Ds between 1.9 and 5.3, and the non-AGR-like FHR are the reactors that lied outside of this domain. For the AGR-like FHR, assembly level thermal-hydraulic models could be found with matching P/Ds and SFs to the unit cell neutronic models; whereas the non-AGR-like FHRs needed further modifications to the thermal-hydraulic results for coupled neutronic and thermal-hydraulic analyses. Several good neutronic designs are summarised in Table 8-3. The best thermal-hydraulic models (lowest LCOE) that matched these neutronic models are summarised in Table 8-4. Since the thermal-hydraulic models used circular lattice for the fuel pins, the resulting P/D in these models were discretised and could not perfectly match the P/Ds of the unit cell neutronic models.

Table 8-3. Best AGR-like neutronic models

type	*fuel*	*coolant*	*Ue5 (wt%)*	*P/D*	*SF (wt%)*	*BU/e (MWd/kg)*	*BU (MWd/kg)*
sol	UC	FLiBe	5	4.4	20	11.1	55
sol	UC	FLiBe	7.5	4.8	60	9.6	72
sol	FCM	FLiBe	17.5	2.4	60	9.5	166
sol	FCM	FLiBe	15	2.4	60	9.4	141

Table 8-4. Best thermal-hydraulic models matching the best AGR-like neutronic models

slvR (cm)	*#rings*	*P/D*	*SF (wt%)*	*T_{in} (°C)*	*Δp (kPa)*	*Pow (MWt)*	*LCOE (£/MWh)*
Solid UC fuel with FLiBe coolant							
10.5	4	4.1	21	648	300	11469	50.2
18.5	4	4.1	59	687	50	10375	55.3
18.5	3	5.3	60	694	50	6145	80.9
Solid FCM fuel with FLiBe coolant							
19.5	7	2.4	60	672	100	16399	42.4

The first thermal-hydraulic model from the solid UC fuel with FLiBe coolant design stream corresponds to the first neutronic model from Table 8-3. Although not perfectly matching the P/D of 4.4 in the first design in Table 8-3, the actual LCOE of the neutronic model could be estimated to be slightly higher than the reported 50.2 £/MWh, as it was found that increasing P/D for designs that are limited by the fuel temperature constraint would increase the reactor's LCOE. The best thermal-hydraulic models that had closest P/Ds to the second neutronic model in Table 8-3 are reported, i.e., the second and third designs in Table 8-4. The LCOE of the perfectly matching thermal-hydraulic model could be estimated by interpolation between these two designs. The last design in Table 8-4 corresponds to the last two designs from Table 8-3.

The last design from Table 8-4 had the lowest LCOE of 42.4 £/MWh among the four reported. This is because it had smaller P/D (2.4), i.e., more fuel pins per assembly to share the power duty. Following it was the UC fuelled counterpart reaching an LCOE of 50.2 £/MWh. It had smaller coolant mass comparing with the other two UC fuelled options and therefore the

average coolant temperature was lower, leaving larger margin for temperature rise across the fuel. In an attempt to reduce LCOE of the reported FHRs, it was found earlier that reducing P/D was more effective than changing SF. However, no better neutronic model with greater P/Ds was identified from feasible domain for the UC fuelled solid pin FHR with FLiBe coolant. For the FCM fuelled design stream, it was found that reducing SF and/or P/D could help with reducing LCOE. The best neutronic design from the feasible neutronic design space identified that matched these criteria is listed in Table 8-5.

Table 8-5. Best solid FCM fuel pin neutronic design with lowest P/D

type	*fuel*	*coolant*	*Ue5 (wt%)*	*P/D*	*SF (wt%)*	*BU/e (MWd/kg)*	*BU (MWd/kg)*
sol	FCM	FLiBe	17.5	2	40	7.2	126

Table 8-6. Best thermal-hydraulic design matching the best solid FCM fuel pin neutronic model with lowest P/D

slvR (cm)	*#rings*	*P/D*	*SF (wt%)*	*T_{in} (°C)*	*Δp (kPa)*	*Pow (MWt)*	*LCOE (£/MWh)*
Solid FCM fuel with FLiBe coolant							
17	8	2.2	41	639	300	22627	37.6

The best matching thermal-hydraulic model for the above neutronic model is listed in Table 8-6. Again, no perfect matches in both P/Ds were found. By reducing P/D, the LCOE of the solid FCM pin FHR reduced from 42.4 £/MWh to 36.7 £/MWh. The actual value could possibly be more optimistic since the P/D, the stronger factor in determining the LCOE for these assembly models, was higher than the value of 2 in the unit cell neutronic models. However, the neutronic performance was somewhat compromised: the BU/e went down from ~ 9.5 MWd/kg to 7.2 MWd/kg.

To address the issue of non-matching P/D and SF in the thermal-hydraulic vs neutronic models, a very important observation was made: the thermal-hydraulic calculations in SCOOP (SODom) used 1-D sub-channel heat transfer models which assumed no knowledge of the design specifics of the fuel/coolant channel and the graphite content outside the channel. This means that the thermal-hydraulic design space of the AGR assembly models can be translated

to any non-AGR like design space with the re-scaling of the P/D and SF, as long as the new design has all of its heat transfer fluid (in-channel coolant salt in this case) in the centre of the assembly. This rescaling can be done in the following way: to map the AGR assembly model onto any arbitrary SF space, the required graphite mass can be derived from the mass of the salt coolant. The P/D must then be adjusted using the new volume. This way, for any given model, any AGR-like assembly model can be mapped onto any targeted SF space by varying the graphite volume. However, after mapping to a new P/D to SF space, the reactors would deviate from the current AGR assembly and core dimensions. Some assumptions were made to CapCost adjust the LCOE accordingly: 1) the total volume of the gaps between and the channels in the middle of the graphite keys remain unchanged in the mapping process and 2) the fixed component of the NPP's electricity cost inversely scales with the size of the core.

Table 8-7. Optimised AGR-like FHR designs

slvR	*#rings*	*Ue5* *(wt %)*	*P/D*	*SF* *(wt%)*	*Asmbl. Pitch* *(cm)*	T_{in} *(°C)*	Δp *(kPa)*	*Pow* *(MWt)*	*BU/e* *(MWd/kg)*	*BU* *(MWd/kg)*	*adj. LCOE* *(£/MWh)*
AGR-like Solid FCM fuel with FLiBe coolant											
18.5	9	17.5	2	40	49.1	638	400	28861	7.2	126	35.3
19	7	17.5	2.4	60	44.8	668	100	16349	9.5	166	41.7
19	7	15	2.4	60	44.8	668	100	16349	9.4	141	41.7
AGR-like Solid UC fuel with FLiBe coolant											
15	3	5	4.4	20	38.2	688	100	6069	11.1	55	65.7

Applying this method, the thermal-hydraulic results of the best AGR-like FHR designs were tailored to match their neutronic models. The specifics of the final optimised AGR-like FHR designs are summarised in Table 8-7, ranked in the order of increasing adjusted LCOE for each of the design streams. The solid FCM fuelled solid pin FHRs had lower LCOEs comparing with the UC fuelled FHRs, but they had somewhat poorer fuel cycle economics comparing with the UC option. The best design reported for the UC fuelled design stream had an LCOE of 65.7 £/MWh and notably smaller assembly pitch of 38.2 cm comparing with the AGR (46 cm assembly pitch). The accuracy of the assumption of LCOE's scaling rule with reactor size is uncertain and shall be further investigated. For the other reactors, there are many ways to fine tune the reactor into AGR dimension, while keeping the P/D and SFs. For example,

adjusting graphite sleeve dimensions, redesign the fuel pin lattice so the number of fuel pins per assembly can be fine-tuned, adding graphite pins into the assembly, adding void channels into the graphite structure, etc. The resulting LCOE and power is not expected to be affected significantly.

The coolant flow velocities of the designs were not considered as the actual design limits for different salt candidate in FHR environments remain unknown. Problems that can potentially be caused by high flow velocities such as flow induced vibration of the fuel pins, corrosion/erosion of the cladding and structural materials, etc., clearly deserve attention. With accumulation of experimental data and emergence of fuel assembly mechanical design, flow velocities would need to be incorporated as a design limit. This information is currently lacking. Therefore, this thesis could only perform some sensitivity studies to understand the trade-offs that might be encountered if coolant flow limit is imposed.

The best solid FCM pin fuelled design options has a coolant velocity of 5.1 m/s. Reducing pressure drop to 50 kPa could reduce the coolant velocity to 2.2 m/s, similar to that of the ORNL AHTR. However, the power would be reduced from 28861 MWt to 20123 MWt (30% power reduction) and LCOE would increase from 35.3 £/MWh to 46.3 £/MWh. The resulting coolant temperature rise across the core (140 °C difference across the core instead of 62 °C) would be slightly larger and would increase the thermal stress in the graphite and other core structures and reduce the power cycle efficiency because of the lower average temperature of heat addition, although it would still be higher than in AGRs. The second best solid FCM pin design has a coolant velocity of 4 m/s. Reducing the core pressure drop to 50 kPa, the flow velocity would be reduced to 2.7 m/s, and the resulting power and LCOE would be 15136 MWt (8% power reduction) and 42.3 £/MWh. The best UC fuelled FLiBe cooled design has a coolant velocity of 5.3 m/s and it was already operating at a very low core pressure drop of 50 kPa. Therefore, reducing the coolant flow velocity would be difficult without substantial lower power reduction. Whether these ranges of coolant velocity are acceptable needs to be confirmed in future analyses.

8.3.2 PWR-like FHR Design

The majority of the best neutronic designs had 80 wt% salt fraction and above, this is well beyond the AGR-like assembly design space. Some even had zero graphite content in the core. With reduced graphite content, the reactors relied solely on coolant to achieve good BU/e and negative coolant temperature reactivity coefficients. No thermal-hydraulic analyses under the

AGR setup were performed that could cover the design space of these reactors. The techniques described earlier were applied to these reactors to map the AGR-like design space into the PWR-like design space with some modifications to assembly configuration. For PWR-like FHRs with such high salt fractions, it would be impossible to keep the graphite key structures. The assembly channel would have to become square and PWR-type lattice must be applied. Figure 8-8 illustrates how the PWR-like FHRs could look like. The SCOOP calculations did not assume any particular fuel pin lattice. One could design a circular pin-lattice within a PWR-like core to take advantage of the existing AGR refuelling machines. It was assumed that all the volume, if any, outside of the coolant channels were filled with graphite, meaning no re-entrant coolant (see Figure 8-8 a). Fortunately, the axial temperature gradient across any FHR design was much smaller than in the AGR. It shall be noted that the using AGR-like thermal-hydraulic models would be underestimate coolant pressure drop if the square sleeves applied to around the assemblies, which adds to the wetted perimeter and therefore frictional pressure drop, or overestimate if a pure PWR configuration with no sleeves is used.

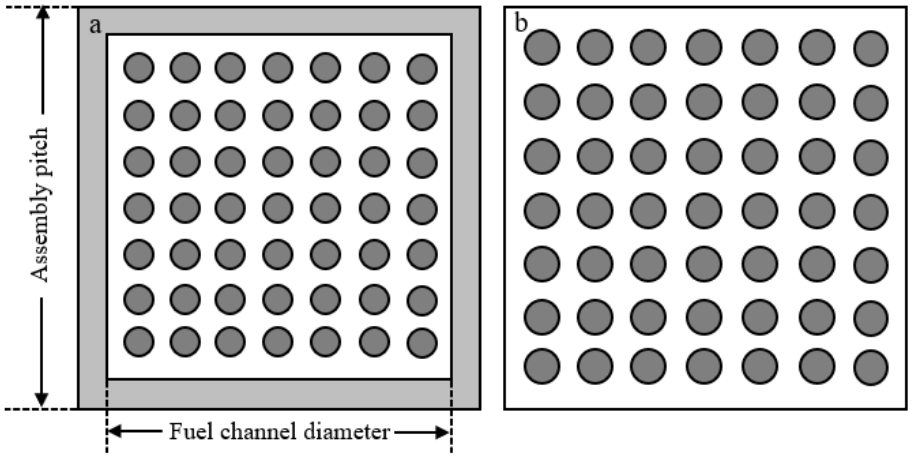

Figure 8-8. Illustrations of PWR-like FHR deigns. a) graphite content > 0 and are wrapped around the PWR-like assembly in form of a sleeve; b) graphite content = 0

After mapping the AGR assembly level thermal-hydraulic models to PWR-like models, only the two solid FCM fuel pin designs, i.e., the third and the fifth best neutronic models from Table 8-8 (which summarises the best PWR-like FHR neutronic models) were found to have matching thermal-hydraulic counterparts. Table 8-9 summarises the neutronic and thermal-hydraulic results (mapped) for these two reactors. For the PWR-type FHR with 100 wt% salt

fraction, the fuel channel diameter is equal to the assembly pitch. As mentioned earlier, the adjusted LCOE considered the size differences between the PWR-like and the AGR-like assembly. Comparing with the AGR-like solid FCM pin FHRs reported in Table 8-7, these PWR-like solid FCM pin FHRs had poorer performance in both thermal-hydraulic (LCOE) and neutronic (BU/e) figures-of-merit. Lower LCOE could be achieved by reducing P/D. However, this would further compromise the neutronic performance. Therefore, it would not bring any additional value to the solid FCM fuel pin design stream by doing so, considering the AGR-like design option had absolute advantage over the PWR-like option.

Table 8-8. Best PWR-like neutronic models

type	*fuel*	*coolant*	*Ue5 (wt%)*	*P/D*	*SF (wt%)*	*BU/e (MWd/kg)*	*BU (MWd/kg)*
sol	UC	FLiBe	7.5	5.6	80	9.7	73
sol	UC	FLiBe	10	5.2	80	9.5	95
sol	FCM	FLiBe	20	2.8	100	8.8	175
sol	UC	FLiBe	10	6	100	8.7	87
sol	FCM	FLiBe	20	2.4	80	8.1	163
ann	FCM	FLiBe	20	5.2	80	3.9	77
ann	FCM	FLiBe	17.5	5.2	80	3.4	60
ann	FCM	FLiBe	20	4.8	100	3.2	65
ann	FCM	FLiBe	20	5.2	100	3.1	61
ann	FCM	FLiBe	15	5.2	80	2.9	44
sol	UC	NaF- ZrF_4	12.5	4.8	100	2.3	29

Table 8-9. Optimised PWR-like FHR designs with solid FCM fuel pins

# of pins	*Ue5 (wt%)*	*P/D*	*fuel channd (cm)*	*Asmbl. pitch (cm)*	*T_{in} (°C)*	*Δp (kPa)*	*Pow (MWt)*	*BU/e (MWd/kg)*	*BU (MWd/kg)*	*adj. LCOE (£/MWh)*
PWR-type FHR Solid FCM fuel with FLiBe coolant (SF = 80 wt%)										
90	20	2.4	30.1	33.4	681	50	8175	8.1	163	51.5
PWR-type FHR Solid FCM fuel with FLiBe coolant (SF = 100 wt%)										
60	20	2.8	31	31	692	50	5502	8.8	175	67.4
60	17.5	2.8	31	31	692	50	5502	8.5	149	67.4

All other PWR-like models in Table 8-8 had P/Ds extending beyond the thermal-hydraulic space even after mapping to the SFs of 80 wt% and 100 wt% spaces. The best PWR-like neutronic models were the UC solid pin FHR using FLiBe coolant with P/Ds of 5.6 and 5.2 with SF of 80 wt%. The largest P/D found for this design stream after mapping the thermal-hydraulic results onto the 80 wt% SF space was 4.5. This is a reactor with 36 fuel pins with a fuel channel diameter of 34.6 cm and an assembly pitch of 38.9 cm, i.e., mapped from the 3-ring AGR-like assembly design with an inner graphite sleeve radius of 19.5 cm. To estimate the LCOEs of the two best neutronic models, second order polynomial fitting was applied to the data as shown Figure 8-9. The points were obtained by mapping the AGR-like assembly models with 36 pins and varying graphite sleeve radii to PWR space with 80 wt% SF. All reactors used in the curve fitting operated at a pressure drop of 50 kPa, which was found to be the optimum condition for all solid UC pin FHRs with 80 wt% SF. Extrapolating the fitted second order polynomial to P/Ds of 5.6 and 5.2, the two best neutronic designs were estimated to have adjusted LCOEs of 106.3 £/MWh and 95.4 £/MWh respectively.

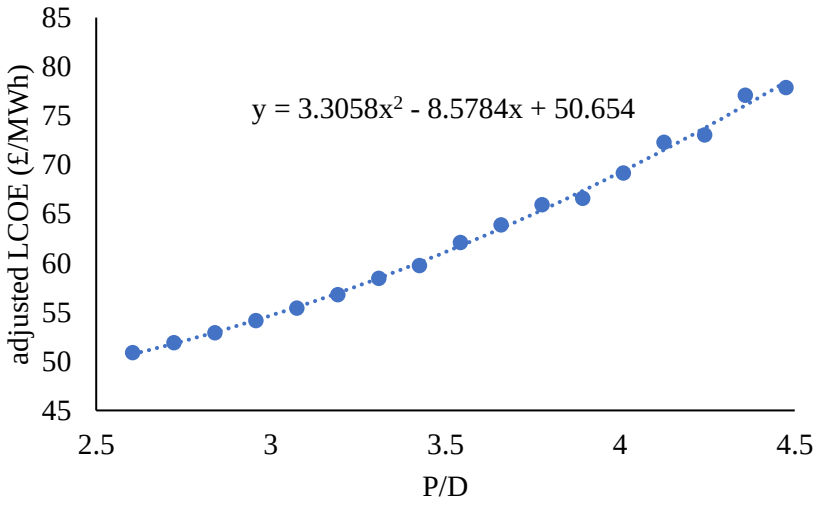

Figure 8-9. Polynomial fit of LCOE against P/D for PWR-like designs mapped from AGR-like assembly models with 36 pins

To lower the LCOE of this design option, P/D must be reduced. The smallest P/D found in the feasible neutronic space for the solid UC pin FHR with 80 wt% FLiBe SF was 4. The best neutronic model had a 20 wt% enrichment, reaching a BU/e of 8.4 MWd/kg and a discharge

burnup of 167 MWd/kg. The corresponding thermal-hydraulic design was mapped from a 3-ring AGR-like assembly model with a graphite sleeve radius of 17.5 cm. The optimum pressure drop for this reactor was 50 kPa, giving the coolant inlet temperature of 692 °C with an output of 6122 MWt and an adjusted LCOE of 69.2 £/MWh. Applying this optimisation method, the specifics of the optimised solid pin designs were obtained and are summarised in Table 8-10. It was again found that the PWR-like FHR design options with solid UC fuel pins had higher LCOEs than their AGR-like FHRs counter parts listed in Table 8-7.

Table 8-10. Optimised PWR-like solid UC fuel pin designs

# of pin	*Ue5* *(wt%)*	*P/D*	*fuel chann. d* *(cm)*	*Asmbl. pitch* *(cm)*	T_{in} *(°C)*	Δp *(kPa)*	*Pow* *(MWt)*	*BU/e* *(MWd/kg)*	*BU* *(MWd/kg)*	*adj. LCOE* *(£/MWh)*
PWR-like FHR Solid UC fuel with FLiBe coolant (SF = 80 wt%)										
36	20	4	31	34.9	692	50	6122	8.4	167	69.2
PWR- like FHR Solid UC fuel with FLiBe coolant (SF = 100 wt%)										
36	20	4	34.6	34.6	695	50	6157	7.8	157	75.5
PWR- like FHR Solid UC fuel with $NaF\text{-}ZrF_4$ coolant (SF = 100 wt%)										
36	12.5	4	34.6	34.6	693	50	5319	1.9	24	79.4

The final design stream analysed was the PWR-like annular FCM pin FHR with FLiBe coolant, a very promising design stream in terms of LCOE. The selected neutronic models had very large P/Ds and, unlike other reactors, at large P/Ds, the annular FCM pin FHR has decreasing LCOE with increasing P/D, which matched very well with the neutronic design recommendations for annular FCM pin FHRs. When the reactor was limited by minimum coolant inlet temperature or minimum Re requirement, larger P/D would increase the power as a result of the larger coolant mass flow rate. As the fuel temperature limit dominated, the coolant velocity and the convective heat transfer coefficient increased with P/D, reducing the temperature difference between the cladding surface temperature and the bulk coolant temperature. Although the coolant inlet temperature rose with P/D, it was found that the more efficient convective heat transfer in fact reduced the cladding surface temperature, thereby allowing larger temperature margin for power uprate. This was true for both annular and solid pin FHRs.

In comparison with the solid pin designs, the annular fuel form took the greater advantage of this effect. Since the heat conduction distance was much smaller in annular pins, for the same increase in temperature margin, the annular fuel pin allowed greater power uprate. For example, the FCM fuelled annular pin PWR-like FHR with FLiBe coolant (mapped from the 5-ring AGR model with annular fuel rod thickness ~ 0.7 cm) saw its power increase from 14516 MWt to 34323 MWt when P/D increased from 2.3 to 3.9 and when operating at a pressure drop of 200 kPa (the optimum operating condition for this design), whereas the solid pin PWR-like design (mapped from the 3-ring AGR model) saw only 127 MWt power increase (from 3141 MWt to 3268 MWt) as P/D increased from 2.3 to 3.9 when operating at its optimum pressure drop of 50 kPa. However, with greater power, the variable component of the LCOE increased. For annular pin FHRs, this increase was much smaller comparing with the cost reduction from power uprate, whereas the reverse was true for solid pin designs. In addition, the power density of the PWR-like FHR, to which the fixed component of the LCOE was assumed to be inversely proportional, was found to decrease with increasing P/D for both annular and solid pin type FHRs, but the rate of decrease in power density was much smaller in annular pin designs. The overall effect of increasing P/D on the PWR-like FHRs was that the LCOE of annular pin designs decreased, whereas the LCOE of solid pin designs increased.

The five neutronic models selected for the PWR-like FHR with annular FCM fuel FLiBe had P/Ds of 4.8 (with 100 wt% SF) and 5.2 (with 80 wt% SF and 100 wt%). No better model was found in the feasible neutronic space during the attempt to further lower LCOE by increasing P/D, making the three reported cases the best design options. Unfortunately, no matching thermal-hydraulic models were found after mapping onto the PWR-like design space for these designs. Keeping the same fuel thickness of ~0.7 cm as in the neutronic models, the largest P/D found for the 80 wt% SF thermal-hydraulic model was 4.4 and for the 100 wt% SF thermal-hydraulic model the largest P/D was 4. The two models were both mapped from the 3-ring AGR-like FHR with inner graphite sleeve radius of 19.5 cm, reaching a power of 34323 MWt with a coolant inlet temperature of 652 °C when operating at the optimum pressure drop of 200 kPa. The adjusted LCOEs for these two designs were 30.5 £/MWh (for SF of 80 wt%) and 30 £/MWh (for SF of 100 wt%) respectively. These were the lowest values found for all FHRs explored in this thesis. Due to complexity of the data for the annular pin FHR, no good polynomial fit could be made to predict the LCOEs at larger P/Ds to match the neutronic models, but it was expected that the LCOE would be even lower. However, this design option

had relatively poor neutronic performance: BU/e of 3.1 MWd/kg to 3.9 MWd/kg. The projected specifics of the optimised annular pin FHRs are summarised in Table 8-11.

Table 8-11. Projected specifics for the optimised annular FCM pin FHR

fuel chann. d (cm)	*Asmbl. pitch (cm)*	*# of pins*	*Ue5 (wt%)*	*P/D*	*SF (wt%)*	*T_{in} (°C)*	*Δp (kPa)*	*Pow (MWt)*	*BU/e (MWd/kg)*	*BU (MWd/kg)*	*adj. LCOE (£/MWh)*
45.3	45.3	36	20	5.2	100	<652	200	>34323	3.1	61	<30
45.3	50.6	36	20	5.2	80	<652	200	>34323	3.9	77	<30.5

The LCOEs reported for the annular FCM pin FHR should be treated with even less confidence comparing with other designs streams. The inner and outer radii of the fuel of the neutronic and thermal-hydraulic models could not be matched. This was because the dimensions of the fuel channels, with which the inner and outer radii were calculated to ensure similar axial temperature rise for internal and external coolant, were different in the unit cell neutronic models and assembly level thermal-hydraulic models. For example, in the PWR-like design with 100 wt% SF, the thermal-hydraulic model used smaller pins (inner and outer fuel pin radii of 1.8 cm and 2.5 cm respectively) than with the neutronic models (inner and outer radii of 3 cm and 3.7 cm respectively). The fuel thickness was kept same when finding matching thermal-hydraulic results for the neutronic models to ensure that heat conduction across the fuel pin can be reasonably well captured. However, the coolant flow and the resulting axial temperature distribution would not be optimal. Despite all the uncertainties and discrepancies in the models, it is expected that the annular FCM pin FHR has the potential to achieve very low LCOE, although with compromised fuel cycle economics.

As mentioned earlier, coolant velocity was not considered as a design constraint in this project due to lack of data, but it would require serious consideration in future studies. The best PWR-like annular fuel design in this thesis had coolant velocities of 5 m/s ~ 6 m/s. This is marginally higher than the nominal coolant flow velocity in the modern operating PWRs (~4.5 m/s), and significantly higher than that in the AHTR design (~2m/s). However, the actual limits for different salts have not yet been established and experimentally validated. In PWRs, coolant flow is limited by pumping power and mechanical assembly design due to flow-induced vibrations. In led-cooled reactors, the flow is limited to less than ~2m/s because of the corrosion/erosion constraints related to the chemical interaction with alloying elements in steel and stability of protective oxide layer at high temperature. The extent of these phenomena or

even their limiting nature might be significantly different in salts. Furthermore, in lead-cooled reactors, new alloys are being developed that would form protective oxide layer, which is stable at much higher temperature, approaching that of FHRs. This would allow to relax the flow velocity limit significantly and allow achieving higher power density.

If similar range of coolant flow velocities as current fleet of reactors were adopted as design criteria for the best designs, the designs would need to operate with lower coolant flow velocities. The reduced flow would result in significantly lower power output and higher LCOE. For instance, if the flow velocity of the FCM annular design were to be reduced to 2.3 m/s - 2.7 m/s (~50% flow reduction), the reactor would have a 19% lower power output 27980 and more than 15.6% higher LCOE of 34.7 £/MWh, with a coolant inlet temperature of 617 °C and the core pressure drop of 50 kPa. The best NaF-ZrF4 cooled PWR-like FHR design has a coolant velocity on the order of 6 m/s, and same as the best UC fuelled FLiBe cooled annular fuel design, operates at a low core pressure drop of 50 kPa. Reducing the flow rate in these two designs, would lead to a greater percentage cost rise than the FCM annular design as the inlet and outlet temperature constraints might become the most limiting factor.

Considering the lack of know and uncertainties of potential flow constraint and their significance, these limits should be established through experiments before incorporating them into the design process.

8.4 Thermal-hydraulic and Neutronic Design summary

Summarising the results presented in this chapter, taking LCOE as the major design target, a ranking of all the design options can be made as follows: 1) PWR-like annular FCM pin FHR with FLiBe (LCOE of less than 30 £/MWh), 2) AGR-like solid FCM pin FHR with FLiBe (LCOE of ~35 £/MWh to ~40 £/MWh), 3) PWR-like solid FCM pin FHR with FLiBe (LCOE of ~50 £/MWh to ~70 £/MWh), 4) AGR-like solid UC pin FHR with FLiBe (LCOE of ~64 £/MWh), 5) PWR-like solid UC pin FHR with FLiBe (LCOE of ~70 £/MWh to ~75 £/MWh) and 6) PWR-like solid UC pin FHR with NaF-ZrF_4 (LCOE of ~80 £/MWh).

Adding neutronics, i.e., fuel cycle economics to the performance measures, the AGR-like solid FCM pin FHR with FLiBe offers the best combination of low LCOE and high BU/e. The AGR-like solid UC pin FHR with FLiBe offered better fuel cycle economics but higher LCOE comparing with FCM fuelled option. The PWR-like variations of these two solid pin FHR design streams had poorer performance in terms of both neutronics and thermal-hydraulics. The cheapest design option was the PWR-like annular FCM FHRs with FLiBe coolant,

however it had much poorer neutronic performance and required much more development effort for the niche fuel form. The $NaF\text{-}ZrF_4$ cooled PWR-like solid UC fuel reactor could solve the tritium problem, but it was the poorest design option in terms of either thermal-hydraulics or neutronics. There are still many other factors that need to be considered other than LCOE and BU/e. The last chapter of this thesis presents a complete and integrated summary and discussion on all the design options.

Chapter 9 Conclusions and Future Work

This thesis is part of an alternative prismatic block type FHR conceptual design project, which proposed to adopt some of the characteristics of the AGR in FHR design. Despite early challenges, the AGRs evolved into very mature designs which have demonstrated good safety and economic performance for over four decades of their successful operation in the UK. By borrowing AGR design features, the FHR could combine all the desirable qualities of the FHR with much of the technology and experience from the AGR, such as the irradiation behaviours and manufacturing of graphite, high temperature operation and maintenance, fuel management, on-power refuelling and more. By applying FHR technologies, some of the issues encountered by the AGRs over the years can also likely be resolved.

9.1 Thesis Summary

As the first investigation into the AGR-like FHR concept, this thesis aimed at exploring a large design space with many degrees of freedom in terms of assembly design, material choice and operating conditions to study the design trade-offs between different options, thereby narrowing down the design space and identifying most attractive designs. The search space considered three fuel configurations (solid pin, annular pin and flat plate), three fuel materials (UO_2, UC and FCM), and three coolant salt candidates (FLiBe, FLiNaK and NaF-ZrF_4), constituting 21 design streams (plate type fuel only considered FCM). The operating conditions were constrained by material limits and the only free operating condition parameter was coolant pressure drop across the core. It was optimised for each design to minimise the LCOE of the NPP. The enrichment of the fuel was also a free variable for neutronic performance optimisation. Several specific objectives were set and met in the project, including: 1) development of computational toolkit and its application to maximise power density, 2) system thermal-hydraulic computational toolkit development and its application to the design optimisation, 3) neutronic design optimisation and 4) final design optimisation with respect to both thermal-hydraulics and neutronics considerations.

The project firstly developed a python code package SCOOP, which incorporated an operating thermal-hydraulic design domain search and power maximisation module (SODom), a heat transfer system optimisation module (sysOpt) and an LCOE estimation module (CapCost). The design work began by exercising SCOOP on FHR assembly models adopting the reference AGR assembly configuration with fuel pins arranged in circular array inside graphite channels and inter-locking key structures. The power uprate and economic potential of the AGR-like

FHR concept were confirmed by the SCOOP results and initial understanding of the trade-offs between different design options was obtained. Preliminary BOL neutronic design space exploration was then performed using AGR-like assembly models with relaxed dimensional constraints. With the accumulation of the preliminary thermal-hydraulic and neutronic design search results, the design space was narrowed down considering power uprate potential, BOL neutronic performance (BOL k_∞ and CTC) and particular features offering strategic value e.g., absence of tritium removal issue or substantial existing experience with fuel manufacturing. Nine potentially valuable design streams were selected, for which BOL calculations were again performed, but in a much larger geometrical design space that extended beyond the AGR physical envelope. In this step, the physical boundaries of the assembly models were relaxed and simplified: homogenised unit cell neutronic models with fewer free design parameters were used to reduced model complexity and enable quicker and more accurate neutronic calculations. Based on the new BOL results, the design space was further narrowed down to four design streams, for which depletion analysis was performed using unit cell models. Several best neutronic designs for each of the four design streams were selected considering fuel cycle economics (BU/e), fuel material limit (BU) and reactor transient response (reactivity coefficients). To obtain thermal-hydraulic performance characteristics of the final four selected design streams, SCOOP calculations were performed using AGR-like assembly models with relaxed boundary conditions to cover as much design space of the homogeneous neutronic models as possible. For the neutronic models outside of the AGR fuel physical dimensions, a mapping technique was applied to transform the AGR-like assembly thermal-hydraulic results to non-AGR like design space. Simultaneous thermal-hydraulic and neutronic optimisation was performed considering power plant economics (LCOE) and fuel cycle economics (BU/e). The best designs for the four selected design streams were identified.

9.2 Summary of Research Findings

In the preliminary thermal-hydraulic analysis, UO_2 was shown to have significantly weaker power uprate potential comparing with UC. Then, it was found in the preliminary neutronic space search that UC and UO_2 had very similar neutronic performance. Although FCM fuel had less attractive neutronic performance than UC fuel, the safety features that come with the robustness of the fuel and its reasonably good thermal-hydraulic performance could potentially prove FCM a valuable fuel candidate and it was included in further studies. No absolute performance advantage was demonstrated by UO_2 over UC and FCM, so that this fuel option was not pursued further. Plate type fuel showed mediocre power uprate potential comparing

with other fuel forms, but it was worth examining if it could work well neutronically with NaF-ZrF_4, which was the most important alternative coolant candidate. Therefore, the NaF-ZrF_4 cooled plate type fuel option was also chosen for further study. Lastly, the preliminary assembly level neutronic analysis showed that FLiNaK had strongly positive CTCs and the salt was therefore removed from consideration in the final design search.

9.2.1 Summary of Neutronic Design Optimisation Findings

After filtering out these options, nine design streams were left in the search space to perform BOL neutronic design optimisation. The NaF-ZrF_4 coolant was assumed to be isotopically enriched in Zr90 to 99 wt% to reduce parasitic neutron absorption. An upward sloping 'optimum frontier' was found to bound the 'good performance end' of the triangular shaped k_∞ vs BOL CTC neutronic space of the FHR. This suggested that there was a trade-off between k_∞ and CTC on the optimum frontier: higher k_∞ was achieved with less negative reactivity coefficients.

It was found that for the solid pin FLiBe-cooled FHR, the P/D was the most important design parameter that determined if a reactor could reach the optimum frontier as it directly translated to moderator to fuel volume ratio (both salt and graphite are moderators in FHRs, although salt has weaker moderating power). P/D of the reactor must fall within a specific range for this to happen. The trade-off between k_∞ and coolant reactivity coefficient was predominantly determined by the salt fraction with some influence of the fuel enrichment. Increasing the salt fraction and/or lowering U235 enrichment drove the design to the lower left part of the performance domain, where the reactivity coefficients were more negative, while k_∞ was lower. Decreasing coolant volume and enrichment has the opposite effect. For the annular pin and plate type fuel FHRs, moderator to fuel volume ratio still governed much of the physics, but since the fuel dimensions varied for each P/D, no clear relationship between P/D and neutronic performance was observed. Reactors with a large range of P/Ds were able to reach the optimum frontier. It was found that these reactor designs all had high fuel enrichments (17.5 wt% to 20 wt%). Changing salt fraction in annular or plate type fuel FHRs again moved the designs along the optimum frontier, determining the trade-off between BU/e and reactivity coefficients in the same way as in the solid pin FHRs. Comparing the two salt options, it was found that while isotopically enriching the Zr in NaF-ZrF_4 to 99 wt% in Zr90 brought the FHR to the feasible neutronic performance domain, this salt still showed far less favourable performance compared with FLiBe. Solid pin fuel showed best performance among the three fuel forms, with UC

slightly outperforming the FCM option. Annular fuel designs worked better when made with FCM fuel instead of UC, although the FCM fuel type showed less attractive neutronic performance in solid pin FHRs. Plate type fuel FHR was the second-best design using NaF-ZrF_4, only losing to the UC solid pin option.

Figure 6-18 in Chapter 6 illustrates the optimum frontier of the BOL neutronic performances of the nine selected design streams. Out of the nine design streams, four were selected from BOL neutronic design study for final neutronic and thermal-hydraulic design optimisation: 1) UC fuelled solid pin FHR with FLiBe coolant as it was the best neutronic design, 2) FCM fuelled annular pin FHR with FLiBe as it had the greatest potential for power uprate, 3) the FCM fuelled solid pin FHR with FLiBe coolant as it was the best design using FCM, which could simplify the safety case and 4) the UC fuelled solid pin reactor with NaF-ZrF_4 as it was the best design using NaF-ZrF_4, which does not generate tritium.

The neutronic design optimisation on the four selected design streams sought to maximise the BU/e, as the figure-of-merit for fuel cycle economics, under three constraints: 1) maximum CTC of -1 pcm/K for FLiBe cooled FHRs and -2 pcm/K for NaF-ZrF_4 cooled reactors, 2) maximum DC of -1 pcm/K for FLiBe cooled FHRs and -2 pcm/K for NaF-ZrF_4 cooled reactors and 3) maximum discharge burnup limit of 100 MWd/kg for UC fuel and 200 MWd/kg for FCM fuel.

Table 7-4 in Chapter 7 presents the best neutronic designs for the four design streams. Among the four design streams, the solid UC pin fuelled FHRs demonstrated the best fuel cycle economy, reaching a BU/e of 11.1 MWd/kg with a discharge burnup of 55 MWd/kg. This is comparable to, or even slightly higher than what the current fleet of LWRs can achieve. The BOL CTC was found to be the most limiting constraint on this design. The solid FCM fuel designs showed slightly worse fuel cycle economics, reaching a BU/e of 9.5 MWd/kg with a 166 MWd/kg discharge burnup. Again, the CTC was the most limiting factor. The best annular FCM FHR reached a BU/e of 3.9 MWd/kg with a 77 MWd/kg discharge burnup. The NaF-ZrF_4 cooled FHR showed increasing CTC with depletion, therefore a larger margin was imposed on the CTC constraint, which significantly affected the achievable BU/e of the design. Only a small BU/e of 2.3 MWd/kg with a discharge burnup of 29 MWd/kg were achieved. An interesting observation was that most neutronically optimised models had little or even zero carbon mass. This deviated from the AGR assembly configuration where significant amount

of graphite remains in the core for the life of the reactor and resembles more PWRs than an AGRs. This opened up more possibilities of design options for the FHR reactor class.

9.2.2 Summary of Thermal-hydraulic Design Optimisation Findings

The four selected design streams were subjected to the thermal-hydraulic design optimisation process, which sought to minimise the LCOE for FHRs using SCOOP. As seen in Figure 9-1, which plots the LCOE against core power for all the reactor designs considered in the last part of the thesis at their optimum operating conditions, the most effective way to minimise LCOE was to maximise power. Although marginal reduction in LCOE with increased power diminished at power levels greater than about 8000 MWt, further power uprate could bring the LCOE down to as low as ~ 30 £/MWh, as seen in the best annular pin FHR design found in this thesis.

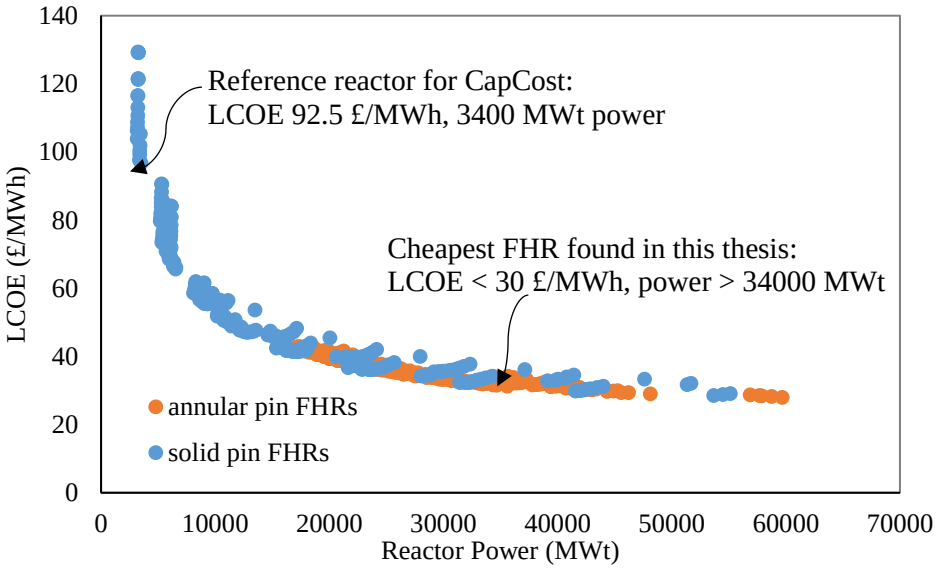

Figure 9-1. LCOE vs reactor power for all optimised unit cell neutronic models

The small peaks along the curve are the designs with very large heat exchanger system costs. Nevertheless, in most cases the cost reduction from high power can compensate for the more expensive heat transfer system. This discontinuity, i.e., the peaks, were in fact introduced by the physical constraint in the AGR model and the limitations from the fuel lattice used in this thesis. Relaxing these constraints should in theory led to reactors that fall on any desired point along the bottom boundary of the curve. It should be noted that reactors with power outputs

reported in the figure are unlikely to be practical. Instead, these cases indicate the size reduction potential. That is, the same power output as that of a conventional AGR can be obtained from a much more compact, and therefore cheaper, reactor. The results show that the core size reduction by up to a factor ~20 is possible.

It was found that among the six LSSSs used to define the maximum power allowable and the operating domain for FHRs, the most restrictive ones were the maximum fuel temperature, the minimum coolant inlet temperature and the minimum Re number constraints. The latter two constraints often dominated in reactors with small coolant content and/or low pressure drop, where the convective cooling capacity of the coolant salt was not fully taken advantage of. The choice of fuel material in these reactors did not affect the power output significantly, whereas the FLiBe offered notably greater power uprate than $NaF\text{-}ZrF_4$. Power in these reactors could be increased by using larger pressure drop and/or larger coolant mass, until the maximum fuel temperature becomes the most limiting factor.

In general, greater power can be achieved in reactor designs restricted by the maximum fuel temperature limit than by the other two limits on coolant. For these designs, increasing SF and/or coolant pressure drop allowed only marginal power increase, and sometimes even led to increase in LCOE (often due to extremely high pumping power requirement). The P/D of the fuel pins, choices of fuel and coolant material and fuel dimension could affect the maximum allowable power in these reactors, with P/D and fuel dimension being the most dominant factors. In most cases, in fact, for all solid pin FHRs, packing more fuel pins per assembly to share the power duty, i.e., using small P/Ds helped to increase power and lower LCOE, as long as the reactor was not limited by coolant inlet temperature or Re number requirements. For annular fuel FHRs, this was not necessarily true. Firstly, fuel thickness, which changed with P/D in assembly models, was a very important parameter in determining the extent of power uprate. Furthermore, with the increase of P/D in these reactors, the convective heat transfer was promoted so that even with higher bulk coolant average temperature, the maximum cladding and fuel temperature was reduced, resulting in larger temperature margins to fuel melting. Therefore, in some annular fuel cases, increasing P/D helps with power uprate. Although this convective heat transfer effect was also observed in solid pin FHRs, the resulting power uprate potential was far weaker, especially in ones with small P/Ds.

In summary, to maximise the reactor output, the reactor should 1) preferably use annular pin instead of solid pins, with large SF and/or pressure drop and thinner pins, 2) use more fuel pins

per assembly if solid pin must be used, 3) use a fuel material with high thermal-conductivity and high fuel melting point, e.g. UC, 4) use FLiBe instead of NaF-ZrF_4 and 5) ensure that the coolant enters the core above the minimum coolant temperature and Re number requirements, which can be achieved by using large SF and/or pressure drops.

The best thermal-hydraulic designs with lowest LCOEs for each of the four selected design streams are presented in Table 9-1. The results confirmed the thermal-hydraulic optimisation recommendations. It can be expected that expanding the design space, e.g., using even larger coolant channels to allow more fuel pins and coolant mass, the LCOE can be further reduced.

Table 9-1. Thermal-hydraulic models with lowest LCOEs

slvR (cm)	*#rings*	R_{in} *(cm)*	R_{out} *(cm)*	*P/D*	*SF (wt%)*	T_{in} *(°C)*	Δp *(kPa)*	*Pow (MWt)*	*LCOE (£/MWh)*
Annular FCM fuel with FLiBe cooalnt									
19.5	5	1.02	1.67	3.34	58	619	600	59685	28
Solid UC fuel with FLiBe coolant									
19.5	9			1.93	55	625	500	53687	28.6
Solid UC fuel with NaF-ZrF_4 coolant									
19.5	9			1.93	65	608	750	51365	31.8
Solid FCM fuel with FLiBe coolant									
19.5	9			1.93	55	642	250	28037	34.4

9.2.3 Summary of Multi-objective Neutronic and Thermal-hydraulic Design Findings

The final design optimisation of the four selected FHR design streams brought together thermal-hydraulic and neutronic results. It sought to minimise LCOE for each design stream, while achieving a reasonable compromise with neutronic performance which should assure that the design had a reasonable burnup with acceptable reactivity coefficients. To subject the neutronic models outside of the physical envelope of AGR to thermal-hydraulic optimisation procedure, a mapping technique was applied to AGR-like assembly to allow configurations with smaller amount of graphite than possible in a standard AGR core or configurations with no graphite at all (PWR-like fuel as illustrated in Figure 8-8). This technique was also applied to the AGR-like designs to match the P/D and SF implied from the neutronic models.

Table 9-2 summarises the specifics of the best designs for the four design streams. In PWR-like models with 100 wt% SF, the fuel channel diameter equalled the assembly pitch. The annular FCM fuelled design stream did not have matching thermal-hydraulic data. Even after

mapping to PWR-like design space, the largest P/D value in the annular fuel thermal-hydraulic models did not reach 5.2 as suggested by the neutronic models. Therefore, as discussed in Chapter 8, no accurate thermal-hydraulic and capital cost estimations could be performed for the annular fuel FHRs. Table 9-2 shows reasonable speculative ranges for coolant inlet temperature, pressure drop and adjusted LCOE for the annular designs.

Table 9-2. Specifications of final optimised FHRs

slvR *(cm)*	*Asmbl. pitch* *(cm)*	*# of pins*	*Ue5* *(wt%)*	*P/D*	*SF* *(wt%)*	T_{in} *(°C)*	Δp *(kPa)*	*Pow* *(MWt)*	*BU/e* *(MWd/kg)*	*BU* *(MWd/kg)*	*adj. LCOE* *(£/MWh)*
AGR-like FHRs											
AGR-like solid FCM fuel with FLiBe coolant											
18.5	49.1	270	17.5	2	40	638	400	28861	7.2	126	35.3
19	44.8	168	17.5	2.4	60	668	100	16349	9.5	166	41.7
19	44.8	168	15	2.4	60	668	100	16349	9.4	141	41.7
AGR-like solid UC fuel with FLiBe coolant											
15	38.2	36	20	4.4	20	688	50	6069	11.1	55	65.7
PWR-like FHRs											
fuel chann. d (cm)	*Asmbl. pitch* *(cm)*	*# of pins*	*Ue5* *(wt%)*	*P/D*	*SF* *(wt%)*	T_{in} *(°C)*	Δp *(kPa)*	*Pow* *(MWt)*	*BU/e* *(MWd/kg)*	*BU* *(MWd/kg)*	*adj. LCOE* *(£/MWh)*
PWR-like annular FCM fuel with FLiBe coolant											
45.3	45.3	36	20	5.2	100	<652	200	>34323	3.1	61	<30
45.3	50.6	36	20	5.2	80	<652	200	>34323	3.9	77	<30.5
PWR-like solid UC fuel with $NaF\text{-}ZrF_4$ coolant											
34.6	34.6	36	12.5	4	100	693	50	5319	1.9	24	79.4

Among the four design options, the FLiBe cooled solid FCM pin FHR with AGR-like assembly had the best combination of low LCOE (35.3 £/MWh to 41.7 £/MWh) and high BU/e (7.2 MWd/kg to 9.5 MWd/kg). The FLiBe cooled solid UC fuel FHR in AGR-like assembly had a higher LCOE (65.7 £/MWh), but better fuel cycle economics (BU/e of 11.1 MWd/kg). The PWR-like variations of these two design streams had less favourable performance in terms of both neutronics and thermal-hydraulics. The annular FCM fuel FHR with FLiBe coolant required PWR-like configuration. It had somewhat lower LCOE (< 30 £/MWh) than the solid FCM fuel design with FLiBe coolant, but much poorer neutronic performance (BU/e of 3.1

MWd/kg to 3.9 MWd/kg). The NaF-ZrF_4 cooled FHR also required PWR-like configuration. Tritium generation problem could be avoided in reactors using NaF-ZrF_4 coolant, but these reactors required Zirconium enrichment and had the poorest neutronic (1.9 MWd/kg BU/e) and thermal-hydraulic performance (LCOE of 79.4 £/MWh) among all four design streams explored.

It should be emphasised that LCOE should be valued more than fuel cycle cost and, therefore, it is worth sacrificing the neutronic performance to achieve higher power density (lower LCOE) as long as no safety constraint is breached.

The LCOEs reported in this thesis were calculated based on many assumptions made in SCOOP. The CapCost module in SCOOP applied a scaling rule for the cost estimations of the whole power plant, which itself had its simplifications and uncertainties. Similarly, the scaling rule applied to adjust the LCOE for designs that deviated from AGR dimensions introduced further uncertainties. Among the variables used in SCOOP, the LCOE was most sensitive to the specifics (especially the power output) of the reference reactor used in CapCost and the maximum fuel temperature limit used in SODom. Increasing the power output of the reference reactor would shift the points in Figure 9-1 horizontally to the right and lowering the fuel temperature limit would decrease the power of the designs constrained by the limit, which was the case for all the designs reported in Table 9-2. Many other factors also influenced the value of LCOE such as the scaling exponent of the variable capital cost with heat transfer system cost, the cost distribution across different components of the NPP and the power peaking factor. Also, the fuel enrichment cost and the difference in manufacturing cost of different fuel materials and fuel forms were not taken into account in SCOOP, although these would be considered less significant factors in the economics for the whole power plant. Despite the assumptions and simplifications made in SCOOP, the trends and trade-off identified from the calculation of LCOE across the design space remain robust and can be used as reference for future design work. Recommendations of future work on SCOOP is included in the last section of this chapter.

9.3 Discussions on FHR Design Options

The PWR-like annular pin FHR using FLiBe coolant had the cheapest electricity cost, making it the most desirable design in terms of economics. It also required little to zero graphite content, which could simplify the operations, maintenance and extend the NPP lifetime. The fuel cycle

economics for this design option is relatively poor but this should not be considered a showstopping factor.

However, the annular fuel pin design stream may not be a viable FHR candidate due to a number of concerns. Firstly, the optimal annular fuel pins were found to be very thin, ~ 0.7 cm, and had relatively large radii. These tube-like fuel designs differed significantly from the previously studied annular pin options, which have much larger fuel thicknesses. [25] The manufacturability, fuel behaviour under irradiation and the coolant flow rate limits for such configurations are largely unknown and must be further investigated. Furthermore, the annular pin designs have very large P/Ds and used FCM fuel, resulting in small HM loading, e.g., 22.5 kg/element in the best annular pin design, comparing with AGR (44 kg/element). The design stream had discharge burnups of ~60 MWd/kg to 80 MWd/kg and a core power greater than 35000 MWt. These designs would need to refuel ~75 to 95 assemblies per month. Comparing with AGR, which refuels about 5 to 7 assemblies per month, this could be difficult to manage. [24] To reduce the refuelling frequency, power must be reduced which would render the annular FCM design stream much less competitive than the solid pin designs. It could be possible to have the annular pins made thicker and used as a replacement for solid pins. This could potentially mitigate the fuel loading and structural integrity issues seen in annular pins while delivering somewhat greater power than the solid pin designs. However, this would come at a cost of less efficient conductive heat transfer compared with the current fuel design. Furthermore, there would be an uneven temperature distribution between the internal and external coolant, which would shift the hottest temperature line in the fuel to the hotter side, increasing the maximum fuel temperature. The actual power uprate potential of this design might not turn out to be substantial enough to compensate for its disadvantages in neutronics. Nevertheless, this could be an attractive design concept for future work, which would require both computational modelling and experimental tests on the fuel form.

The second-best design stream (in terms of LCOE), the AGR-like FLiBe cooled solid pin FHR, uses a more traditional fuel form and the better understood AGR-like assembly design. It also considerably lower than the Hinkley Point C strike price. Fuel loading is still a problem for the FCM fuelled option: with a HM loading ranging from 14 kg/element to 23 kg/element, the best three FCM fuelled solid pin FHRs have to refuel ~ 25 to 37 assemblies per month, i.e., roughly one assembly per day. If the safety case for refuelling at full-power can be made for AGR-like FHR, this refuelling scheme could be manageable without affecting the economics of the reactor. Otherwise, this design stream would have to reduce power to lower the refuelling

frequency. The refuelling scheme for the UC fuelled solid pin FHRs is much simpler. With a HM loading of 63.9 kg/element, this design stream requires ~6 assemblies to be replaced per month, which is about the same frequency as the reference AGR operation.

In addition to the problems with fuel loading and fuel form, as discussed in Chapter 8.3, the high coolant flow velocity in the final optimised FHRs also requires attention. If such high values prove to be problematic for FHRs, power density and LCOE may need to be compromised. It was found that the greatest performance impact of such restriction on flow velocity would be on the best UC fuelled FLiBe cooled design streams. In future studies, limits on flow velocity for different salts under different operating conditions shall be experimentally established and applied as a design constraint for the FHR.

Integrating the above analyses, the solid pin AGR-like reactor with FLiBe coolant appears to be the most promising option in the design space covered in this thesis. Although tritium produced in the FLiBe coolant would require extra investments in tritium removal systems, the high power density is still likely to help make a very appealing economic case for the reactor. Comparing the fuel material options, the FCM fuel is more attractive than UC fuel in terms of both NPP economics and fuel cycle economics. The coolant flow velocity was also smaller in in the FCM fuelled designs. Considering construction time and practicality of grid connection in future energy market, the SMR variant of the solid FCM fuelled FHR with AGR-like assembly design and FLiBe coolant would be recommended as the best future FHR option derived from this thesis for further study. Based on the thermal-hydraulic data obtained in this thesis, such an FHR with ~1600 MWt power would have an active core size of ~28 m^3. In a smaller core, the safety case for online-refuelling at full power would also be easier, which is crucial for this design option which relies on a rather short refuelling cycle.

The NaF-ZrF_4 cooled PWR-like FHR using solid UC fuel pins would be the best backup design option explored in this thesis in case the tritium problem turns out to be a showstopper for Li and Be containing salts. This design option can fit within AGR core dimensions. Therefore, many of the AGR technologies can be borrowed directly and the research and development requirements can be reduced. The best NaF-ZrF_4 cooled design achieved power uprate by a factor of about 3.2 from AGR level, had a reasonable LCOE of 79.4 £/MWh and similar discharge burnup as the AGRs. However, it used much higher U235 enrichment (12.5 wt%) than AGRs, resulting in poorer fuel cycle economics (BU/e of 1.9 MWd/kg). The refuelling frequency for this design is ~13 assemblies per month, which is reasonably manageable. A

rather conservative constraint on the reactivity coefficients was applied on the reactors with NaF-ZrF_4 coolant, which greatly limited the reactors' neutronic potential. It is possible to have this constraint made less conservative to allow better neutronic performance. In which case the NaF-ZrF_4 cooled FHR might work with solid FCM fuel, which would have much smaller P/Ds than the UC fuelled ones and therefore could achieve higher power and lower LCOE.

9.4 Recommendations for Future Work

9.4.1 Refinement of Assumptions

Some understanding of the design space was established in this thesis, and four final design streams were recommended. However, to make efficient use of time and resources, some important design limits were applied without validation in FHR environment or neglected completely. These assumptions should be rigorously verified with experiments and/or more sophisticated computational models.

Firstly, future work shall examine whether the constraints on reactivity coefficients can be made less restrictive. The reactivity feedback limit used in this thesis can likely be relaxed. They were set for BOL CTC and DC separately at BOL for conservatism, where, in fact, the combined reactivity feedback effects of all components of the core determine the transient behaviours even though the reactivity feedbacks act at different time scales. Also, both CTC and DC become more negative with depletion in all FLiBe cooled reactors, so the core average reactivity coefficient of an on-line refuelled reactor during operation would be lower than its BOL reactivity coefficients. As found during the design work for LS-VHTR, careful fuel management can help to 'lock in' the core average reactivity feedbacks to the desired range. [65] This is important because the optimum frontiers that govern the trade-off between CTC, DC and BU/e were all very flat. This means that considerably better neutronic performance can be achieved if the reactivity coefficient limit is raised slightly. For example, if a -1pcm/K limit on BOL CTC and DC instead of the -2pcm/K limit was used, the NaF-ZrF_4 cooled reactor could reach BU/e of 4.8 MWd/kg with a discharge burnup of 84 MWd/kg. The resulting optimum design would also be expected to have less coolant and more graphite, which would lead to different assembly configurations. In order to establish what value is acceptable, a full range of operational transients and accident scenarios needs to be analysed. Of course, the feasibility and affordability of highly enriched Zirconium in NaF-ZrF_4 also needs to be a subject of investigation.

Another design constraint that requires attention is the coolant flow velocity limit. It was acknowledged in this thesis and some simple sensitivity study results were reported. However, the flow velocity constraint was not incorporated as a design limit in the computational design tools. This must be established in future work as it may limit the power output of the reactors and may render some of the best designs identified in this thesis less competitive. Furthermore, the maximum fuel temperature limit during normal operation should be experimentally validated in future work although reasonable assumptions of the fuel temperature limits for different fuel materials were made in this thesis. This limit directly relates to the allowable power, thermodynamic efficiency and, ultimately, the economics of a reactor. Traditional reactors operate with very large margins to fuel failures, but salt cooled systems reactor provide greater thermal inertia than LWRs and AGRs which may allow higher operating temperatures. Similarly, realistic power peaking factor assumptions should be incorporated in the analysis and validated using full core neutronic simulations. There are also other limits used in this thesis that need further validation. For example, the critical heat flux criterion, maximum discharge burnup limit, minimum coolant inlet temperatures limit, minimum Re limit, etc. Experimental studies on these limits are recommended.

9.4.2 Refinement of Computational Tools

Modification of the computational tools built in this thesis and development of more accurate and sophisticated models and computational schemes is recommended for future work. The thermal-hydraulic design space exploration module SODom and the system heat transfer design optimisation module optSys developed in SCOOP employed widely accepted heat transfer correlations and a set of realistic simplifying assumptions. Although this framework of tools could provide reasonable level of accuracy and confidence for the purposes of the preliminary reactor design, as the research work evolves to more advanced design stages, greater confidence in the models would be required, especially for reactors using unconventional geometries and materials, for which the traditional correlations and heat transfer data might not be applicable. Therefore, SODom and sysOpt should ideally incorporate 3-D computational fluid dynamics solvers in latter stages of the FHR development. Multiphysics computational tools that couple 3-D thermal-hydraulic solvers with neutronic solvers would be desirable for this application. Also, other intermediate heat transfer loop salt options, such as FLiNaK, shall be investigated in optSys in future studies.

All reactor designs in this thesis were assumed to have a core outlet temperature of 700 °C, i.e., highest possible bulk coolant temperature assuming Hastelloy N material limits. This was based on the assumption that higher coolant outlet temperature could lead to greater power cycle efficiencies. However, this might not be the optimum operating condition considering power maximisation and cost reduction. Firstly, it is the average core temperature, instead of the core outlet temperature, that determines the power cycle efficiency. Also, it was seen from the operating domains for FHRs (e.g., in Figure 3-5) that 'maximum power boundary' had a negative slope. This means that by reducing coolant outlet temperature and cycle efficiency, greater power density could be achieved. To determine the optimum operating point along the boundary, a power cycle design optimisation module should be implemented in SCOOP and coupled to the optSys module. This module should be able to produce the optimised sCO_2 power cycle design and the corresponding power conversion efficiency given the intermediate loop temperature conditions. This work can be performed for example using a Brayton Cycle optimisation code CYCLE and a heat exchanger design code KAIST-HXD, from the result of which the sCO_2 cycle design was used in this thesis. [57][58][66]

The CapCost module only considered the cost of the heat exchangers and the pumps in the primary and intermediate loop as a reference for variable cost scaling. The cost of other components within the plant could also be incorporated into the CapCost to provide more justifiable cost estimations. Also, the capital cost scaling rule in CapCost used a plant average scaling exponent for all plant components. In future studies, a more sophisticated cost scaling rule can be developed with different scaling exponents for different power plant components. CapCost should also ideally incorporate different cost estimations schemes for SMRs and large reactors. Additionally, the cost of heat exchangers and pumps were estimated using many assumptions, such as the price of electricity, the cost of manufacturing and cost of materials. Although these assumptions were justified in previous research work, they could change depending on evolving market conditions, technological advancements etc. and therefore should be re-evaluated in future work to keep the calculations realistic and up to date with the current development of the technology and market for heat exchangers and pumps. [39][40] Furthermore, fuel enrichment, burnup and fuel fabrication cost factors shall be quantified and incorporated in CapCost.

For the neutronic simulations, due to availability of computational resources and limited time frame, homogeneous unit cell models were used to represent the assembly level models and power was assumed to be three times that of the AGR. In future work, the development of

representative assembly models that can replicate the performance of the unit cell models and coupling to thermal-hydraulic solvers are needed. For SMR-sized FHRs, full core 3-D models is recommended to identify the power profile, power peaking factor and leakage.

9.4.3 Further Work on Reactor Design, Materials and Engineering

All four design streams recommended in this thesis and some less attractive candidates that were ruled out due to hard design limits assumed in this study worth more detailed design optimisation to finalise the designs and evaluate their performance, safety, and economic trade-offs.

Firstly, future modelling may consider an SMR setup: all three FLiBe cooled design streams recommended in this thesis would require much smaller core sizes to be compatible with grid demand. A small reactor would have different thermal-hydraulics and neutronics from the AGR-like assembly and unit cell models used in this thesis. The fuel channels would be shorter, which would lead to different pumping requirements and coolant flow conditions. The power peaking factor would also be higher in a smaller core. In terms of neutronics, neutron leakage would be much greater and harder spectrum would be expected in an SMR. Therefore, future thermal-hydraulic and neutronic studies on the first three design streams shall be carried out using SMR dimensions. The SMR-sized solid pin fuelled AGR-like FHR is recommended as the baseline design in future work as it has good thermal-hydraulic and neutronic performance and requires the least design modification to the well-understood AGR configuration. The biggest concern for this design stream is its high refuelling frequency (~25 to 37 assemblies per month). The safety case for online refuelling at full power, i.e., the assembly drop accident shall be investigated in future work. Experimental tests of dropping unfuelled elements into SMR assembly-sized channels filled with liquid with similar thermal-physical properties as FLiBe is recommended.

Secondly, future work should perform local design space optimisation with finer resolution on all design parameters as all neutronic models in this thesis were created with a relatively coarse resolution for varying the SF and P/D parameters, and the thermal-hydraulic design space was tailored to fit the neutronic model specifications. Therefore, there is a potential for further optimisation of all the recommended models in this thesis which deserves extensive research. Variations of the proposed designs also worth evaluating. For example, the graphite can be made into graphite pins or tubes instead of graphite cylinder (or box in some PWR-like designs) so that there is no physical boundary between the assembly channels, essentially making the

cores completely PWR-like. Such assembly models would have less heterogeneity and would be expected to agree better with the unit cell neutronic models. Although the thermal-hydraulics would be different, revisiting thermal-hydraulics with SCOOP is fast and convenient. Furthermore, thicker annular pins might be allowed under the design target of consistent internal and external axial coolant temperature profiles. If not, this limit can be relaxed, so that the pins can be made thicker with smaller internal channels. This fuel form could potentially replace the solid pins in the AGR-like FHRs for greater power density. Thermal-hydraulic and neutronic modelling and experimental tests shall be performed to examine its feasibility.

Thirdly, cost benefit analysis should be carried out to quantify the design trade-offs among all design options. The FCM fuel offers greater cost reduction and has better inherent safety than UC as well as non-proliferation features, but it would have higher fuel fabrication and reprocessing costs. UC fuelled AGR-like designs have higher LCOE, but much more manageable refuelling schemes. Although UO_2 has less attractive heat transfer properties, it is also recommended for future studies as it is the most understood fuel material in nuclear industry and has similar neutronic performance as UC. FLiBe outperforms NaF-ZrF_4 considerably both in terms of neutronics and thermal-hydraulics. However, to use FLiBe coolant, tritium removal and storage systems must be in-place. If this proves to be prohibitively complex or economically undesirable, the PWR-like solid UC pin fuelled reactor with NaF-ZrF_4 coolant can be a good backup design option. The FCM fuelled reactors with NaF-ZrF_4 coolant design was not recommended in this thesis because it did not meet the reactivity coefficient requirement. In future research for the NaF-ZrF_4 cooled design stream, depletion simulations with high statistics and transient simulations should be carried out to obtain more realistic estimations of the limits on reactivity coefficients. If these limits turn out to be less restrictive than the ones used in this thesis, there is potential for significant neutronic performance improvement for the NaF-ZrF_4 cooled reactors. In the best-case scenario, the NaF-ZrF_4 coolant might be able to work with solid FCM pins with smaller P/Ds, where the power would be much greater and LCOE would be much lower than the recommended UC fuel with NaF-ZrF_4 option. Other tritium-free salts should also be investigated.

The annular FCM pin design stream has the lowest LCOE in this thesis but has unpractically high refuelling frequency. To address this issue, UC and other fuel materials with high fissile loading shall be investigated in annular fuel form. Although it was shown that the UC annular fuel option was prohibitively thin, the dimensions are not finalised. In fact, all the annular fuel

dimensions in the thermal-hydraulic and neutronic design spaces in this thesis did not match perfectly. This was due to the geometrical difference between the unit cell models and the assembly models used in the neutronic and thermal-hydraulic simulations. Nevertheless, the fuel pins in both models were tube-like, i.e., thin and large diameter with relatively small fuel loading and unknown fuel behaviour. In future work, coupled assembly level thermal-hydraulic and neutronic design work shall firstly be carried out using fuel materials with higher fissile loading and with less restrictive constraints on CTC, if possible. If the resulting fuel pin still turns out to be thin and large, experimental tests shall be conducted to examine the manufacturability, robustness and other qualities of the fuel form.

Once the optimised design is identified and materials properties are experimentally validated, more neutronic, multi-physics and engineering research work must be carried out to refine the designs. This work should include but not limited to 1) evaluation of shut down margin requirements with depletion and design of the necessary reactivity control mechanisms, 2) reactor transient behaviour, 3) in-core fuel management, 4) heat transfer system and power conversion cycle optimisation, 5) emergency shut-down and decay heat removal systems, 6) consideration of Beyond-Design-Basis accidents, 7) spent fuel management and 8) NPP system design optimisation. Tightly coupled multi-physics and system power conversion design platforms shall be developed for these tasks.

References

[1] V. Masson-Delmotte, P. Zhai, H. O. Pörtner *et al.* 2018: Global warming of 1.5°C: An IPCC Special Report on the impacts of global warming of 1.5°C above pre-industrial levels and related global greenhouse gas emission pathways, in the context of strengthening the global response to the threat of climate c. Intergovernmental Panel on Climate Change, 2018.

[2] Technology roadmap update for Generation IV Nuclear Energy Systems. Nuclear Energy Agency, Organisation for Economic Co-operation and Development, 2014.

[3] C. Forsberg, L. Hu, P. Peterson *et al*. Fluoride-salt-cooled High Temperature Reactor commercial basis and commercialization strategy. MIT Cent. Advanced Nucl. Energy Syst., MIT-ANP-TR-153, 2014.

[4] R. Hecker, W. Rausch, and R. Schulten. Development of high temperature thermal reactors in Germany. EUR 3493. Kernforschungsanlage Jülich des Landes Nordrhein-Westfalen e.V. Jülich, Germany, 1967.

[5] C. Forsberg. Alternative passive decay-heat systems for the advanced high-temperature reactor. In *proceedings of ICAPP'06*, Reno, NV USA, June 4-8, paper 6055, 2006.

[6] C. Forsberg, P. F. Peterson, and L. Ott. The Advanced High-temperature Reactor (AHTR) for producing hydrogen to manufacture liquid fuels. In *proceedings of Americas Nuclear Energy Symposium*, Miami Beach, Florida, USA, Oct 6 2004.

[7] L.Qingnuan. Current U.S. & world status of Fluoride salt-cooled High-temperature Reactors. CAS Center for Excellence in TMSR Energy System, Shanghai, 2014.

[8] G. Locatelli, M. Mancini, and N. Todeschini. Generation IV nuclear reactors: Current status and future prospects. *Energy Policy*, vol. 61, pp: 1503–1520, 2013.

[9] J. H. Germer. Radiant vessel auxiliary cooling system. US Patents, Contract No. DE-AT03-83SF11699 in 24BR04755, 07-Jul-1987.

[10] J. J. Powers, W. J. Lee, F. Venneri *et al*. Fully Ceramic Microencapsulated (FCM) replacement fuel for LWRs. Oak Ridge National Lab.(ORNL), Oak Ridge, TN, US, KONL/TM-2013/173, KAERI/TR-5136/2013,2013.

[11] C. Andreades, A. Cisneros, J. Choi *et al.* Technical description of the 'Mark 1'pebble-bed fluoride-salt-cooled high-temperature reactor (PB-FHR) power plant. UCBTH-14-002, University of California, Berkeley, Sep 2014.

[12] Y. Lee, N. Z. Cho, Steady-and-transient-state analyses of fully ceramic microencapsulated fuel loaded reactor core via two-temperature homogenized thermal-conductivity model. *Annals of Nuclear Energy*, vol. 76, pp: 283–296, 2015.

[13] C. Forsberg, L. Hu, P. F. Peterson *et al*. Fluoride-Salt-Cooled High-Temperature Reactors for power and process heat. 2012 World Nucl. Univ. Inst., pp: 1–2, 2012.

[14] C. Forsberg, P. F. Peterson. Basis for Fluoride Salt–Cooled High-Temperature Reactors with Nuclear Air-Brayton Combined Cycles and Firebrick Resistance-Heated Energy Storage. *Nuclear Technology*, vol. 196 (1), pp: 13–33, Oct. 2016.

[15] T. Kim, T. Taiwo, and W. Yang. Preliminary neutronic studies for the Liquid-Salt-

cooled Very High Temperature Reactor (LS-VHTR). Argonne National Lab., Argonne, USA, ANL-GenIV-052, 2005.

[16] P. Peterson, H. Zhao. A flexible base-line design for the advanced high-temperature reactor utilizing metallic reactor internals (AHTR-MI). In *proceedings of ICAPP'06*, Reno, USA, June 4-8, 2006.

[17] A. Cisneros, Pebble bed reactors design optimization methods and their application to the Pebble Bed Fluoride Salt Cooled High Temperature Reactor (PB-FHR). Doctoral dissertation, Massachusetts Institute of Technology, Cambridge, Boston, MA, 2013.

[18] A. Griveau, F. Fardin, H. Zhao, and P. F. Peterson. Transient thermal response of the PB-AHTR to loss of forced cooling. In *proceedings of Global 2007*, Boise, Ohio, Sep 3-17, 2007.

[19] P. Bardet, E. Blandford, M. Fratoni *et al*. Design, analysis and development of the modular PB-AHTR 3D fuel management for breed-and-burn reactors View project AP600/AP1000 Containment Cooling Design Basis View project Design, Analysis and Development of the Modular PB-AHTR. In *proceedings of ICAPP'08*, Anaheim, CA USA, June 8-12, 2008.

[20] R. Hong, S. Huber, K. Lee *et al*. Reactor safety and mechanical design for the annular pebble-bed advanced high temperature reactor. 2009 NE 170 Senior Design Project, University of California, Berkeley, May 19 2009.

[21] D. Ilas, D. E. Holcomb, and V. K. Varma. Advanced High-Temperature Reactor neutronic core design. In *proceedings of Physor 2012, Linking Res. Ind. Educ.*, Knoxville, Tennessee, USA, April 15-20, 2012.

[22] G. P. C. Forsberg, J. Richard, J. Pounders, R. Kochendarfer, K. Stein, E. Shwageraus. Development of a Fluoride-Salt-Cooled High-Temperature Reactor (FHR) using Advanced Gas-Cooled Reactor Technology. In *transactions of ANS Summer Meeting*, San Antonio, TX, 2015.

[23] A. Qualls, N. Brown, B. Betzler *et al.*, Fluoride salt-cooled high-temperature demonstration reactor point design. Oak Ridge Natl. Lab. (ORNL), Oak Ridge, TN, US, ORNL/TM-2016/85, 2016.

[24] E. Nonbøl et. al. Description of the advanced gas cooled type of reactor (AGR). Nordisk Kernesikkerhedsforskning, Risø National Lab., Rskilde, Denmark, NKS/RAK2(96)TR-C2, 1996.

[25] M. S. Kazimi, P.Hejzlar *et al.* High performance fuel design for next generation PWR. Center for Advanced Nuclear Energy Systems, MIT., MIT-NFC-OR-082, Jan 2006

[26] C. Forsberg, P. Peterson, and P. Pickard. Molten-Salt-Cooled Advanced High-Temperature Reactor for production of hydrogen and electricity. *Nuclear Technology*, vol: 144(3) pp: 289–302, Dec. 2003.

[27] D. F. Williams. Assessment of candidate molten salt coolants for the NGNP/NHI heat-transfer loop. Oak Ridge National Lab.(ORNL), Oak Ridge, TN, US, ORNL/TM-2006/69, 2006.

[28] Z. Xu. Design strategies for optimizing high burnup fuel in pressurized water reactors. Doctoral dissertation, Massachusetts Institute of Technology, Cambridge, Boston, MA, January 2003.

[29] J. Leppänen. Serpent – a continuous-energy Monte Carlo reactor physics burnup calculation code. VTT Tech. Res. Cent. Finl., vol. 4, 2013.

[30] Y. Shaposhnik, E. Shwageraus, and E. Elias. Thermal-hydraulic feedback module for BGCore system. In *proceedings of the 24th Conference of the Nuclear Societies in Israel*, Dead See, Israel, Feb 2008.

[31] V. Bobkov, L. Fokin, E. Petrov, *et al*. Thermophysical properties of materials for nuclear engineering: a tutorial and collection of data. Int. At. Energy Agency, Vienna, Austria, 2008.

[32] M. S. Sohal, M. A. Ebner, P. Sabharwall, and P. Sharpe. Engineering database of liquid salt thermophysical and thermochemical properties. Idaho National Lab. (INL), Idaho, US, INL/EXT-10-18297, 2010.

[33] N. Todreas and M. Kazimi. *Nuclear systems Volume II: Elements of thermal hydraulic design*, Taylor and Francis, ISBN 1-56032-079-6, 1990.

[34] P. Avigni. Thermal hydraulic modeling of the advanced high temperature reactor for the evaluation of steady state and transient conditions. Masters' thesis, Politecnico Di Milano, 2013.

[35] N. Todreas and M. Kazimi. *Nuclear Systems Volume I: Thermal Hydraulic Fundamentals*. Hemisphere Publishing Corporation, ISBN 1-56032-051-6, 1989.

[36] J. Hesselgreaves, R. Law, and D. Reay, *Compact heat exchangers: selection, design and operation*. A. Kramden, Ed., ANS, La Grange Park, Illinois, p. 25, 2008.

[37] V. Dostal. A supercritical carbon dioxide cycle for next generation nuclear reactors. Doctoral dissertation, Massachusetts Institute of Technology, Cambridge, Boston, MA, 2004.

[38] P. Sabharwall, E. Kim, A. Siahpush. Feasibility study of secondary heat exchanger concepts for the advanced high temperature reactor. Idaho Natl. Lab. (INL), Idaho, US, INL/EXT-11-23076, 2011.

[39] Department for Business Energy & Industrial Strategy. Electricity generation costs. HM Government, 2015.

[40] E. Kim, *et al*., Simplified optimum sizing and cost analysis for compact heat exchanger in VHTR. *Nuclear Engineering and Design*, vol: 238 pp: 2635-2647, 2008.

[41] Generation IV Economic Modelling Working Group. Cost estimation guidelines for Generation IV nuclear energy systems. IAEA, GIF/EMWG/2007/004, 2007

[42] M. D. Carelli et al., Economic features of integral, modular, small-to-medium size reactors. *Progress in Nuclear Energy* vol.52 (52) pp: 403-414, 2010.

[43] T. Fei. Innovative design of uranium startup fast reactors. Doctoral dissertation, Massachusetts Institute of Technology, Cambridge, Boston, MA, 2012.

[44] EEDB (Energy Economic Data Base). Phase IX update (1987) report for the EEDB program (DOE/NE-0091), United Engineers & Constructors Inc. and Oak Ridge National Laboratory, Philadelphia, 1988.

[45] C. A. Lloyd. Modular manufacture and construction of small nuclear power generation systems. Doctoral dissertation, University of Cambridge, Cambridge, United Kingdom,

2019.

[46] J. Leppänen *et al*., Performance of Woodcock delta-tracking in lattice physics applications using the Serpent Monte Carlo reactor physics burnup calculation code. *Annals of Nuclear Energy*, vol: 37 (5) pp: 715-722, 2010.

[47] J. Leppänen *et* al., Two practical methods for unionized energy grid construction in continuous-energy Monte Carlo neutron transport calculation, *Annals of Nuclear Energy*, vol: 36 (7) pp: 878-885, 2009.

[48] S. Greene *et al*., Pre-conceptual design of a fluoride-salt-cooled small modular advanced high-temperature reactor (SmAHTR). Oak Ridge Natl. Lab. (ORNL), Oak Ridge, TN, US, ORNL/TM-2010/199, 2010.

[49] J. Phillips, C. Barnes, and J. Hunn. Fabrication and comparison of fuels for advanced gas reactor irradiation tests. Idaho Natl. Lab. (INL), Idaho, US, INL/CON-10-18865, 2010.

[50] J. Hunn, R. Morris, C. Baldwin *et al*., Safety Testing of AGR-2 UCO compacts 6-4-2 and 2-3-1. Oak Ridge Natl. Lab. (ORNL), Oak Ridge, TN, US, ORNL/TM-2017/439, 2018.

[51] J. Hunn, C. Baldwin, F. Montgomery *et al*., Initial examination of fuel compacts and TRISO particles from the US AGR-2 irradiation test. Oak Ridge Natl. Lab. (ORNL), Oak Ridge, TN, US, Contract No. DE-AC05-00OR22725, US Dept. of Energy, 2018.

[52] J. Stempien, R. Ballinger, and C. Forsberg. A model of tritium transport and corrosion in salt-cooled reactors. In *Transactions of the ANS Winter Meeting*, Washington D.C, 2015, vol. 15081, pp: 8–12.

[53] C. Forsberg, J. Stempien, R. Ballinger. Tritium removal from salt-cooled reactors using carbon. In *Transactions of the ANS Winter Meeting and Nuclear Technology Expo*., Washington D.C, 2015.

[54] R.Romatoski, L. Hu, C. Forsberg. Thermal hydraulic licensing limits for a prismatic core Fluoride-salt-cooled High-temperature Reactor," In *proceedings of ICAPP'14*, Charlotte, NC, April 6-9, 2014.

[55] R. E. Gehlbach and H. E. McCoy. Phase instability in Hastelloy N. in *International Symposium on Structural Stability in Superalloys (Warrendale, PA: TMS, 1968)*, pp. 346–366, 1968.

[56] D. E. Holcomb, D. Ilas, V. K. Varma *et al*. Core and refueling design studies for the Advanced High Temperature Reactor. Oak Ridge Natl. Lab. (ORNL), Oak Ridge, TN, US, ORNL/TM-2011/365, Sep. 2011.

[57] Y. Ahn, S. Bae, M. Kim *et al*. Review of supercritical CO_2 power cycle technology and current status of research and development. *Nuclear Engineering and Technology*, vol: 47 (6) pp: 647-661, 2015.

[58] W. S. Jeoung, J. I. Lee, Y. H. Joeng. Potential improvements of supercritical recompression CO_2 Brayton cycle by mixing other gases for power conversion system of a SFR. *Nuclear Engineering and Design*, vol: 241 (6) pp: 2128-2137, 2011.

[59] D. Southall, R. Le Pierres, and S. J. Dewson, Design considerations for compact heat exchangers. In *proceedings of ICAPP'08,* Anaheim, Jun 8-12 2008.

[60] E. Ronander, H. Strydom, J. Vijoen. ASP separation technology for isotope and gas separation. Klydon (Pty) Ltd, CSIR Campus, Meiring Naude Rd, Brummeria, Pretoria, South Africa, 2012.

[61] H. Strydom, E. Ronander, J. Viljoen, G. Kemp, and J. Grant. Production of 100 Mo for Cyclotron conversion to 99m Tc. Klydon (Pty) Ltd, CSIR Campus, Meiring Naude Rd, Brummeria, Pretoria, South Africa, 2016.

[62] M. Driscoll, T. Downar, and E. Pilat, *The linear reactivity model for nuclear fuel management*. American Nuclear Society, pp:233, 1990.

[63] C. Vitanza and M. Hrehor. Review of high burn-up RIA and LOCA database and criteria. Nuclear Energy Agency, NEA/CSNI/R(2006)5, 2006.

[64] H. Smyth, L. Lecoeuvre, P. Vaesken. Co-creation of value and the project context: Towards application on the case of Hinkley Point C Nuclear Power Station. *International Journal of Project Management*, vol: 36 (1) pp: 170-183, 2018.

[65] D. T. Ingersoll, *et* al. Status of physics and safety analyses for the liquid-salt-cooled very high-temperature reactor (LS-VHTR). Oak Ridge Natl. Lab. (ORNL), Oak Ridge, TN, US, ORNL/TM-2005/218, 2005.

[66] Y. Ahn, & J. I. Lee. Study of various Brayton cycle designs for small modular sodium-cooled fast reactor. *Nuclear Engineering and Design*, *276*, 128-141. 2014

Appendix A - FHR Technology Background

A.1 The Pebble Bed FHR

A.1.1 Mark-1 (Mk1) PB-FHR

The Mk-1 PB-FHR is the commercial prototype FHR preconceptual design under the NEUP IRP. It is a pebble bed FHR reactor with 236 MWt (100 MWe) output operating with coolant core inlet and outlet temperatures between 600 ºC to 700 ºC respectively. The reactor vessel diameter was limited to 3.5 m and could be transported by railway or trailer truck. The reactor is coupled to Nuclear Air-Brayton Combined Cycle (NACC) based upon a modified General Electric 7FB gas turbine with a 100 MWe baseload output. Using gas co-firing, this power can be ramped up to 242 MWe for peak electricity generation. The small size is intended to benefit from modularisation and limit the risk associated with large scale reactors.

The reactor core is annular shaped like the PB-AHTR and fuelled with pebbles with 19.9 wt% enriched TRISO particles fuel. The pebbles are 3 cm in diameter. They are formed by three layers: the inner low-density graphite kernel, the fuelled layer and the high-density graphite surface layer. Inside the core, the fuel containing pebbles are surrounded by a layer of graphite reflector pebbles which shield the outer structural components. All pebbles are inserted into the core from the bottom and are collected at the top of the core. The Mk1 FHR is primarily controlled by manging the fuel pebble insertion rate and the control rod insertion. There are also shutdown blades that can be inserted into the core in accident scenarios. Figure A-1 shows the vertical cutaway view of the Mk1 FHR reactor vessel. [11] A schematic plot of the PB-FHR power plant is shown in Figure A-2.

FLiBe coolant flows through the core in axial direction (bottom to top) as well as in radial (from inner reflector assembly) direction. It is then mixed at the outlet plenum, where it is collected and pumped through the coiled tube air heaters (CTAHs) and then returns to the core through the downcomer around the reactor vessel. The secondary loop takes the heat from the CTAHs and sends it to a NACC power conversion loop. [11]

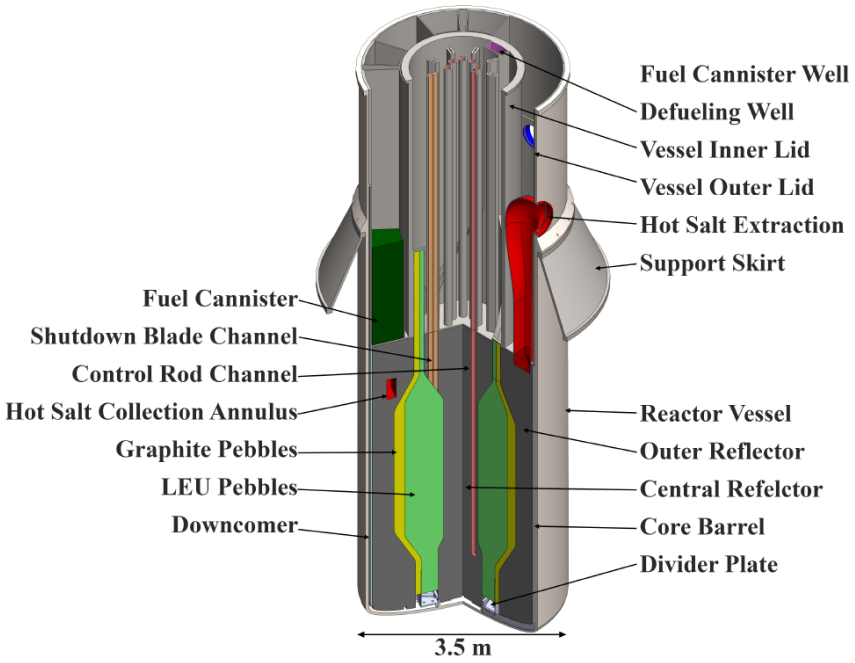

Figure A-1. Cut-away view of the Mk1 core and reactor vessel [17]

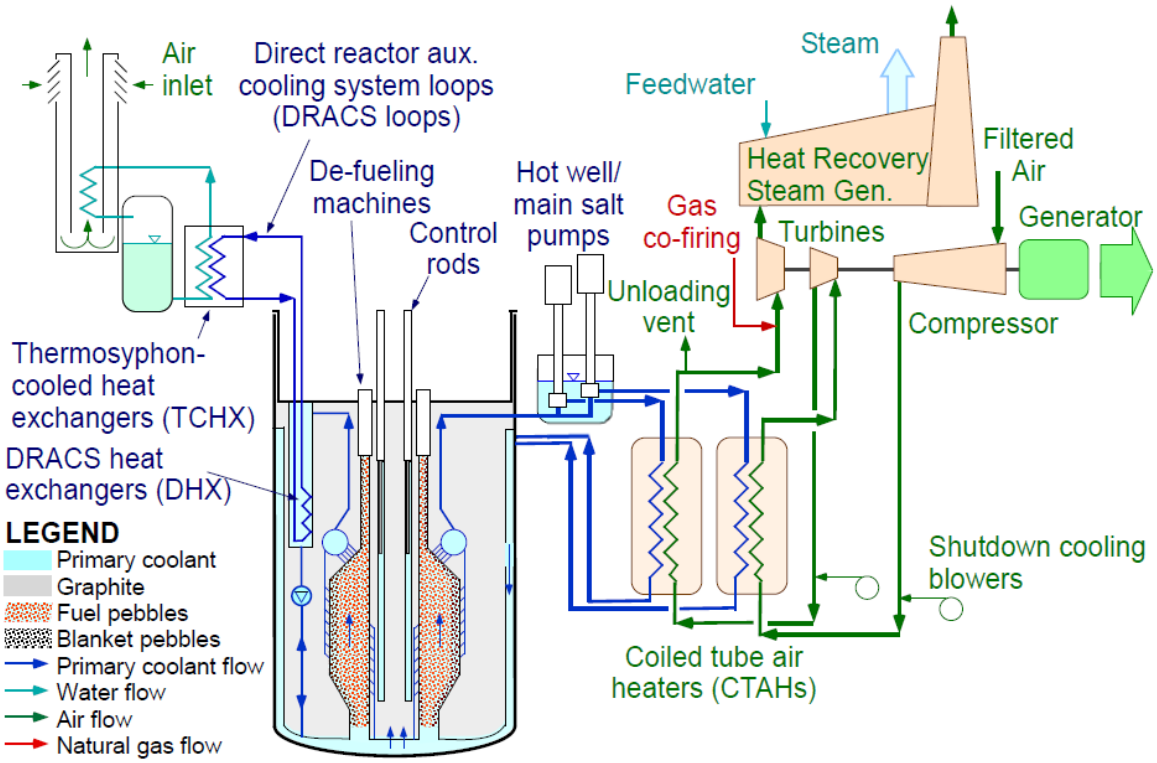

Figure A-2. Schematic plot of the PB-FHR power plant [17]

A.2 The Prismatic Block FHR

A.2.1 Liquid Salt-cooled Very High Temperature Reactor (LS-VHTR)

LS-VHTR is a variation of the VHTR design with liquid coolant and is the predecessor of the later ORNL AHTR designs.

The 2005 baseline LS-VHTR is a large, high-power (2400 MWt), high-temperature (850 to 1000 ºC) reactor with a core power density of 10MWt/m^3. A high-temperature Brayton cycle used for power conversion. The reactor operates with a two-batch refuelling to achieve 18-month fuel cycle with 156MWd/kgHM burnup. As shown below, the baseline LS-VHTR core design from 2005 had some changes from its original 'annular-type' core arrangement from 2004. The total number of fuel channels increased from 324 to 265 while the central reflector blocks were removed, and the core power density increased from 8.3 MW/m^3 to 10 MW/m^3. To reach the burnup, power density and cycle length target, the 2005 version used 15 wt% (increased from the 2004 version's 10 wt%) enriched graphite-coated uranium oxicarbide particle fuel with 25 vol% packing fraction (reduced from the 2004 version's 30 vol%) of the particles in fuel compacts. Same as most FHR designs, the baseline coolant choice for LS-VHTR is 2LiF-BeF2 (FLiBe). [15][65]

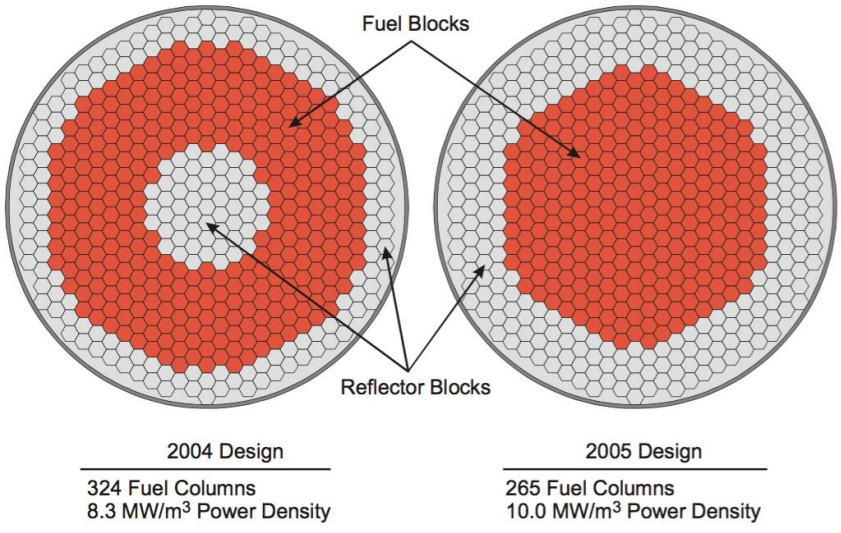

Figure A-3. Comparison of the original LS-VHTR core to an improved design [65]

The reference LS-VHTR features the same prismatic block fuel as the reference VHTR, General Atomics' Gas Turbine Modular High Temperature Reactor (GT-MHTR) as shown below. The hexagonal fuel block has a pitch of 360 mm, height of 793 mm and a fuel pitch of 19 mm. The 216 fuel channels and 108 coolant channels are arranged in a 'homogeneous hexagonal lattice inside the block. At the centre of the fuel assembly, a central hole is reserved for fuel handling. [65]

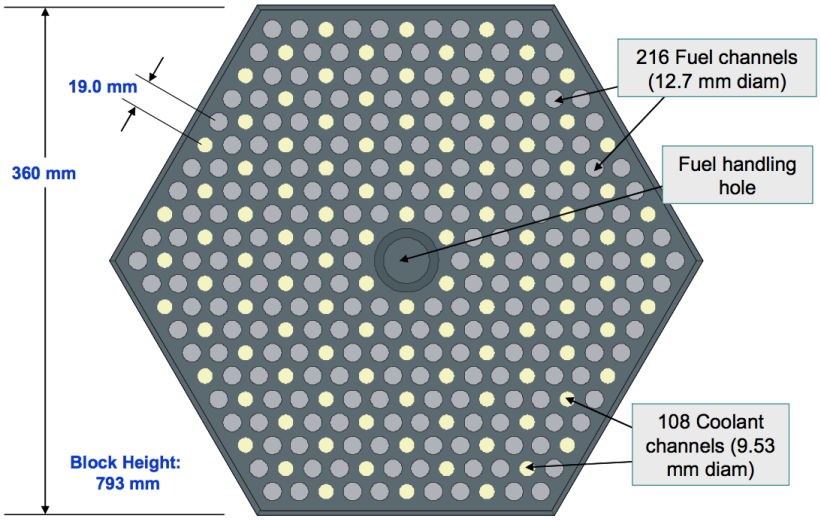

Figure A-4. Cross-sectional view of the LS-VHTR prismatic fuel assembly

There were some concerns for the reference assembly design. Since the LS-VHTR has significantly greater power density and a larger core compared to other NGNP candidates, to achieve NGNP's target burnup and cycle length, the baseline LS-VHTR requires 3-4 times as many fuel blocks and therefore a much more complicated refuelling and fuel handling. Also, with almost all graphite content in the core packed in the form of fuel assemblies and needs to be replaced and abandoned at refuelling, the fuel cycle cost became excessively high due to wasted graphite cost. To address these issues, alternative fuel assembly designs with 'clustered-rod' type fuel lattice were proposed: a tight-pitch array of fuel rods within a single coolant channel surrounded by the graphite block. This is illustrated in Figure A-5. These clustered-rod designs have much simpler refuelling (smaller removable assembly cluster) and improved thermal performance. Much cost can be saved on graphite as the graphite block now becomes part of the permanent structure of the core and need not be replaced at refuelling. [65]

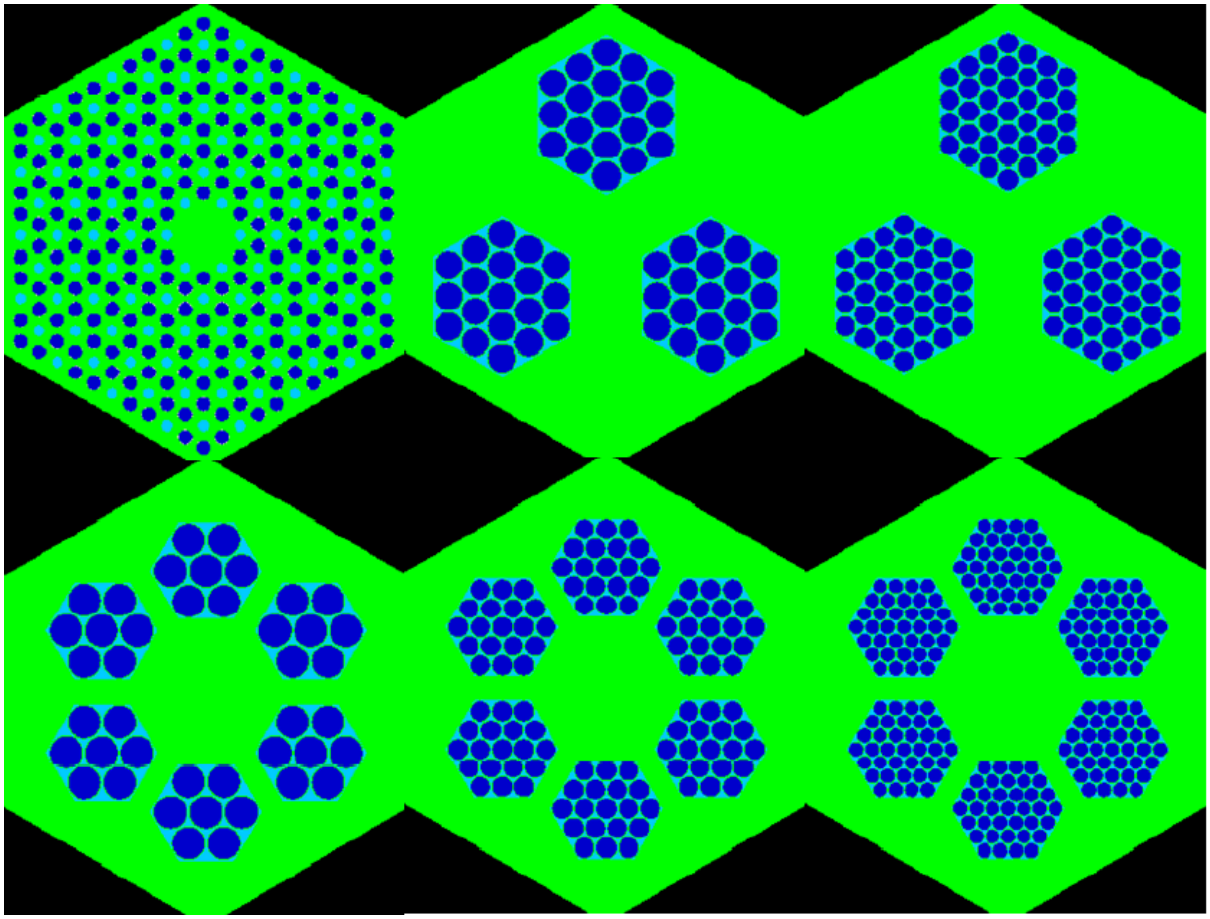

Figure A-5. Basic (top-left) and clustered-rod fuel block configurations of the AHTR

Although LS-VHTR has strong negative fuel temperature feedbacks, molten salt has strong absorption and therefore potentially leading to an unstable core under transient with positive coolant void reactivity (CVR)/ To make CVR more negative, some measures have been tested. Firstly, it was found that CVR becomes more negative with burnup. Therefore, careful fuel management can help to 'lock in' the CVR of the average core to a desired range. Secondly, it was found that the use of burnable poisons that result in spectral shift of neutrons can help make CVR more negative. Also observed was that larger coolant channels can make CVR more negative due to a harder spectrum around the fuel, which increases resonance absorption in U-238. In this regard, the 'clustered-rod' assembly design can be fine-tuned to achieve similar effect. Axial layering also showed to effectively strengthen negative CVR. Lastly, it was discovered that increasing the molar fraction of the BeF_2 in FLiBe can lead to more negative CVR. This is straight forward since Lithum-6 and 7 are the main absorbers in FLiBe. [15][65]

A.2.2 Small Modular Advanced High Temperature Reactor (SmAHTR)

SmAHTR is a small modular version of ORNL's main FHR branch design Advanced High-Temperature Reactor (AHTR) with a 125 MWt power output and a power density of 9.4 MWt/m^3. The core has an active height of 4 metres and an effective diameter of 2.2 metres. With this size, the SmAHTR reactor vessel can be transported via a standard tractor-trailer. The FLiBe coolant enters the core at 650 ºC and exits the core at 692 ºC. With this temperature range, supercritical carbon dioxide (s-CO_2) power cycle was considered as the most attractive power cycle for use with SmAHTR.

Three fuel assembly configurations were explored. The first assembly type uses 72 fuel rods and 19 graphite rods arranged tightly in a triangular lattice, which sits in a large cylindrical coolant channel and is enclosed by a hexagonal graphite block. TRISO fuel particles with a kernel diameter of 500 μm and a U-235 enrichment of 19.75 wt% are encapsulated by graphite matrix with a packing fraction of 40 vol% to form fuel pellets. The fuel pellets and graphite rods all have a diameter of 1.4cm. Each assembly blocks are 80cm tall with a flat-to-flat pitch of 45 cm. Five of these assembly blocks are stacked together in a stringer manner to form a full assembly. Figure A-6 presents an illustration of the cross-section of this assembly design.

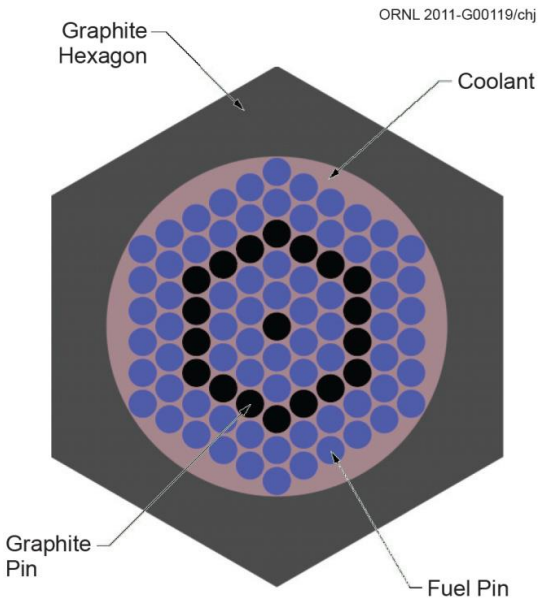

Figure A-6. Stringer-type fuel assmelby evaluted for use with SmAHTR

However, it was considered unfeasible to manufacture the micro-encapsulated fuel pellets to the designed dimension such that it would survive the core operating conditions. [48][49] In addition, how to structurally lock-in the fuel and graphite pins remained a challenge. Therefore, a second stringer-type design was proposed. Instead of using solid cylindrical fuel pellets, the second design used larger, annular fuel 'beads' with a central hole for tie rod. Each fuel bead is 5 cm tall, with 3.25 cm outer diameter and 1.1 cm in inner diameter. Same packing fraction and specifications for TRISO particles was used for the new annular fuel. Fifteen of these fuel rods and 4 solid graphite blocks constitute one assembly, which again has a cylindrical coolant channel surrounded by a hexagonal graphite block. Figure A-7 presents an illustration of the cross-section of the annular pin stringer-type assembly design.

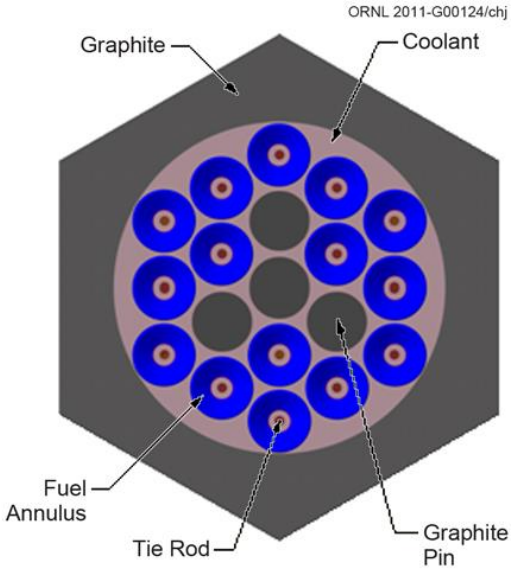

Figure A-7. Annular-pin stringer type fuel bundle evaluated for use in the SmAHTR

The third assembly design abandoned the stringer-type geometry and opted for a plate shape fuel. Keeping the same outer dimension, the assembly is mounted into a carbon-carbon (C-C) composite frame and separated into three diamond shaped fuel zones, each with several full-height fuel plates (4 m) of 2.4 cm thick and 23.4 cm wide. The fuel plates are made with TRISO particles dispersed in carbonaceous ceramic material. On each fuel plate, there are two unfuelled semi-circular 'spacer ridges' that run on one side of the fuel plate along its entire length to provide mechanical rigidity and prevent flow-induced vibration. A representative

plate type fuel bundle is shown as Figure A-8 and Figure A-9. The top and bottom 15 cm of the plate-type assembly are unfuelled and are notched for a C-C retention band to be placed.

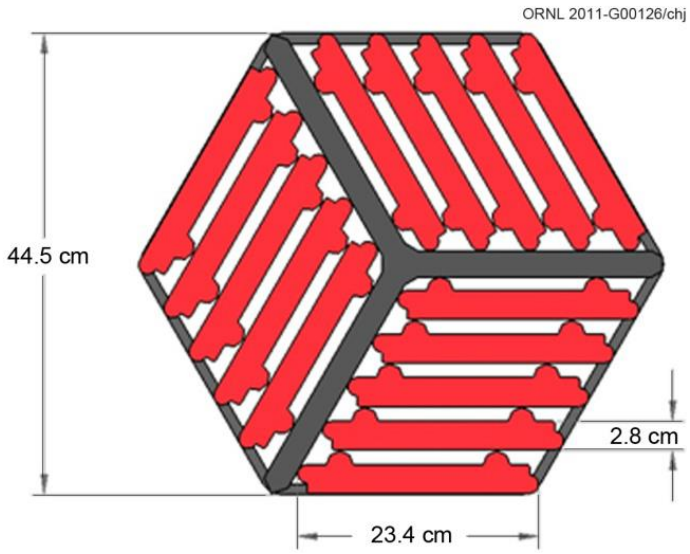

Figure A-8. Cross-sectional view of the SmAHTR plate-type fuel assembly

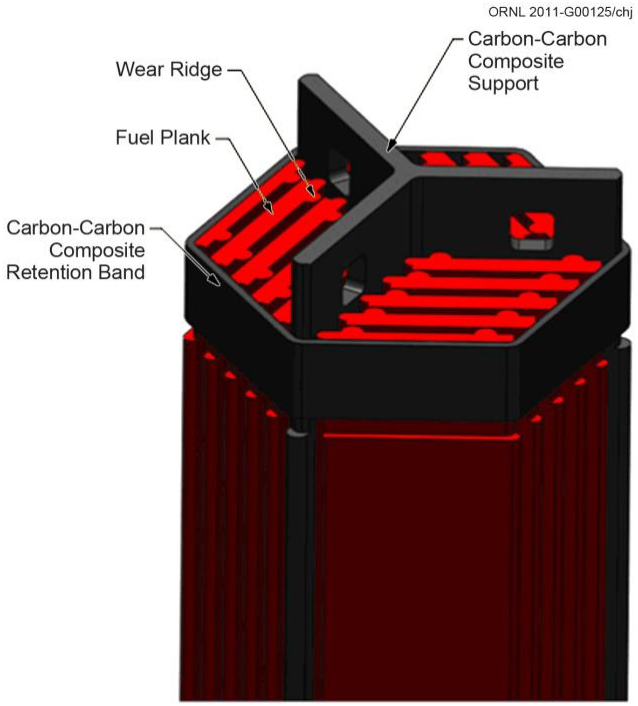

Figure A-9. Isometric view of a plate-type fuel assembly for the SmAHTR

Nineteen fuel assemblies form the SmAHTR active core, which is surrounded by a radial graphite reflector with an outer diameter of 3 m. Eighteen cylindrical coolant channels run vertically through the graphite reflector, each with a diameter of 12 cm. The control rod design differs when using different assembly configurations. The stringer-type assemblies have channels within each assembly reserved for control rods, while the plate type core has some fuel assemblies in which one-third of the volume is filled with control plates instead of fuel plates. Figure A-10 shows an example of the top-down view of the SmAHTR core using the plate type assembly.

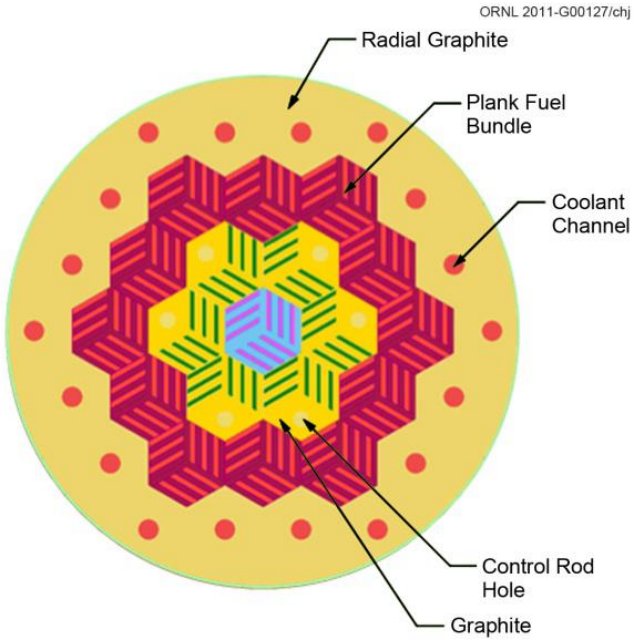

Figure A-10. Cross-sectional view of the SmAHTR core

A.2.3 Commercial-Size Advanced High Temperature Reactor (AHTR)

The AHTR core is 6 m tall with 5.5 m of active core height and reflectors on top and bottom. The core diameter is 9.56 m including radial reflector with 7.81 m wide of fuelled region. AHTR has a power density of 12.9 MMt/m^3 and a once through cycle length of 2.2 years. AHTR also uses FLiBe as the baseline coolant. The power conversion system consists of the primary loop using FLiBe, the intermediate loop of KF-ZrF_4 and the supercritical water power cycle. The in-core coolant temperature ranges between 650 ºC to 700 ºC, allowing a peak steam temperature of 650 ºC in its supercritical water power cycle with a thermal efficiency of 45%.

[34] DRACS is also incorporated in the AHTR, using the similar heat transfer salt to that of the intermediate loop.

The AHTR uses hexagonal prismatic box assembly of 6 m tall and 45 cm from flat-to-flat surface of the hexagon. The outer wall of the assembly is 1 cm thick and also made of C-C composite. The three symmetrical diamond shaped fuel regions are separated by a 4 cm thick Y-shaped C-C structure. Six fuel plates are placed inside each fuel region with 7 cm separation between the plates. The assemblies are placed adjacent to but not directly in contact with each other. FLiBe coolant flows in the 'interassembly gap'. [21] Instead of having semi-fuelled assemblies with control plates used in SmAHTR, the AHTR has control rods in every fuel assembly. |In the centre of the Y-shaped supporting structure of the AHTR assembly, there is a smaller Y-shaped channel for control blade insertion. Figure A-11 illustrates the schematic cross-section of a fuel assembly inside the core.

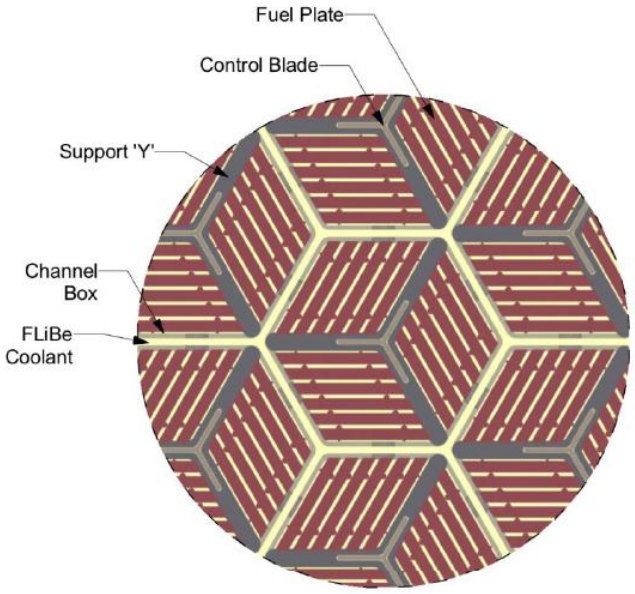

Figure A-11. Cross-sectional view of the AHTR plate-type fuel assembly

Within each AHTR fuel plate, TRISO fuel particles are distributed in two layers (fuel meat) separated by a central carbonaceous material. The fuel meat layer contains tightly packed (40 vol% packing fraction) TRISO particles in graphite matrix and is separated from the coolant salt by a thin (1mm thick) sleeve of carbon material, which prevents the TRISO fuel particles from erosion. The fuel kernel in TRISO particles is UCO enriched to 19.75 wt% in U235. Same

as in the SmAHTR, on each fuel plate, there are also two unfuelled semi-circular ‘spacer ridges’ to provide mechanical rigidity and prevent flow-induced vibration. Figure A-12 shows a vertical cutaway view of the fuel plates.

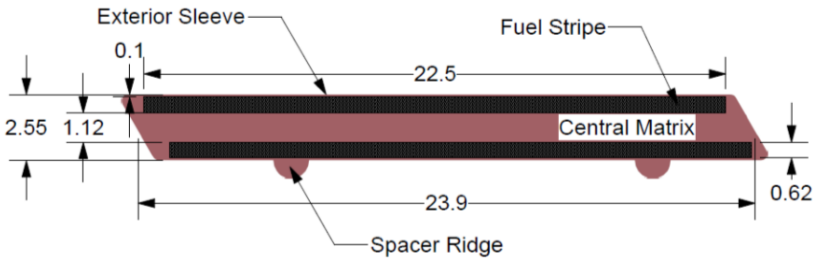

Figure A-12. Cross-sectional View of the updated AHTR fuel plate (dimensions in cm)

Appendix B – Benchmark of TH_Sol with THERMO

THSol (using iterative method) was benchmarked with THERMO using a test assembly design with solid pellets. The power profile was chosen to be a chopped cosine shape. The channel was divided into 83 axial nodes, each 10 cm tall.

Table B-1 summarises the specifications of the test case.

Table B-1. TH_Sol-THERMO benchmarking test case specifications

Mass flow rate per assembly	200000	g/s
Assembly peak power	100000	W
Number of rings	3	
Number of non-fuel pins	1	
Number of fuel pins	36	
Inlet coolant temperature Tin	600	°C
Full core total power	2035	MWt
V average coolant flow velocity	4.67	m/s
Graphite sleeve inner radius	9.5	cm
Pellet outer radius	0.763	cm
Pellet inner radius	0.725	cm
Assembly active height	830	cm
Pitch	2.565	cm
Fuel rod diameter	1.526	cm

Figure B-1 plots the absolute values of the errors between the temperatures of different assembly components the reported by the two solvers.

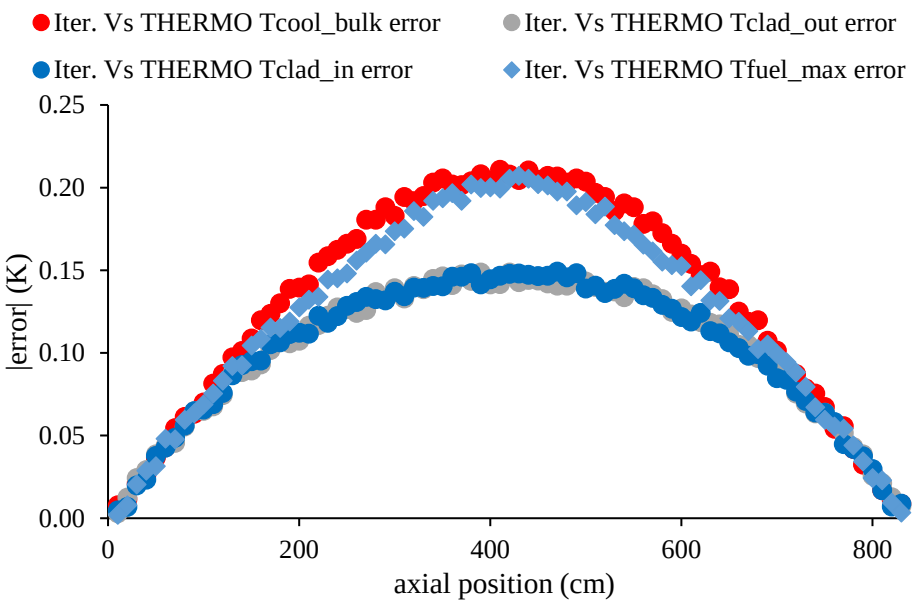

Figure B-1. Absolute Error in temperature profiles between TH_Sol and THERMO

Appendix C – Verification of calcHX model

The heat exchanger simulation subroutine calcHX was validated against published INL report *Feasibility Study of Secondary Heat Exchanger Concepts for the Advanced High Temperature Reactor*. [38] The heat exchanger used is a PCHE. The test case is summarised as follows:

- **Heat exchanger operating conditions:**

Heat transfer duty: 3400 MW

The primary loop of this study is the intermediate loop of an AHTR, the conditions of which are as follows:

Primary loop coolant inlet temperature of the PCHE hot channel: 679 °C

Primary loop coolant outlet temperature of the PCHE hot channel: 587 °C

Primary loop pressure: 0.1MPa

The secondary loop of this study is a Rankin power conversion cycle, the conditions of which are as follows:

Secondary loop inlet temperature of the PCHE cold channel: 251°C

Secondary loop outlet temperature of the PCHE cold channel: 593°C

Secondary loop pressure: 25MPa

- **Material properties:**

The properties of the primary and secondary loop of the PCHE are summarised as follows:

Fluid	*Density (kg/m^3)*	*Thermal conductivity (W/mK)*	*Heat Capacity*	*Viscosity (poise)*
Molten salt	2800	0.45	1046.7	0.051
Water	337	0.29	6510	5.23×10^{-4}

Hasalloy N was chosen as the heat exchanger material, the thermal conductivity of which is 23.5 W/mK.

- **PCHE specifications:**

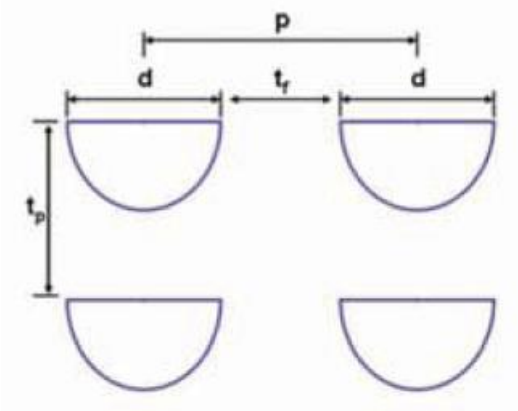

Figure C-1. Channel arrangement of PCHE used in the benchmark study

The specifications of the PCHE (as showed in Fig C.1) modelled in the benchmark study are summarised as follows:

The PCHE is arranged that there are two hot channels per cold channel

- Channel diameter: d = 0.003 m
- Channel pitch: p = 0.0033 m
- Plate thickness: t_p = 0.00317 m
- Channel horizontal distance: $t_f = 3\times10^{-4}$ m
- Total flow area (hot channel): 13m^2
- Total flow area (cold channel): 6.5 m^2

- **Benchmark results:**

The simulation results reported by calcHX and INL report on the heat exchanger case above are summarised as above:

- Number of channels required:
  - calcHX: 3.680×10^6
  - INL report: 3.678×10^6
- Heat exchanger channel length requirement:
  - calcHX: 0.859 m
  - INL report: 0.860
- Pressure drop in hot channel:

calcHX: 4.0526×10^6 Pa

INL report: 4.0530×10^6 Pa

- Pressure drop in cold channel:

  calcHX: 1.5206×10^6 Pa

  INL report: 1.521×10^6 Pa

Appendix D – Verification of sizeHX model

E. S. Kim et al. came up with a set of analytical equations to determine the optimum heat exchanger size and aspect ratio, hereon referred to as analytical solutions, which are summarised as follows: [40]

$$A_{opt} = \left(\left(\frac{3 - b + i}{b} \right) \left(\frac{K_2}{K_1} \right) \right)^{\frac{1}{3+i}} \tag{D.1}$$

where A_{opt} is the frontal free flow area of the optimised PCHE. The optimum aspect ratio is

$$\frac{H_{opt}}{L_{opt}} = \frac{{A_{opt}}^{1.5-b}}{\sigma^{1.5}\text{FACT4}} \tag{D.2}$$

where

$$K_1 = C_{HXvol}(1 - \sigma)\text{FACT4} \tag{D.3}$$

$$K_2 = C_{pump} Y \left(\frac{\dot{m}_h \text{FACT5}}{\rho_h} + \frac{\dot{m}_c \text{FACT6}}{\rho_c} \right) \tag{D.4}$$

$$\text{FACT1} = \left(\frac{a k_h}{d_e} \right) \left(\frac{d_e \dot{m}_h}{0.5\mu} \right)^b {Pr_h}^c \tag{D.5}$$

$$\text{FACT2} = \left(\frac{a k_c}{d_e} \right) \left(\frac{d_e \dot{m}_c}{0.5\mu} \right)^b {Pr_c}^c \tag{D.6}$$

$$\text{FACT3} = \frac{1}{(1/\text{FACT1}) + (1/\text{FACT2})} \tag{D.7}$$

$$\text{FACT4} = \frac{2Q}{\beta \text{FACT3LMTD}} \tag{D.8}$$

$$\text{FACT5} = \left[e \left(\frac{d_e \dot{m}_h}{0.5\mu_h} \right)^i \left(\frac{{\dot{m}_h}^2}{\rho_h} \right) \left(\frac{8}{d_e} \right) \right] \sigma \text{FACT4} \tag{D.9}$$

$$\text{FACT6} = \left[e \left(\frac{d_e \dot{m}_c}{0.5\mu_c} \right)^i \left(\frac{{\dot{m}_c}^2}{\rho_c} \right) \left(\frac{8}{d_e} \right) \right] \sigma \text{FACT4} \tag{D.10}$$

where Q is the heat exchanger duty; σ, β, d_e are the ratio of total frontal flow area to the total frontal area, surface area density and hydraulic diameter of the heat exchanger respectively; ρ, k, μ, and $\dot{m}$ are the density, thermal conductivity, viscosity and mass flow rate of the fluids

respectively; the subscript *h* and *c* represent hot and cold channel fluids respectively. Parameters *a*, *b*, *c*, *e* and *i* are the parameters in the correlations for calculating Nusselt number and friction factor:

$$Nu = aRe^{b}Pr^{c} \quad (D.11)$$

$$f = eRe^{i} \quad (D.12)$$

For the selected PCHE base specifications in this study, σ = 0.338, β = 737.252 1/m, d_e = 1.833 mm. In the Hesselgreaves universal correlations used in this study, a = 0.125, b = 0.64, c = 0.33, e = 1.0425 and i = -0.76.

These equations were derived based some simplifying assumptions: 1) the heat exchanger cost calculation assumed no discounting on the capital investment and a 100% capacity factor for the reactor. 2) a 100% efficiency of heat transfer was assumed in calculating secondary fluid heat addition and a perfect isentropic efficiency of pumps was also assumed. 3) The code only considered frictional pressure loss when calculating required pumping power. 4) the thermal resistance of the heat exchanger wall is assumed to be zero. 5) In both calcHX and in the analytical optimisation derivations, the longitudinal heat loss was assumed to be zero.

To benchmark sizeHX with the analytical optimisation solutions, Assumption 1 and 2 in the analytical optimisation solution are corrected based on the assumptions made in calcHX, i.e., discounting was introduced, heat exchanger effectiveness is assumed to be 98% and pump efficiency is assumed to be 89%. Assumption 3 and 5 were also made in calcHX and thus unchanged in the analytical equations. However, introducing assumption 4 to the analytical equations would render the derivation invalid and assumption 4 was therefore left unchanged. A PCHE sizing exercise was performed using both sizeHX and the analytical method for an example set up of a primary heat exchanger for a proposed FHR: 6000MWt power with FLiBe coolant salt which enters the hot channel at 700°C and exits at 640°C. The secondary coolant salt NaF-ZrF_4 enters the cold channel at 614°C and exits at 675°C. The size optimisation results using the two methods are presented in Table 4.1. The optimum annual costs predicted using sizeHX and the analytical method for the heat exchanger differed by 10.4%. The differences in the results were speculated to be due to assumption 4 made in analytical optimisation derivation. Assumption 4 overestimates the overall heat transfer coefficient of the heat exchanger and thus, the analytical method would underpredict the required heat transfer area and therefore underestimates the required capital investment in heat exchanger.

Table D-1. Benchmarking results for an example primary heat exchanger condition

Parameters	*sizeHX*	*Analytical*	*error (%)*
Min total annual cost(m$)	47.25	42.74	-10.04
PCHE length (m)	2.37	2.20	-7.68
PCHE volume (m^3)	86.81	75.67	-13.72
Min annual capital cost (m$)	35.02	30.53	-13.72
Min annual operating cost (m$)	12.23	12.21	-0.17

To separate and quantify the effects of this assumption and thus validate the optimisation code sizeHX, two more benchmark cases were carried out. 1) molten salt coolants are replaced with CO_2, which has larger thermal resistance and would make assumption 4 more realistic, and 2) the thermal resistance of the wall was assumed zero by brute force in calHX calculation routine. Table 4.2 shows the results from the first test. The differences between the values obtained using the two methods were smaller in the CO_2 case. Almost identical (less than 0.1% difference) results were obtained using analytical optimisation solution and sizeHX in the second test. This confirmd that the difference in optimum PCHE design found by the two methods was the result of assumption 4 used in the analytical derivation. Although requiring marginally more computational time than does the analytical method, calHX produced more realistic results for heat exchanger size optimisation.

Table D-2. Benchmarking results for an example heat exchanger using CO_2

Parameters	*sizeHX*	*Analytical*	*error (%)*
Min total annual cost(m$)	68.5	63.9	-6.9
PCHE length (m)	1.3	1.3	-5.3
PCHE volume (m^3)	124.4	113.2	-9.4
Min annual capital cost (m$)	50.2	45.7	-9.4
Min annual operating cost (m$)	18.3	18.3	-0.1

Appendix E –Power Scaling vs Heat Transfer System Cost Scaling

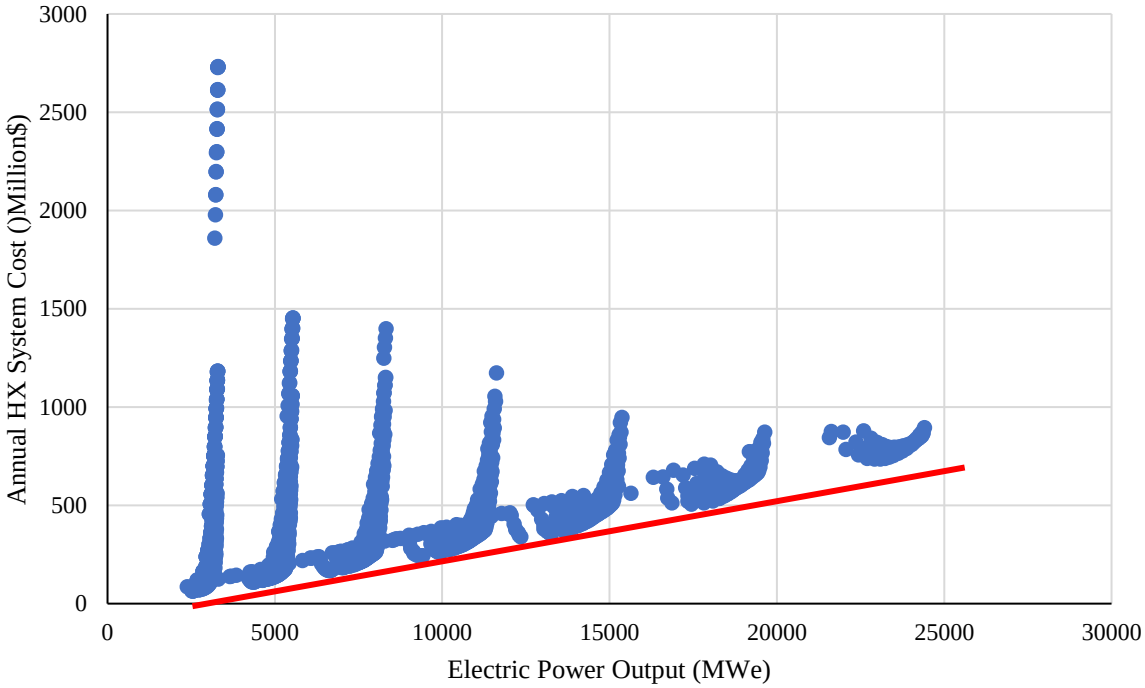

Figure E-1. Relationship between power scaling and heat transfer system cost scaling

The above figure plots the annual HX system cost against electric power output for all FLiBe cooled UC fuelled solid pin type FHRs (similar behaviour is likewise expected for other design streams). For each design, a wide range of pressure drops was covered: 50kPa to 1000kPa. The optimised pressure drop chosen by SCOOP for a given design would be the one that minimises the annual HX system cost, i.e. the red line that connects the lower frontier of the scatter plot. The spikes on the above plot represent the designs with un-optimised operating conditions, i.e., pressure drop and temperature drop.

The figure shows that the optimised HX cost has a linear behaviour with power. To check whether the ratio of HX cost is similar to that of the power, two arbitrary optimised design results (ones that lie on the red line) were chosen:

Table E-1. Comparison of heat transfer system cost ratio and power ratio

Power (MWe)	optimised_HXcost(Million $)
4496	123.91
18088	523.04
Q/Q ratio =	4.023
HXcost/HXcost ratio =	4.221

This study shows that HX cost ratio, P, is similar to the ratio Q_s/Q_r, i.e., power ratio, and this behaviour is stable across the whole design space covered in the thesis.

Appendix F – Alternative Unit Cell Depletion Results

The depletion results for the alternative design streams are summarised as follows:

F.1 Solid FCM pin FLiBe cooled FHR

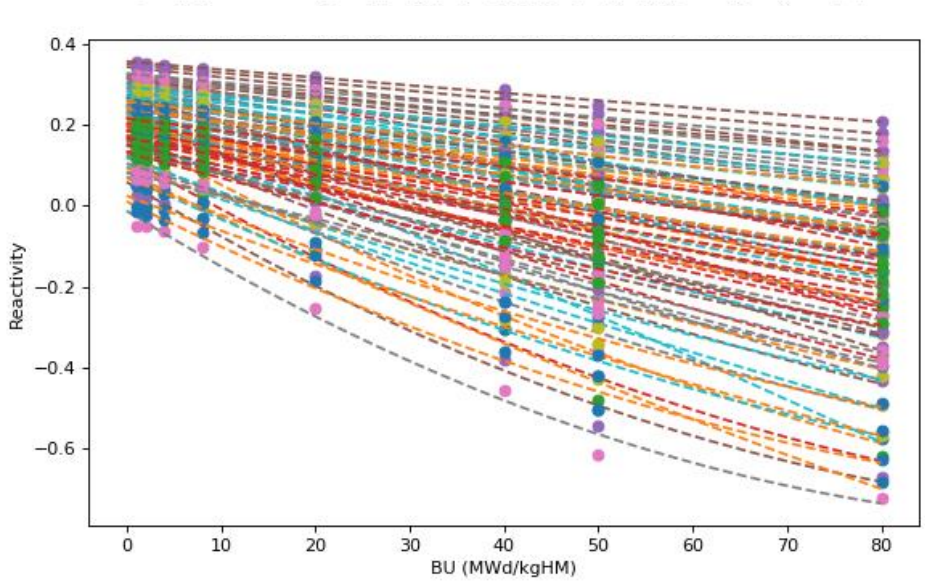

Figure F-1. Depletion curves for all selected solid pin FCM pin FLiBe cooled models

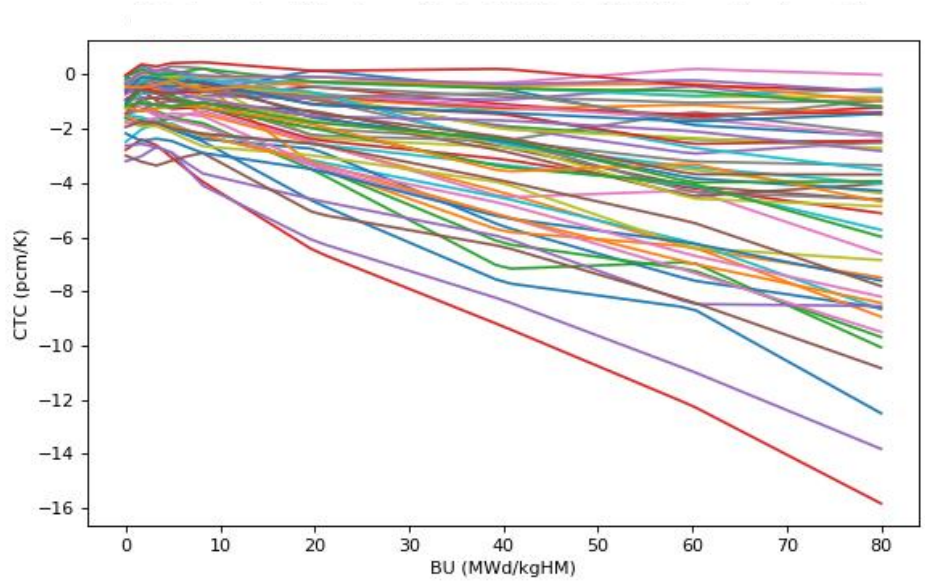

Figure F-2. CTC depletion behaviour for solid UC pin FLiBe cooled models

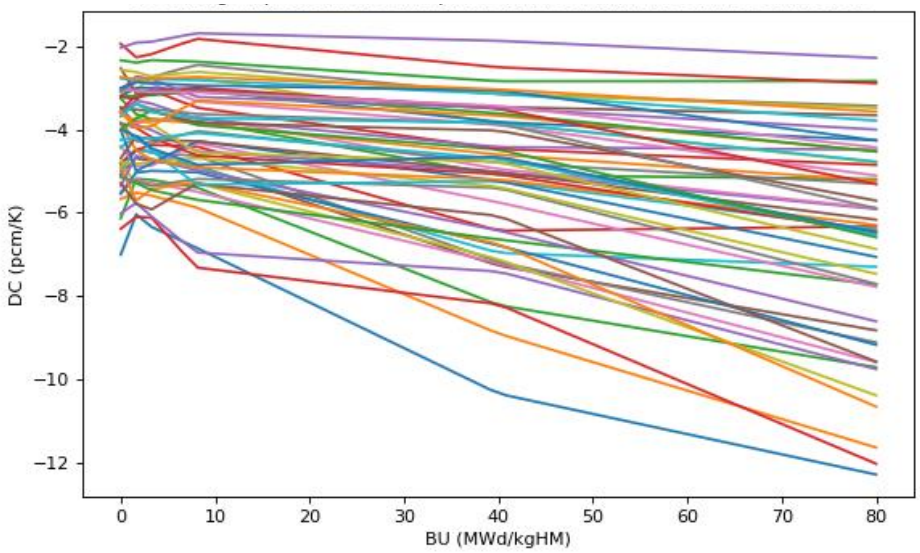

Figure F-3. DC depletion behaviour for solid UC pin FLiBe cooled models

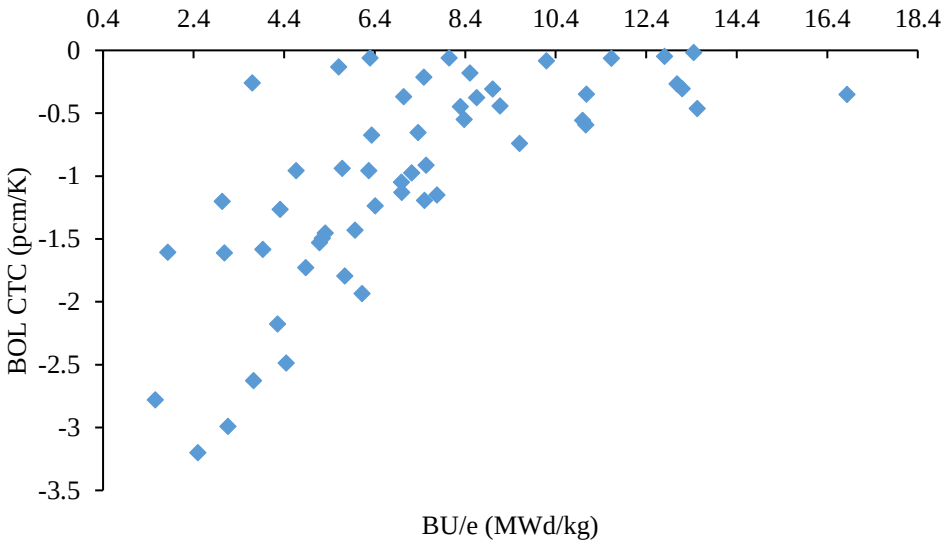

Figure F-4. BOL CTC vs BU/e performance domain for solid FCM pin FLiBe cooled models

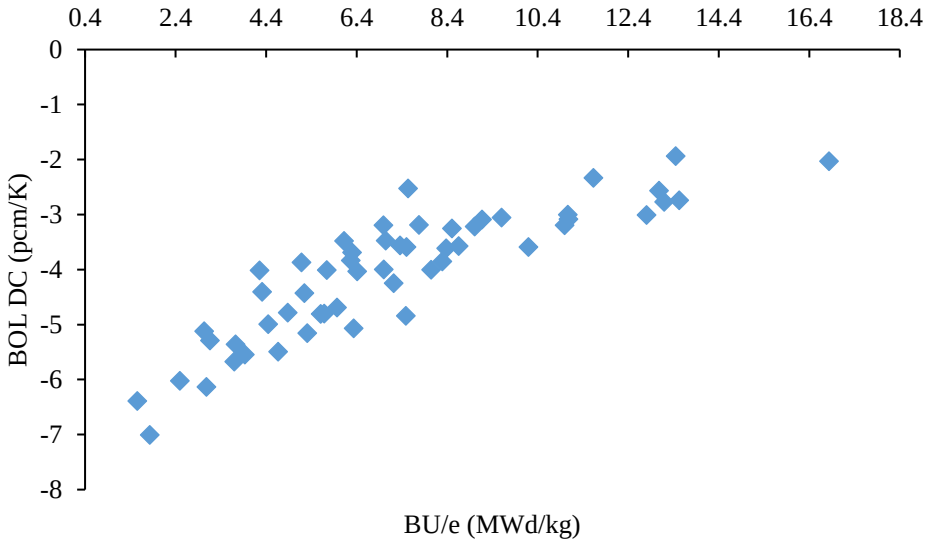

Figure F-5. BOL DC vs BU/e performance domain for solid FCM pin FLiBe cooled models

F.2 Annular FCM pin FLiBe Cooled FHR

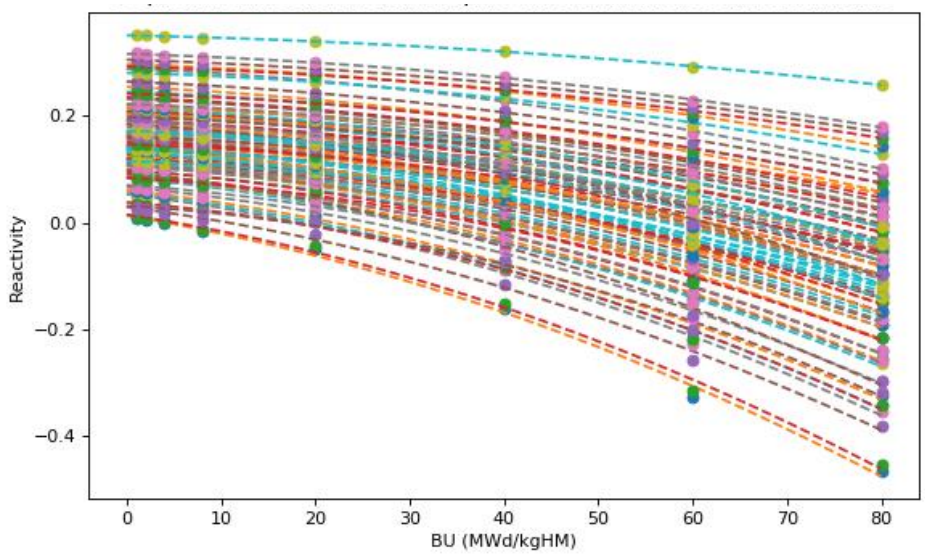

Figure F-6. Depletion curves for all selected annular pin FCM pin FLiBe cooled models

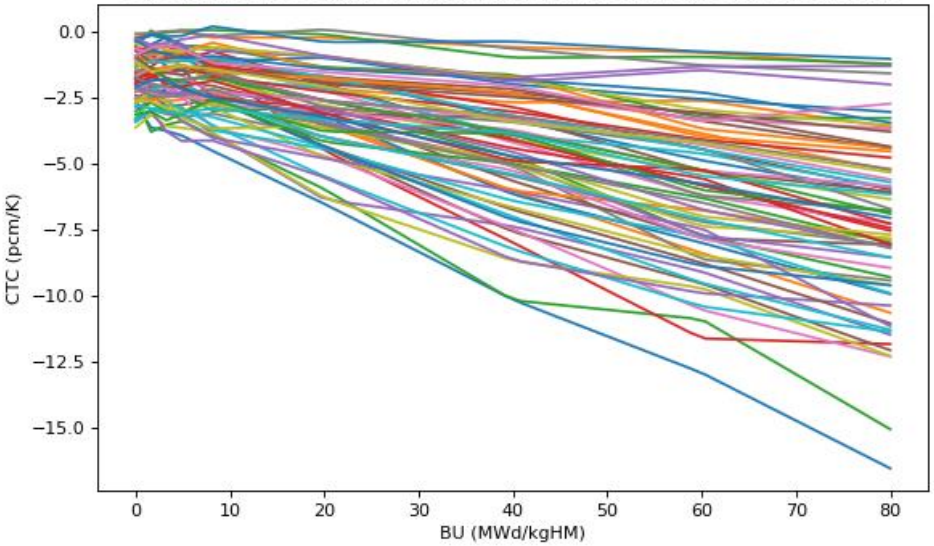

Figure F-7. CTC depletion behaviour for annular pin FCM pin FLiBe cooled models

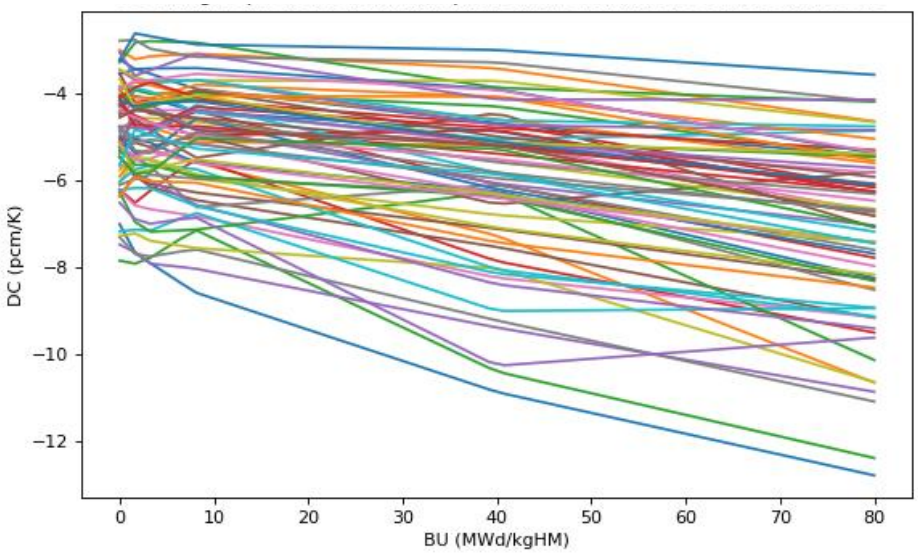

Figure F-8. DC depletion behaviour for annular pin FCM pin FLiBe cooled models

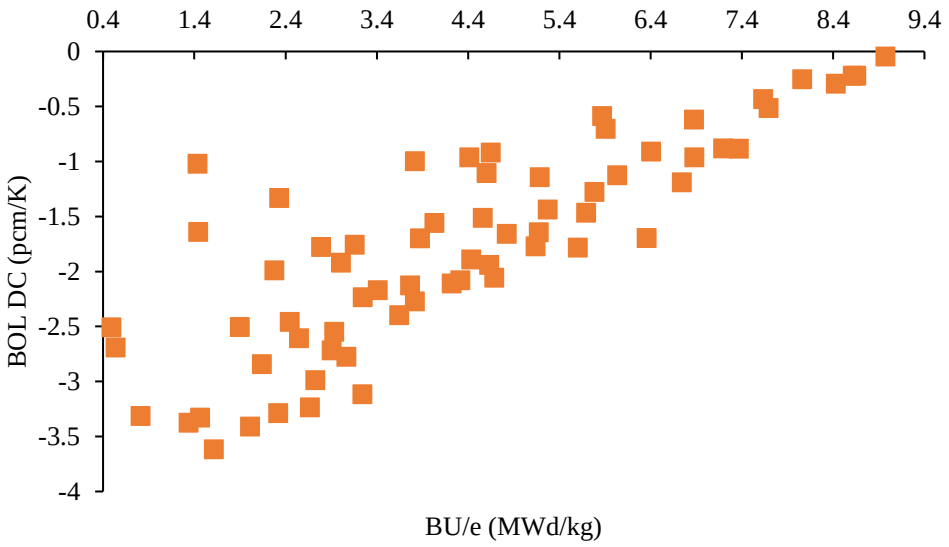

Figure F-9. BOL CTC vs BU/e domain for annular FCM pin FLiBe cooled models

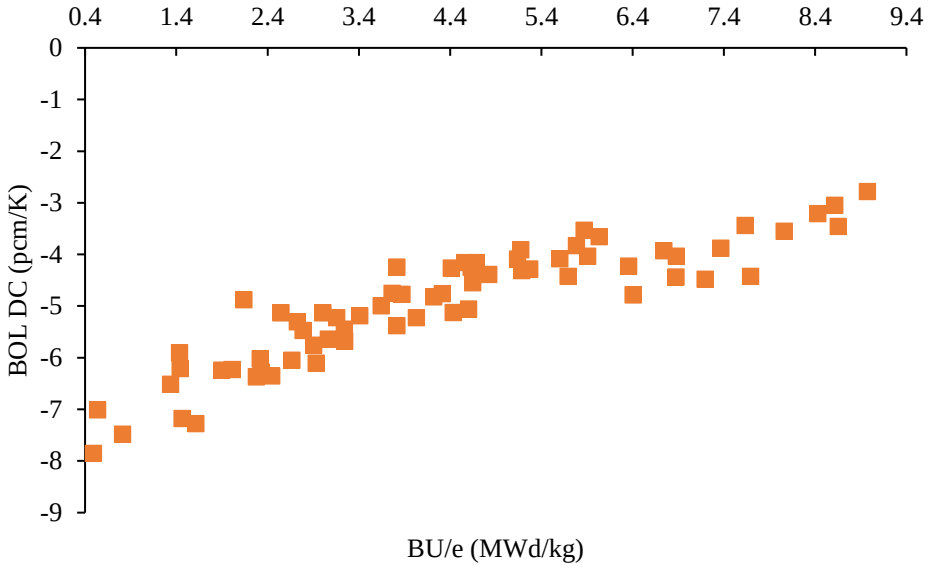

Figure F-10. BOL CTC vs BU/e domain for annular FCM pin FLiBe cooled models

F.3 Solid UC pin NaF-ZrF_4 Cooled FHR

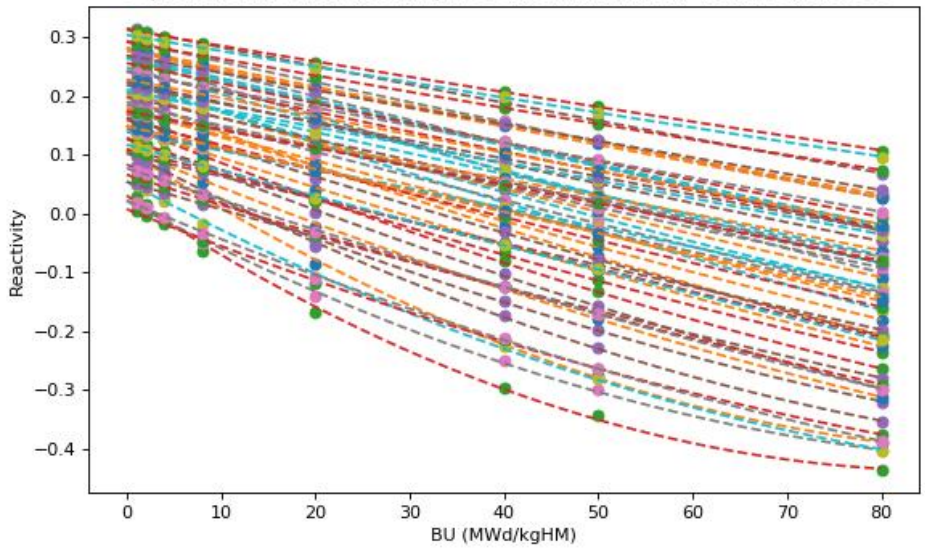

Figure F-11. Depletion curves for solid pin UC pin NaF-ZrF_4 cooled models

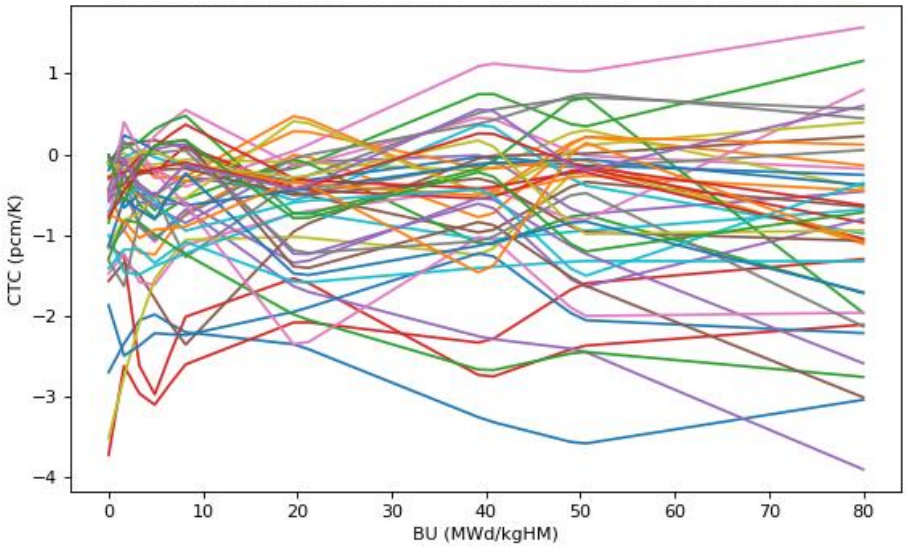

Figure F-12. CTC depletion behaviour for solid pin UC pin NaF-ZrF_4 cooled models

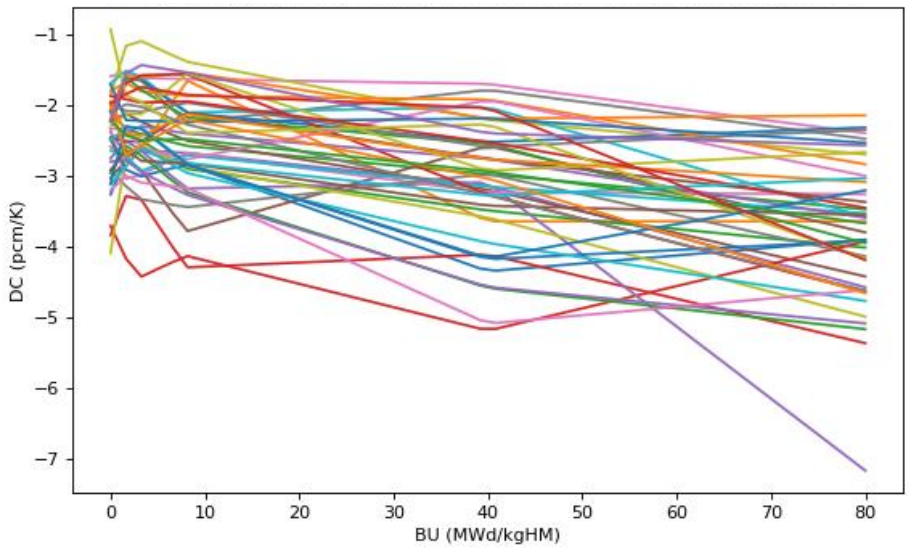

Figure F-13. DC depletion behaviour for solid pin UC pin NaF-ZrF_4 cooled models

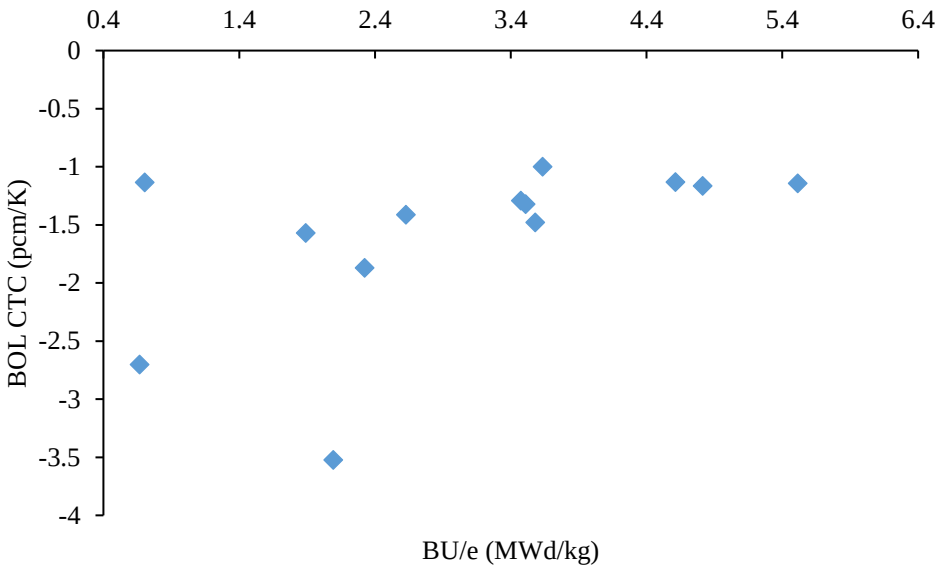

Figure F-14. BOL CTC vs BU/e domain for solid UC pin NaF-ZrF_4 cooled models

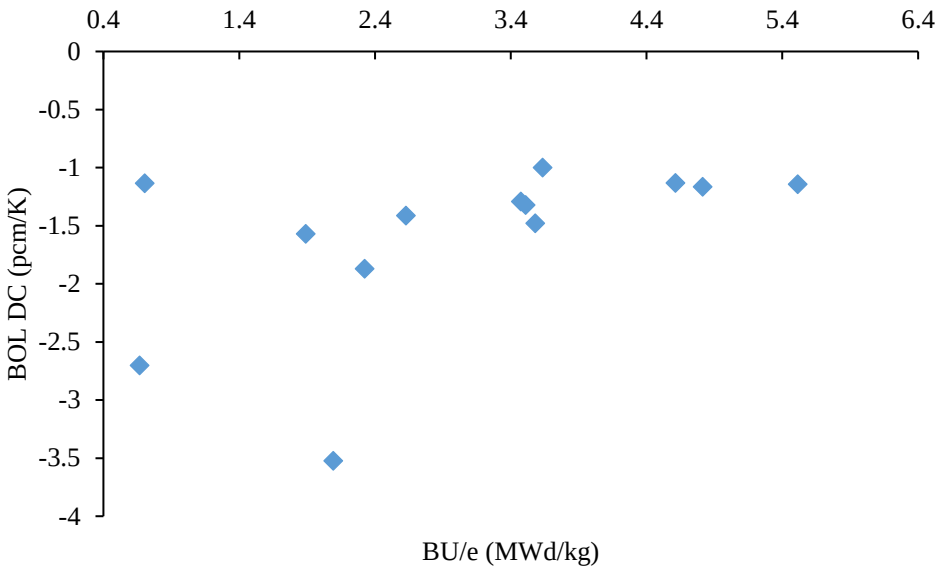

Figure F-15. BOL DC vs BU/e domain for solid UC pin NaF-ZrF_4 cooled models

Appendix G – Effects of P/D and SF on LCOE and Power for Annular Pin FHRs

Figures representing the effects of P/D and SF on the LCOE and maximum achievable power for annular pin FHRs are summarised as follows. The different shades of the points represent different fuel thicknesses.

The follow two figures were plotted using 3-ring annular FHR with varying inner graphite channel radii at $\Delta p = 200$ kPa.

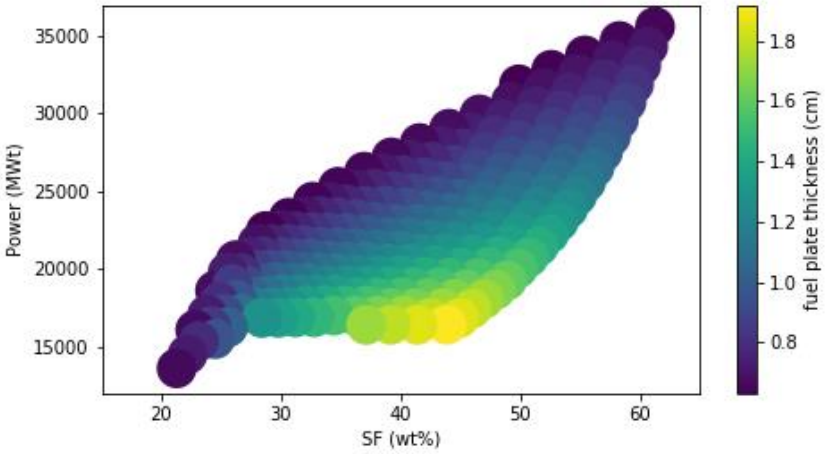

Figure G-1. Maximum achievable power vs SF and fuel thickness for annular pin FHRs

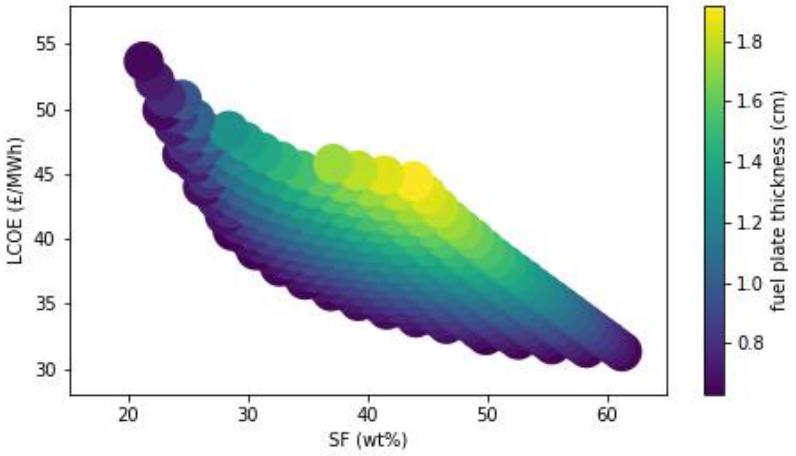

Figure G-2. LCOE vs SF and fuel thickness for annular pin FHRs

The follow two figures were plotted using inner graphite channel radius of 19.5 cm with 3-ring, 4-ring and 5-ring assembly designs at $\Delta p = 200$ kPa.

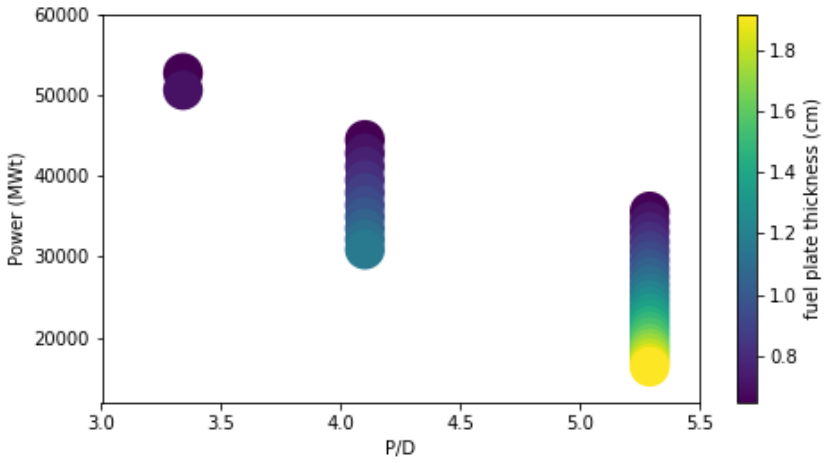

Figure G-3. Maximum achievable power vs P/D and fuel thickness for annular pin FHRs

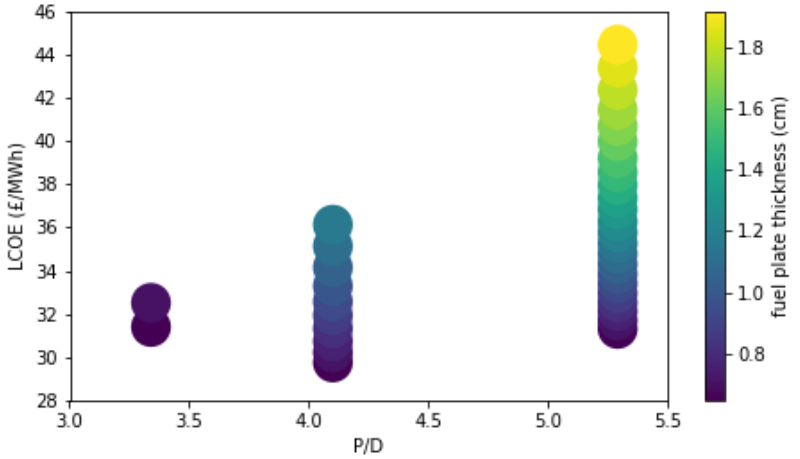

Figure G-4. LCOE vs P/D and fuel thickness for annular pin FHRs